Creep: Time-dependent brittle deformation in rocks

Michael John Heap

A thesis submitted to the University College London

For the degree of Doctor of Philosophy

2009

Department of Earth Sciences

University College London

Abstract

The characterization of time-dependent brittle rock deformation is fundamental to understanding the long-term evolution and dynamics of the Earth's crust. The chemical influence of pore water promotes time-dependent deformation through stress corrosion cracking that allows rocks to deform at stresses far below their short-term failure strength. Reported here are results from a study of time-dependent brittle creep in a suite of sandstones and a basalt under triaxial stress conditions. Results from conventional creep experiments show that creep strain rate is heavily dependent on the applied differential stress, a reduction of only 10% in differential stress results in a decrease in creep strain rate of more than two orders of magnitude. Conventional creep experiments have also demonstrated the possible existence of a critical damage threshold at the onset of the tertiary creep phase. The level of damage in the samples at the onset of acceleration to failure, regardless of the applied differential stress and the creep strain rate, is approximately similar. Furthermore, the relative proportions of the three phases classically used to describe creep are approximately the same, regardless of creep strain rate and rock type.

Sample variability results however in significant scattering in the experimental data and numerous experiments are needed to clearly define a relation between the strain rate and the applied stress. Hence, it is demonstrated that stress-stepping creep experiments provide a means to successfully overcome this problem. The influence of effective stress was investigated in stress-stepping experiments with effective confining pressures of 10, 30 and 50 MPa (whilst maintaining a constant pore fluid pressure of 20 MPa). In addition to the expected purely mechanical influence of an elevated effective pressure results also demonstrate that stress corrosion appears to be inhibited at higher effective pressures. The influence of doubling the pore fluid pressure however, whilst maintaining a constant

effective pressure, is shown to have no effect on the rate of stress corrosion. Stress-stepping creep experiments have also demonstrated that the influence of an elevated temperature (from 20° to 75°C) has a profound effect on stress corrosion. For the same applied constant stress, creep strain rates are seen to increase by up to three orders of magnitude in sandstone. For basalt however, creep strain rates are only modestly affected. This is likely to be due to the high quartz content of sandstone that has been shown previously to be greatly influenced by temperature in double-torsion experiments. All of the results are discussed in the context of microstructural analysis, acoustic emission hypocentre locations, mineralogy and fits to proposed macroscopic creep laws and a creep flow law.

Elastic moduli are crucial parameters for defining relationships between stress and strain. Importantly, volcano monitoring techniques routinely running at Mt. Etna for example, such as seismic tomography and ground deformation modelling, rely on accurate knowledge of elastic moduli. Increasing-amplitude stress-cycling experiments have been performed on two extrusive basalts and two porous sandstones. Experiments have shown that stress-cycling results in a reduction in sample stiffness, equating to a decrease in Young's modulus and an increase in Poisson's ratio. These changes are attributed to the growth of new cracks and the extension of pre-existing cracks during each stress cycle and, hence, an increase in the total crack density. This interpretation is supported by the observation of the Kaiser 'stress-memory' effect, where cracking-associated microseismicity (acoustic emission or AE) on any stress cycle only occurs when the maximum stress in any previous cycle has been exceeded. It is also shown that in stress cycles in which the previous maximum stress is not exceeded, no AE output is generated and there are no further changes in elastic moduli. The results are interpreted in relation to measurements of tectonic-volcano (VT) seismicity and deformation at Mt. Etna volcano.

List of figures (thesis contains 174 figures)

List of tables (thesis contains 30 tables)

List of abbreviations, selected units and symbols

VT	volcano-tectonic
DT	double-torsion
LVDT	linear variable differential transducer
XPL	cross-polarized light
PPL	plane-polarized light
SEM	scanning electron microscope
AE	acoustic emission
AMS	anisotropy of magnetic susceptibility
pAMS	void space anisotropy
mAMS	magnetic anisotropy of a dry rock matrix
tAMS	total magnetic anisotropy
UCS	unconfined compressive strength
P_p	pore fluid pressure
P_c	confining pressure
P_{eff}	effective confining pressure
T	temperature

cS	centistokes
dB	decibels
Pa	pascal
MPa	megapascal

A_{arb}	arbitrary internal or external surface of area
F	uniformly distributed force
T_r	resultant stress or traction
σ_n	normal stress
τ	shear stress
T_n	stress vector
σ_1	greatest principal stress
σ_2	intermediate principal stress
σ_3	least principal stress
L	final length
L_0	original length
ε	strain
V	final volume
V_0	original volume
ε_v	volumetric strain
ε_s	shear strain
ε_n	strain vector
ε_1	greatest principal strain
ε_2	intermediate principal strain
ε_3	least principal strain

ψ	change in angle caused by shear strain
ρ	rock density
g	acceleration due to gravity
z	depth in the Earth
σ	stress
ρ_w	density of water
σ_t	theoretical (cohesive) strength of rock
A_{eq}	equilibrium spacing
E	Young's modulus
σ_∞	uniform tensile load
$2C$	crack length
W	work exerted by an external boundary force
U_e	internal stain energy
U_s	energy expenditure
U	total energy for a static crack
U_m	stored elastic strain energy or mechanical energy
y	length of rod
σ_{crit}	critical stress at which a crack will be at equilibrium
d	thickness of mica flake
h	height of mica flake
G	crack extension force
K	stress intensity factor
r	distance from the crack tip
θ	angle measured from the crack plane
v	Poisson's ratio
K_c	critical stress intensity factor
G_c	critical crack extension force
K_{Ic}	fracture toughness
f	function to represent at least one characteristic of a material
$tan\varphi$	coefficient of internal friction
C	cohesive strength
C'	onset of shear-induced dilatancy
C^*	onset of shear-enhanced compaction
P^*	onset of grain crushing and pore collapse
D'	transition from compaction-dominated to dilatancy-dominated deformation
μ	coefficient of friction
σ_H	hydrostatic pressure
σ_L	lithostatic pressure
α	constitutive relation of poroelasticity multiplier or effective stress coefficient
σ_n'	effective normal stress
H^+	hydrogen ions
Na^+	sodium ions
HCl	hydrochloric acid
Si	silica
O	oxygen
P	load on double-torsion sample
W_{DT}	width of double-torsion sample
L_{DT}	length of double-torsion sample

a	length of the propagating crack in double-torsion sample
d_{DT}	thickness of double-torsion sample
OH^-	hydroxyl groups
K_0	stress corrosion limit
Q	applied differential stress
$\dot{\varepsilon}$	strain rate
A	constant in power law creep model
M	constant in exponential creep model
η	constant in power law creep model
β	constant in exponential creep model
v_c	crack velocity
R	universal gas constant
T_a	absolute temperature
n	stress corrosion index
Ω_t	total strain
Ω_I	amplitude of the primary creep component
Ω_{III}	amplitude of the tertiary creep component
T_t	transient time
t_f	asymptotic failure time
m	positive power law exponent
u	positive power law exponent
σ_f	fundamental strength of time-dependent deformation
E_a	stress free activation energy
V_a	activation volume
ρ_{ct}	radius of the curvature of the crack tip
V_m	molar volume of glass
γ	interfacial surface energy between the glass and the reaction products
M_{dry}	dry mass
M_{wet}	wet mass
M_{arch}	submersed mass
ϕ	porosity
A_{exp}	bulk experimental elastic anisotropy
V_{max}	maximum experimentally measured ultrasonic velocity
V_{min}	minimum experimentally measured ultrasonic velocity
V_{mean}	mean experimentally measured ultrasonic velocity
V_p	P-wave velocity
V_s	S-wave velocity
σ_p	short-term peak stress
P	number of crack intersections
$P_\perp$	crack intersections orientated normal to the axial loading direction
$P_\parallel$	crack intersections orientated perpendicular to the axial loading direction
P_v	crack densities per unit volume
A_c	anisotropy of the crack distribution
S^*_c	compressive strength

Publications to arise from this study

[1] **Heap, M. J.**, S. Vinciguerra, P. G. Meredith, 2009. The evolution of elastic moduli with increasing damage during cyclic stressing of a basalt from Mt. Etna volcano. *Tectonophysics*, **471**, 153-160.

[2] **Heap, M. J**., Baud, P., Meredith, P. G., Bell, A. F. and Main, I. G., 2009. Time-dependent brittle deformation in Darley Dale sandstone. *J. Geophys. Res. In press.*

[3] Ventura, G., Vinciguerra, S., Moretti, S. Meredith, P. G., **Heap, M. J**., Baud, P., Shapiro, S. A., Dinske, C. and Kummerow, J. 2009. Understanding slow deformation before dynamic failure. *Invited contribution to UNESCO International Year of Planet Earth special issue book series (Ed: Tom Beer). In press.*

[4] **Heap, M. J**., Baud, P. and Meredith. P.G., 2009. The influence of an elevated temperature on brittle creep in sandstones. *Submitted to GRL.*

[5] **Heap, M. J**., Baud, P., Meredith, P. G., Vinciguerra, S., Bell, A. F. and Main, I. G., 2009. Time-dependent brittle deformation in Etna basalt. *In prep.*

[6] **Heap, M. J**., Faulkner, D. R., Vinciguerra, S. and Meredith, P. G., 2009. Elastic moduli evolution and accompanying stress changes with increasing crack damage during the cyclic stressing of rocks. *In prep.*

Acknowledgements

Firstly, I express my appreciation to my supervisors: Phil Meredith, Patrick Baud and Sergio Vinciguerra. Their extensive knowledge, encouraging support and contrasting styles have helped mould me into a more rounded scientist. Indeed, some of the visits to Strasbourg helped in making me 'especially rounded'. Above all, these three are quality individuals and have greatly contributed to my enjoyment of the last three years.

I express endless gratitude to Neil Hughes, Steve Boon and John Bowles. Without their tireless dedication and patience to repair my minor mishaps I would still be sitting in the lab. Help was always free-flowing despite the 'do you know who I am' attitude. Albeit, I'm sure all three came very close to punching me in the face on several occasions. Socially, these guys were just as reliable. I will certainly miss football on Fridays, the occasional foray to the pub, not to mention the highly agreeable level of abusive banter on a daily basis.

Thanks go to the many members of the lab, coffee club and Ph.D/staff community that have made my time at UCL memorable. Namely, Ed, Simon, Almar, Rosie, Dan, Sami, Pete, Phil, Ellie, Ben, Helen, Adrian, David, Peter, Ian, Chris and Ruth. Thanks must also go to Jim, Sean, Ron, Jen, Celine, Leisa, Richard and Danuta for their technical and administrative support. I gratefully acknowledge the assistance of the people I have been fortunate to collaborate with during my time at UCL. Thanks must go to Andy Bell, Ian Main, Dan Faulkner, Phil Benson and Alex Edwards. I also acknowledge the UCL Graduate School for providing essential conference funding and NERC for funding the studentship.

Finally, I'd like to thank my mum and dad.

'It is somehow scary to think that while we have our daily routine things are creeping somewhere'

Dr. Patrick Baud (01/11/07).

Chapter one

1. Introduction

1.1 Introduction to the project

There are three broad ways in which rock is stressed in the Earth's brittle crust: (1) by a constant displacement or driving force e.g. the relative constant motion of tectonic plates, (2) by cyclic stress loading e.g. pressurization/depressurization cycles within a volcanic edifice and (3) constant stress loading e.g. the high constant stress exerted by a pressurized volcanic edifice. This study tackles the latter two modes of deformation and their applications to common geophysical problems. The main focus of this study however is on the time-dependent brittle deformation of rock caused by a constant applied stress.

Earthquake rupture and volcanic eruptions are the most spectacular manifestations of dynamic failure of critically-stressed crust. However, these are actually rather rare, discrete events in both space and time. Most of the crust spends most of its time in a highly-stressed but sub-critical state. Furthermore, water is ubiquitous in the crust. It is well-known that water-rock chemical reactions can lead to time-dependent deformation enabling rocks to fail over extended periods of time at stresses far below their short-term failure strength; a phenomenon known as 'sub-critical crack growth' [e.g. see Anderson and Grew, 1977; Atkinson and Meredith, 1987].

Quantifying sub-critical crack growth is crucial to unravelling the complexities of the evolution and dynamics of the brittle crust. The presence of cracks allows the crust to store and transport fluids, and even modest changes in crack size, density or linkage can produce major changes in fluid transport properties. Time-dependent brittle deformation is a fundamental and pervasive process in the Earth's brittle upper crust. Hence, the characterization of time-dependent processes is a critical pre-requisite understanding its long-term behaviour and strength. Time-dependent rock deformation therefore has

both a scientific and a socioeconomic impact since it controls the duration and detectability of any precursory phase of important geohazards such as earthquake rupture and volcanic eruptions, and also influences effective recovery of hydrocarbon and geothermal energy resources, and the integrity of long-term storage facilities for hazardous waste.

The majority of rocks forming the Earth's crust, even those at depth, contain microporosity comprising some or all of open pores between grains, triple-junction voids between crystalline phases, grain boundary voids and open microcracks. Water and aqueous solutions are ubiquitous in the upper crust, and below a few hundred metres most rocks are saturated. The presence of a fluid phase not only affects the mechanical behaviour of rock, but also allows chemical rock-fluid interactions to occur. In a purely mechanical sense, a pressurized pore fluid acts to reduce all the applied normal stresses and thus allows rocks to fail at lower differential stress than would otherwise be the case [Terzaghi, 1943; Jaeger *et al.*, 2007]. Chemically, aqueous solutions affect the deformation of rock in two main ways: (1) they act to weaken the rock via the reduction of surface free energy as the result of the absorption of pore fluid onto the internal pore surfaces [Orowan, 1944; Rehbinder, 1948; Andrade and Randall, 1949], and (2) they also weaken rocks by promoting subcritical crack growth, of which stress corrosion is the most important mechanism [Anderson and Grew, 1977; Atkinson, 1984; Atkinson and Meredith, 1987; Costin, 1987].

Stress corrosion describes the reactions that occur preferentially between a chemically active pore fluid, most commonly water, and the strained atomic bonds close to crack tips. In a silicate-water system, bridging bonds close to crack tips, the main stress-supporting components, are replaced by weaker hydrogen bonds, thus facilitating crack growth at lower levels of stress than would otherwise be the case [Michalske and Freiman, 1982;1983; Freiman, 1984; Hadizadeh and Law, 1991]. The velocity of

cracks propagating by stress corrosion has been shown to increase when the stress intensity (a function of the applied stress and the crack length) at the crack tip is increased in a wide variety of rock types, [see Atkinson, 1984; Atkinson and Meredith, 1987, for reviews]. However, the majority of experimental data on stress corrosion cracking has been derived from experiments on single cracks at ambient pressure, and few data exist on the bulk behaviour of rock containing a population of cracks. Nevertheless it has been hypothesized that, for bulk rock deforming in a brittle manner under triaxial stress conditions, stress corrosion will lead to highly non-linear time-dependent deformation [e.g. Main, 2000]. This allows rocks to deform even under a constant applied differential stress over extended periods of time; a phenomenon known as *brittle creep* (or *static fatigue* in the engineering literature). Rock deformed in this manner exhibits an apparent trimodal behavior when axial strain is plotted against time (commonly known as a *creep curve*, see Fig. 1.1). The three stages of the creep curve have conventionally been described as; (1) primary or decelerating creep, (2) secondary or steady-state creep, and (3) tertiary or accelerating creep (Fig. 1.1).

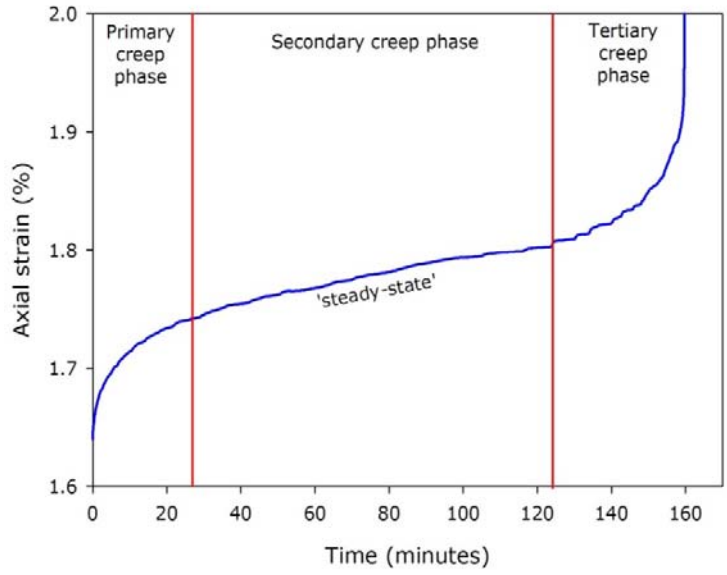

Figure 1.1. A classic trimodal creep curve. Curve shown is from experimental data on Darley Dale sandstone at a confining pressure of 50 MPa and pore fluid pressure of 20 MPa [sample DD-40-45Z].

There have only been relatively few studies of brittle creep in bulk rock samples of sandstone [Lockner and Byerlee, 1975; Rutter and Mainprice, 1978; Baud and Meredith, 1997; Ngwenya *et al.*, 2001; Ojala *et al.*, 2003]. However, only Baud and Meredith [1997] and Ngwenya *et al.* [2001] investigated the influence of applied differential stress on creep strain rates. Studies on granitic rocks have touched upon the influence of effective confining pressure and temperature on time-to-failure [Kranz, 1980; Kranz *et al.*, 1982], but neglect their influence on creep strain rate. No commensurate studies exist on other rock types; in general, time-dependent brittle deformation in rocks is a poorly understood phenomenon.

Double-torsion experiments have studied the growth of single tensile cracks in basic rocks by stress corrosion [e.g. Meredith and Atkinson, 1983]; however, to date, no studies have investigated the time-dependent brittle behaviour of a bulk sample of basic rock where cracks can interact and coalesce in compression and under a confining pressure. Despite this, stress corrosion cracking is the mechanism considered most likely to be responsible for the time-dependent precursory cracking, displacement and accelerating seismic activity that commonly precedes volcanic eruptions [Voight, 1988;1989; Cornelius and Scott, 1993; McGuire and Kilburn, 1997; Kilburn and Voight, 1998; Main, 1999; Kilburn, 2003]. Furthermore, many of the forecasting models that use seismic precursors to volcanic eruptions incorporate or imply the influence of the mechanism of stress corrosion [e.g. Voight, 1988;1989]. Stress corrosion has also been linked with the seismic activity that commonly precedes earthquake rupture [Scholz, 1968a; Scholz, 1972; Rudnicki, 1980; Das and Scholz, 1981; Atkinson, 1982; Crampin *et al.*, 1984; Main and Meredith, 1991; Main *et al.*, 1992]. Stress corrosion cracking of asperities on sliding surfaces has been shown to explain the strain-rate dependence of the frictional strength of rock [Kato *et al.*, 1993], has been used to explain the growth and development of joints [Olson, 1993; Renshaw and Pollard, 1994; Savalli and Engelder, 2005] and is important when assessing the instability potential of underground excavations [Diederichs and Kaiser, 1999].

The stress history of rock is generally more complex than a constant loading rate e.g. a volcanic edifice is subject to repeated cycles of stress over time due to the combination of magma emplacement from deep reservoirs to shallow depths and superimposed tectonic stresses. It is well-known that the values of elastic moduli are frequency dependent [e.g. Vinciguerra *et al.*, 2006]. Therefore, fluid saturation has a significant influence on dynamic elastic moduli measured at ultrasonic frequencies [Winkler and Murphy III, 1995; Vinciguerra *et al.*, 2006], due to rapid energy dissipative mechanisms such as 'fluid squirt'. However, static elastic moduli have a frequency some nine orders of magnitude lower than ultrasonic frequencies, it can therefore be expected that water-saturation will only affect the mechanical/elastic behaviour of the rock through the law of effective stress. However, values of elastic moduli routinely used in elastic deformation models are derived from seismic waves [Cayol and Cornet, 1998; Bonaccorso and Davis, 1999; Obrizzo *et al.*, 1994; Lungarini *et al.*, 2005]. Therefore, accurately quantifying the mechanical properties, such as the static elastic moduli and peak stress, for the rocks constituting a volcanic edifice for example is a crucial goal for the reliability of the modelling inversions of deformation patterns. Furthermore, models commonly use a constant value for elastic moduli. It has been shown that there is an underestimation of the source depth and volume change for the migration and accumulation of magma beneath volcanoes due to the interpretation of geodetic data using homogeneous models [Manconi *et al.*, 2007].

1.2 Aims for the project

'*Glass could statically support a given weight for a time and then would fail... this fact was appreciated by the French champagne makers of the time who never used the same bottle twice, although bottles were expensive, thus saving many a good bottle of wine from destruction*.' [Grenet, 1899].

The main objectives of this project are:

(1) To greatly expand our knowledge on time-dependent brittle deformation in rocks.

(2) To perform the first study on brittle creep in basalt.

(3) To provide an expansive dataset to test macroscopic creep laws and failure prediction models.

(4) To investigate the evolution of static elastic moduli with increased damage during stress-cycling.

1.3 Thesis outline

The thesis is broadly divided into three main sections (1) background theory and previous experimental work on the studied topics (2) detailed rock characterization, description of the test equipment and an account of how the data were acquired and (3) results, discussion and conclusions. These three main sections are subdivided into twelve chapters. A brief description of each is given below.

- Chapter Two outlines the current state of knowledge and understanding of theories and experimental observations in experimental rock physics.
- Chapter Three explains the current state of knowledge on the contribution of a pore fluid on brittle deformation, focusing on the chemically-driven process of stress corrosion.
- Chapter Four provides detail on the testing equipment used in the study, how it was calibrated prior to testing and how the data were acquired.
- Chapter Five describes the methods and results of the characterization the rock types used in the study.
- Chapter Six shows experimental results from stress-cycling uniaxial experiments devised to investigate how an increase in crack damage influences the evolution of static elastic moduli in rocks.

- Chapter Seven discusses the results of the stress-cycling uniaxial experiments presented in Chapter Six.
- Chapter Eight presents experimental results on the time-dependent brittle deformation behaviour of Darley Dale sandstone.
- Chapter Nine shows experimental results on the influence of temperature on brittle creep in three sandstones of contrasting mineralogical and microstructural properties.
- Chapter Ten presents experimental results on the time-dependent brittle deformation behaviour of Etna basalt.
- Chapter Eleven discusses the results presented in Chapters Eight, Nine and Ten on time-dependent brittle creep.
- Chapter Twelve presents the conclusions of the project.

Chapter two

2. Theories and Experimental Observations in Experimental Rock Physics

2.1 Introduction

Tectonic stresses, present in the Earth's crust, are responsible for its deformation. They act sub-horizontally and commonly superimpose lithostatic or overburden pressure, due to the weight of overlying rock, and pore fluid pressure, due to the pressurization of trapped pore fluids, present within the crust. Therefore, if the tectonic stresses exceed the lithostatic stress present in a unit volume of crust then deformation can occur. The distribution and magnitude of forces in rock masses is central to our understanding of rock physics as well as more fundamental geological processes such as plate tectonics, regional deformation and the mechanics of earthquakes and faulting. The magnitudes of such crustal stresses can be measured using several different techniques. They can be measured directly using borehole breakouts [Leeman, 1964; Babcock, 1978; Bell and Gough, 1979; Bell, 2003] and hydraulic fracturing [Kehle, 1964; Fairhurst, 1965; Cornet and Valette, 1984]. However, although these direct methods are useful they both involve drilling into the crust, which is not only very expensive but can also alter the stress-strain history of the rock [for a review on in-situ stress estimation in rock see Fairhurst, 2003]. Tectonic stresses can also be indirectly determined by earthquake focal mechanisms [Isacks *et al.*, 1968; Gephart and Forsyth, 1984; Michael, 1987], regional patterns of present day tectonic stresses [Zoback *et al.*, 1989] and by anelastic strain recovery [Matsuki and Takeuchi, 1993].

An alternative is to measure stresses, strain and mechanical and physical properties of rock using laboratory rock physics experiments. Techniques in rock physics have long been used to understand how crustal rock deforms and many different techniques exist that have been subsequently developed over the years to further improve our understanding of crustal deformation processes. Also, the stress history of a rock sample can be estimated from laboratory experiments by observing the Kaiser 'stress memory' effect [see Li and Nordlund, 1993; Holcomb, 1993; Lockner, 1993 and Lavrov, 2003].

The aim of this chapter is to provide a detailed account of the current state of knowledge on theories and experimental observations in brittle rock deformation and their uses. The chapter will first discuss the principles of stress and strain and the mechanisms responsible for their development in the crust. The chapter then deals with the theory behind brittle rock failure before discussing experimental observations during brittle rock deformation experiments.

2.2 Stress and strain

2.2.1 Stress

There are two basic types of force that act upon a body to produce a stress (1) surface forces, that act on a particular surface of a body and (2) body forces, that act on each element of a body, independent of the surrounding material. Body forces exert on each body of rock a force that is proportional to the mass within that volume. The most important body force is the force formed due to the acceleration due to gravity. Surface forces are produced when one body comes into contact with another. This can be across the surface of contact between the bodies or across an internal surface. The intensity of a force is known as the traction or resultant stress. If an arbitrary internal or external surface of area A_{arb} is subjected to a uniformly distributed force F then the resultant stress or traction (T_r) acting on that surface can be simply calculated by:

$$T_r = \frac{F}{A_{arb}} \qquad [2.1]$$

It is possible to resolve the stress at a particular point into two components (1) a stress that acts normal to the surface, σ_n, and (2) a shear stress that acts at a tangent to the surface, τ. For this two-dimensional

case, the state of stress can be represented by a stress ellipse (Fig. 2.1), provided that the normal stresses are either all compressive (pressing the material together across the surface) or all tensile (pulling the material apart across the surface).

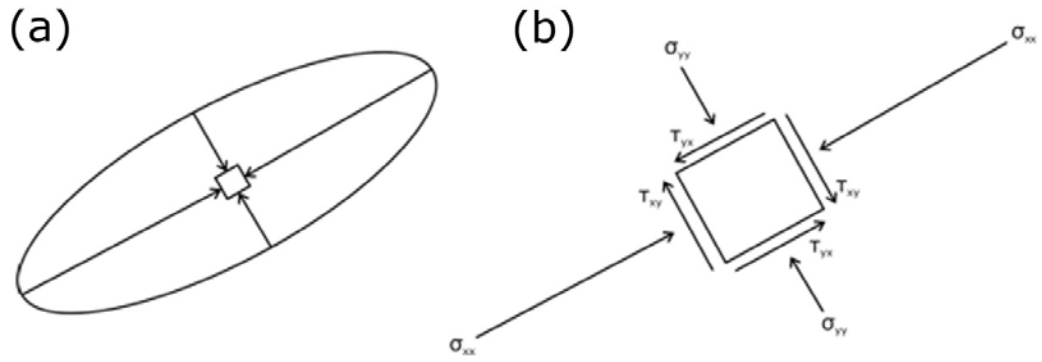

Figure 2.1. (a) Stress ellipse for two-dimensional stress at a point represented by the square in the centre of the ellipse. Arrows indicate the surface stresses acting on the point. (b) A magnified view of the point at the centre of the stress ellipse with all surface stresses, both normal and shear, included. The first subscript denotes the plane upon which the stress component acts and the second subscript denotes the direction in which the stress component acts [adapted from Twiss and Moores, 1992].

This two-dimensional state of stress acting on a point can be represented by the following stress tensor:

$$T_n = \begin{bmatrix} \sigma_{xx} & \tau_{xy} \\ \tau_{yx} & \sigma_{yy} \end{bmatrix} \qquad [2.2]$$

However, for three-dimensional analysis, the resultant stress associated with a particular surface must be resolved into components along the x, y and z axes. This is achieved by extrapolating its description in two-dimensions and can be represented by a strain ellipsoid. The three-dimensional analysis of stress yields nine components and is represented by the three-dimensional stress tensor:

$$T_n = \begin{bmatrix} \sigma_{xx} & \tau_{xy} & \tau_{xz} \\ \tau_{yx} & \sigma_{yy} & \tau_{yz} \\ \tau_{zx} & \tau_{zy} & \sigma_{zz} \end{bmatrix} \qquad [2.3]$$

The nine Cartesian components required for the three-dimensional analysis of stress are shown in Fig. 2.2.

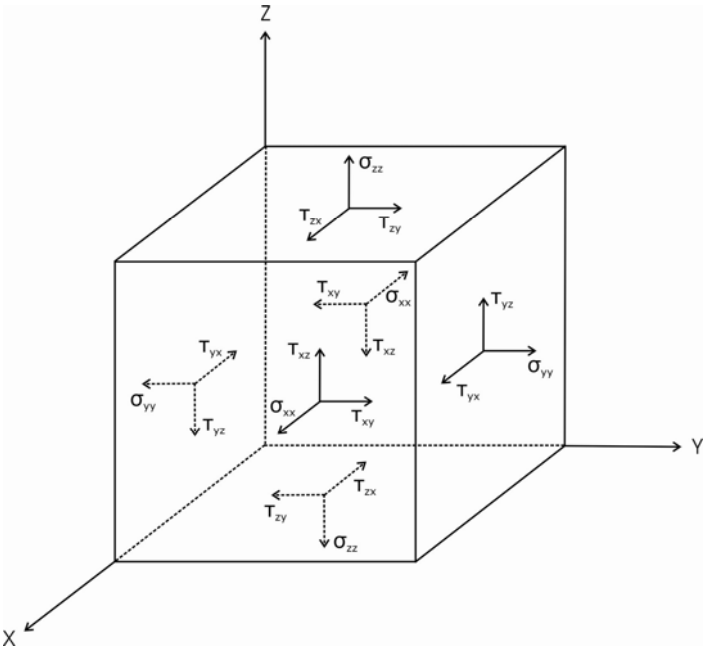

Figure 2.2. Schematic diagram of a cubic element showing the nine Cartesian stress components [redrawn from Dally and Riley, 1991].

The resultant stress vector T_n therefore depends on the choice of plane upon which the stress acted; if these are coincident then the shear stress τ is reduced to zero. If this is true then the selected plane is referred to as the principal plane and the normal stress acting along it as the principal stress. From the three-dimensional stress tensor is it clear that three principal stresses exist, and are referred to as σ_1, σ_2 and σ_3.

$$T_n = \begin{bmatrix} \sigma_1 & 0 & 0 \\ 0 & \sigma_2 & 0 \\ 0 & 0 & \sigma_3 \end{bmatrix} \qquad [2.4]$$

σ_1 is the greatest principal stress, σ_2 is the intermediate principal stress and σ_3 is the least principal stress. For these stresses, positive signs indicate tension and negative signs indicate compression. Therefore, the state of stress can be defined by either (1) the full matrix of stress components or (2) the principal stresses and their orientations.

2.2.2 Strain

If a solid body is subject to a stress then it can experience a change in shape and size called strain. This is caused by the movement of individual points within a solid body, a vector quantity called a displacement. Displacements can result in changes in length, volume and angle between segments within a solid body. If the change in shape and size are identical for each segment of the body and the body as a whole then the body has experienced homogenous strain. If they are different then the body has experienced inhomogeneous strain. Strain results in three-dimensional changes in a body and is therefore best described in three-dimensions. However, it is much simpler to grasp the concepts of strain by considering it in two-dimensions – this is called plane strain.

There are three main types of plane strain (1) linear strain (2) volumetric strain and (3) shear strain. Linear strain, or extension, is generally expressed as a ratio of the change in length to the original length. This can be expressed as follows, where L is the final length and L_0 is the original length.

$$\varepsilon = \frac{L - L_0}{L_0} \qquad [2.5]$$

Volumetric extension is calculated using the same formula as in Equation [2.5], where *V* is the final volume and V_0 is the original volume.

$$\varepsilon_v = \frac{V - V_0}{V_0} \qquad [2.6]$$

However, a body can change shape without changing volume – the result of a shear strain. A shear strain is calculated using the change in angle caused by the strain (ψ).

$$\varepsilon_s = 0.5 \tan\psi \qquad [2.7]$$

Similar to stress, strain can be resolved into a strain ellipse (for two-dimensions) and a strain ellipsoid (for three-dimensions). The three-dimensional analysis of strain, similar to that of stress, yields nine components and can be represented by the following three-dimensional strain tensor.

$$\varepsilon_n = \begin{bmatrix} \varepsilon_{11} & \varepsilon_{12} & \varepsilon_{13} \\ \varepsilon_{21} & \varepsilon_{22} & \varepsilon_{23} \\ \varepsilon_{31} & \varepsilon_{32} & \varepsilon_{33} \end{bmatrix} \qquad [2.8]$$

The principle strains are those that act along the principal plane where shear strains are zero. The three-dimensional strain tensor defines three principal strains.

$$\varepsilon_n = \begin{bmatrix} \varepsilon_1 & 0 & 0 \\ 0 & \varepsilon_2 & 0 \\ 0 & 0 & \varepsilon_3 \end{bmatrix} \qquad [2.9]$$

The strain produced a stress can be either (1) elastic strain, which is recoverable deformation or (2) inelastic strain, which is permanent deformation. Elastic strain can be described by Hooke's Law, which states that, during elastic deformation, strain is proportional to stress.

2.2.3 Conditions in the Earth's crust

Stresses and strains present in the crust form complex relationships due to its vast heterogeneity. The lithosphere, comprised of the crust and the uppermost mantle, is divided into a number of nearly rigid plates (see Fig. 2.3). The movement and interaction of these plates at their boundaries results in tectonic stresses and ultimately the deformation of the crust. The three most important tectonic stresses that result in crustal deformation are (1) ridge push, a compressive stress that acts normal to the ridge axis (2) slab pull, a tensile stress that acts normal to the trench axis and (3) trench suction, a tensile stress that pulls the overriding plate towards the trench. Deformation occurs where these tectonic stresses exceed the lithostatic stress present in a unit volume of crust. The magnitudes of these tectonic stresses are estimated at 20-30 MPa, 0-50 MPa and 20 MPa respectively. The World Stress Map Project (WSMP) has compiled in situ stress measurements from borehole breakouts, hydraulic fracturing, style of active faulting, volcanic alignment, seismic focal mechanisms and transform fault azimuths from all over the world (Fig. 2.3). In several plates, the maximum horizontal stress is subparallel to the direction of absolute plate motion. It has been suggested that the forces driving the plates also dominates the stress distribution in the plate interior [Zoback *et al.*, 1989; Zoback and Magee, 1991].

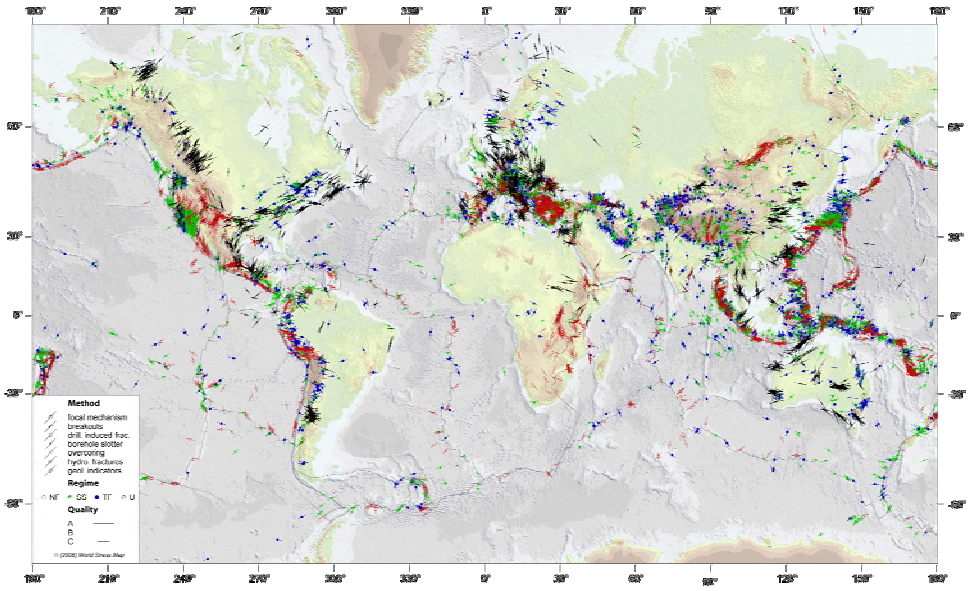

Figure 2.3. The World Stress Map taken from the World Stress Map Project. The length of the line indicates its reliability, the different colours indicate different tectonic regimes and the different symbols indicate the method by which the data was gathered [Heidbach *et al.*, 2008].

Lithostatic or overburden pressure, caused by the weight of overlying rock, can be calculated for a particular point in the crust using the following relationship, where ρ is rock density, g is the acceleration due to gravity and z is the depth.

$$\sigma = \rho g z \qquad [2.10]$$

This is true for the vast majority of conditions in the crust; however, there are a few situations where vertical pressure is not completely controlled by this relationship [see Price, 1966]. Lithostatic stresses are often superimposed by a pore fluid pressure (P_p) that act normal to the surface of the grains and results in the reduction of the effect of the external applied stresses on the rock. It is often assumed that P_p increases linearly using the following relationship, where ρ_w is the density of water, g is the acceleration due to gravity and z is depth. However, this is an oversimplification of the relationship

between P_p and depth (see Chapter Three for a comprehensive report on the influence of P_p on deformation).

$$P_p = \rho_w g z \qquad [2.11]$$

Tectonic strain rates seen in nature are typically of the order of 10^{-14} s^{-1} [Whitten, 1956; Wood, 1973]. However, such low strain rates cannot be used in laboratory experiments due to the unfeasibility of performing an experiment that could potentially take years to complete. Strain rates as slow as 10^{-8} s^{-1} are achievable in the laboratory, although the strain rate typically used in a conventional constant strain rate test is 10^{-5} s^{-1}. These can then be extrapolated to realistic strain rates using theoretical models [e. g. Rutter, 1995]. Temperature, except in special circumstances, increases with depth in the crust. The temperature gradient or geotherm varies from approximately 100°C/km in active volcanic areas to as little as 10°C/km in deep sedimentary trenches. The average geothermal gradient for crustal rock is between 30-50°C/km [see Fowler, 2005].

2.3 Theories of brittle failure

2.3.1 Introduction

Traditionally, there have been two contrasting approaches in the development of a theory for the failure of brittle rock that predicts the macroscopic fracture stress. The first, fracture mechanics, comprises of empirical attempts to define criteria of failure that agree with observed failure conditions in laboratory experiments. However, such theories, the most famous being those of Mohr and Coulomb [see Paul, 1968; Jaeger, 1969], do not incorporate a great deal in terms of the physical mechanisms of failure.

Furthermore, Mohr-Coulomb theory does not take into account the intermediate principal stress, which has been shown to influence brittle failure [see Haimson and Chang, 2000; Chang and Haimson, 2000; Haimson and Chang, 2002; Haimson, 2006]. The second approach focuses on creating a physical model for the failure of brittle rock that attempts to represent the important aspects of the actual physical mechanism of fracture and hopes to provide a platform for establishing the criteria of failure applicable to the general state of stress. This is called the Griffith theory of brittle fracture. This section will first introduce Griffith crack theory, and then explain the principles of fracture mechanics before describing the macroscopic failure criterion and the Mohr-Coulomb failure criterion.

2.3.2 Griffith crack theory

2.3.2.1 The theoretical strength of rock

The theoretical (cohesive) strength of rock (σ_t) can be expressed simply in terms of the energy required to overcome atomic bonds across a lattice plane (Fig. 2.4). Fig. 2.4 demonstrates that an increase in stress (σ) results in an increase in atomic separation from an equilibrium spacing (A_{eq}) [Orowan, 1949]. As soon as a critical stress is reached (σ_t) the atomic spacing will continue to increase without any additional stress increase. From this, the theoretical strength (σ_t) is related to the Young's modulus (E) by a relatively simple anharmonic calculation of atomic forces:

$$\sigma_t = \frac{E}{2\pi} \qquad [2.12]$$

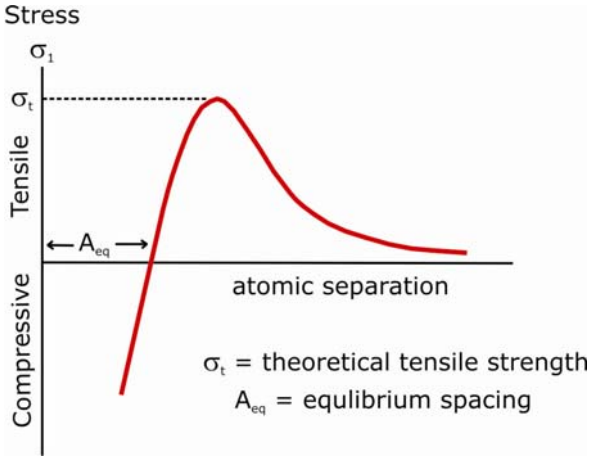

Figure 2.4. Graphical representation of the theoretical strength of rock. The figure shows the relationship between stress and atomic separation.

However, the values for theoretical strength are typically several orders of magnitude greater than the strength of real materials determined from laboratory experiments. This observation highlighted the need for a reappraisal of the understanding of rock fracture at a fundamental level. A possible cause for such a huge discrepancy was postulated by Griffith [1920], who predicted that all real materials contain very small scale defects or imperfections. This formed the basis of the Griffith crack theory [Griffith, 1920; Griffith, 1924].

2.3.2.2 Stress concentrations around defects

One of the most fundamental theories in rock mechanics, Griffith crack theory, proposes that the strength of brittle materials, including rocks, is governed by the presence of an existing population of microcracks [Griffith, 1920]. Griffith postulated that failure would occur when the most vulnerably-orientated microcrack within a population of randomly orientated microcracks extends under an applied stress equal to that needed to overcome the interatomic cohesion of the material [Griffith, 1924]. The presence of such microcracks proposed by Griffith was entirely hypothetical at this time, without

modern tools such as electron microscopy; hence they were referred to as 'Griffith cracks'. This built on previous work [Inglis, 1913], who had demonstrated that cavities or notches in a material can act to magnify stresses near the crack tips. As a result, rock failure can occur at much lower stresses than those predicted from the theoretical strength. There are two important defects to consider (1) microcracks, which are surface defects that can lead to brittle deformation and fracture separation and (2) dislocations, which are internal line defects that can lead to ductile deformation and plastic flow. The stress-concentrations produced by defects depend on orientation, length and radius of curvature at the tip of the crack.

The stress concentrations caused by material defects are shown in Fig. 2.5. Fig. 2.5a shows a circular hole within a plate that has been subjected to a uniform tensile load (σ_∞). Elastic theory predicts that there will be a compressive stress of magnitude $-\sigma_\infty$ at the top and bottom of the hole and a tensile stress of magnitude $3\,\sigma_\infty$ along both sides. Such stress concentrations decrease rapidly from the edge of the hole and are the result of its lack of load-bearing capacity. Since the magnitude of the stress concentrations is controlled by the geometry of the hole, it differs greatly with different shaped holes. The stress concentration at the ends of an elliptical hole increase proportionally to *C/B* (Fig. 2.5b). As the cracks lengthen the stress concentration increases further, eventually leading to the dynamic failure of the material.

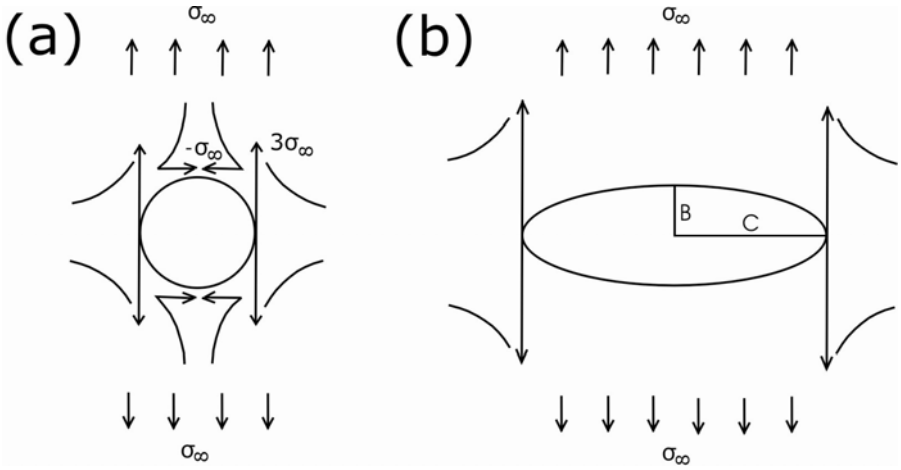

Figure 2.5. Stress concentrations around (a) a circular hole and (b) an elliptical hole subjected to uniform tension (σ_∞).

2.3.2.3 Griffith energy balance

Griffith [1920, 1924] proposed an explanation for the problem of theoretical brittle failure in the form of an energy balance for crack propagation (Fig. 2.6), modelling a static crack as a reversible thermodynamical system.

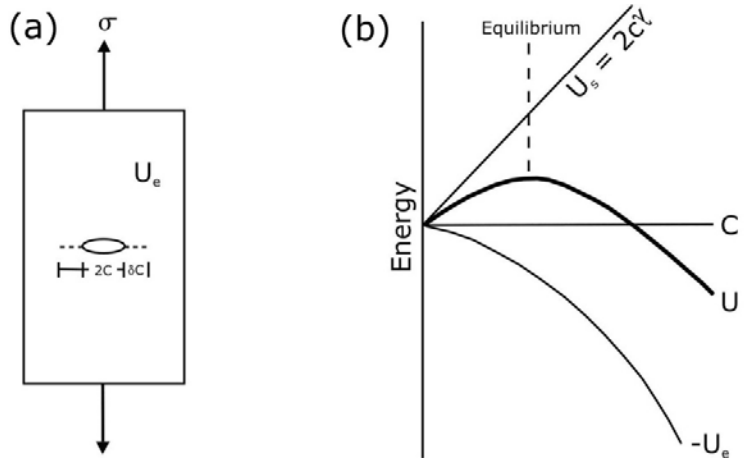

Figure 2.6. (a) Griffith static crack model for crack propagation. (b) The energy partition for the process.

The system involves a crack, of length 2*C*, within an elastic body, which is loaded by an external boundary force, σ. The small extension in crack length, δ*C*, is a result of the work, *W*, exerted by the external boundary force. This results in a change in the internal stain energy, U_e, and an energy expenditure, U_s. Therefore, the total energy for a static crack, *U*, within the system will be:

$$U = \left(-W + U_e\right) + U_s \qquad [2.13]$$

The combined term in brackets denotes the total mechanical energy in the system. As the crack length increases, the stored elastic strain energy or mechanical energy (U_m) decreases as long as the applied force remains constant. Since the U_s and the U_m are the only energy changes in the system, and the first law of thermodynamics must apply, the total energy in the system, *U*, must also be the some of these two terms:

$$U = U_m + U_s \qquad [2.14]$$

If the cohesion between the incremental extension surfaces (δC) were removed, the crack would accelerate outward to a new lower energy configuration. Therefore, surface energy increases and mechanical energy decreases with crack extension. For the crack to extend there must therefore be a reduction in the total energy of the system (*U*). Or, in order to maintain equilibrium, there must be a balance between the mechanical and surface energies. This condition for equilibrium is simply given by:

$$\frac{dU}{dC} = 0 \qquad [2.15]$$

From this, a crack could extend or contract in small increments from the equilibrium length depending on whether the left-hand side of the above equation was positive or negative. This criterion remains one of the most important first-principals in all brittle fracture theory.

To illustrate this Griffith analyzed the case of a rod, of length *y* and Young's modulus *E*, subjected to a tensile stress (σ). During uniform tensile loading, the strain energy of the rod will be given by:

$$U_e = y\left(\frac{\sigma^2}{2E}\right) \qquad [2.16]$$

If a crack of length *2C* is then introduced into the system, the stain energy is increased by $\sigma^2\pi C^2/E$ to give:

$$U_e = \sigma^2\left(\frac{y + 2\pi C^2}{2E}\right) \qquad [2.17]$$

So, if the work, *W*, needed to initiate the crack is given by $W = 2\pi\sigma^2C^2/E$ and the change in surface energy is $U_s = 4C\gamma$ then the energy balance equation becomes:

$$U = -\pi c^2\left(\frac{\sigma^2}{E + 4C\gamma}\right) \qquad [2.18]$$

From this we can obtain an expression for the critical stress at which the crack will be at equilibrium:

$$\sigma_{crit} = \sqrt{\frac{2E\gamma}{\pi c}} \qquad [2.19]$$

The above equation defines the position of unstable equilibrium in the energy partition diagram for the system (Fig. 2.6). As soon as this condition is satisfied, the crack will propagate unstably and without limit, resulting in the catastrophic failure of the material. Griffith proved the validity of this theory by experimentally determining the failure stress of glass rods. We can now see that the failure stress is dependent on crack length and the equation is based upon fundamental physics related to the breaking of atomic bonds within the material.

2.3.2.4 Obreimoff's experiment

Obreimoff [1930], to further illustrate the applicability of Griffith's [1920; 1924] thermodynamic approach, performed experiments on the cleavage strength of mica [Obreimoff, 1930]. In contrast to Griffith's formulation, the experiments of Obreimoff [1930] led to the study of stable crack configuration. He measured the cleavage strength by driving a rigid wedge, of height *h*, along the cleavage surface of a single crystal of mica (Fig. 2.7a).

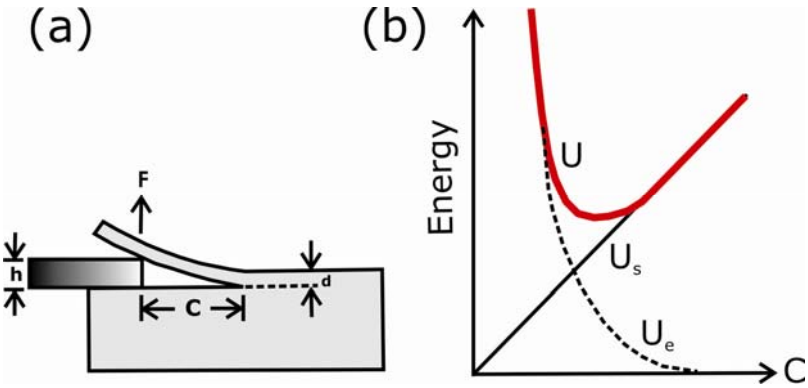

Figure 2.7. (a) The configuration of Obreimoff's mica experiment and (b) the energy partition for the process.

At the equilibrium crack length (*C*) the force applied to the system (*F*) is constant is undergoes no displacement since the wedge is assumed to be perfectly rigid. The strain energy of the crack system can be investigated by calculating the strain energy of the mica flake (thickness, *d* and height, *h*):

$$U_e = Ed^3 \frac{h^3}{8C^3} \qquad [2.20]$$

Using $U_s = 2C\gamma$ and the condition $dU/dC = 0$ as defined by Griffith, the equilibrium crack length can then be given by:

$$C = \left(\frac{3Ed^3 h^2}{16\gamma} \right)^{1/4} \qquad [2.21]$$

The energy partition for this process in shown in Fig. 2.7b, clearly showing that, in this case, the crack is in a state of equilibrium. This is because the crack advanced only as far as the wedge advanced. Obreimoff [1930] found that stability is not a material property, but is controlled by the system response. Another important observation was that the cracks only reached their equilibrium length after a period of creep following the initial sudden crack growth. However, he did not observe this under a vacuum. In conclusion, the loading configuration implemented by Obreimoff [1930] produces a stable equilibrium or minimum energy effect, whereas Griffith's [1920; 1924] loading configuration produces an unstable equilibrium or maximum energy effect.

2.3.2.5 Modified Griffith closed-crack theory

Griffith's theory [Griffith, 1920;1924] assumed open, cylindrical microcracks with flattened elliptical cross sections that contain no fluid under pressure; he also only worked in two-dimensions. However, even under a low confining pressure, many cracks orientated perpendicular to the applied load are likely to be closed. This also brings about frictional effects previously unconsidered by conventional Griffith theory.

This theory has been extended to include the closing of Griffith cracks during compression with the development of frictional forces along the crack surfaces [McClintock and Walsh, 1962; Murrell, 1963;1964; Murrell and Digby, 1970]. McClintock and Walsh [1962] calculated the conditions for crack extension under biaxial stress using a threshold confining pressure to determine whether the microcracks perpendicular to the macroscopic stress component would be closed. This theory is similar to that proposed by Murrell [1964] and was later extended by Murrell and Digby [1970] who provided a three-dimensional solution to the problem and considered a general case of an ellipsoid crack in an arbitrary triaxial stress field with an internal pore pressure.

2.3.3 Linear elastic fracture mechanics – a continuum mechanics approach

"…the fracture of materials in terms of the laws of applied mechanics and the macroscopic properties of materials. It provides a quantitative treatment based on stress analysis, which relates fracture strength to the applied load and structural geometry of a component containing defects." [Irwin and de Wit, 1983].

Fracture mechanics is a continuum mechanics approach in which the crack is idealized as a mathematically flat and narrow slit in a linear elastic medium [definition from Scholz, 2002]. It derives from early work [Griffith, 1920;1924; Irwin, 1958] and centres on the idea that a crack as a stress concentrator is the most fundamental concept in controlling the fracture of brittle solids. This overview is by no means absolute and a further, more in-depth review of fracture mechanics can be found elsewhere [Irwin and de Wit, 1983; Atkinson, 1987; Scholz, 2002].

Griffith's [1920; 1924] analysis was incomplete since it only evaluated the equilibrium length for uniform tension and it modelled an idealized thermodynamic system and did not take into account other forms of energy dissipation that occur during crack propagation such as heat generation, friction or tractions across rough surfaces and sound and seismic wave generation. Linear elastic fracture mechanics is therefore required for the solution of general crack problems and so that other loading configurations can be considered. It extends Griffith's approach by considering the stress tensor close to the tip of an atomically sharp two dimensional crack.

The approach, pioneered by Irwin and his co-workers in the 1950's, involves the analysis of the stress field surrounding a crack tip and two intrinsic fracture strength parameters known as the crack extension force, *G*, and the stress intensity factor, *K*. From this a fracture criterion based on certain critical parameters of the stress field can be formulated. Therefore, the macroscopic strength of a rock is related to the intrinsic strength of the material through the relationship between the crack-tip and applied stresses and the deformation and fracturing process at the crack tip can be ignored since the crack is treated as residing in a continuum.

The displacement field of cracks can be divided into three different failure modes (Fig. 2.8). Mode I, 'opening or tensile mode', involves normal displacements relative to the crack. Modes II, 'in-plane shear or sliding mode', and III, 'antiplane-shear or tearing mode', are both shear modes that involve parallel displacements relative to the crack.

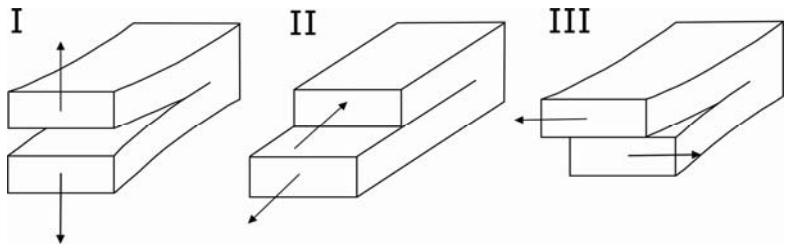

Figure 2.8. Schematic drawings of the three modes of fracture. Mode I – tensile, mode II – in-plane shear and mode III – anti-plane shear.

Approximations to the crack-tip stress and displacement fields, assuming that the crack in planar, perfectly sharp and there is no cohesion between the crack walls, can be expressed as:

$$\sigma_{ij} = K_n (2\pi r)^{-1/2} f_{ij}(\theta) \qquad [2.22]$$

Where *K* is the stress intensity factor, *r* is the distance from the crack tip and θ is the angle measured from the crack plane (Fig. 2.9). The stress field surrounding each of the different fracture types can be characterized in terms of their distance from the crack tip and angle from the crack plane [Lawn, 1993].

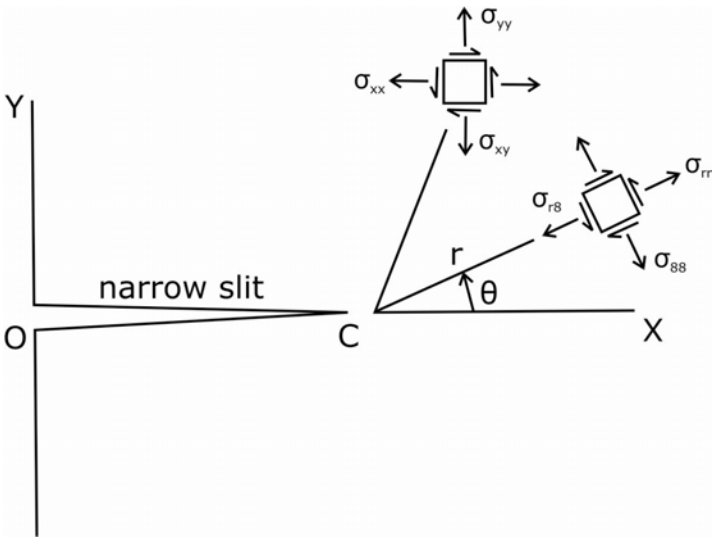

Figure 2.9. The stress field surrounding a crack tip, in both Cartesian and polar coordinates [from Lawn, 1993].

The stress intensity factor, *K*, is the magnitude of the crack tip stress field for a particular mode in a homogeneous linear elastic material. It is the key parameter in linear elastic fracture mechanics and depends on the geometry and magnitude of the applied stress and the length of the crack. It aims to give a measure of the forces acting at the crack tip that will ultimately determine whether it propagates in a stable or unstable manner. The stress intensity factor can be related to the Griffith energy balance by the crack extension force, *G*:

$$G = -d\left(\frac{-W + U_e}{dC}\right) \qquad [2.23]$$

$$\text{where } G = K^2\left(\frac{1-v^2}{E}\right) \qquad [2.24]$$

Where *E* is the Young's modulus and *v* is the Poisson's ratio. The distribution of stress around the crack tip requires the assumption of linear elasticity. However, if non-elastic and non-linear elastic effects are

operative at the crack tip, which is the case for many materials, alternative analyses can be implemented [McClintock and Irwin, 1965; Rice, 1968a; Rice, 1968b]

The crack extension force, or strain energy release rate, is the loss of energy per unit of new crack separation area formed during an increment of crack extension. Although contributions to *G* are mainly from the crack tip region, it is not a local parameter and includes contributions from all parts of the system. The crack extension force can be applied to both stationary and running cracks due to the fact it is calculated for infinitesimal increments of new separation area. Stress intensity factor, *K*, and crack extension force, *G*, are different depending on the mode of displacement and are written as, for example, K_I, K_{II} and K_{III}.

Once a critical stress intensity factor (K_c) or crack extension force (G_c) has been reached then microcracks can propagate quickly and unstably and no further stress increase is required before failure. K_{Ic} or the fracture toughness is a material property; the variability in K_{Ic} for crustal rock is shown in Fig. 2.10. Therefore, the condition for crack propagation will be met when:

$$G_c = K_c^2 \left(\frac{1 - \nu^2}{E} \right) \qquad [2.25]$$

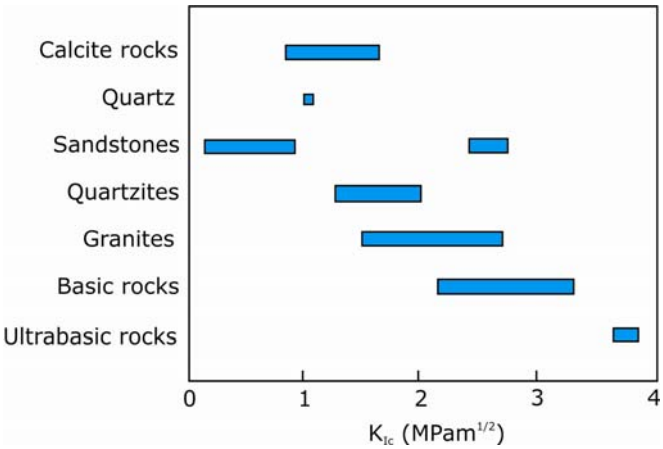

Figure 2.10. Variability in K_{Ic} for a variety of crustal rocks [from Atkinson, 1984].

2.3.4 Macroscopic fracture criterion

No simple universal law exists for the fracture stress of rock; this is due to the complex interaction of numerous factors. In order to describe rock strength and fracture in a more general manner, a semi-empirical approach that incorporates the relationship between all three principal stresses is used. The condition, that defines a failure envelope, is written in the form:

$$\sigma_1 = f\left(\sigma_2, \sigma_3\right) \qquad [2.26]$$

This condition is known as a criterion of failure, where the function f represents at least one characteristic of the material in question.

Shear failure under compressive stress states is often described by the Mohr-Coulomb criterion (sometimes referred to as the Navier-Coulomb criterion) and involves the greatest and least principal stress but neglects the influence of the intermediate principal stress [see Haimson, 2006]. The Mohr-

Coulomb failure criterion can be expressed as follows, where *tanφ* is the coefficient of internal friction, *C* is the cohesive strength and τ and σ_n are the shear and normal stresses. This can also be represented graphically on a Mohr diagram (Fig. 2.11).

$$\tau = C + \sigma_n \tan\phi \qquad [2.27]$$

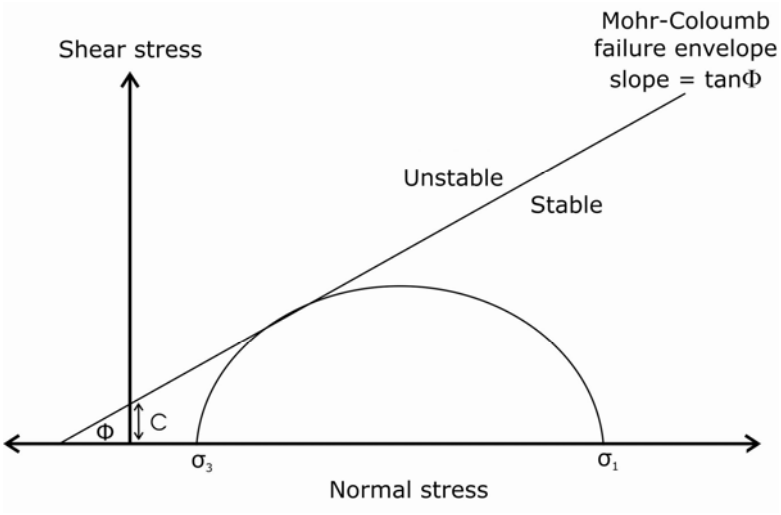

Figure 2.11. Illustration of the Mohr-Coulomb failure criterion by means of a Mohr diagram.

The Mohr-Coulomb criterion satisfactorily describes failure in compression of many rock types, whereas Griffith [Griffith, 1924] and the modified Griffith criteria [McClintock and Walsh, 1962] give a good description of tensile failure. These criteria can be combined to produce a more accurate description of brittle failure [see Scholz, 2002]. Some observations have, within experimental error, agreed with the Mohr-Coulomb criterion for failure [Brace, 1964]; however, there is usually some discrepancy between values of failure due to extension predicted from compression measurements [Heard, 1960; Murrell, 1965; Handin *et al.*, 1967; Mogi, 1967].

2.4 Experimental studies on brittle deformation

2.4.1 Introduction

Experiments are the bread and butter for understanding rock physics. Many different types of experimental methods exist to investigate the multitude of factors that influence rock deformation and brittle failure. This section aims to provide a detailed account the types of experimentally-induced fractures, the stress-strain response to deformation, some important principals in the deformation of porous rocks and the important factors that influence brittle rock deformation. The section also includes a brief review of frictional and sliding behaviour and the current state of understanding on AE behaviour during brittle deformation.

2.4.2 Types of brittle fractures

Increasing the stress on a rock sample beyond a critical point promotes permanent deformation that is manifested as dilatant microcracks. If the rock is stressed further then more and more microcracks nucleate and they begin to grow, interact and coalesce. Brittle failure occurs when there are sufficient microcracks to form a discrete fault or fracture that ruptures the sample (see *2.4.3 The evolution of physical properties during brittle failure*). The way in which the sample fractures depends on the way it was deformed. There are two principal modes of brittle failure (1) extension fracturing, where displacement is normal to the fracture surface and (2) shear fracturing, where displacement is parallel to the fracture surface [Griggs and Handin, 1960]. Rock deformation experiments have been devised to promote and study the different types of brittle fractures (Fig. 2.12).

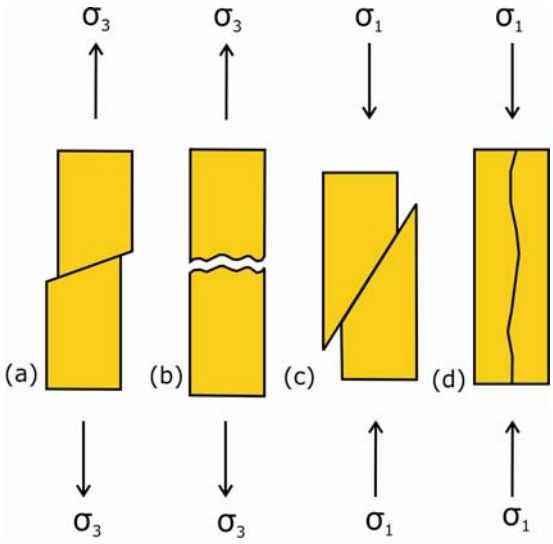

Figure 2.12. The different types of rock fractures. (a) Shear fracture during extension. (b) Extension fracture during extension. (c) Shear fracture during compression. (d) Extension fracture during compression (also called axial splitting).

During triaxial deformation experiments shear fracturing (Fig. 2.12c) is the most common method of rock failure. The angle of the shear fractures produced under triaxial deformation rarely departs from between 20-30° [Lockner, 1993; Reches and Lockner, 1994; Healy *et al.*, 2006]. True triaxial experiments demonstrate that for the same least horizontal stress the main fracture dip angle increases as a function of the intermediate principal stress [Haimson and Chang, 2000]. Axial splitting dominates under uniaxial compression [Heap and Faulkner, 2008] (Fig. 2.12d) but can be suppressed by even very mild effective confining pressures during triaxial deformation [Paterson, 1958; Heard, 1960; Wawersik and Fairhurst, 1970; Wawersik and Brace, 1971].

2.4.3 The evolution of physical properties during brittle failure

Many researchers have investigated the stress–strain behaviour of brittle rock under compression. The failure process can be broken down into a number of stages characterized by changes in the axial and

radial strain response recorded during uniaxial compression tests [Brace, 1964; Brace *et al.*, 1966; Bieniawski, 1967; Jaeger *et al.*, 2007; see also Heap and Faulkner, 2008] (Fig. 2.13a). The stages include: OA, the region where the stress–strain response is concave upwards due to the compaction of pores and the closure of favourably orientated pre-existing microcracks. This region may be absent or truncated at high effective stresses, as pre-existing microcracks will already be closed due to the application of the confining pressure, and is usually associated with a moderate amount of AE output. AB is the region where the stress–strain behaviour is very nearly linear and is attributed to the elastic deformation of the grains. The lack of microcrack activity during this region results in a very low AE output, although the complete absence of AE is uncommon. Some hysteresis has been observed during this region [Cook and Hodgson, 1965]; however, its explanation remains inconclusive. BC is the region where the stress–strain response is concave downwards and marks the onset of the formation of new microcracks – dilatancy.

Dilatancy has been shown to greatly affect rock physical properties. Elastic wave velocities [Birch, 1960;1961; Walsh, 1965; Anderson *et al.*, 1974; O'Connell and Budiansky, 1974; Soga *et al.*, 1978; Sayers and Kachanov, 1995; Gueguen and Schubnel, 2003; Reuschle *et al.*, 2003; Fortin *et al.*, 2005; Takemura and Oda, 2005] and electrical resistivity [Glover *et al.*, 1996; Yoshida *et al.*, 1998; Eccles *et al.*, 2005] both decrease whilst AE [Scholz, 1968; Sammonds *et al.*, 1992; Cox and Meredith, 1993; Stanchits *et al.*, 2006; Fortin *et al.*, 2006], pore volume (crack damage) change [Benson *et al.*, 2007] and permeability [Zoback and Byerlee, 1975; Brace, 1978; Zhu and Wong, 1997; Oda *et al.*, 2002; Mitchell and Faulkner, 2008] all increase (see Fig. 2.13b) with increasing dilatancy. During this region, the distribution of microcracking is distributed throughout the sample; although, there is usually some anisotropy associated with the microcracking as they preferentially develop parallel to the direction of the maximum principal stress. C marks the position of the peak stress of the sample and is defined by the localization of microcracking onto a discrete fault plane. As more and more microcracks coalesce along

the fault plane a macroscopic fracture forms that causes the dynamic failure of the sample associated with an exponential increase in AE output, permeability and pore volume change and an exponential decrease in elastic wave velocity and electrical resistivity (Fig. 2.13b). Post-peak behaviour [see Wawersik and Fairhurst, 1970 for details] can be seen following the peak stress.

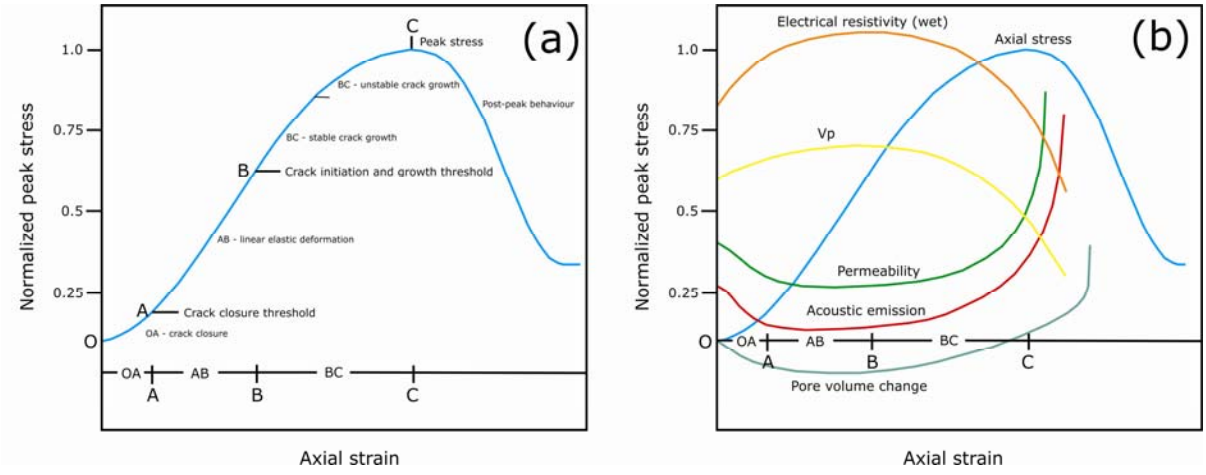

Figure 2.13. (a) Schematic diagram showing the general shape of the stress-strain curve subdivided brittle deformation regions (see text for details) during a typical compression test and (b) the variation of rock physical properties during a typical compression test [modified from Paterson and Wong, 2005].

Many of the experimentally-derived relationships described (Fig. 2.13) have characterized the influence of crack damage on rock properties through single stage loading. However, the stress history of rock is generally more complex than a constant loading rate e.g. a volcanic edifice is subject to repeated cycles of stress over time due to the combination of magma emplacement from deep reservoirs to shallow depths and superimposed tectonic stresses. Experiments were the stress is repeatedly cycled also allows the calculation of the evolution of physical properties in rock for 'crack damage increments', it is also the only viable method of measuring changes in static elastic moduli prior to failure. Experiments have demonstrated that static elastic moduli change during deformation [Alm *et al.*, 1985; Martin and Chandler, 1994; Eberhardt *et al.*, 1999; Lau and Chandler, 2004; Heap and Faulkner, 2008]. Heap and

Faulkner [2008] showed that, for Westerly granite, Young's modulus decreased by a total of 11% and Poisson's ratio increased by a total of 72% over the course of eight increasing-amplitude stress cycles. Mitchell and Faulkner [2008] investigated the evolution of permeability in samples of Westerly granite during increasing-amplitude stress-cycling. They found that permeability increased by 200-300% of the starting permeability for each of the first few cycles; however, beyond the cycle that peaked at 80% of the short-term peak stress the permeability increased by over an order of magnitude prior to failure. They concluded that higher levels of differential stress are very important for permeability evolution.

2.4.4 Important factors that influence brittle deformation

2.4.4.1 Influence of strain rate on brittle deformation

The influence of strain rate on brittle deformation depends heavily on the environmental conditions, especially temperature. Brittle fracture (low temperature) is relatively insensitive to changes in strain rate when compared to that for ductile deformation (high temperature) [see Rutter, 1972]. Triaxial experiments on a suite of igneous rock and limestone at room temperature found that there is an increase in the fracture stress of rock by approximately 10% for each 10^3 increase in strain rate [Brace and Martin, 1968; Masuda *et al.*, 1987; Masuda, 2001]. Commensurate effects have been noted during uniaxial compression tests [Sano *et al.*, 1981; Olsson, 1991; Li and Xia, 2000].

2.4.4.2 The influence of effective confining pressure on brittle deformation

Effective confining pressure (P_{eff}) exerts a significant influence of the deformation of rock [Paterson, 1958; Byerlee, 1967; Rummel and Fairhurst, 1970; Wawersik and Brace, 1971; Ohnaka, 1973; Baud *et al.*, 2000]. In the brittle field, an elevated P_{eff} reduces the ease at which microcracks can overcome the energy barrier required to continue to propagate [Francois and Wilshaw, 1968]. Therefore, an increase in the P_{eff} usually results in an increase in the differential stress that a rock can sustain before dynamic failure. Paterson [1958] studied the effect of P_{eff} on deformation in marble in great detail and found that the yield stress, the strain reached before macroscopic failure and the degree of strain hardening all increase with P_{eff} (Fig. 2.14). Paterson [1958] also found that the mode of failure changed at different values for P_{eff} (Fig. 2.15). However, it must be noted in this case, that beyond P_{eff} = 14 MPa the rock displays characteristic ductile behaviour. The value of 3-5% strain usually defines the position of the brittle-ductile transition [Heard, 1960; Evans *et al.*, 1990]. Rummel and Fairhurst [1970] and Baud *et al.* [2000] have also shown that an increase in P_{eff} can also result in the peak stress occurring at a higher % strain and a shallower post-peak curve.

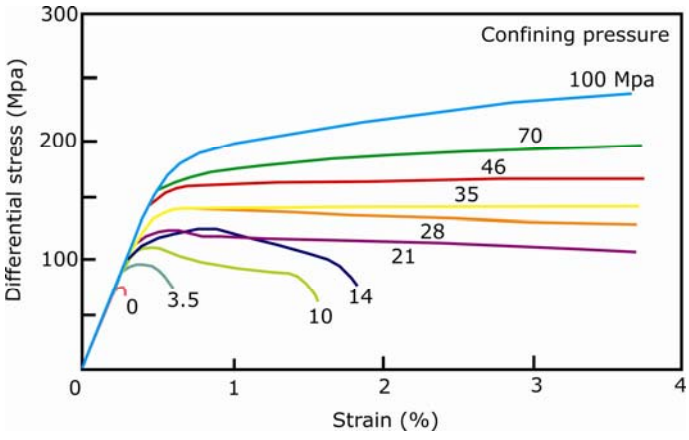

Figure 2.14. The effect of increasing the effective confining pressure on stress-strain curves during the triaxial deformation of Wombeyan marble [Paterson, 1958].

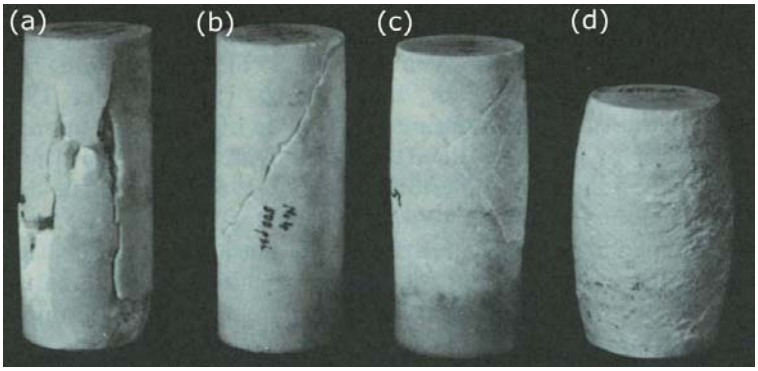

Figure 2.15. Types of fractures and flow in Wombeyan marble under different confining pressures (a) axial splitting at 0 MPa (b) single shear fracture at 3.5 MPa (c) conjugate shear fractures at 35 MPa (d) ductile flow and sample 'barrelling' at 100 MPa [Paterson, 1958].

The failure mode and volumetric response of porous rock during deformation is dependent on the P_{eff}. At low P_{eff} (under about 60-80 MPa in porous sandstones) the mode of failure is dilatant and arises from the nucleation, propagation and coalesce of pre-existing and stress-induced cracks. The initiation of dilatancy results in an increase in the volume of the rock sample and is termed shear-induced dilatancy. This phenomenon is also referred to as the onset of dilatancy and is termed *C'* (Fig. 2.16). Experimentally, the position of *C'* is inferred from the start of a volume-increasing deviation from hydrostatic deformation or 'hydrostat' [see Wong *et al.*, 1997; Baud *et al.*, 2006] (Fig. 2.16). At higher P_{eff} (above about 60-80 MPa in porous sandstones) compactant failure occurs and the mode of failure is homogenous cataclastic flow [Handin *et al.*, 1963; Curran and Carroll, 1979; Menéndez *et al.*, 1996; Baud *et al.*, 2006; Townend *et al.*, 2008]. This results in a decrease of volume in the rock sample and is termed shear-enhanced compaction, with the onset of such behaviour referred to as *C** (Fig. 2.16). Experimentally, the position of *C** is inferred from the start of the enhanced rate of volume-decreasing compaction with respect to the 'hydrostat' (Fig. 2.16). When hydrostatic deformation is continued beyond a critical point, termed *P**, the sample starts to undergo permanent inelastic deformation, namely grain crushing and pore collapse [see Fig. 2.16 and Zhang *et al.*, 1990].

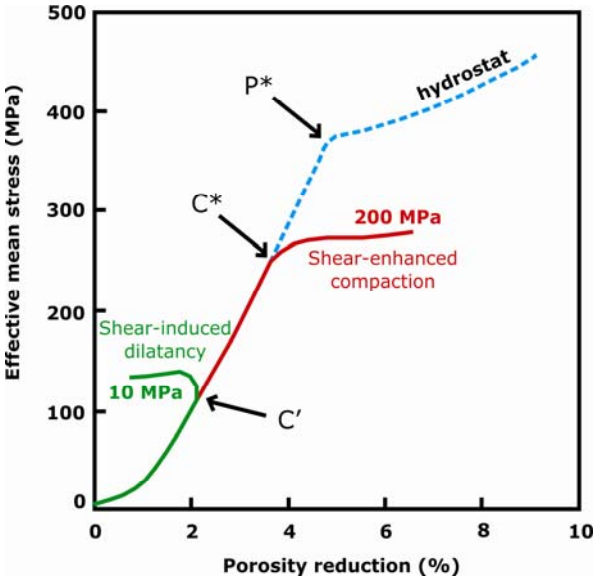

Figure 2.16. Schematic plot of effective mean pressure against porosity reduction for triaxial experiments on a porous sandstone. The figure shows the hydrostat and two experiments at 10 and 200 MPa effective confining pressure demonstrating the two modes of failure. The positions of *C′*, *C** and *P** are all labelled.

2.4.4.3 The influence of temperature on brittle deformation

Observations during deformation experiments consistently show that there is a decrease in rock strength with an increase in temperature [Wong, 1982; Tullis and Yund, 1992; Hirth and Tullis, 1994] (Fig. 2.16). At moderate temperatures the decrease in strength is very modest; however, at higher temperatures, the more pronounced decrease may reflect the approach to the brittle-ductile transition. Brittle deformation has therefore only modest temperature sensitivity, in the absence of mechanism changes.

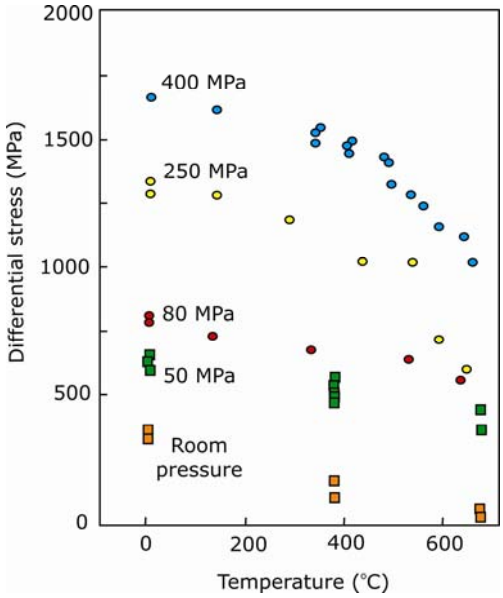

Figure 2.16. The influence of temperature on peak differential stress at different confining pressures. Squares – Charcoal granodiorite [Freidman et al., 1979]. Circles – Westerly granite [Wong, 1982]. Redrawn from Paterson and Wong [2005].

2.4.4.4 The influence of the intermediate principal stress on brittle deformation

Recent experimental observations have highlighted the importance of the role of the intermediate principal stress in the deformation of rock [Haimson and Chang, 2000; Chang and Haimson, 2000; see Haimson, 2006 for a review]. This creates a problem for the widely used Mohr-Coulomb failure criterion (see *2.3.4 Macroscopic fracture criterion*) that neglects the influence of σ_2 on brittle fracture strength. Haimson and Chang [2000] performed numerous true triaxial experiments on Westerly granite to investigate the influence of σ_2 on peak stress (Fig. 2.17). In general, the peak value of σ_1 increases as σ_2 is increased for a constant σ_3 in the case of brittle shear fractures. However, there is no general agreement about the form of the σ_2 dependence [see Handin *et al.*, 1967; Mogi, 1967;1971;1972; Haimson and Chang, 2000; Chang and Haimson, 2000].

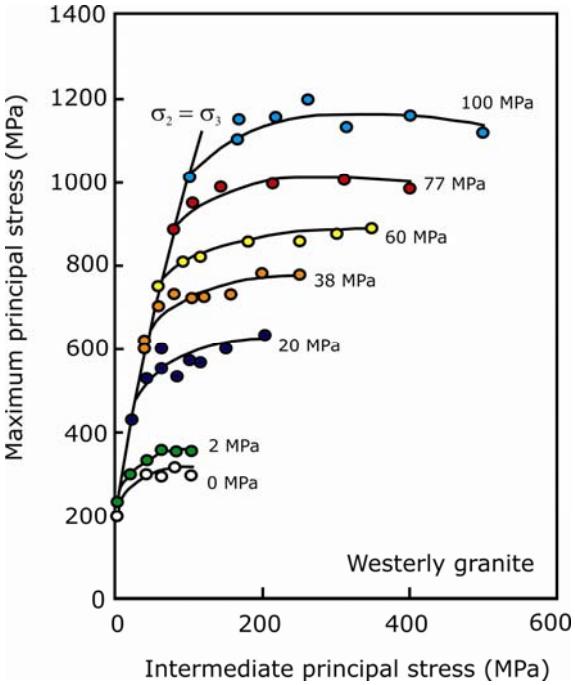

Figure 2.17. Peak maximum principal stress plotted against intermediate principal stress for a range of constant least principal stresses from true triaxial experiments on Westerly granite [Haimson and Chang, 2000].

2.4.5 Friction and sliding behaviour

If a rock is stressed beyond the point of dynamic failure then the two surfaces of the resultant fault can slide past one another. The resistance to sliding on an interface is expressed in terms of the coefficient of friction, μ, defined as the ratio of shear stress to the normal stress required to initiate a sliding surface (internal friction), initiate sliding on the surface (static friction) or maintain the sliding on the surface (dynamic friction). For rock, values of μ are usually within the range 0.2-0.8 [Ohnaka, 1975; Byerlee, 1978; Jaeger *et al.*, 2007]. Byerlee [1978] proposed, using a considerable volume of data, that the friction between rocks can be explained by the following two expressions, referred to as Byerlee's rule for rock friction (see Fig. 2.18).

$$\tau = 0.85\sigma \text{ (for } \sigma < 200 \text{ MPa)} \quad [2.28]$$

$$\tau = 50 + 0.6\sigma \text{ (for } 200 < \sigma < 1700 \text{ MPa)} \quad [2.29]$$

The friction between two sliding interfaces can also lead to the formation of gouge. Gouge is nearly always present within fault or fracture zones and is a product of wear created by the shearing of asperities and the fracturing of the surrounding material. In sufficiently think gouge layers, deformation structures within the gouge can be observed [Logan *et al.*, 1992; Faulkner *et al.*, 2003]. An increase in temperature has been shown to result in both a sudden and transient change in the frictional resistance to sliding [Chester, 1994].

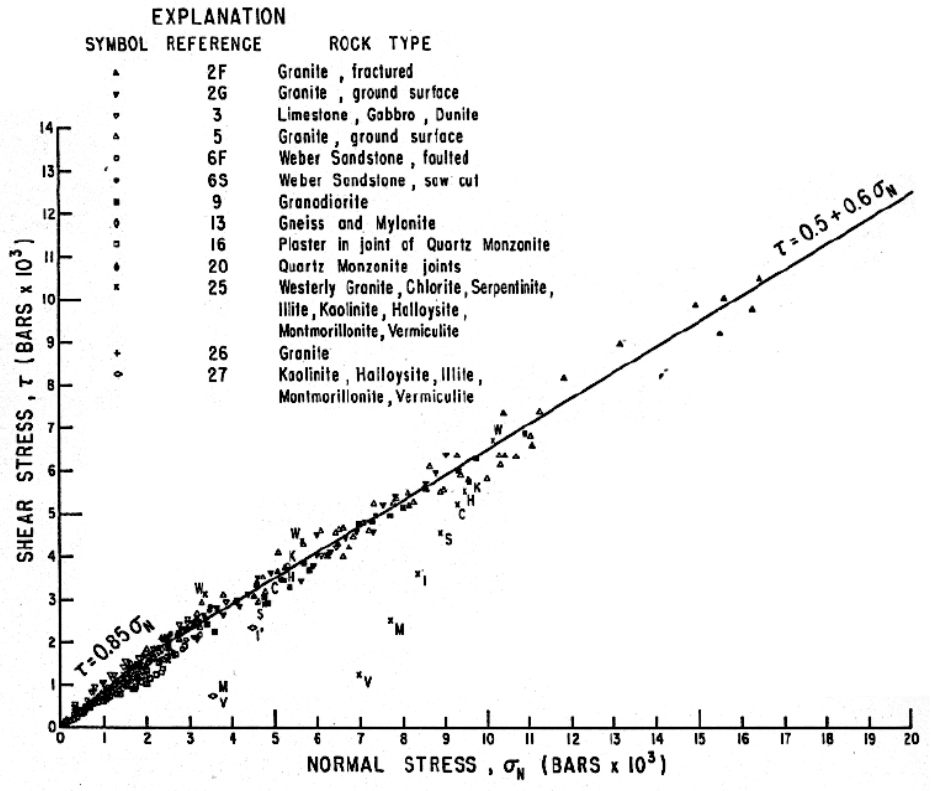

Figure 2.18. Dependence of friction on normal stress for a suite of different rock types and gouges [Byerlee, 1978].

More recently, using high-speed rotary shear frictional testing machines [e.g. Shimamoto and Tsutsumi, 1994], high-velocity frictional properties have become popular in the study of earthquake mechanics [e.g. Tsutsumi and Shimamoto, 1997; Goldsby and Tullis, 2002; Di Toro *et al.*, 2004].

2.4.6 Acoustic emission behaviour during brittle deformation

Acoustic emission (AE), defined as a transient elastic wave generated by a rapid release of energy within a material, is an increasingly important tool in the study of rock deformation. In the laboratory, where sample size prevents the monitoring of larger seismic events, microseismicity produced by flaws on the grain scale are recorded typically within in the 100-2000 kHz range. There have been many studies that have shown that AE output increases exponentially with increasing stress in rock, especially immediately prior to macroscopic failure [Scholz, 1968; Sammonds *et al.*, 1992; Cox and Meredith, 1993; Stanchits *et al.*, 2006; Fortin *et al.*, 2006] and so AE output is considered to be a reliable proxy for crack growth within a sample. Zang *et al*. [1996] also observed differences in the AE output of dry and wet sandstone samples. Multi-channel recording systems have been used to determine the location or 'hypocentre' of the AE events within the sample [Lockner *et al.*, 1991;1992; Lockner, 1993 Lockner and Byerlee, 1992; Lockner, 1993; Zang *et al.*, 1996; Lei *et al.*, 2000; Lei *et al.*, 2004] (Fig. 2.19). More recently, AE locations during deformation have been recorded using a Giga RAM Recorder that allows the recording of continuous ultrasonic waveforms for a significant period of time [Thompson *et al.*, 2006; Benson *et al.*, 2007; Townend *et al.*, 2008].

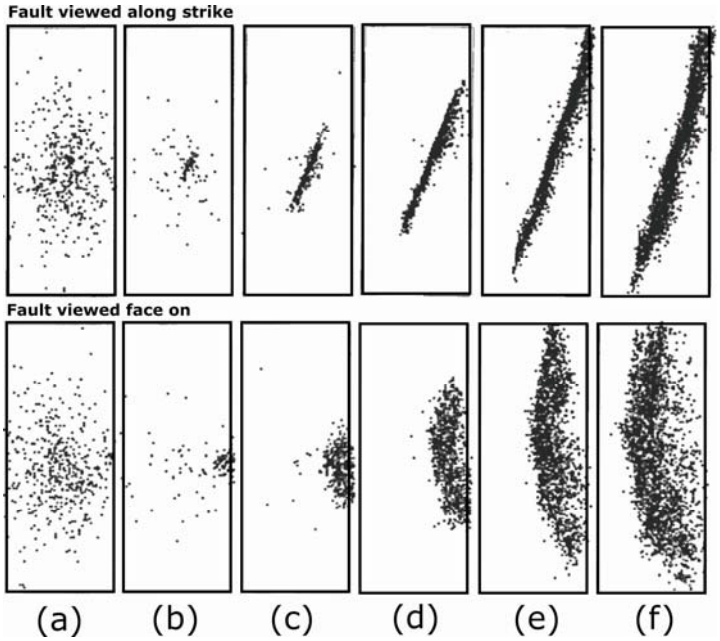

Figure 2.19. Sequential plots of locations of AE events with upper plots showing events viewed along strike of the eventual fault plane and lower plots showing the same events viewed face on. The fault nucleates in (b) and propagates across the sample in (c) – (f) [Lockner *et al.*, 1991].

Previous AE studies of microcracking in rocks have demonstrated that, in general, new microcrack damage is generated only once the previous maximum stress has been exceeded during cyclic stressing. This phenomenon was first reported in metals [Kaiser, 1953] and is now known as the Kaiser 'stress-memory' effect [see reviews by Li and Nordlund, 1993; Holcomb, 1993; Lockner, 1993; and Lavrov, 2003]. AE output has also been recorded during brittle creep experiments [Wu and Thomsen, 1975; Ohnaka, 1983; Yanagidani *et al.*, 1985; Hirata *et al.*, 1987; Nishizawa and Noro, 1990; Baud and Meredith, 1997]; this is explained in much more detail later (see Chapter Three, section 3.5.3.5 Acoustic emission during brittle creep experiments).

Chapter three

3. The Role of Pore Fluids in Brittle Rock Deformation

3.1 Introduction

3.1.1 Pore fluids in the crust

The majority of rocks forming the Earth's crust, even those at depth, contain microporosity comprising some or all of open pores between grains, triple-junction voids between crystalline phases, grain boundary voids and open microcracks. Water and aqueous solutions are ubiquitous in the upper crust, and below a few hundred metres most rock is saturated; therefore, the pores and cracks in rock are likely to contain a fluid phase. The presence of a fluid phase can greatly affect the behaviour of both mechanical and chemical interactions within the rock (see **3.2 The influence of pressurized pore fluids on brittle rock deformation**).

As porosity is reduced by lithostatic pressure during burial, trapped pore fluids are forced to occupy a smaller volume – this generates a pressure. The pressure built up by this action is called a pore fluid pressure (P_p) and exerts a hydrostatic pressure normal to the surface of the grains. The pore fluid trapped within pores and cracks act to resist their closure caused by the external applied stresses surrounding the rock. The consequence of an elevated P_p can exert a considerable influence on brittle rock deformation. The magnitude of P_p in rock in the Earth's crust, except under special circumstance, increases with depth (Fig. 3.1).

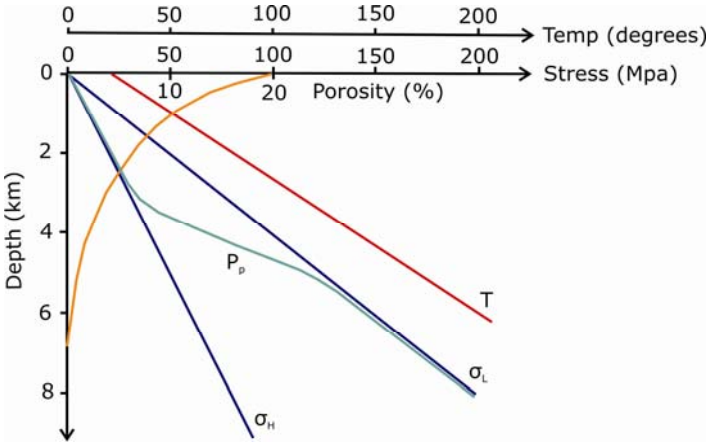

Figure 3.1. Pore fluid pressure (P_p) variation with depth. σ_H – hydrostatic pressure, σ_L – lithostatic pressure and T – temperature.

The reasons for the relationships shown in Fig 3.1 include: (1) closure of cracks and necks between pores by mechanical compaction, (2) sealing of cracks and pore spaces by diagenetic cementation processes, the swelling of clay minerals and precipitation of hydrothermal fluids, (3) the development of impermeable layers in sedimentary sequences, (4) water production by metamorphic dehydration reactions and (5) partial melting at high pressures and temperatures. The combination of these effects results in a P_p that can exceed the hydrostatic pressure but not the lithostatic pressure, due to hydraulic fracturing (Fig. 3.1).

3.2 The influence of pressurized pore fluids on brittle rock deformation

The presence of P_p in rock affects brittle rock deformation in two main ways: (1) mechanically and (2) chemo-mechanically, and will now be discussed in turn. However, this chapter will concentrate on the chemo-mechanical effects of the presence of pore fluid, focusing on subcritical crack growth.

3.2.1 Mechanical effects of pore fluids on brittle deformation

3.2.1.1 Mechanical water-weakening of brittle rock

The mechanical role of pressurized pore fluids is to weaken and embrittle rock. Previous experimental studies have shown that the presence of the most common fluid phase, water, acts to reduce the brittle strength of porous rock (Fig. 3.2) [Rutter and Mainprice, 1978; Chester and Logan, 1986; Hadizadeh and Law, 1991; Dewers and Hajash, 1995; Zang *et al.*, 1996; Masuda, 2001; Baud *et al.*, 2000], and even low-porosity crystalline rock [Lajtai *et al.*, 1987; Dennis and Atkinson, 1982]. Water-weakening behaviour has also been seen to affect the cataclastic flow regime [Bernabé and Brace, 1990; Read *et al.*, 1995; Zhu and Wong, 1997].

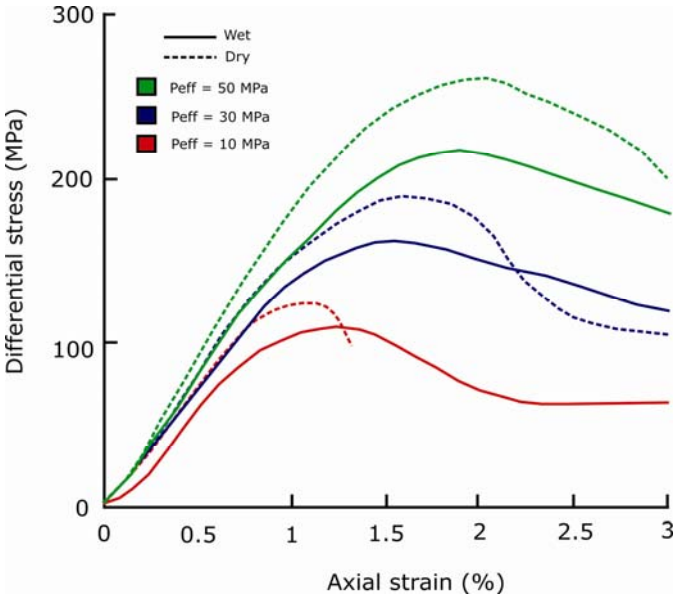

Figure 3.2. Stress-strain curves to demonstrate the weakening effect of water on brittle strength at various effective pressures in Darley Dale sandstone [redrawn from Baud *et al.*, 2000].

3.2.1.2 The law of effective stress

Mechanically, pressurized pore fluid acts to reduce the normal stress required to promote macroscopic rock failure. The gross mechanical behaviour of a porous rock depends on the total macroscopic stress and the P_p. This notional macroscopic stress, termed the effective stress, can be treated as the only stress variable that governs a particular observed behaviour [Skempton, 1961; Robin, 1973; Berryman, 1992]. Alternatively, the effective stress can be defined as the total macroscopic stress minus the P_p (assuming that the poroelastic multiplier is equal to one, this is explained in more detail in 3.2.1.3 Experimental observations of the mechanical effect of pore fluids) [Lamb and Whitman, 1969; Jaeger *et al.*, 2007] (Fig. 3.3).

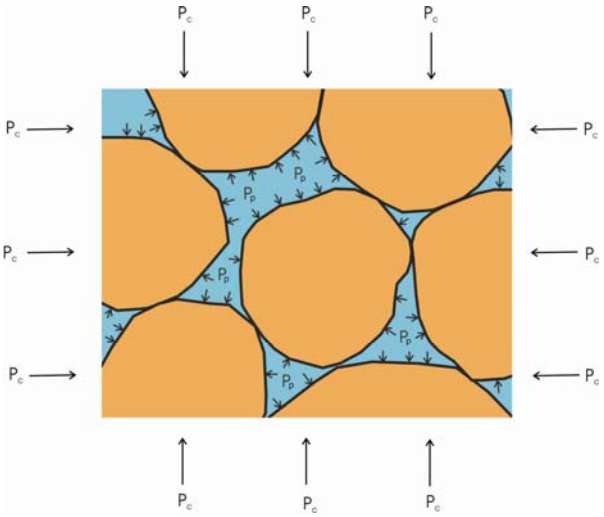

Figure 3.3. Schematic diagram to demonstrate how pore fluid pressure (P_p) resists the closure of pore space due to external compressive pressure or confining pressure (P_c).

This can be explained, at least for isotropic behaviour, in terms of Terzaghi's principle [Terzaghi, 1943] or the law of effective stress:

$$\sigma_n{}' = \sigma_n - \alpha P_p \qquad [3.1]$$

Where σ_n is the total normal macroscopic stress, α is the constitutive relation of poroelasticity multiplier called the effective stress coefficient and P_p is the pore fluid pressure [see Terzaghi, 1943; Lambe and Whitman, 1969; Jaeger *et al.*, 2007]. This can be represented graphically on a Mohr-Coulomb diagram (Fig. 3.4), where *tanΦ* is the coefficient of internal friction and *C* is the cohesive strength.

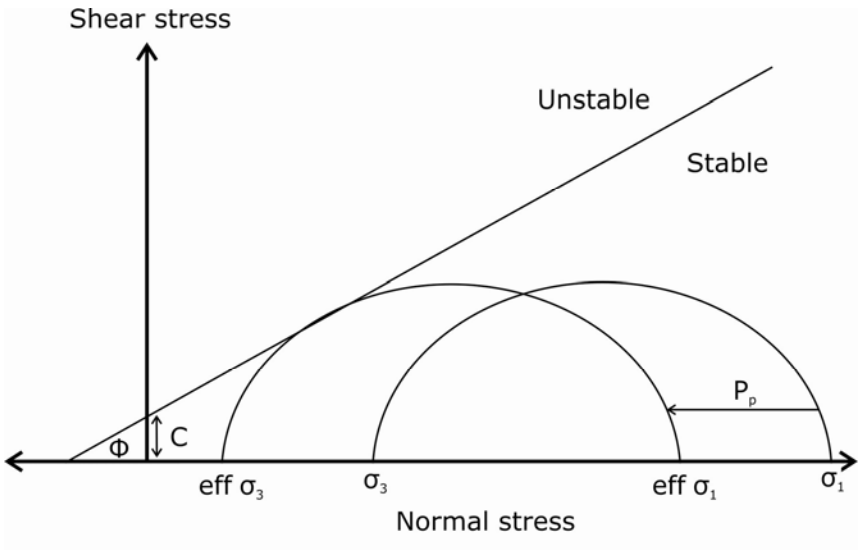

Figure 3.4. A Mohr-Coulomb diagram (as in Chapter Two, Fig. 2.11) showing the mechanical effect of an elevated pore fluid pressure.

An elevated pore fluid pressure only affects the normal stress acting on a rock – the shear stress remains unaffected – this results in a 'left-shift' of the Mohr stress circle and hence promotes failure in an otherwise stable rockmass (Fig. 3.4). The Mohr-Coulomb failure criterion is thus modified from equation [2.27] to:

$$\tau = C + \mu\left(\sigma_n - P_p\right) \quad [3.2]$$

3.2.1.3 Experimental observations of the mechanical effect of pore fluids

During a drained test the P_p is maintained at a constant value by an external pressure source connected to the pore system of the rock e. g. a pore fluid intensifier (see Chapter Four, section 4.3.5.1 Intensifiers/pore volumometers). Numerous experimental studies on a wide variety of rock types have found a good approximation to Terzaghi's law of effective stress (Fig. 3.5). Terzaghi's principle [Terzaghi, 1943] dictates that α must equal one, which is consistent with experimental studies on the inelastic behaviour of rock. Fig. 3.5 shows that, for sandstone, the differential stress for shear failure is approximately equal at the same P_{eff} [Murrell, 1965]. However, it must be noted that values of α that differ from one have been reported in experimental work on porous rock [Boitnott and Scholz, 1990; Kwon *et al.*, 2001], crystalline rock [Bernabé, 1986] and in modelling [Gangi and Carlson, 1995]. In general, the law of effective stress holds for rocks only when the loading rate is less than a critical value that depends on the permeability of the rock, viscosity of the pore fluid and sample geometry [Brace and Martin, 1968].

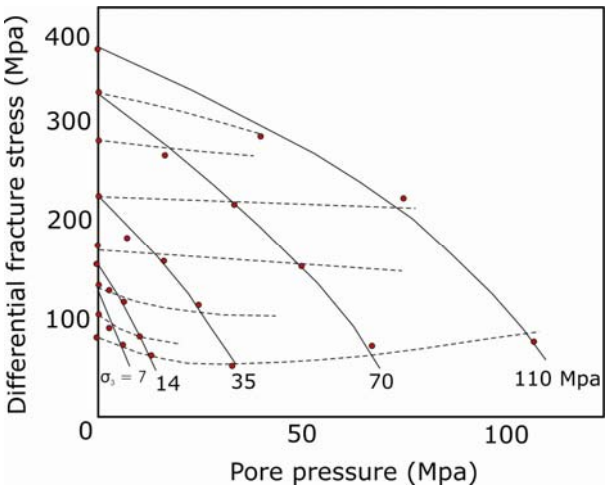

Figure 3.5. The influence of pore pressure on differential stress at various confining pressures for sandstone [Murrell, 1965].

During an undrained test the pore fluid the rock sample is isolated from an external pore fluid intensifier. This therefore allows P_p to change during the experiment as a result of the changes in

porosity that accompany deformation (Fig. 3.6a). A decrease in porosity caused by compaction results in an increase in the P_p, due to the fact that the same volume of fluid must now occupy a smaller pore volume. Therefore, an increase in porosity during dilatancy leads to a decrease in the pore pressure, so a greater differential stress is then required to continue deformation. This phenomenon is known as dilatancy hardening (Fig. 3.6b).

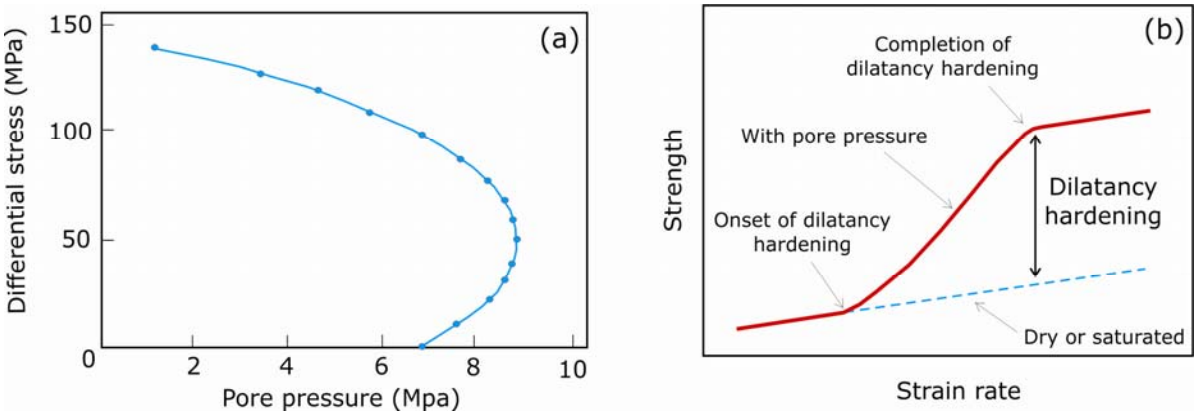

Figure 3.6. (a) The change in pore pressure with increasing differential stress for an undrained triaxial test on sandstone [Heck, 1972] and (b) graph to demonstrate the concepts of dilatancy hardening [Brace and Martin, 1968].

3.2.2 Chemo-mechanical effects of pore fluids on brittle deformation

The chemo-mechanical influence of P_p also acts to weaken the rock (1) through the reduction of surface free energy [Orowan, 1944; Rehbinder, 1948; Andrade and Randall, 1949] and (2) by mechanisms of subcritical crack growth such as stress corrosion [Anderson and Grew, 1977; Atkinson, 1984; Atkinson and Meredith, 1987; Costin, 1987], both of which can occur simultaneously. This section will only briefly discuss weakening via the reduction of surface free energy and will concentrate on subcritical crack growth, in particular the mechanism of stress corrosion.

Other chemically-activated, water-weakening mechanisms do occur however. In carbonates in particular, water-weakening has been observed due to the increased solubility of calcite in water and increased pressure solution at elevated stresses [Hellmann *et al.*, 2002], leading to the formation of stylolites. In chalks, water saturation removes menisci or bridges between grains that act to pull grains together and increase cohesion hence weakening the rock [Delage *et al.*, 1996]. Typically, dry and partially-saturated samples are significantly stronger than those fully-saturated. The chemically-enhanced weakening of chalk by chemical dissolution/precipitation processes has also been observed experimentally [Heggheim *et al.*, 2005].

3.2.2.1 The reduction of surface free energy

The reduction of surface free energy is the result of the absorption of pore water, or any other fluid, onto the internal pore surfaces. The pore fluid lowers the interfacial free energy that reduces the work-hardening component due to the pile-up of dislocations at the crystal-fluid interface and therefore increases the probability of the emergence of dislocations onto the grain boundary [Rehbinder, 1948]. This effect is sometimes referred to as the *Rehbinder effect*. The work by Rehbinder [1948] built on previous work by Orowan [1944] who, using values of surface energy obtained for mica, considered that the reduction in surface energy owing to the presence of water lowers the critical stress required for crack propagation. This corresponding reduction in strength with time is consistent with experimental observations for glass [Baker and Preston, 1946].

3.2.2.2 Subcritical crack growth

Once a critical stress intensity factor (K_c) or crack extension force (G_c) has been reached during brittle deformation of linear elastic solid, microcracks can propagate unstably and at speeds close to the speed of sound [Irwin, 1958]. This results in dynamic failure of the solid. However, at lower values of *K* and *G* microcracks remain stable (quasi-static). This traditional fracture mechanics approach has been successfully used to predict failure caused by microcrack propagation in metals, ceramics and glasses. Failure predictions are also good for rock subjected to short-term loading; however, during long-term loading, predictions are not so reliable. This is especially true if there is an abundance of an environmental agent or active species (commonly water) or elevated temperatures. In this scenario, and even despite values of *K* and *G* well below the critical thresholds, the rate of microcrack growth becomes substantial due to a mechanism known as subcritical crack growth. Subcritical crack growth has been experimentally observed in rocks and minerals [see Atkinson, 1984 for review], but was first discovered in experiments on glass [Grenet, 1899] and later in ceramics [Wiederhorn, 1968].

Subcritical crack growth, defined as stable crack growth below the K_c or G_c, can be due to several competing processes. Such mechanisms are environment-dependent and are influenced by the presence of a chemically active pore fluid. For crustal rock, this is most commonly water. Therefore the prevalent process depends heavily on the chemical and environmental conditions. A number of competing mechanisms have been suggested to explain how microcracks in rock can propagate subcritically: stress corrosion, dissolution, diffusion, ion exchange and microplasicity [see Atkinson, 1984 for a review]. All of the mechanisms are discussed in turn below.

3.2.2.3 Mechanisms of subcritical crack growth

Stress corrosion. Stress corrosion is the foremost mechanism of subcritical crack growth [see Atkinson, 1982] and is the primary process under investigation in this laboratory study. It will therefore be discussed in great detail in the next section (**3.4 Stress corrosion**).

Diffusion. Diffusion, a mass transport process, becomes an important process at higher temperatures and at deeper crustal levels. It is only likely to become important in the upper crust at very low strain rates and crack velocities. Also, at temperatures typical of the upper crust, it is likely that diffusion-controlled subcritical crack growth will only be significant at low values of stress intensity. At higher stress intensities, other mechanisms of subcritical crack growth will be much more prevalent. Along grain boundaries is likely to be the most important and quickest diffusion path, however lattice or bulk diffusion, surface diffusion and vapour transport diffusion will be occurring contemporaneously. Crack growth velocities in quartzite controlled by grain boundary diffusion, as calculated by Atkinson [1984], indicate that although diffusion velocities are slow, they are not insignificant on geological timescales. However, diffusion can be the most prevalent mechanism in ceramics and high homologous temperatures [Karunaratne and Lewis, 1980; Evans and Blumenthal, 1983]. Stress-directed diffusion can occur near the crack tips during crack propagation due to dissolved chemical impurities present in some materials and can result in weakening reactions that aid crack extension [Dutton, 1974].

Dissolution. Dissolution has been best observed in binary alkali-silicate glasses aqueous solutions. The observed crack velocity plateau in tensile *K-v* diagrams is likely to be due to the solubility of these glasses in water resulting in silica dissolution controlling the crack growth rate [Simmons and Freiman, 1981]. At low stress intensity factors, provided that the dissolution rate is fast enough, there is no reason why dissolution should not be an important process in geological materials. However, if

dissolution products are not removed from the crack tip and precipitation of the new material takes place then subcritical crack growth will be inhibited [Ito and Tomozawa, 1982].

Ion exchange. Lattice strains, which result in crack extension, can occur if the chemical environment contains species that can undergo ion exchange with species in the solid phase, provided that there is a large difference in the size of the different species. Wiederhorn [1978] observed this process and found that, for silicate glasses, an exchange of H^+ for Na^+ occurred. Ion exchange can also alter the chemistry of the reactive species at the crack tip. For example, a basic solution is produced at the crack tip in a glass/water system due to the exchange of hydrogen ions for alkali ions. The limited volume of the fluid at the crack tip can cause the pH can change very quickly. However, the importance of ion exchange reactions will depend heavily on how easily the crack tip solution is modified by diffusional exchange with the bulk external environment [Wiederhorn, 1978]. The crack growth behaviour of the process is dependent on the crack velocity, rate of reaction between the material at the crack tip and the external environment and the chemistry of the solid near the crack tip [Wiederhorn and Johnson, 1973]. Wiederhorn and Johnson [1973] studied the effect of H^+-Na^+ ion exchange studying crack velocity in soda-lime silicate glass immersed in *HCl* solutions. They observed a small, but measurable effect, on crack propagation of stresses resulting from H^+-Na^+ ion exchange. At high crack velocities it is controlled by the chemical composition of the new crack surfaces; whereas, at low crack velocities it is controlled by the chemistry of the external environment.

Microplasticity. Microcracks of random orientation and position, within a fault damage zone, will initiate by inhomogeneous plasticity when local conditions for slip or twinning are satisfied. These microcracks will eventually grow, coalesce and facilitate locally episodic extension of the fault. Macroscopically, this process will appear as quasi-static subcritical crack growth, favoured by low strain rates and high

homologous temperatures. Microplasticity may be an important mechanism of crack extension in silicates and could potentially result in subcritical crack growth [Atkinson, 1982], as long as homologous temperatures and structurally bound water concentrations are high enough. However, electron microscopy analysis of quartz shows that there is no significant plastic flow at crack tips during chemically enhanced subcritical crack growth [Martin and Durham, 1975; Dunning *et al.*, 1980]. For some materials however, such as calcite and galena, microplasticity can be observed even at low stresses and temperatures.

3.4 Stress corrosion

3.4.1 Introduction

Stress corrosion is considered to be the most important and prevalent mechanism of subcritical crack growth in the upper 20 km of the Earth's brittle upper crust. This is corroborated by fracture deformation maps for quartz (Fig. 3.7) [Atkinson, 1982]. Stress corrosion crack growth occurs because the chemical action of an environmental agent or active species, commonly water, weakens the strained bonds at crack tips and so facilitates crack propagation [definition from Atkinson and Meredith, 1987]. The theory behind stress corrosion has been developed using a simplistic system of water and silicate and as a result will receive much of the focus within this section. However, due to the abundance of silica in the crust, the time-dependent behaviour of a silica-water system is of particular importance. For reviews on stress corrosion crack growth see Anderson and Grew [1977] and Atkinson [1984].

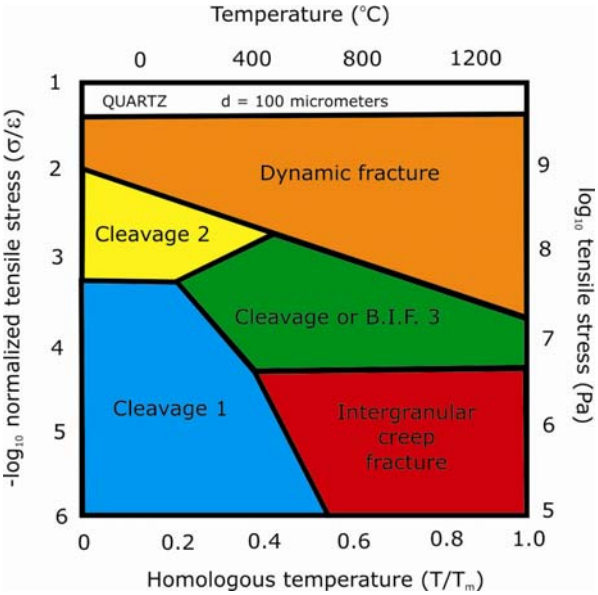

Figure 3.7. Fracture mechanism map for quartzite, where grain size is 100μm [redrawn from Atkinson, 1982].

3.4.2 A molecular mechanism for stress corrosion

3.4.2.1 General concept of chemically-induced bond rupture

A simple atomistic view of a generic chemically-induced crack tip interaction is shown in Fig. 3.8. The intrusive environmental molecule *A*-*A* has reached the crack tip and reacts dissociatively with the intact bridging bonds at the crack tip -*B*-*B*-*B*- to form two terminal *A*-*B* bonds:

$$(A-A)+(-B-B-)\rightarrow(-B-A\cdot A-B-) \qquad [3.3]$$

This chemical process lengthens the crack and results in the exposure a new crack tip bonds that can react with the next incoming environmental molecule.

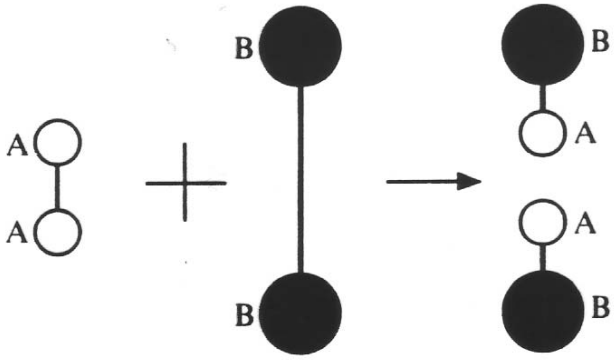

Figure 3.8. Simplistic chemically-induced bond rupture [from Lawn, 1993].

The rate of chemical-induced extension of the crack is therefore dependent on the rate at which these dissociative reactions can occur. The rate of crack extension by this chemically-induced process exhibits trimodal behaviour as the stress intensity factor at the crack tip is increased. This relationship is best illustrated by a stress intensity factor - crack velocity or *K*-*v* diagram (Fig. 3.9).

Each of the three regions in Fig. 3.9 is characterized by a different rate controlling mechanism. In region 1 the crack velocity is controlled by the rate of reaction of the environment active species with the chemical bonds at the crack tip [Wiederhorn, 1967]. Region 1 is important as it is the region where slow-growing cracks spend most of their growth period. As the stress intensity at the crack tip increases further, the chemical weakening reactions occur with a higher frequency. At a particular crack velocity, the rate at which the active species can diffuse through to the crack tip becomes slower than the dissociative reaction rate. This results in a plateau in the crack velocity, since increasing the stress intensity further does not influence the diffusion of the active species to the crack tip, and signifies the start of region 2. Region 3 denotes the part of the curve where the crack velocity is mechanically controlled by the applied stresses and is shown to be independent of concentration of active species

[see Wiederhorn, 1967; Freiman, 1974; Wiederhorn *et al.*, 1982; Freiman, 1984]. See Freiman [1984] for a comprehensive review of the three regions.

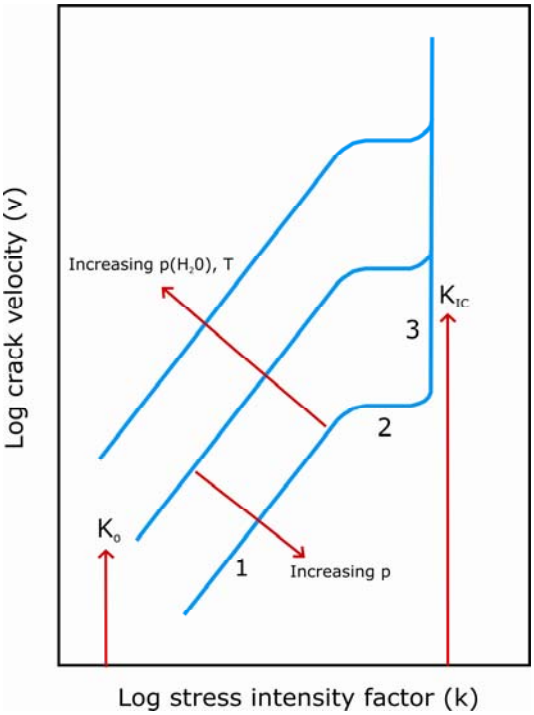

Figure 3.9. Schematic stress intensity factor/crack velocity diagram (*K-v* diagram) showing the different regions of a typical tensile crack growth curve due to stress corrosion at constant temperature, pressure and activity of the corrosive environmental species.

3.4.2.2 Chemically-induced bond rupture in a silica-water system

We can now consider this process in a silicate and water system. Silicates are comprised of $[SiO_4]^{-4}$ tetrahedral units that are linked at their corners by bridging *Si-O-Si* (siloxane) bonds. The network structure of SiO_2 is a relatively 'open' structure that allows intrusive reactive species to have direct contact with the bridging bonds at the crack tip (Fig. 3.10) [Lawn, 1993].

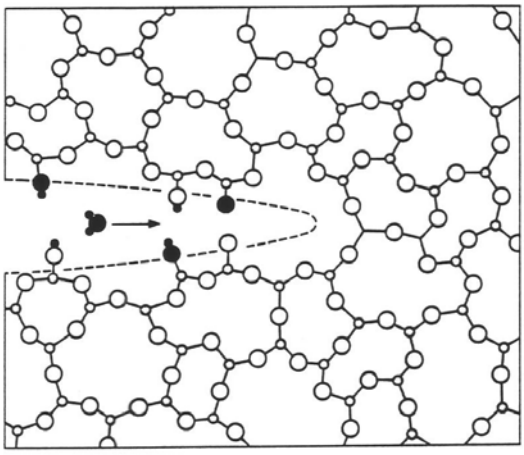

Figure 3.10. Schematic two-dimensional diagram illustrating water-induced bond rupture in silicates. Filled circles denote environmental water species and open circles denote the silicon (small circles) and oxygen (large circles) of the silicate material [from Lawn, 1993].

The bridging *Si-O* bonds present at crack tips are the stress-supporting component and are therefore the most important when considering the extension of cracks. The result of the increased strain on the *Si-O* bonds leads to an increased availability for *Si* and *O* atoms to bond with other species, water molecules for example. The interaction between a strained bridging bond at the crack tip in silica and a water molecule is of prime importance in the theory of stress corrosion. This interaction has been described as a three stage molecular orbital process of absorption, reaction and separation (Fig. 3.11) [Michalske and Freiman, 1982; Michalske and Bunker, 1987].

(1) A water molecule from the environment attaches to one of the bridging *Si-O-Si* bonds at the crack tip. The water molecule aligns itself by forming a hydrogen bond with the *O* in the bridge and the orbital interaction of the *O* in the water.

(2) Proton transfer from the *O* in the bridge and electron transfer from the *O* in the water to the *Si* takes place simultaneously. This forms two new bonds, one between the *O* from the water and the Si and one between hydrogen and the *O* in the bridge. The original bonding is destroyed.

(3) The bond between the *O* from the water and hydrogen is destroyed. The hydrogen is assimilated and results in terminal *Si-O-H* (silanol) groups on both sides of the crack tip surface. Due to the weakness of the newly formed hydrogen bond it can be broken at lower stresses, thus extending the crack. This step generally has a very short duration.

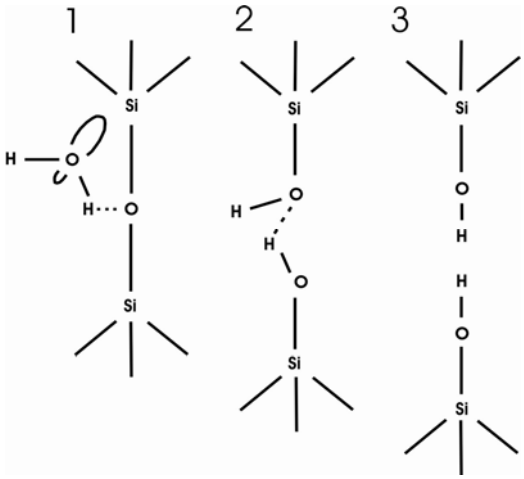

Figure 3.11. Model for the stress-induced chemical reaction of water with amorphous silica (1) absorption (2) reaction and (3) separation [redrawn from Michalske and Freiman, 1983].

The three stage model proposed by Michalske and Freiman [1983] demonstrates that there is no requirement for the dissociation of the water molecule before the reaction takes place and that reaction products need to be removed from the crack tip. It also allows the process to be conducted by other environmental species, provided that they contain a proton donor and lone-pair orbitals at either end of the molecule and that it is a similar size to the *Si-O* bond. The intrinsic chemical bond rupture for a

silicate and water system, as described in Equation [3.3], can now be written as follows [Scholz, 1972; Martin, 1972; Swain *et al.*, 1973; Atkinson, 1979].

$$(H-O-H)+(-Si-O-Si-)\leftrightarrow(-Si-OH\cdot HO-Si-)\leftrightarrow 2\,(Si-OH) \qquad [3.4]$$

3.5 Experimental observations on stress corrosion cracking

3.5.1 Introduction

Experimental studies on stress corrosion fall into two categories (1) double-torsion (DT) experiments on single cracks and (2) brittle creep experiments on bulk rock samples. The majority of experimental data on stress corrosion cracking has been derived from experiments on single cracks at ambient pressure and only few data exist on the bulk behaviour of rock containing a population of cracks. This section will describe the current state-of-knowledge of both methods in turn.

3.5.2 Experiments on a single crack: double-torsion (DT) experiments

3.5.2.1 Introduction

Crack propagation by subcritical crack growth in materials, including rocks and minerals, has been most-extensively studied in DT experiments [see reviews in Atkinson, 1982;1984; Atkinson and Meredith, 1987]. There is also a substantial volume of work on subcritical crack growth in glass and ceramics, some of which will be discussed here. A schematic of a DT specimen is shown in Fig. 3.12. The specimen, a simple rectangular plate, is supported on two parallel rollers and the load is applied via two

hemispheres attached to an upper plate. The crack then begins to propagate along the length of the specimen, guided by an axial groove that ensures the crack propagates along the specimen axis [see Evans, 1972 for more details on the DT method]. One of the major advantages of the DT method is that a complete *K*-*v* plot (as in Fig. 3.9) can be generated from a single load relaxation (or constant displacement) experiment and that K_I is independent of crack length over much of the experiment. Indeed, a wide range of data on subcritical crack growth can be obtained from a single experimental run. There are however limitations to the DT method. Firstly, it only allows the propagation of the single crack to be studied; in a bulk rock sample cracks would interact and coalesce. There are also problems associated with the dimensions of the specimen with respect to key parameters, such as the stress corrosion index, amongst others [see Atkinson, 1984; Swanson, 1984 for a review of the limitations].

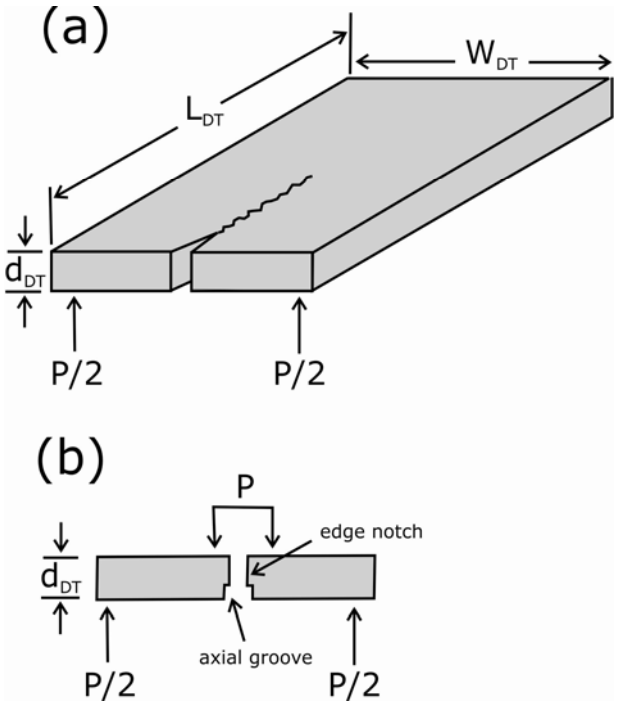

Figure 3.12. Schematic diagram of the specimen configuration for a double-torsion experiment (a) general view (b) axial cross section view showing the axial groove and edge notch. P – load; d_{DT} – thickness of specimen; W_{DT} – width of specimen; L_{DT} – length of specimen; a – length of the propagating crack.

This section will outline previous work on stress corrosion cracking using DT experiments and is split into headings that represent specific areas of interest that have commanded significant attention in the literature.

3.5.2.2 The influence of mineralogical composition from DT experiments

Experimental data from DT experiments for a wide range of geological materials in liquid water at 20°C are presented in Fig. 3.13 [Atkinson, 1984]. Fig. 3.13 shows that, for a given stress intensity factor, cracks will propagate at different velocities in different materials. In general, the more complex the microstructure, the lower the susceptibility to subcritical crack growth [Swanson, 1984]. A review of the volume of DT experimental data in a wide variety of minerals and rock types is given in Atkinson [1984] and Swanson [1984]. Experiments on anisotropic granite have also shown that crack velocity can vary for anisotropic rock depending on propagation direction of the crack [Nara and Kaneko, 2006].

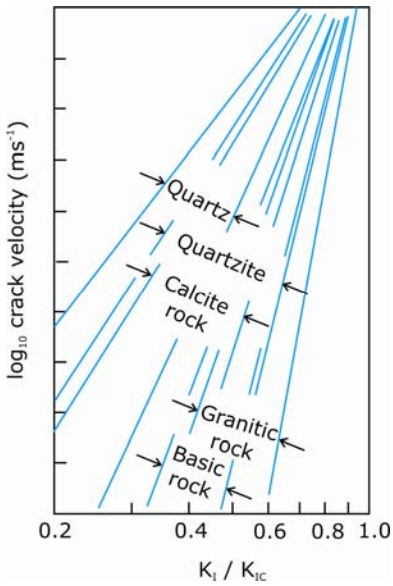

Figure 3.13. Schematic diagram showing variation of subcritical tensile crack growth behaviour in different rock types. Arrows indicate the range of data for a specific rock type [data compiled by Atkinson, 1984].

3.5.2.3 The influence of different corrosive environmental species from DT experiments

Although water is the most common pore fluid in the Earth's upper lithosphere, other aqueous solutions such as carbon dioxide, hydrocarbons, brine and acids and alkalis are commonly present. However, nearly all of the accumulated experimental data to study process of stress corrosion cracking on rock has been limited to water or air as the reactive chemical species [see Atkinson, 1984]. Despite this, the few experiments conducted to study the influence of different environmental fluids on stress corrosion in rock have proved it to be substantial.

Atkinson and Meredith [1981] studied the effect of 2N hydrochloric acid and 2N sodium hydroxide solutions on stress corrosion in synthetic quartz using a DT testing apparatus. They found that for a given value of stress intensity, the crack velocity increases as the hydroxyl (OH^-) concentration is increased (Fig. 3.14a). This agrees with the theory of stress corrosion (explained in terms of a silica-water system, see 3.4.2.2 Chemically-induced bond rupture in a silica-water system) since it is the hydroxyl groups (OH^-) that are attracted to the silicon sites (Si^+). More hydroxyl groups (OH^-) would therefore increase the rate of stress corrosion cracking, as long as the number of activation sites is not the limiting factor. Fig. 3.14a shows that at high values of stress intensity the effect of pH is minimal; however, at low values of stress intensity, the effect is significant. At high crack velocities, the crack growth rate is controlled by the composition of new crack surfaces. At low crack velocities, it is controlled by the chemistry of the bulk external environment and results in the marked difference at high stress intensities [Atkinson and Meredith, 1981]. However, there may not be such a simple and direct correlation between pH and *K-v* behaviour [Dunning *et al.*, 1994]. Using a double cantilever beam experimental configuration, Dunning *et al*. [1994] investigated stress corrosion cracking in synthetic quartz using three different bases of the same pH. Although the rates of silica dissolution were the

same, the subcritical crack and fracture behaviour were different. However, in the presence of two acidic solutions of the same pH, crack velocities were found to be very similar [Dunning *et al.*, 1994].

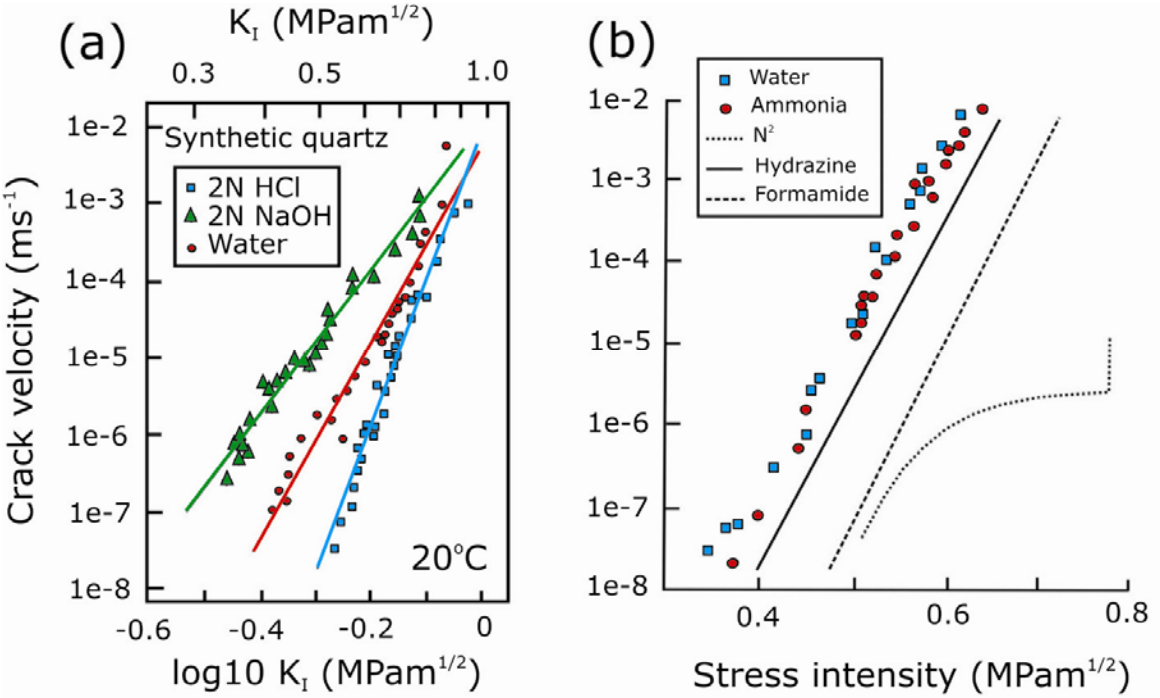

Figure 3.14. (a) The influence of pH of aqueous fluid environment on subcritical tensile crack growth in synthetic quartz at 20°C [redrawn from Atkinson and Meredith, 1981] and (b) *K-v* diagram showing the influence of different environmental species on subcritical crack growth in vitreous silica at room temperature [redrawn from Michalske and Freiman, 1983].

Similar effects have also been observed in glasses and ceramics [Wiederhorn and Johnson, 1972; Wiederhorn and Johnson, 1973; Wiederhorn, 1978; Wiederhorn *et al.*, 1982; Michalske and Freiman, 1982; 1983; Freiman, 1984; Michalske and Bunker, 1987]. Fig. 3.14b shows the effect of ammonia, hydrazine, formamide, nitrogen gas and water on crack growth curves for vitreous silica [Michalske and Freiman, 1983]. The most important feature of this plot is the absence of any plateau in the curves for ammonia, hydrazine, or formamide. The plateau occurs because crack-growth rates controlled by small

amounts of the water in a liquid or gas eventually become limited by the rate at which the water can diffuse to the crack tip.

Plateaus in *K*-*v* curves occur when crack growth rates, controlled by small volumes of water, become limited by the rate at which the water molecules can diffuse into the crack tip. Wiederhorn [1974] established that, for water-saturated gas, the plateau would occur at 10^{-4} ms^{-1} and would be even lower for liquid water [Wiederhorn *et al*. 1982]. Michalske and Freiman [1983] concluded that the absence of a plateau in ammonia, hydrazine and formamide suggests that their reaction at the crack tip controls the crack velocities in preference to water.

3.5.2.4 The influence of temperature on stress corrosion from DT experiments

The influence of temperature on a *K*-*v* diagram is shown in Fig. 3.15a [Atkinson, 1984]. All three of the regions (see Fig. 3.9) are influenced are affected by an increase in temperature (Fig. 3.15a). Few studies are focused on the influence of an elevated temperature on stress corrosion cracking. Meredith and Atkinson [1982] studied the effect of a temperature in synthetic quartz at 20°, 100° and 200°C under a water vapour pressure of 300 Pa. The effect of temperature was to dramatically increase crack velocity for a given stress intensity factor [Meredith and Atkinson, 1982; see also Atkinson, 1979] (Fig. 3.15b). A similar time-dependent, temperature-dependence in quartz had been observed previously in crack growth experiments by Martin [1972]. The influence of temperature on stress corrosion cracking has also been reported for Whin Sill dolerite [Meredith and Atkinson, 1983]. Meredith and Atkinson [1983] saw that stress corrosion cracking was enhanced at higher temperatures, albeit a lesser influence than observed on synthetic quartz. Almost identical trends have been observed in glasses [Wiederhorn and

Bolz, 1970]. Crack velocities were even observed to decrease in Black gabbro and Westerly granite at an increase of 100°C, before increasing at much higher temperatures [Meredith and Atkinson, 1985].

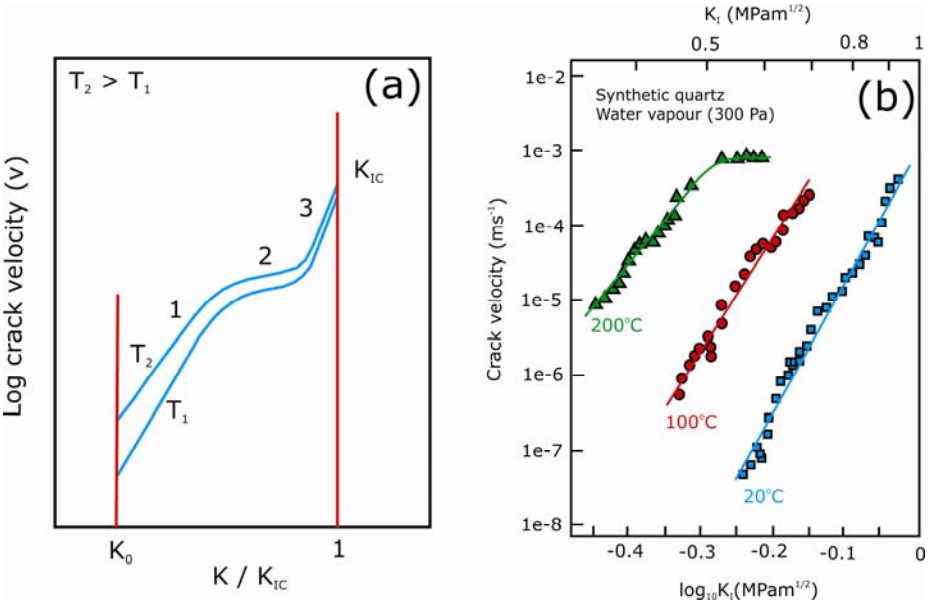

Figure 3.15. (a) *K-v* diagram showing the influence of temperature on subcritical crack growth in a rock undergoing stress corrosion [redrawn from Atkinson, 1984] and (b) The influence of temperature on stress corrosion in synthetic quartz under a 300 Pa water vapour pressure [redrawn from Meredith and Atkinson, 1982].

3.5.2.5 The stress corrosion limit

An important concept in subcritical crack growth is the idea of a stress corrosion limit or K_0 (see Fig. 3.9). It defines the conditions whereby a brittle material will not fail by the processes of subcritical crack growth regardless of how long it is held under a constant stress. However, due to the limit of achievable experimental timescales and uncertainty in the threshold value, such conditions have proved very difficult to quantify. Experiments are yet to constrain the position, or even existence, of a stress corrosion limit in rock [see Atkinson, 1979; Atkinson, 1984 for reviews] even for crack velocities as low as 10^{-12} [Wilkins, 1980]. Theoretical calculations based on reaction rate theory predict that the value of

K_0 will be a very small fraction (10-20%) of the critical stress intensity factor [Atkinson, 1984]. However, more progress has been made in the study of simpler systems such as those of glasses and ceramics, and will be therefore discussed below.

Wiederhorn and Bolz [1970] observed a stress corrosion limit in experiments on soda-lime silicate and chemically-resistant borosilicate glasses immersed in water at 25°C (Fig. 3.16). For both glasses the crack velocity depends exponentially on the stress intensity factor for velocities greater than about 10^{-7} ms^{-1}. At slower velocities, the stress intensity factor does not decrease further thus defining a possible position for the stress corrosion limit. Similar *K-v* curves have since been reported by other authors [Michalske *et al.*, 1991; Gehrke *et al.*, 1991; Kocer and Collins, 2001]. However, experiments have shown that the existence of the stress corrosion limit in glass is dependent on chemical composition, only glasses that contained alkali ions exhibited such behaviour [Wiederhorn and Bolz, 1970; Michalske, 1983; Gehrke *et al.*, 1991].

There has been much debate as to the mechanisms behind why a stress corrosion limit is observed in glass. Many authors have attributed the blunting of cracks by corrosion as the principal reason [Charles and Hillig, 1962; Wiederhorn and Bolz, 1970; Wilkins and Dutton, 1976; Michalske, 1983]. However, more recent studies, using atomic force microscopy, have proved this theory questionable [Wiederhorn *et al.*, 2002;2003; Guin and Wiederhorn, 2003]. Other proposed mechanisms include an ion-exchange leached layer that forms on the surface of the crack [Gehrke *et al.*, 1991] and that surface corrosion rate is no longer fastest at the crack tip, but at an angle to the original crack plane [Chuang and Fuller, 1992; Hénaux and Creuzet, 1997; Wiederhorn *et al.*, 2002].

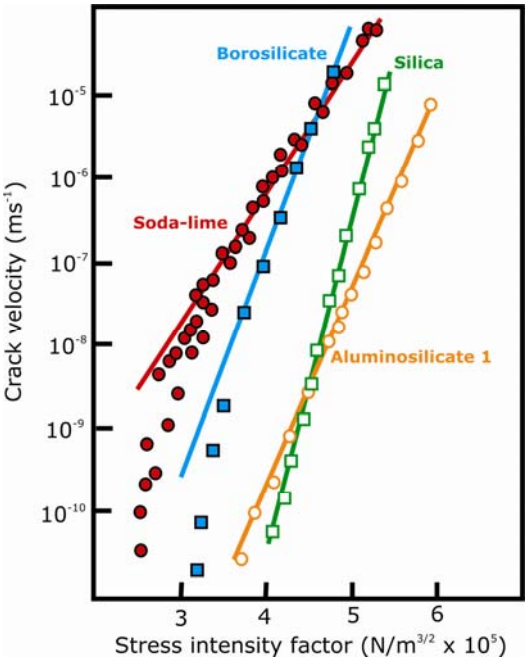

Figure 3.16. Stress intensity factor/crack velocity diagram (*K-v* diagram) showing the fracture behaviour of glass at 25°C [redrawn from Wiederhorn and Bolz, 1970].

Using a combination of experimental and theoretical data, Michalske [1983] established that a stress corrosion limit may exist in a lime glass/water system under room temperature. His technique, based on the principle that an increase in crack tip radius below the fatigue limit will result in non-unique *K-v* data above the fatigue limit, demonstrated that the stress corrosion limit was encountered due to the corrosive action of water rounding the crack tips. Charles and Hillig [1962] demonstrated that below a critical applied stress, the radius of curvature of the tip of the crack increased; whilst above the critical stress, the crack sharpened as it grew longer. This increase in curvature radius, or 'crack tip blunting' was considered by Charles and Hillig [1962] to represent the stress corrosion limit. This has also been corroborated by experiments [Michalske, 1983]. In Michalske's [1983] experiments, a time delay was observed after increasing the stress intensity factor from below to above an apparent crack growth threshold, after applying a constant stress below the apparent crack growth threshold for a 16 hour period. The time delay was credited to the time needed to sharpen and restart crack growth after crack

blunting had occurred. It was found that the higher the applied stress above the apparent crack growth threshold, the shorter the time delay needed to restart crack growth. The time delay to restart cracking is dependent on the hold time, glass composition and the pH of the immersion solution [Gehrke *et al.*, 1991]. However, Gehrke *et al*. [1991] discounted the role of crack tip blunting and attributed their observations to the leaching of glass at the crack surface.

3.5.3 Experiments on a bulk sample: brittle creep experiments

3.5.3.1 Introduction

Brittle creep (or '*static fatigue*' in the engineering literature) is a term used to describe the inelastic deformation of a solid material held under a constant, long-term level of stress that is below the short-term failure stress of the material. It has been hypothesized that, for bulk rock deforming in a brittle manner under triaxial stress conditions, stress corrosion will lead to highly non-linear time-dependent deformation [Main *et al.*, 1993; Main, 2000]. The mechanism deemed largely responsible for this behaviour is stress corrosion. Brittle creep experiments have been used to investigate the response of a bulk rock sample to time-dependent brittle deformation, notably stress corrosion cracking. This section will outline previous work on brittle creep in rock using triaxial experiments and is split into headings that represent specific areas of interest that have commanded significant attention in the literature.

3.5.3.2 The classic brittle creep curve

The style of deformation produced by brittle creep experiments has conventionally been described as exhibiting an apparent trimodal behavior when axial strain is plotted against time. This is commonly

known as a *creep curve* and has been observed by many authors [Lockner, 1993; Baud and Meredith, 1997; Main, 2000 for example, amongst others]. The three stages of the creep curve have conventionally been described as (1) primary or decelerating creep, (2) secondary or steady-state creep, and (3) tertiary or accelerating creep (Fig. 3.17). It is likely however that this does not represent three distinct mechanisms, but the product of a decelerating and accelerating mechanism [Main, 2000]. Main's [2000] theory is discussed in more detail in section **3.6 Theory and models of stress corrosion crack growth**. The primary creep phase is characterized by an initially high strain rate that decreases with time to reach a quasi-linear secondary phase that is often interpreted as steady-state creep. After an extended period of time, a tertiary phase is entered, characterized by accelerating strain. This eventually results in macroscopic failure of the samples by propagation of a shear fault. Creep strain rates are calculated from the quasi-linear portions of the creep curves.

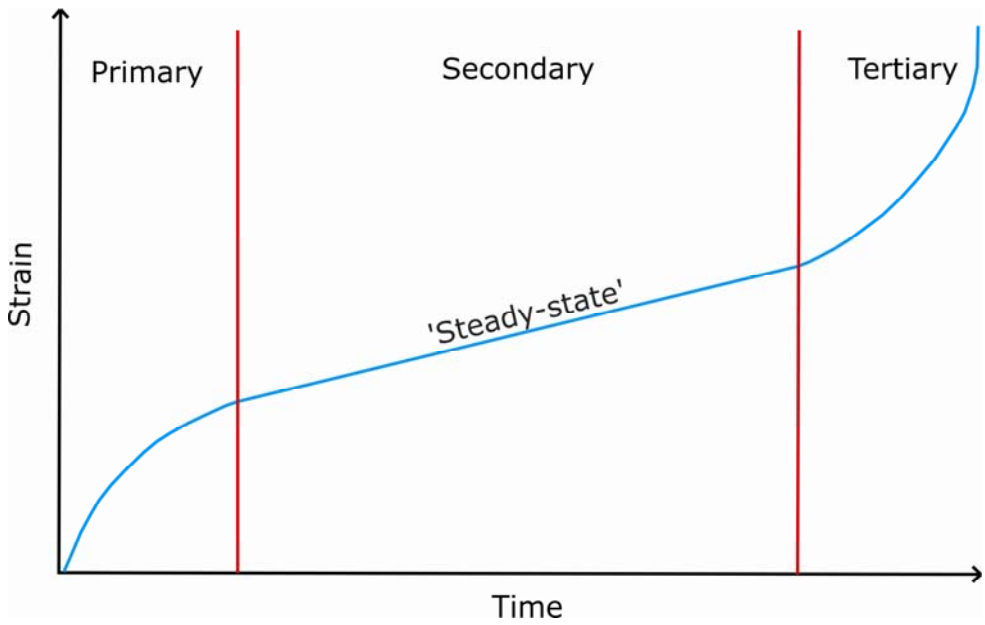

Figure 3.17. The classic trimodal creep curve showing the three distinct phases of brittle creep (1) primary or decelerating creep, (2) secondary or pseudo-steady-state creep and (3) tertiary or accelerating creep.

3.5.3.3 The influence of an applied differential stress on brittle creep

Several studies have shown that applied differential stress exerts a crucial influence on brittle creep in rock. Kranz [1980] found that increasing the stress on a sample of Barre granite by only a few kbars resulted in a decrease in time-to-failure by up to an order of magnitude. Similar to previous findings on the stress corrosion of quartz under uniaxial compression [Scholz, 1972]. Baud and Meredith [1997] found that the level of differential stress has a substantial effect on the creep strain rate and the time-to-failure. Decreasing the percentage of the short-term failure stress from 90% to 80% increased the time-to-failure from 30 minutes to almost 24 hours and reduced the creep strain rate from 7.0×10^{-7} s^{-1} to 3.0×10^{-9} s^{-1} (Fig. 3.18). Ngwenya *et al.* [2001] investigated brittle creep using a suite of different sandstones. They found that, in general, increasing the applied differential stress by about 10 MPa resulted in an order of magnitude increase in the creep strain rate [Ngwenya *et al.*, 2001]. The influence of applied differential stress on brittle creep is summarized in Fig. 3.19.

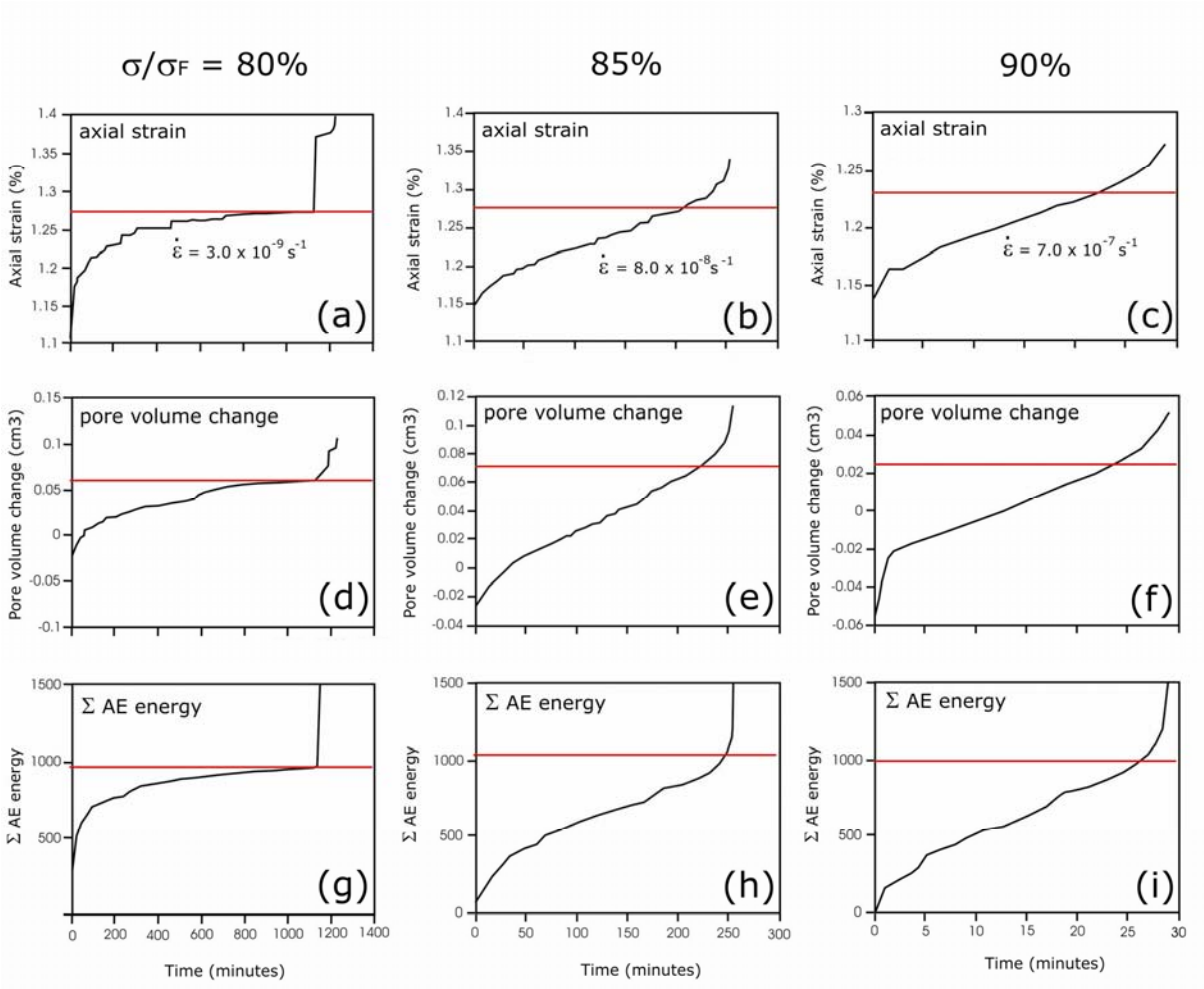

Figure 3.18. Graphs showing axial strain, pore volume (P_v) change and cumulative AE energy for 80%, 85% and 90% of the short-term peak stress during conventional creep experiments on Darley Dale sandstone. Red lines indicate the onset of acceleration to failure or the postulated critical damage threshold [from Baud and Meredith, 1997].

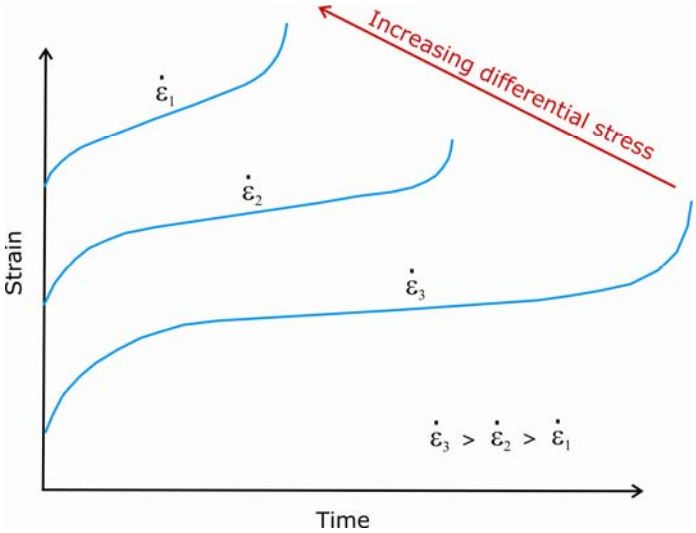

Figure 3.19. Schematic diagram of three creep curves demonstrating the influence of applied differential stress. Graph illustrates that as stress is increased creep strain rate is increased and time-to-failure is decreased.

3.5.3.4 Theory of the critical damage threshold

Griggs [1939; 1940], from uniaxial compression tests on alabaster, suggested that rock failure occurs after a critical amount of time-dependent stain or creep has accumulated in the sample. A similar idea to that of Wawersik and Brown [1973], who stated that time-dependent failure occurs when a rock has been strained a 'critical amount'. Cruden [1974] suggested that, for rocks exhibiting static fatigue, there is a critical density of microcracks in the specimen at which the cracks begin to intersect and that these intersections grow at an accelerating rate which ultimately leads in sample failure. Cruden [1974] introduced a static fatigue law:

$$n \log\left(\frac{\sigma_1}{\sigma_2}\right) = \log\left(\frac{t_2}{t_1}\right) \qquad [3.5]$$

Where *t* is the time to the onset of accelerating creep in a sample and *n* is the exponent of the power law dependence of corrosion rate on stress. Cruden's [1974] criterion was based exclusively on the concept of critical crack density and the probability of crack interaction. Work by Kranz and Scholz [1977] supports the hypothesis that the instability that marks the final creep curve stage will not commence until the rock has sustained a 'critical amount of inelastic volumetric strain'. The magnitude of the critical inelastic strain varies with rock type and is related to brittle fracture strength. Kranz and Scholz [1977] found that Barre granite entered the tertiary creep phase about half way through their experiments and the Cheshire quartzite at around 90% of the fracture time. Thus, failure strength may not be proportional to 'creep toughness' [Kranz and Scholz, 1977].

Much of the previous work on the critical damage threshold typically involved uniaxial compression experiments carried out on crystalline rock. Baud and Meredith [1997] investigated creep on Darley Dale sandstone using a triaxial deformation apparatus to examine the process of time-dependent brittle deformation on rock under 'all-round compression'. They found that their measured proxies for damage (axial strain, pore volume change and output of AE energy) were approximately equal that the onset of acceleration to failure regardless of the level of applied differential stress (Fig. 3.18).

3.5.3.5 Acoustic emission during brittle creep experiments

Acoustic emission (AE) output has been monitored during brittle creep experiments on rock [Wu and Thomsen, 1975; Lockner and Byerlee, 1975; Ohnaka, 1983; Yanagidani *et al.*, 1985; Hirata *et al.*, 1987;Nishizawa and Noro, 1990; Baud and Meredith, 1997], metals [Ohno *et al.*, 1994; Chmelík *et al.*, 2002] and glass [Maes *et al.*, 1998].

AE output over time in rock during a brittle creep experiment mirrors the relationship of the classic time-strain creep curve [Wu and Thomsen, 1975; Ohnaka, 1983; Baud and Meredith, 1997]. Only very few authors have investigated the localization of AE events during brittle creep in rock, mostly on dry crystalline rock samples under uniaxial compression [Yanagidani *et al.*, 1985; Nishizawa *et al.*, 1984; Hirata *et al.*, 1987; Nishizawa and Noro, 1990]. Yanagidani *et al.* [1985] studied the localization of AE events during uniaxial creep experiments on dry granite. They found that clustering and localization of AE hypocenters occurred as early as the primary creep stage. After the primary creep stage they observed that AE events were concentrated onto one of the clusters, whilst activity at the other clusters gradually decayed. During tertiary creep and just prior to failure, their AE events localized at the specimen surface. Nishizawa *et al.*, [1985] found that, during a uniaxial creep experiment on dry andesite, AE clusters formed during secondary creep. During tertiary creep, initiated by a small step in stress, a new cluster formed that formed a discrete fault that ruptured the sample. The clusters formed during secondary creep did not continue to propagate. AE event clustering during secondary creep was also observed by Nishizawa and Noro [1990]. Yanagidani *et al*. [1985], Nishizawa *et al.*, [1985] and Nishizawa and Noro [1990] however, were constricted to dry experiments under uniaxial conditions. Hirata *et al*. [1987] located AE hypocenters during brittle creep on dry granite under triaxial stress conditions. Their calculated fractal dimensions decreased as creep progresses through to tertiary creep indicating that the clustering of AE events accelerates during creep.

3.5.3.6 The influence of temperature on brittle creep

The influence of temperature on brittle creep is a poorly understood phenomenon. Kranz *et al*. [1982] studied brittle creep under triaxial conditions on Barre granite at both 24° and 200°C. They found that the time-to-failure was reduced by about two orders of magnitude from 24° to 200°C when samples

were held at a constant stress (Fig. 3.20). This is however, to the author's knowledge, the only study focused on the influence of temperature on brittle creep.

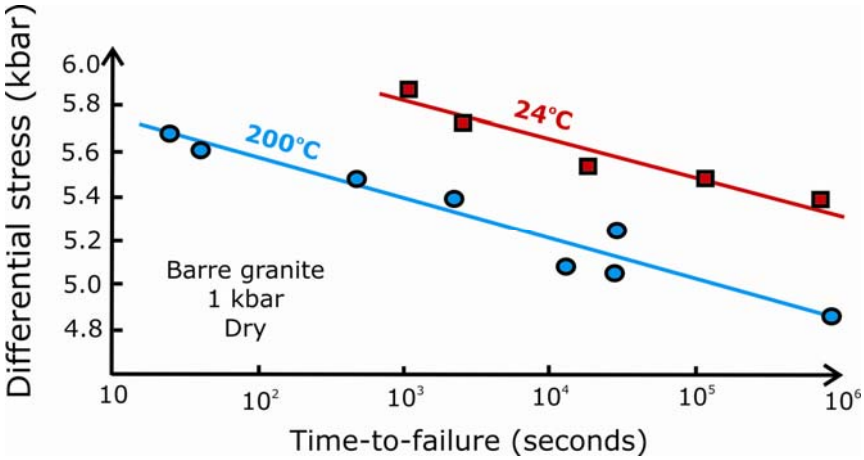

Figure 3.20. Time-to-failure in Barre granite under a constant stress of 1 kbar at both 24° and 200°C [Kranz *et al.*, 1982].

3.5.3.7 The influence of effective confining pressure on brittle creep

There are three main ways in which P_{eff} can influence stress corrosion, it can (1) alter the stress tensor of the deforming solid, (2) alter the mechanical properties of the environmental species in the cracks and pores and (3) alter the chemical reactions between the environmental species and the material at the crack tip [Anderson and Grew, 1977]. The application of a higher P_{eff} will reduce applied tensile stresses and stress intensity factor across crack tips and hence reduce the speed at which microcracks can propagate. A greater applied differential stress (Q) is therefore required to achieve the same crack tip stress intensity to propagate the microcrack at the same velocity as before. The influence of P_{eff} may also affect both the mechanical properties of the environmental species and the ease at which it can dissociatively react with the material at the crack tip. For water, for example, pressure serves to increase the activity of the hydrogen and hydroxyl ions (Fig. 3.21).

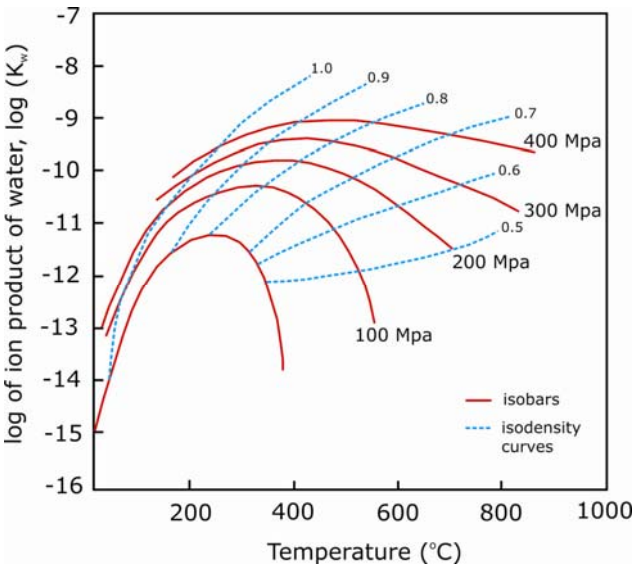

Figure 3.21. Log of the ion product of water as a function of temperature, density and pressure [from Fyfe *et al.*, 1978].

The most systematic study of the effect of P_{eff} on stress corrosion is that by Kranz [1980]. Kranz [1980] showed that, for crystalline rock, the effect of an increase in the P_{eff} is to increase the time-to-failure due to time-dependent processes. He postulated that the ancillary pressure effects caused by an increase in P_{eff} could decrease the rate at which corrosive agents can reach crack tips and also decrease the interaction of cracks prior to the onset of acceleration to failure. However, one of the limitations of the work of Kranz [1980] is that only dry samples were used; therefore they were performed in the absence of a pore fluid and P_p. The study of Kranz [1980] also focused on time-to-failure during creep experiments at different values of P_{eff} and neglected its potential influence on the creep strain rate during the steady-state creep phase.

Other work on the influence of P_{eff} on stress corrosion can be found in Wawersik and Brown [1973] and Ngwenya *et al.* [2001]. Wawersik and Brown [1973] performed brittle creep experiments on sandstone and granite at confining pressures of 7, 35 and 70 MPa and found that an increase in P_{eff} resulted in a decrease in creep strain rates. Ngwenya *et al.* [2001] performed stress-stepping brittle creep

experiments on three sandstones of varying physical properties. They found that the influence of P_{eff} is to shift the individual curves of strain rate systematically towards higher differential stresses; in accordance with the law of effective stress. However, it must be noted that Wiederhorn and Johnson [1971] observed no contribution of P_{eff} on stress corrosion in glass in DT experiments.

3.6 Theory and models of stress corrosion crack growth

3.6.1 Introduction

A molecular description of stress corrosion is very important; however, to apply stress corrosion to geophysical problems, a theory is needed so that it can be described on a more macroscopic scale. An accurate predictive model for the long-term strength of the continental lithosphere is important in a wide range of geophysical and geodynamic problems. Models used to describe creep are generally of two forms: (1) power law form,

$$\dot{\varepsilon} = A\left(Q\right)^{\eta} \qquad [3.6]$$

or (2) exponential form,

$$\dot{\varepsilon} = Me^{\beta Q} \qquad [3.7]$$

Where $\dot{\varepsilon}$ is the creep strain rate, Q is the applied differential stress and A, M, β and η are all constants.

3.6.2 Power law form

Since the classic work by Griffith [Griffith, 1920;1924] there have been a number of equations proposed to modify his theory to account for time-dependent and environment-dependent fracture. They have generally used stress-assisted reaction rate theory to account for time-dependent mechanisms operative at the crack tip [see Anderson and Grew, 1977 and Atkinson, 1982 for reviews]. The most widely-used and accepted theory of stress corrosion is Charles' power law [Charles, 1958]:

$$v_c = v_{c0} \exp\left(-\frac{H}{RT}\right) K^n \qquad [3.8]$$

Where v_c is the crack velocity, R is the universal gas constant, T_a is the absolute temperature, K is the stress intensity factor and n is the stress corrosion index. The stress corrosion index is a measure of the susceptibility of a specific material to stress corrosion crack growth in a specific environmental fluid at a specific temperature. Typically n varies experimentally between 20-50 for crack growth by stress corrosion in ceramic materials and rocks [Atkinson, 1984; Atkinson and Meredith, 1987]. Charles' power law [1958] has been used to describe virtually all experimentally determined data for geological materials [see Meredith and Atkinson, 1983; Atkinson, 1984; Swanson, 1984]. The stress corrosion index is generally calculated from DT experiments [Atkinson, 1984]; however, it could also be possible to determine n from triaxial brittle creep experiments where failure is compressive [Main and Meredith, 1991]. Also, the power law is consistent with the growth of multiple cracks in a stochastic granular medium [Main, 1999].

More recently, mean-field theory of damage mechanics have been developed [Lockner, 1998; Main, 2000] that invokes a two stage process: (1) a phase of strain hardening involving distributed crack damage, and (2) a phase of strain softening involving crack interaction and coalescence. Phase (1) dominates in the early stage of deformation and phase (2) dominates in the later stage of deformation. Such models also therefore postulate a critical damage threshold where crack interaction leads to a rapid acceleration to failure on a localized fault plane. As the stress intensity at a crack tip is influenced by the length of the crack, given suitable conditions, the nonlinear relation between strain rate and stress given by stress corrosion theory means the rate at which a crack grows in time can accelerate even under a constant boundary stress. For a population of cracks growing in a rock sample held at constant stress, this process is embodied by accelerating strain rate and AE with time. In field data, where it is difficult to determine the absolute stress conditions, accelerating strain and seismic activity have been used to infer an underlying stress corrosion mechanism. The rate of deformation precursors to volcanic eruptions show both power law and exponential accelerations with time [Voight, 1988;1989], is shown to be theoretically consistent with a stress corrosion process at constant boundary stresses [Main, 2000] and exactly predicts the modified form of Omori's law for aftershock and foreshock sequences.

In Main's [2000] model, 'mixed mode' secondary creep is quantitatively shown to be an emergent property of competing distributed and localized processes (Fig. 3.22). The model is based on constitutive laws that are based upon subcritical crack growth in laboratory experiments i.e. Charles' law. No specific allowance is given for the plateau at intermediate velocities that may be a consequence of diffusion-limited crack growth, although the theory could be modified to include this. In a compressive stress field, initial tensile brittle crack growth, once nucleated, is quickly inhibited through negative feedback. This negative feedback leads to distributed deformation and a decelerating creep rate. Once cracks

begin to interact however and, in particular, begin to localize in an incipient shear zone, positive feedback processes lead to accelerating creep. The superposition of both processes leads spontaneously to an apparent 'steady-state' creep. The model demonstrates that the evolution of total strain, Ω_t, with time can be described through the equation:

$$\Omega_t = \Omega_I \left(1 + \frac{t}{T_t}\right)^m + \Omega_{III} \left(1 + \frac{t}{t_f}\right)^{-u} \quad [3.9]$$

Where Ω_I and Ω_{III} are amplitudes of the primary and tertiary creep components, T_t is the transient time ($T_t = m\tau_1$), t_f is the asymptotic failure time ($t_f = u\tau_3$) and m and u are positive power law exponents. Ngwenya *et al.* [2001] proposed a modified power law creep based on the theory of Main [2000] of the form:

$$\dot{\varepsilon} = A\left(Q - \sigma_f\right)^{\eta} \quad [3.10]$$

Where A and η are constants, $\dot{\varepsilon}$ is the steady-state creep strain rate and Q and σ_f are differential stress and fundamental strength of time-dependent deformation respectively.

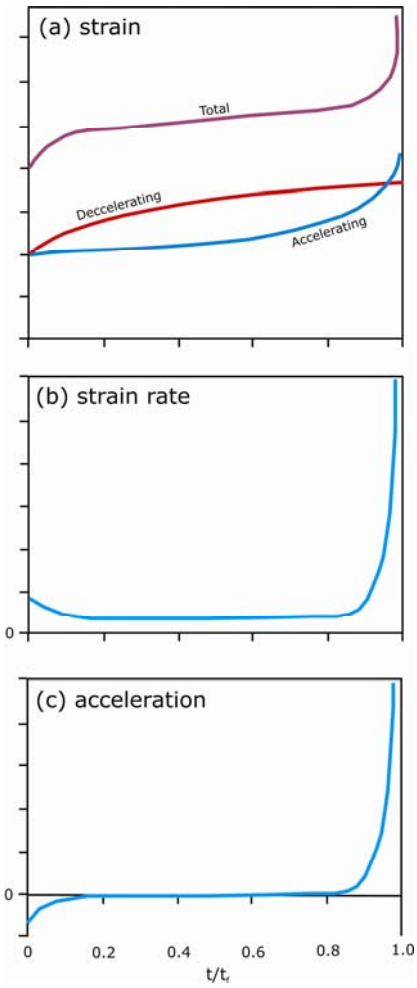

Figure 3.22. (a) Strain versus time for Equation [3.9] against normalized time-to-failure, showing the individual components of decelerating and accelerating creep. The total is simply the sum of the two parts. (b) Strain rate against normalized time-to-failure i.e. the 1st derivative of the total curve in (a). (c) Acceleration against normalized time-to-failure i.e. the 2nd derivative of the total curve in (a) [modified from Main, 2000].

3.6.3 Exponential form

Other than Charles' law, another of the more popular theories for stress corrosion is the simplification of Charles and Hillig's theory [Charles and Hillig, 1962] by Wiederhorn and Bolz [1970]. Charles and Hillig [1962] proposed a new theory based on the assumption that static fatigue in glass is controlled by a

chemical reaction between silica and water. They postulated that static fatigue is an activated process that occurs most rapidly where the at the crack tip where stress concentration is the greatest. Based on these conclusions they produced a new exponential, quantitative theory for stress corrosion:

$$v_c = v_{c0} \exp \frac{\left(-E_a + V_a\right)\sigma - V_m \gamma}{\rho_{ct}} \div R\left(T_a\right) \qquad [3.11]$$

Where v_c is the crack velocity, E_a is the stress free activation energy, V_a is the activation volume, σ is the stress at the crack tip, V_m is the molar volume of glass, γ is the interfacial surface energy between the glass and the reaction products and ρ_{ct} is the radius of the curvature of the crack tip. However, the Charles and Hillig [1962] theory was derived for a two-dimensional Griffith crack. At stresses greater than the fatigue limit crack sharpening can occur and ρ decreases to a small value limited by the structure of the glass. Wiederhorn and Bolz [1970] proposed a new modified Charles and Hillig [1962] theory, referred to as the Charles-Hillig-Wiederhorn theory:

$$v_c = v_{c0} \exp \frac{\left(-E_a + 2V_a\right)K_I}{\sqrt{\pi \rho_{ct}}} \div R\left(T_a\right) \qquad [3.12]$$

Costin [Costin, 1987], Lawn [Lawn, 1993] and Lockner [Lockner, 1993;1998] also used exponential forms to describe creep behaviour. Similar to Main [2000], steady-state creep is an emergent process in Lockner's [1998] model and occurs in a region where microcrack growth and fault nucleation balance. Lockner's [1998] model includes an explicit instability criterion for dynamic failure that predicts the sudden and dynamic increase in strain rate at the onset of tertiary creep.

However, due to the very strong dependence of v_c on K it may not be possible to distinguish any difference between applying either a power law or an exponential fit on experimental data. Most data has shown that both can fit equally as well [see Ngwenya *et al.*, 2001]. In general, the power law is more easily incorporated into time-dependent failure models [e.g. Das and Scholz, 1981; Main, 2000] while the exponential law works better for the growth of a single crack [Atkinson, 1982; Freiman, 1984; Lockner, 1993], since it does not take crack interaction into account. Results of Ngwenya *et al.* [2001] suggest that the exponential form provides a better mathematical description for more brittle samples (low porosity), while the power law is more suitable for ductile samples (high porosity).

3.6.4 Modelling the form of the primary creep curve

Classically, the form of the primary creep curve has been interpreted in terms of either (1) Andrade creep or (2) logarithmic creep. Both are described in turn below. However, it must be noted that such theory is generally confined to metals deforming at high temperatures; they will therefore not be discussed in great detail [for a more detailed review see Cottrell, 1997]. In general, Andrade creep dominates when strain hardening is 'weak' and logarithmic creep when it is 'strong'.

3.6.4.1 Andrade creep

Andrade creep is usually explained in terms of strain increments that are each triggered by a microscopic thermal activation. As creep strain increases, the work hardening reduces the strain increment that can be produced by a given thermal fluctuation [Andrade, 1910;1914; Cottrell, 1996 Cottrell, 1997]. As the creep strain increases, Andrade creep states that strain increases as the cube root of time.

3.6.4.2 Logarithmic creep

Two explanations have been given for the logarithmic creep of a solid under constant stress during the primary creep phase (1) strain hardening theory and (2) exhaustion theory. Exhaustion theory is usually explained in terms of the activation energy required to force dislocation lines across localized obstacles. Obstacles that require a small activation energy are quickly 'exhausted' [although there is some regeneration, see Cottrell, 1997] leaving only those that require a larger activation energy, therefore reducing the strain rate. As the creep strain increases, logarithmic creep states that strain increases as the log of time.

Chapter four

4. Details of the Testing Equipment, the Acquisition of Experimental Data and Equipment Calibrations

4.1 Introduction

This chapter first describes all the experimental apparatus used during this study and then explains the methods used for the acquisition of data. Finally, the necessary calibrations for the various experimental testing equipment are presented.

4.2 The uniaxial compression apparatus

4.2.1 Introduction

Uniaxial compression experiments are widely used in engineering practice, but they are also very useful in experimental rock deformation. Uniaxial compression experiments have an advantage over triaxial experiments in the fact that they are simpler in principle and practice; therefore, it is easier to perform many experiments over a comparatively short period of time. They also have the added advantage that they readily allow a multitude of auxiliary measurements such as radial strain and ultrasonic wave velocities to be recorded. However, uniaxial compression experiments are unconfined and therefore both σ_2 and σ_3 are zero [for a review of uniaxial compression see Hawkes and Mellor, 1970 and Vutukuri *et al.*, 1974].

4.2.2 The loading frame, actuator piston and load cell

The uniaxial compression apparatus used in this study is located in the Rock & Ice Physics Laboratory (RIPL), University College London (Fig. 4.1).

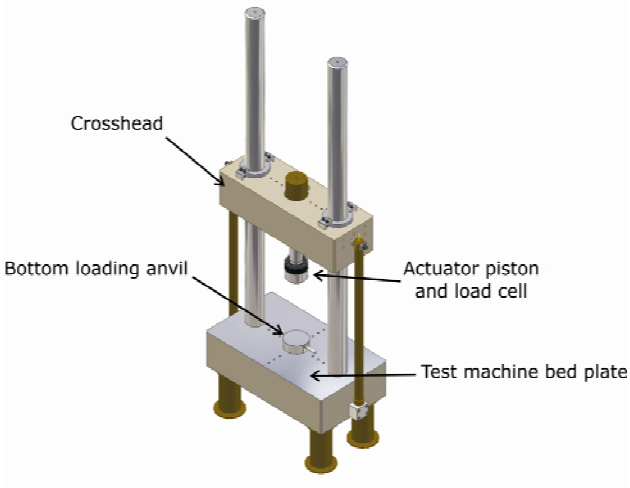

Figure 4.1. Three-dimensional Autodesk Inventor diagram of the uniaxial compression apparatus situation in the Rock & Ice Physics Laboratory (courtesy of N. Hughes).

The uniaxial compression apparatus is servo-controlled and can exert a maximum compressive load of 200 kN. The main components of the uniaxial compression apparatus are shown in Fig. 4.1. The actuator piston, powered by a hydraulic ringmain, can be controlled by the servo-controlled valve using a number of different feedbacks in a closed loop control. Apart from its smaller capacity loadframe, the uniaxial compression apparatus operates under the same principles as the triaxial ensemble.

4.2.3 Sample assembly and auxiliary measurements

The sample assembly for the uniaxial compression apparatus is shown in Fig. 4.2. The uniaxial compression apparatus can be set up to record a number of auxiliary measurements. Axial displacement is measured using a magnetically clamped LVDT displacement transducer positioned in an axial orientation (Fig. 4.2a). Radial displacement is measured using an LVDT displacement transducer clamped into a custom-built radial strain jig (Fig. 4.2b), designed and constructed by J. Bowles, which is held in place using a magnetic stand clamp. The output of acoustic emission (AE) hits and energy are recorded

using a piezo-electric crystal transducer, located within the bottom loading anvil (Fig. 4.2a), and is connected to a MISTRAS-2001 AE recording system (for more information see *4.4.2 AE data recording systems and logging software*) via a coaxial cable. The hemispherical seat ensures that the sample is evenly loaded during experimentation.

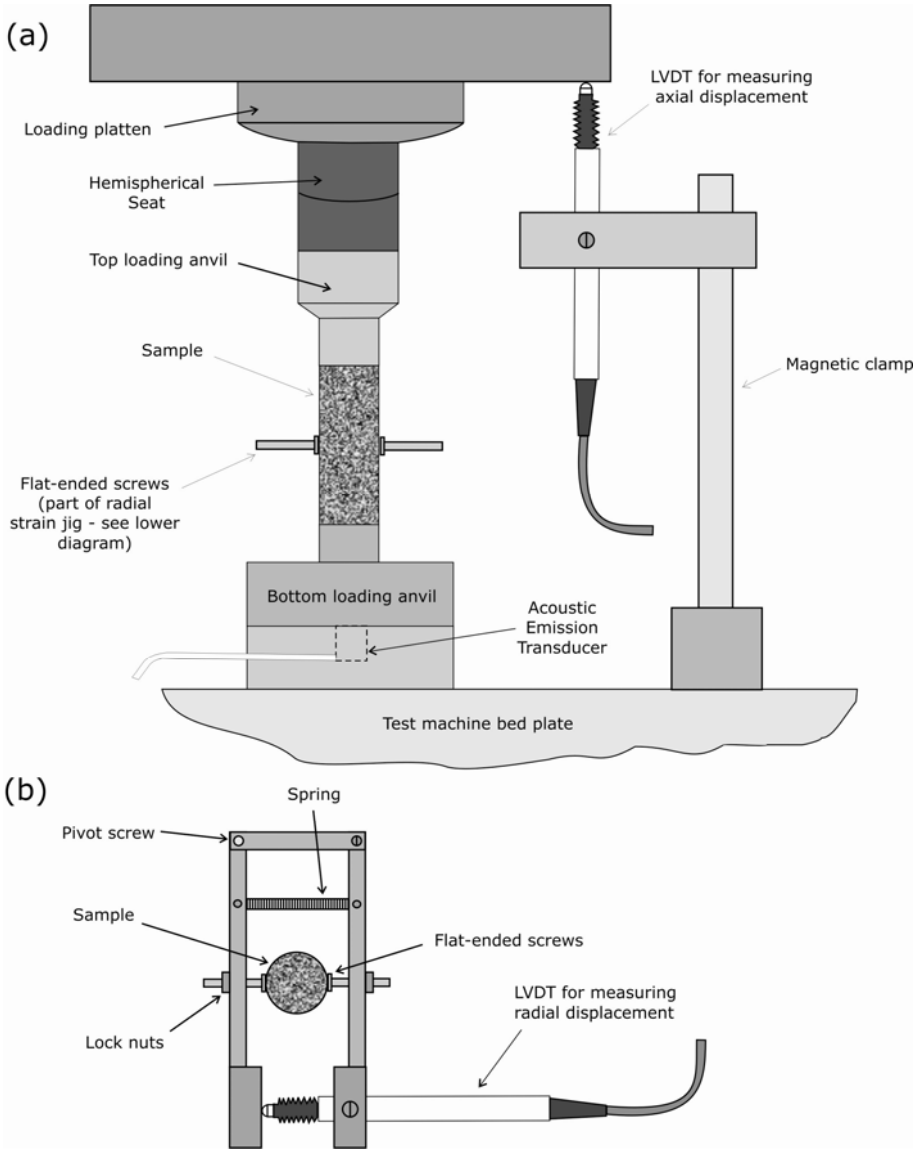

Figure 4.2. Schematic diagrams of the sample set-up (a) side view showing main apparatus components and positions of the axial displacement, P- and S- wave and AE transducers (b) top down view displaying the radial strain jig components and position of the radial displacement transducer.

4.3 The triaxial deformation ensemble

4.3.1 Introduction

The most widely used procedure to simulate the natural stress state present within the Earth's crust is to perform triaxial deformation experiments. The pioneering apparatus of von Kármán [1911], which contained all of the major components still used today, paved the way for future redevelopments and improvements such as the introduction of a pore fluid pressure and furnace capabilities. A detailed review of the history of triaxial testing apparatus can be found in Paterson and Wong [2005].

The triaxial ensemble used during this study is located in the Rock & Ice Physics Laboratory (RIPL) at University College London (Fig. 4.3). It is a 'conventional' triaxial ensemble; therefore the sample is deformed uniaxially under hydrostatic stress conditions (i.e. in the presence of a confining pressure). As a result σ_2 and σ_3 are always equal during experimentation.

4.3.2 The pressure vessel

The pressure vessel is 1060 mm in length and has an internal diameter and external diameter of 130 mm and 400 mm respectively. It is rated up to confining pressures of 400 MPa (equal to the hydrostatic pressure present at approximately 15 km depth) and therefore is a useful tool for studying deformation processes operative within the Earth's brittle crust. The vessel is made from a 3.5% nickel chrome alloy steel and weighs approximately 750 kg. The pressure vessel includes a balanced ram assembly (Fig. 4.4) that ensures the ends of the sample are loaded to the same pressure as the applied confining pressure

prior to any external loading by the actuator piston. The pressure vessel is connected to the actuator piston and the load cell via a yoke (Fig. 4.3).

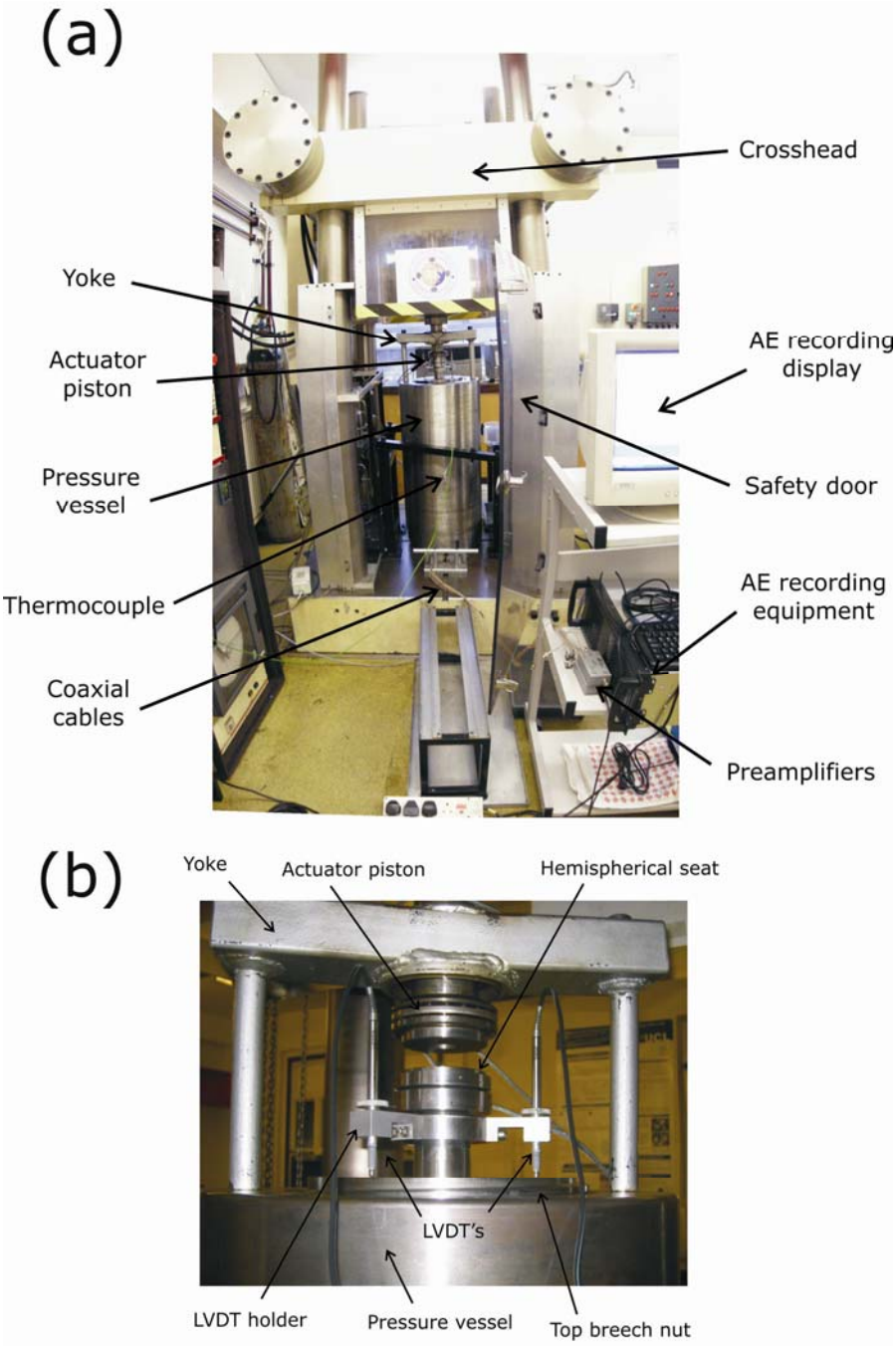

Figure 4.3. Photographs of the triaxial ensemble situated at the Rock & Ice Physics Laboratory (a) all of the main components (b) the components at the top of the pressure vessel.

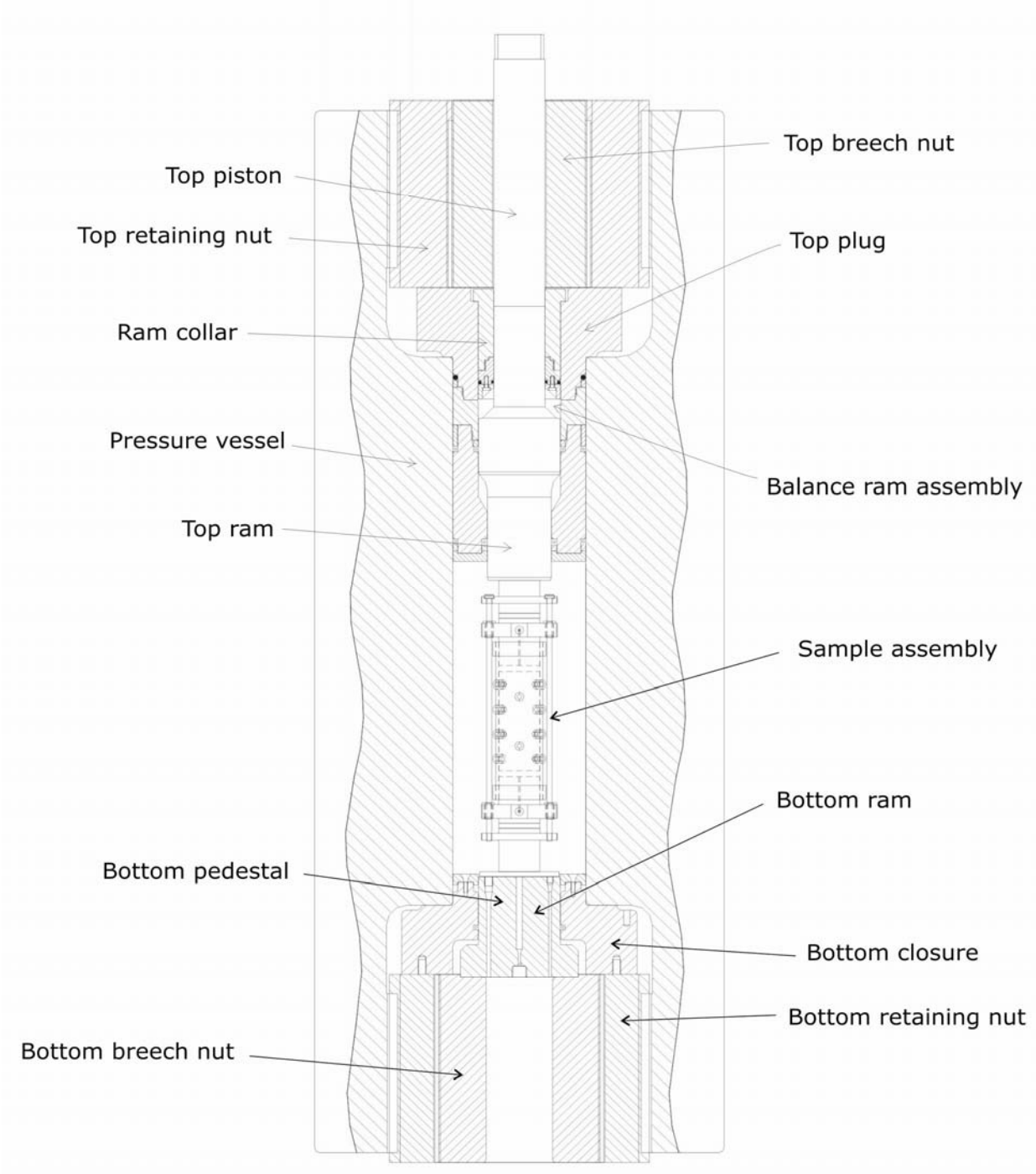

Figure 4.4. Two-dimensional Autodesk Inventor cross-section of the triaxial ensemble situated in the Rock & Ice Physics Laboratory (courtesy of N. Hughes).

4.3.3 The actuator piston and load cell

The actuator piston and connected load cell are mounted onto a moving machine crosshead (Figs. 4.3 and 4.4). The crosshead is controlled independently from the actuator piston using a hydraulic clamping/unclamping mechanism. The hydraulic actuator piston that applies the axial load during experimentation via the top ram can achieve a maximum compressive load of 1.5 MN (approximately 150 tonnes) on 40 mm diameter samples and is capable of moving in both down (load) and up (unload) directions. The microprocessor based servo-controller enables closed-loop control of the actuator piston, powered by a hydraulic ringmain, using a variety of transducers (either load transducers within the load cell, a large internal LVDT or more sensitive external LVDT's) to provide the feedback signal. This enables the actuator piston to provide precision control of load, displacement or pressure as well as enabling control of various operative processes within the sample. Using a ramp generator, the actuator can be set to advance at a constant rate, using electronic feedback signals from the two externally mounted LVDT's in Fig. 4.3b), resulting in the application of a constant axial strain rate (set at 1.0×10^{-5} s^{-1} for the purpose of this study) on the sample. The actuator can also be set to maintain a constant loading rate, using electronic feedback signals from the load transducers in the load cell, resulting in the application of a constant axial stress rate on the sample. It is also possible to exert a constant applied load on the sample (i.e. to perform a conventional creep or 'static fatigue' experiment). The hemispherical seat ensures that the sample is evenly loaded during experimentation.

4.3.4 Sample assembly

The sample assembly, as shown in Fig. 4.5, is located within the pressure vessel during experimentation (see Fig. 4.4). Details of the jacketing system and how data were relayed from inside the pressure vessel using a lead-through system are described below.

4.3.4.1 The jacketing system

To isolate the pore fluid pressure and the confining pressure a jacketing system was designed and developed by Peter Sammonds and Laszlo Lombas (Laszlo Lombas Consultancy) (Fig. 4.5). The jackets are made from fluoroelastomer nitrile and are rated for pressures up to 400 MPa and temperatures up to 100°C. They have an internal diameter of 40 mm, so that the sample can slide inside, and are 3 mm thick. The jacket is sealed onto the pore fluid endcaps using two fluoroelastomer nitrile cuffs that are stretched over each end of the jacketed sample. When a confining pressure is applied the jacket is pressed against the sealing surface and the sample thus improving the seal. The jackets are reusable from experiment to experiment unless the frictional sliding on the surface of a shear fault is substantial enough to puncture the jacket.

The jacket contains twelve 'nipples' (Fig. 4.5) that each house concave stainless steel inserts that are in direct contact with sample. The angular position of each of the steel inserts, which can have a variety of different uses, is shown in Fig. 4.6. The angular position of each numbered inserts in '3D space' was inputted into the Vallen ASKY-2 AE recording software so that AE hypocentre locations could be calculated (see *4.4.2 AE data recording systems and logging software*).

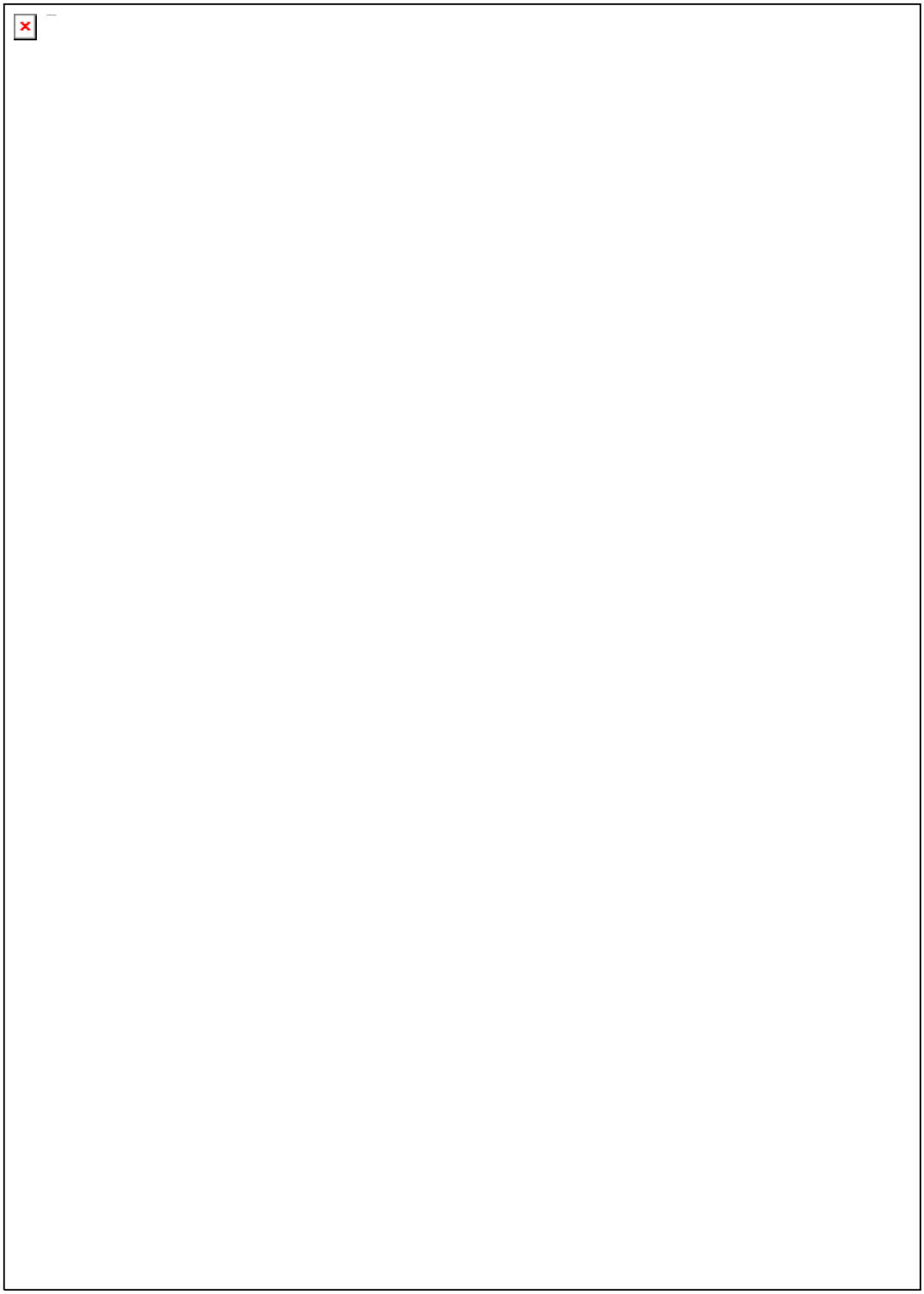

Figure 4.5. (a) Three-dimensional Autodesk Inventor diagram of the sample assembly. (b) Two-dimensional Autodesk Inventor cross-section of the sample assembly (courtesy of N. Hughes).

For the most part, the steel inserts were used to attach PZT-5A (lead zirconate titanate) compressional crystals (manufactured by Boston Piezo-Optics, Inc.) so that AE hits and energy could be recorded during experimentation. The PZT compressional crystals (0.118'' ± 0.003'' diameter with a fine-lapped finish and chrome/gold electrodes on both sides) are glued directly onto the inserts using silver-loaded epoxy adhesive. Small copper discs (of the same diameter as the PZT compressional crystal) that contain soldered gold-plated pins are glued, using silver-loaded epoxy adhesive, on top of each of the PZT compressional crystals (Fig. 4.7a). Each stainless steel insert also contains a 1 mm diameter hole with gold-plated pin inside, this used to provide an earth for the coaxial cables used to relay the data (Fig. 4.7a) (see 4.3.4.2 The lead-through system). Specially modified steel inserts were also used for the furnace calibration (see **4.5 Calibration of the experimental equipment**). To ensure that the stainless steel inserts remain sealed at pressure, stainless steel cuffs are pushed over each of the 'nipples' (see Fig. 4.7a and b).

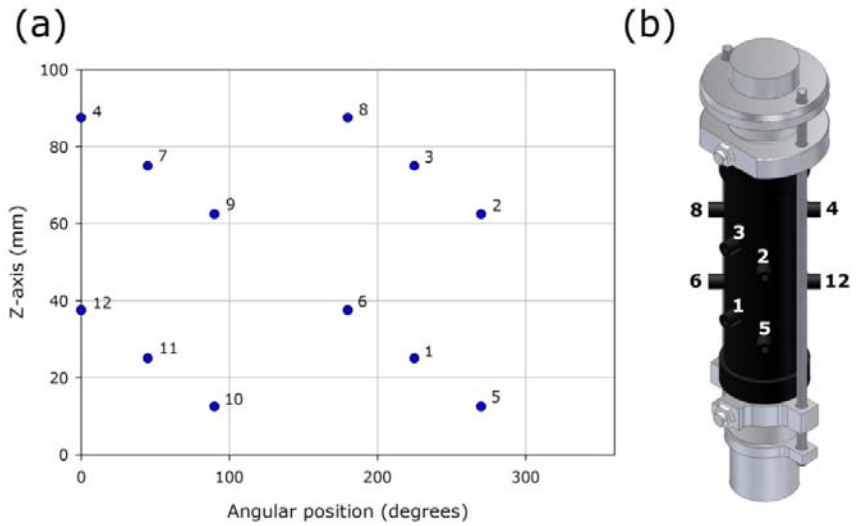

Figure 4.6. (a) Angular position of each of the inserts on the sample jacket. The numbers correspond to the specific number given to each insert. The positions in '3D space' of each of the inserts were inputted into the Vallen ASKY-2 AE recording software so that AE hypocentre locations could be determined. (b) Three-dimensional Autodesk Inventor diagram of the sample assembly showing the positions of the numbered inserts.

4.3.4.2 The lead-through system

A lead-through system that allows coaxial cables to relay data collected from inside to outside the pressurized vessel was used throughout this study (Fig. 4.7). The lead-throughs consist of a plug that houses a silver steel connector pin that is electrically isolated from the plug by a ULTEM® (unfilled polyetherimide – an amorphous polymer offering high strength heat resistance) cone and insulator (Fig. 4.7d). Coaxial cables are soldered to either side of the silver steel conductor pin and are earthed using two brass screws connected to each end of the plug (Fig. 4.7c). The coaxial cables soldered to the end of the conductor pin near the top of the plug reside inside the pressure vessel, and can be connected to the gold-plated pins (see 4.3.4.1 The jacketing system) on the stainless steel inserts via gold-plated sockets (as in Fig. 4.7b), this allowed AE data to be relayed from inside the pressure vessel. The coaxial cables soldered at the bottom of the plug are fed through the bottom breech nut and can be connected to either the National Instruments data acquisition card or an AE recording system (see 4.4 Measurement and data logging), depending on the type of relayed information. The UTLEM cone is responsible for providing a seal for the coaxial cables and the plug is sealed using a standard o-ring and PTFE backing ring arrangement (Fig. 4.7d). Modified lead-throughs were used during the implementation of the furnace. In this instance, blank plugs that contain two 2 mm drilled holes were used. Thermocouples, braised into place, pass through each of the holes and into the vessel (Fig. 4.7e) (see *4.3.6 The furnace* for more information).

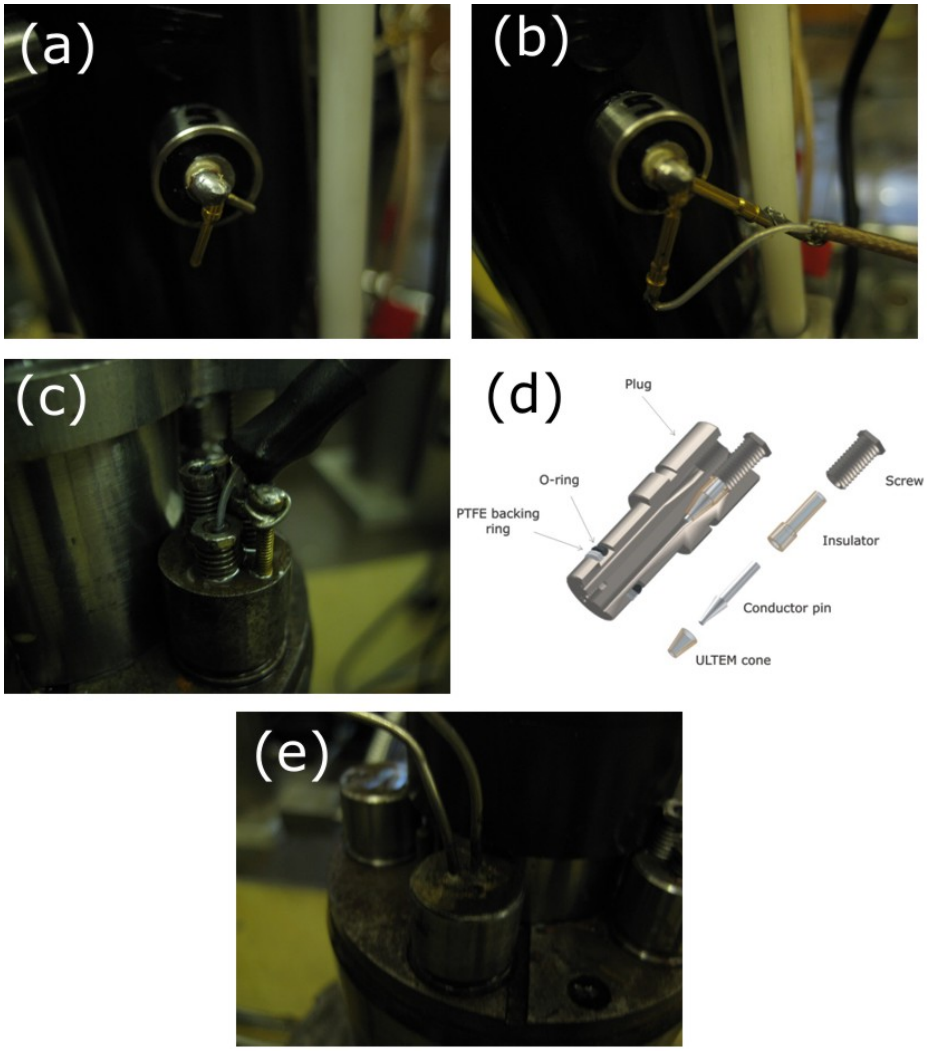

Figure 4.7. The lead-through system. (a) Photograph of the steel insert and mounted piezoelectric crystal and gold-plated pins (b) Photograph of the coaxial cable connected to the gold-plated pins via gold-plated sockets. (c) Photograph of the top of the leadthrough plug showing three coaxiable cables entering the vessel earthed using the brass earthing screw. (d) Autodesk Inventor diagram of the lead-through system and its components. (e) Photograph of a modified blank leadthrough plug allowing two thermocouples to enter the vessel (Inventor diagram courtsey of N. Hughes).

4.3.5 Pressure application systems

4.3.5.1 Intensifiers/pore volumometers

The intensifiers/pore volumometers provide a high precision method for controlling and maintaining both the pore pressure and the confining pressure. The intensifiers located at the Rock & Ice Physics Laboratory (RIPL) incorporate servo-hydraulic and closed-loop control techniques in order to achieve the high accuracy and resolution required during experimentation. The high-response servo-valves achieve the control response whilst maintaining the pressure stability requirements. This is especially important during brittle creep experiments in which a constant pore fluid and confining pressure is paramount. During this study, the pore pressure was controlled by a 10 cc volume intensifier and the confining pressure by a high-capacity, double-acting 22 cc volume intensifier (Fig. 4.8). The larger area of the low pressure piston relative to the high pressure piston results in the ability to accurately control the higher pressure in the high pressure cylinder, depending on the ratio of the piston areas. The LVDT monitors the position of the piston and so records the pore volume change in the rock sample during experimentation.

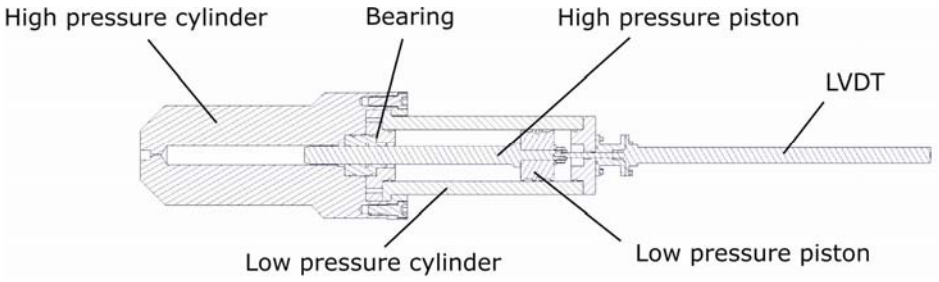

Figure 4.8. Two-dimensional Autodesk Inventor cross-section of an intensifier/pore volumometer at the Rock & Ice Physics Laboratory (courtesy of N. Hughes).

4.3.5.2 Confining pressure

The confining pressure exerts a hydrostatic pressure on the rock sample during deformation. The confining medium used in this study was a silicone oil of viscosity 100 cS (purchased from Dow Corning Limited) and was used due to its low coefficient of volume expansion, high boiling point (150°C) and the fact that it is non-conductive. Pressure was achieved using a large two-stage hydraulic pump (manufactured by Stanstead Fluid Power) capable of producing a maximum confining pressure of 400 MPa. A relief valve, situated at the top of the vessel, allowed an escape for the displaced air as the silicone oil was pumped into the vessel. As soon as silicone oil started to flow through the relief valve then the vessel was free of air. At this point, the relief value was closed and then the vessel could begin pressurization. It is very important during experimentation, especially for brittle creep experiments, that the confining pressure is maintained constant. This was achieved using a high-capacity 22 cc servo-controlled intensifier (see 4.3.5.1 Intensifiers/pore volumometers). The confining fluid was isolated from the sample by a fluoroelastomer nitrile jacket (see 4.3.4.1 The jacketing system). During experiments that utilized the furnace, a silicone oil of viscosity 20 cS was used to prevent the oil from polymerizing (see *4.3.6 The furnace*).

4.3.5.3 Pore pressure

As outlined in Chapter Three, most rock at depth is saturated with a fluid phase that exerts a hydrostatic pressure normal to the surface of the grains resulting in the reduction of the effect of the external applied stresses on the rock. The pore fluid (distilled water) is introduced to the sample, via high pressure piping, through the top and bottom endcaps of the sample assembly (see *4.3.4 Sample assembly*). The maximum pore pressure achievable is 400 MPa and is maintained constant by a 10 cc

servo-controlled intensifier (see 4.3.5.1 Intensifiers/pore volumometers). As with the confining pressure, it is very important that the pore fluid pressure maintains constant throughout experimentation.

4.3.5.4 Pressure application protocol

The protocol for applying the confining pressure was to ensure that the sample is never exposed to an effective confining pressure (P_{eff}) of more than the target P_{eff} required for that experiment. Care was also taken so that the pore fluid pressure (P_p) never exceeded the confining pressure (P_c), during this situation the silicone oil would enter the jacket and ruin the experiment. The majority of experiments were performed at a P_c of 50 MPa and a P_p of 20 MPa. In this scenario, the P_c was first taken to 30 MPa, then the 20 MPa P_p was applied before taking the P_c up to 50 MPa. The experimental set-up was then left overnight to ensure complete rock sample saturation (see Chapter Five, section *5.2.4 Saturating samples*) and to allow time for the pressures within the vessel to fully stabilize.

4.3.6 The furnace

4.3.6.1 Details of the furnace and sample assembly

Some experiments were performed in conjunction with the internal electric furnace designed and first implemented by D. Eccles and E. Benbow [Eccles, 2005] (Fig. 4.9), based on a previous design by V. Rocchi [Rocchi, 2002]. The furnace is incorporated into a modified bottom closure, and therefore resides inside the pressurized vessel above the bottom breach nut and retaining nut (see Fig. 4.4). The furnace is a two-zone furnace and contains two upper and two lower heating coils that are wrapped around a copper tube inside the furnace so that it forms a continuous coil over the whole length of the sample

(Fig. 4.7b). The individual heating coils, manufactured by ARi Industries (Illinois, USA), have a maximum wattage output of 1 kW giving the furnace a maximum output of 4 kW.

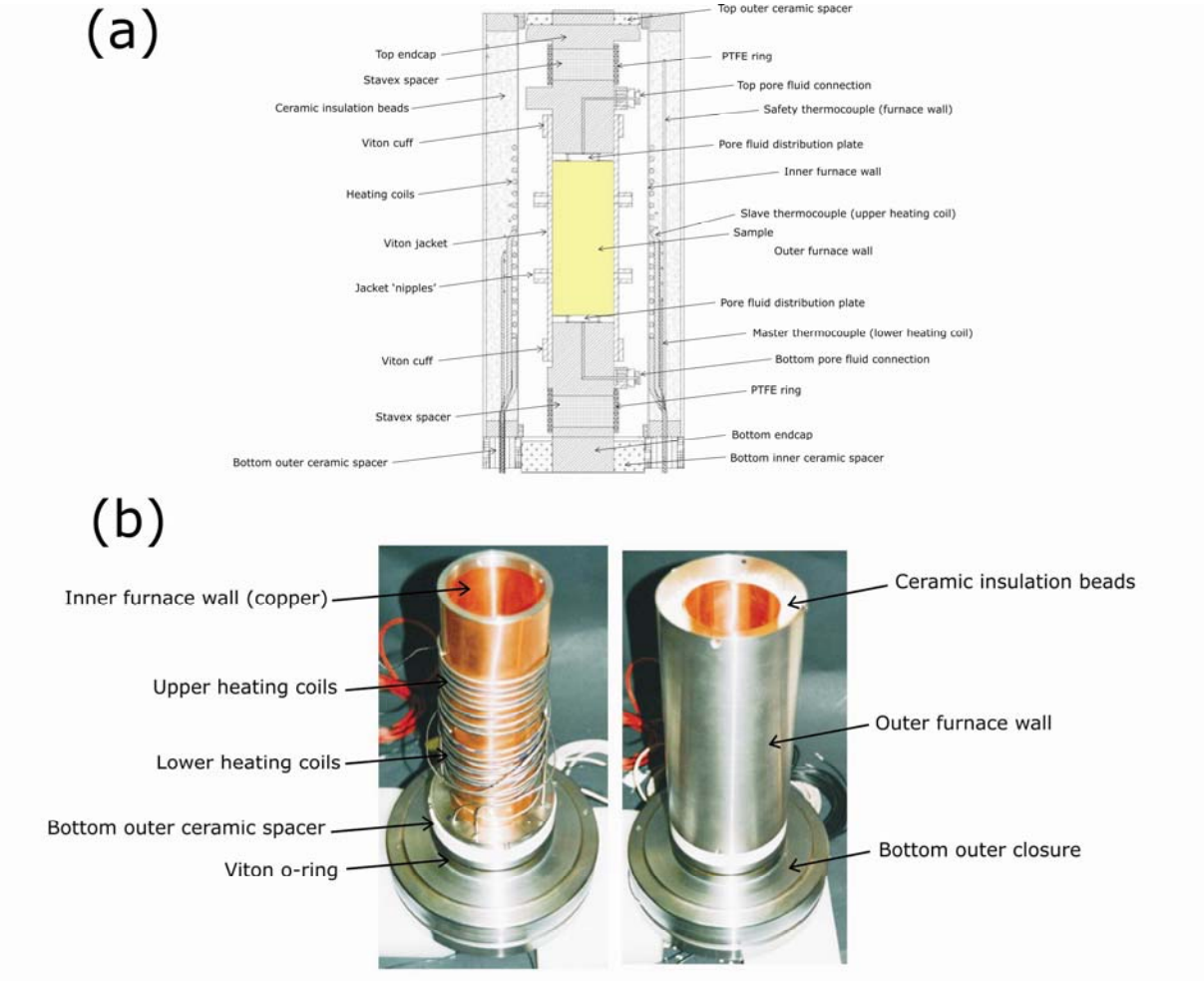

Figure 4.9. (a) A two-dimensional Autodesk Inventor cross-section of the furnace and sample assembly highlighting all the major components. (a) Photographs of the furnace with major components labeled [taken from Eccles, 2005].

The furnace contains three internal K-type thermocouples (1) a master thermocouple located in the lower part of the furnace, (2) a slave thermocouple located in the upper part of the furnace and (3) a cut-off thermocouple located in the furnace wall. The cut-off thermocouple was configured so that if the temperature exceeded 175°C all power would be cut off from the furnace. The furnace is controlled by

the master and slave thermocouples using a type 815 Eurotherm controller. The master thermocouple, located adjacent to the lower heating coils, is connected to the master input within the control unit and can vary the power output to the heating coils via a feedback loop. Thermal insulation was provided by the ceramic discs located at the top and bottom of the sample assembly (Fig. 4.9) and by the ceramic insulation beads that completely filled the void between the inner and outer furnace walls (Fig. 4.9).

The cables that supply the power to the furnace and the three thermocouples used in its control are fed through the bottom of the modified bottom closure and exit the pressure vessel via three 7 mm diameter holes in the vessel wall. A wire protection disc, attached to the bottom of the modified bottom closure, ensured that cables did not accidently shear against the bottom ram. Also, since locking the vessel involves rotating it by approximately 45°, a steel pin was inserted into a fourth hole to prevent the furnace from moving during rotation and shearing the cables. Further details on the design of the furnace can be found in Eccles [2005].

4.3.6.2 Modifications to the original set-up

A couple of modifications to the experimental set-up were required for the normal running of the triaxial deformation ensemble. Firstly, all of the o-rings in the vessel were changed from nitrile to viton o-rings. Nitrile will degrade at high temperatures over a long period of time and will therefore decrease the probability of the vessel sealing. Viton o-rings are rated to 260°C, much higher than the target temperature of any of the experiments. For the same reason, the nitrile jacket was also replaced with a viton jacket (manufactured by Ergotech, UK). Secondly, the 100 cS silicone oil would polymerize when exposed to high temperatures over a long period of time. Therefore, the oil was changed to 20 cS

silicone oil (purchased from Dow Corning Limited). This oil also has a higher flash point and so is less likely to ignite if any leaks are present during experimentation.

4.3.6.3 Temperature application protocol

For the experiments performed in this study the overall power to the furnace was set at 15%, with the master thermocouple set at 30% and the slave thermocouple set at 5%. This was found to be the power set-up that resulted in the lowest thermal gradient across the sample (see also *4.5.3 Calibration of the furnace*). Since hot oil will rise, the oil near the top of the sample will be the hottest. Therefore, the best configuration was to set the slave thermocouple (controlling the upper heating coils) to a low power rating and the master thermocouple (controlling the lower heating coils) to a high power rating.

During this study, the majority of experiments conducted at elevated temperatures were performed at a constant 75°C. The experimental protocol for this was to increase the P_c to 28 MPa before the application of a P_p of 20 MPa. The sample was then left exposed to these pressures overnight. The furnace was then set to a target temperature of 105°C, the ramp generator to 5 °C/minute and the ramping program was initiated. The increasing temperature will slowly increase the P_c, due to the expansion of the oil, up to approximately 50 MPa. At this point the value isolating the confining pressure intensifier was opened to allow the P_c to be adjusted to and held at exactly 50 MPa. To allow the temperature of the oil and sample to stabilize, the set-up was left for 120 minutes before experimentation was initiated (see *4.5.3 Calibration of the furnace*). Once the experiment had finished, the ramp generator was deactivated to allow the oil to cool before taking the sample out as normal.

4.4 Measurement and data logging

4.4.1 Parametric data recording systems and logging software

The parametric experimental data were acquired using a National Instruments CB-68LP data acquisition cards. The cards were connected to a desktop computer positioned next to both of the deformation apparatus and the program LabVIEW (version 7.28) records and saves the data. The data acquisition cards have multiple channels and can record signal voltages from the different transducers, these voltages are then converted into values of length, volume, pressure and force by specific conversions calculated from the equipment calibrations (see **4.5 Calibration of the experimental equipment**). These values can then be used to control the hydraulic actuator piston via a microprocessor based servo-controller. During experiments that were performed in conjunction with the furnace, an additional CB-68LPR data acquisition card was used to provide enough channels for the six thermocouples used for calibration. LabVIEW plots the incoming data onto graphs in real time so that the experiments can be monitored throughout. The trigger interval for saving data could be varied during experimentation. For constant strain rate and stress-cycling experiments, data points were collected every other second. For long-term brittle creep experiments, data points were collected at minute intervals.

4.4.2 AE data recording systems and logging software

AE activity during all uniaxial experiments was recorded using a MISTRAS-2001 AE recording system. The piezoelectric crystal, located inside the bottom anvil (Fig. 4.2), was connected to the MISTRAS-2001 via a preamplifier using a coaxial cable. The low-level AE signals emitted from the sample were converted into electrical signals by a sensor, amplified to usable voltage levels by the preamplifier (set at a relative gain

of 40 dB) and measured in the AEDSP-32/16 card. The data from the card were then passed onto the PC where it was stored and plotted onto onscreen graphs in real time so that the experiments could be monitored throughout.

During triaxial experiments, AE activity was recorded by a multi-channel Vallen AMSY-5. A variety of AE data can be recorded using the multi-channel Vallen AMSY-5 AE recording system including waveform characteristics, AE energy and hits and AE location data. The Vallen AMSK-5 was also setup to simultaneously record parametric data. Low-level signals from the piezo-electric crystals (see 4.3.4.1 The jacketing system) were relayed from inside the pressure vessel using the lead-through system (see 4.3.4.2 The lead-through system) where they were amplified by a preamplifiers (set at a relative gain of 40 dB) before reaching the acoustic signal preprocessor located inside the AMSY-5 system. The 32-bit AMSY-5 acquisition program collects the data, which could be monitored throughout the experiment using the programs VisualAE and VisualTR. The threshold for each of the channels was nominally set to 40 dB at the start of experimentation; however, due to the slightly different susceptibility of the piezo-electric crystals to pick up background noise, the threshold was adjusted so that no channels were picking up noise before experimentation began.

A typical acoustic emission waveform recorded during experimentation is shown in Fig. 4.10. The event begins when either of the event thresholds (inputted into the Vallen AMSY-5), marked as dashed lines in Fig. 4.10, is breached. This is generally followed by the peak amplitude of the event, which is related to the intensity of the source in the rock producing the AE event. The ring-down counts are defined as each time the signal crosses the preset event threshold. In general, more ring-down counts are produced for larger events. The event duration is simply defined as the time between when the waveform first

crosses the threshold to the last time it crosses the threshold, in this case the AE event lasted approximately 8 μs.

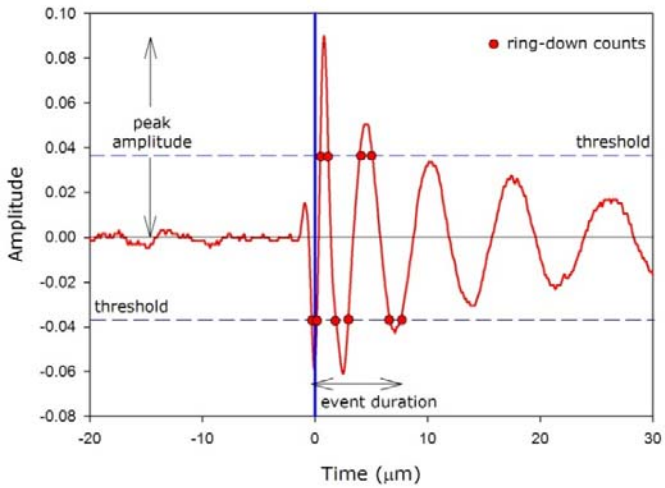

Figure 4.10. Characteristic brittle fracture acoustic emission waveform from the Vallen AMSY-5 AE recording equipment showing waveform parameters from a constant strain rate (1.0 x 10^{-5} s^{-1}) triaxial experiment on DDS [sample DD-40-12Z].

4.5 Calibration of the experimental equipment

4.5.1 Introduction

The calibration of testing equipment is an essential precursor for any experimental study, since the accuracy of the experiment data heavily rely on the accuracy of the transducers and equipment that measure it.

4.5.2 Calibration of the experimental equipment

The load cell for the uniaxial compression apparatus was calibrated using a proving ring (manufactured and calibrated by ELE Limited). The proving ring was positioned within the apparatus and loaded until

the centre dial read 25 kN, the resulting output voltage from the load cell was then recorded. This method was repeated for successive steps of 25 kN until 200 kN. The load cell was then calibrated in LabVIEW so that 1 volt equals 25 kN (Fig. 4.11c). The load cell for the triaxial ensemble requires a much larger proving ring and so was accurately calibrated on purchase.

The LVDT's for both testing machines were accurately calibrated using a barrel micrometer (manufactured by Mitutoyo, UK) that has a resolution of 0.002 mm. Each LVDT was clamped in turn into the micrometer and the barrel was moved in 1 mm increments, the output voltage was measured from the LVDT at each increment and displayed in the program LabVIEW. Since the LVDT's have a range of ±5 volts, they were calibrated in LabVIEW so that 1 volt equals 1 mm (Figs. 4.11a, 4.11b, 4.12a and 4.12b).

The pressure transducers for the pore fluid and confining pressure intensifiers were both calibrated using a dead-weight tester (manufactured by DH Budenburg). Each pressure transducer was connected to the dead-weight tester and weights of known mass were applied. The output voltage was then measured from the pressure transducer. Since the pressure transducers have a range of ±10 volts and the maximum pressure the pore fluid intensifier can achieve is 400 MPa, it was calibrated in LabVIEW so that 1 volt equals 40 MPa (Fig. 4.12c). However, since the confining pressure intensifier constantly drives forward during deformation in a creep experiment, the pressure transducer in the confining pressure intensifier was calibrated in LabVIEW so that 1 volt equals 50 MPa to avoid the intensifier losing control (4.12d).

A problem associated with the uniaxial compression apparatus is that the LVDT setup to measure the axial strain within the sample also records strain in the components that make up the sample assembly (see Fig. 4.2). To avoid this issue, a dummy steel sample of known Young's modulus and dimension was

loaded in the uniaxial compression apparatus. However, the calibration indicates that there is a non-linearity in the loading curve up to an axial stress of about 40 MPa (Fig. 4.14d). Repeat calibrations on the dummy sample confirmed that the non-linearity was reproducible. The cause of the non-linearity, excluded from the experiments in this study using this calibration, is likely to be due to the progressive bedding-in of the contacting surfaces at low loads.

The strain calculated for the dummy sample (red line in Fig. 4.14d) was simply subtracted from the total strain recorded (green line in Fig. 4.14d). The resultant curve i.e. the strain only in the components of the loading column (blue line in Fig. 4.14d) was fitted with a third order polynomial so that strain within the components could be calculated for any value of axial stress and excluded from any experimental data. In the future, it will be necessary to ascertain the exact cause of the non-linearity. This can be achieved by loading the dummy sample with strain gauges mounted on opposite sides of the sample, thus only measuring the strain across the sample.

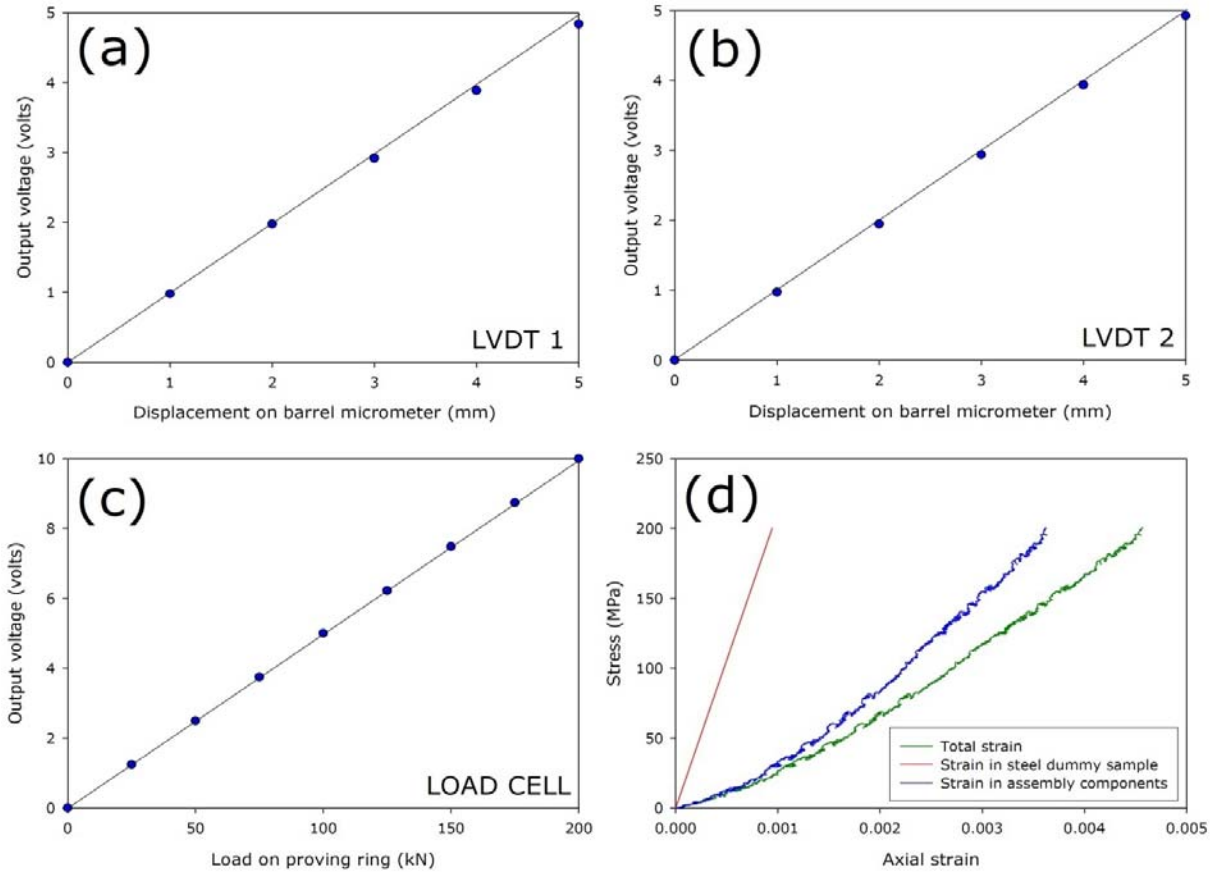

Figure 4.11. Calibrations for the uniaxial compression apparatus (a) LVDT one (b) LVDT two (c) load cell and (d) strain in the sample assembly components.

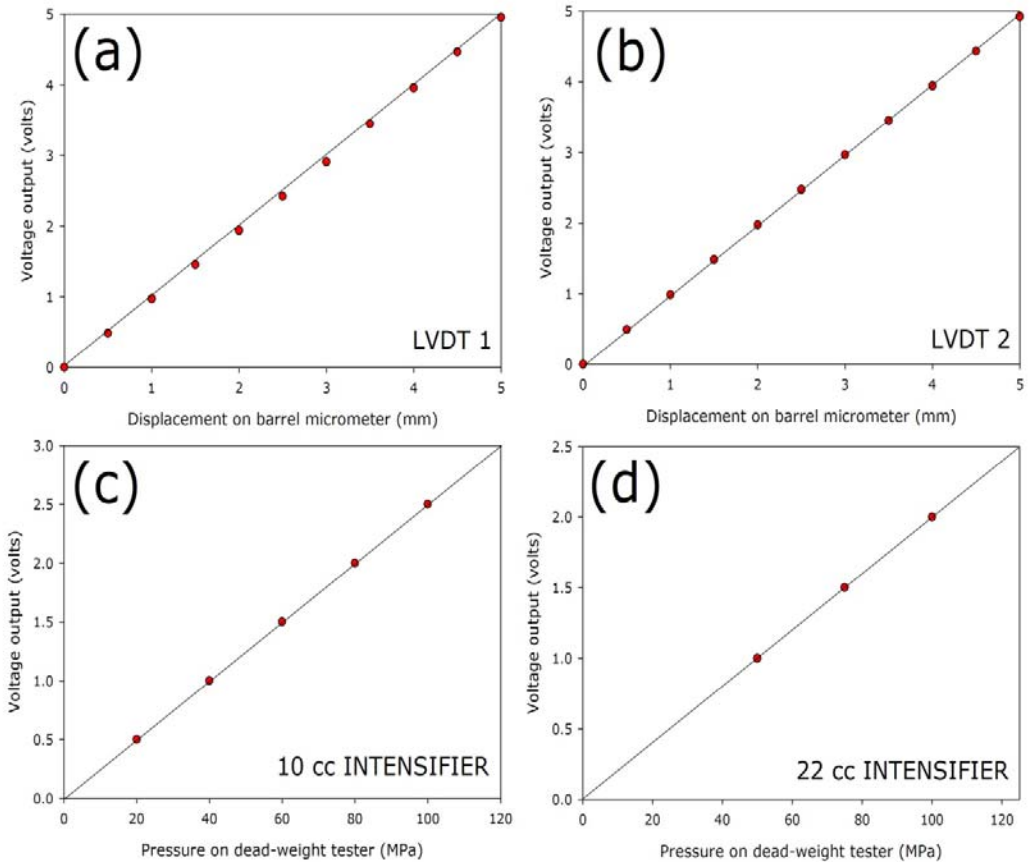

Figure 4.12. Calibrations for the triaxial ensemble (a) LVDT one (b) LVDT two (c) 10 cc intensifier (used to control the pore fluid pressure) and (d) 22 cc intensifier (used to control the confining pressure).

4.5.3 Calibration of the furnace

The thermocouples inside the furnace control the heating coils and therefore only measure the temperature next to the coils. However, due to convection, the temperature of the oil and inside the sample will be different to that of the heating coils. It was essential therefore to ascertain the temperature within the sample for a given heating coil temperature. This was achieved using six thermocouples, three located inside the sample and three located in the oil within the pressurized vessel. Firstly, all six of the thermocouples were calibrated using ice as a reference temperature. They

were each submersed in icy water and the offset was adjusted in LabVIEW for each channel so that the thermocouples read 0°C.

The three thermocouples used to measure the temperature within the sample were located in the centre of the sample at the top, middle and bottom. The thermocouples used to measure the temperature of the oil were located in the oil adjacent to the thermocouples within the sample. A sample of Darley Dale sandstone (see Chapter Five for detailed rock descriptions) that contained three 2 mm diameter by 20 mm deep drilled holes (Fig. 4.13a) was used for the calibration. The holes were drilled so that they were in line with three steel inserts (see 4.3.4.1 The jacketing system) positioned as close as possible to the top, middle and bottom of the sample (Fig. 4.13d). The thermocouples entered the pressurized vessel through modified blank leadthrough plugs (Fig. 4.7e) and entered the sample through modified steel inserts that were drilled down the centre so that the thermocouples could pass through (Figs. 4.13b and 4.13c). The tip of the thermocouples protruded 20 mm from the edge of the modified steel insert so that they would fit comfortably in the drilled holes and would measure the temperature at the centre of the sample (Fig. 4.13c). The steel insert was pushed through the appropriate jacket 'nipple' (4.13d) and a stainless steel cuff was used to ensure a successful seal (Fig. 4.13c).

During the calibration experiments, the furnace was heated to 80, 90, 96 and 105°C and the temperature from the six thermocouples (three within the sample and three within the oil) recorded (Fig. 4.14). Fig. 4.14 shows a plot of the furnace temperature against the average measured sample temperature. Using this plot, the temperature of the sample can be estimated from the furnace temperature. The knowledge of the oil temperature at such target temperatures was also important and was used to double-check the temperature within the sample during experimentation. The oil

temperature thermocouples were also used as a safety measure and helped monitor the smooth running of the furnace.

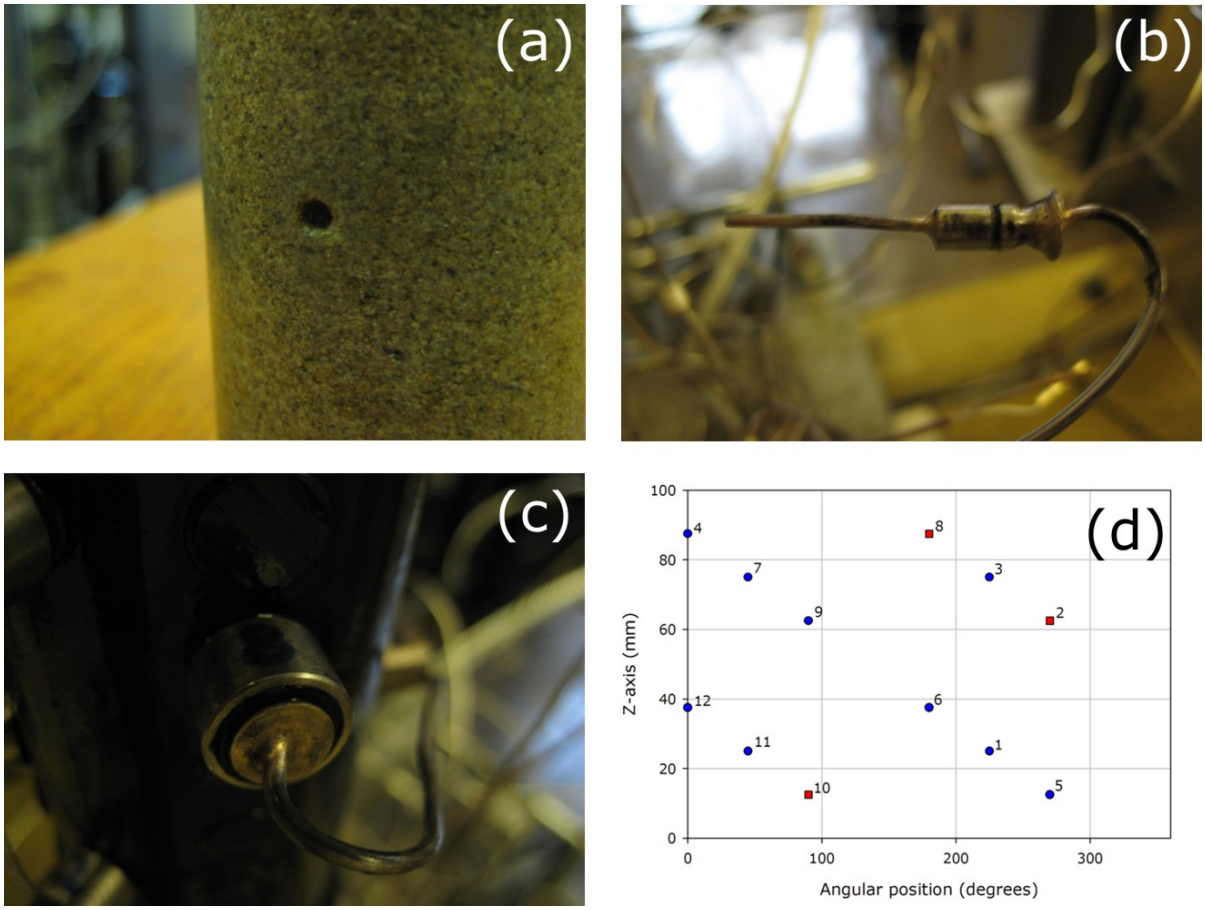

Figure 4.13. (a) Photograph of one of the 20 mm deep holes drilled into the sample of DDS. (b) Photograph of a modified steel jacket insert with thermocouple braised into place, the thermocouple protrudes 20 mm from the end of the insert. (c) Photograph of the modified steel insert inside the jacket 'nipple' so that the thermocouple enters the middle of the sample. (d) The angular position of the inserts on the jacket, the red squares indicate the position of the modified inserts.

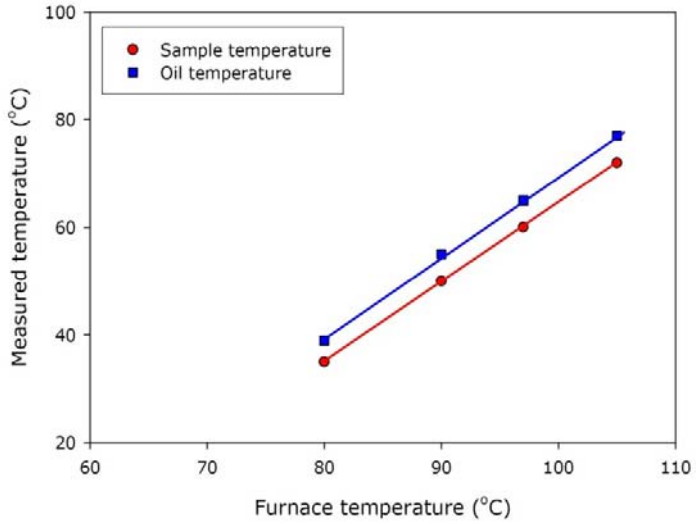

Figure 4.14. Compilation of the calibration experiments plotted as furnace temperature versus measured temperature for both the sample and oil. Furnace temperature was controlled using the thermocouples present in the furnace walls and the sample and oil temperature were measured using thermocouples located within the centre of the sample at the top, middle and bottom (see Fig. 4.13d) and in the oil near the top, middle and bottom of the sample respectively. The values plotted here are the averages of the temperatures recorded by the thermocouples.

It was also important to ascertain the length of time required before the temperature within the sample became stable and to determine the extent of any temperature gradient present along the sample length during the heating of the furnace. The influence of heating on the confining pressure, pore fluid pressure and pore volume change was also monitored. An example of one of the furnace calibrations, where the furnace temperature was set at 105°C, is shown in Fig. 4.15. Fig. 4.15 demonstrates that when the furnace is turned on both the temperature of the sample and oil increase. At this target temperature, the temperature within both the sample and oil reached a maximum after about 50 minutes and then began to stabilize. It was therefore decided that, during the normal running of an elevated temperature experiment, the set-up would be left for 120 minutes to stabilize prior to experimentation. This gives the system ample time to reach the target temperature and stabilize at that temperature. The stability of the temperature can also be monitored using the thermocouples present

within the oil during experimentation. Fig. 4.15 also demonstrates that a temperature gradient of about 9°C exists across the length of the sample. A thermal gradient of less than 0.1°C/mm is considered to be more than acceptable.

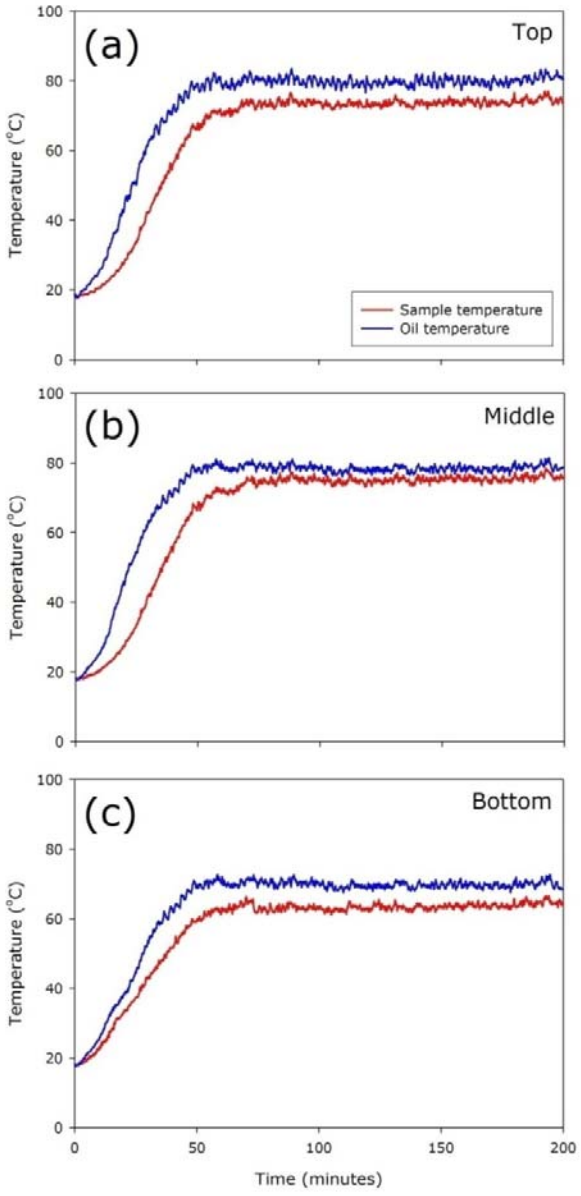

Figure 4.15. Temperature measured at the centre of the sample at the (a) top, (b) middle and (c) bottom of the sample length plotted with the temperature of the adjacent oil when the furnace was heated to 105°C. The furnace of switched on at 0 minutes.

During heating, the silicone oil expands thus increasing the confining pressure; this, in turn, drives water out of the sample due to the increased confinement (Fig. 4.16). An important goal was to confirm that the P_p remained constant throughout the heating process (Fig. 4.16). Since it is important that the sample is not exposed to a higher P_{eff} than that selected for the experiment, the increase in P_c caused by the expansion of oil was factored into the pressure application protocol (see 4.3.6.3 Temperature application protocol).

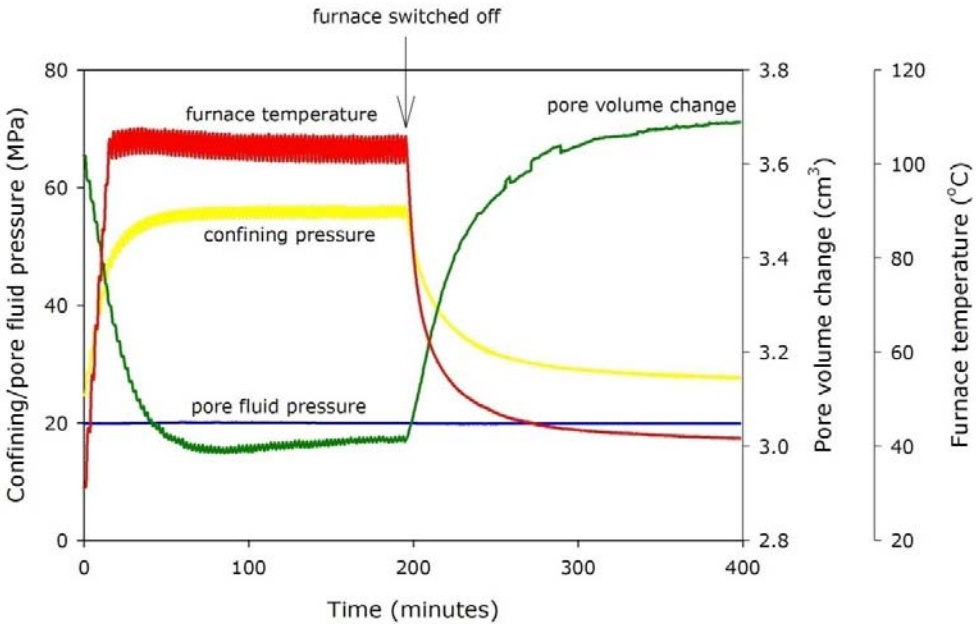

Figure 4.16. The variation in confining pressure, pore fluid pressure and pore volume change during the heating of the electric internal furnace within the triaxial ensemble. The furnace was switched on at time 0 minutes and switched off where indicated by the arrow, at about 200 minutes.

Chapter five

5. Sample Preparation, Experimental Materials and Rock Characterization Techniques

5.1 Introduction

Two rock types that exhibit widely contrasting physical and mechanical properties were selected for this study. They are a high porosity, lithic-rich sandstone (Darley Dale sandstone, DDS) and a low porosity, fractured basalt (Etna basalt, EB). Extensive rock type characterization is an essential precursor to any experimental program. A detailed understanding of the characteristics of a rock is required in order to fully understand its complex behaviour during experimentation. This chapter outlines how the samples were carefully prepared for experimentation and the procedures and results of the characterization of each of the two main experimental materials used in this study. A brief characterization of other rock types used during this study is also explained at the end of the chapter.

5.2 Rock sample preparation

5.2.1 Introduction

The careful preparation of rock samples is of paramount importance throughout any experimental study. It helps to reduce experimental error and therefore improves results and saves time. To this end, a consistent and rigorous method for the preparation of samples was devised before any experiments were conducted. This section describes the preparation of samples to be used in the triaxial ensemble and the uniaxial compression apparatus; sample preparation for specific characterization techniques are explained in their respective sections.

5.2.2 Orientation of samples

Firstly, an orientation system using orthogonal X-, Y- and Z-axes to define a common co-ordinate reference system was devised to be used throughout this study (Fig. 5.1). Since DDS does not show any visible bedding or fabric in hand specimen, the Z-axis was taken as normal to micro-scale bedding determined by preliminary benchtop ultrasonic velocity measurements. Preliminary ultrasonic velocity measurements for EB found it to be perfectly isotropic, therefore no Z-axis could be determined. In this circumstance all the samples were cored in the same direction, as determined by the size and shape of the received block. A more comprehensive ultrasonic velocity study for both of the rock types can be found later in this chapter.

Sets of closely spaced parallel lines were then drawn on each of the blocks using different coloured pens for each orthogonal axis (Fig. 5.1). Therefore, after coring, the samples could be easily re-orientated relative to the block.

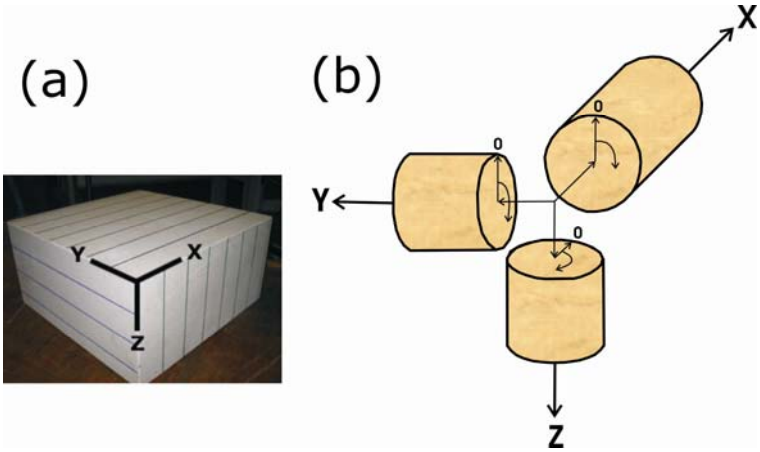

Figure 5.1. (a) A fully orientated block of sample material showing the positions of the orthogonal axes and (b) Cores for each of the orthogonal axes. 0 – the measurement starting position for both benchtop ultrasonic velocity and AMS measurements [after Benson *et al*., 2003].

5.2.3 Coring and grinding

For use in the triaxial ensemble, cylindrical samples of 40 mm diameter were cored to a length of 130 mm using a diamond impregnated coring drill. Samples prepared to be used in the uniaxial compression apparatus were 25 mm in diameter and cut to a length of 100 mm. The block of material was clamped in place to prevent any movement during the coring process. Water was used to cool the coring drill during coring and it was lowered into the block at a slow and constant rate so to avoid damaging the sample and coring apparatus.

The ends of the samples were then trimmed using a diamond sintered circular saw before they were ground down to a precise 100 mm for triaxial samples and 75 mm for uniaxial samples using a diamond sintered grinding wheel. This ensures that all the samples have a length:diameter ratio of 2.5:1 [Mogi, 1966; Hawkes and Mellor, 1970]. The cylindrical samples were held in place during grinding using stainless steel v-clamps, which were locked onto the grinding plate using a magnetic locking mechanism. A water-oil (Ultragrind lubrication oil) mixture was used to lubricate the grinding wheel whilst it was slowly lowered onto the sample in very small increments to prevent damaging the sample and grinding apparatus. The grinding wheel ensures that the ends are parallel to an accuracy of ±0.02 mm, thus preventing an uneven distribution of stress on the sample during experimentation [Hawkes and Mellor, 1970]. After the grinding process was completed the samples were washed with water to remove any excess oil and then placed in an oven (laboratory standard of 80 °C) to dry. At this temperature no thermal cracking is observed [see Glover *et al.*, 1995].

5.2.4 Saturating samples

Water-saturated samples were used in most of the experiments presented in this study. To saturate, samples were fully submersed in a bell jar of distilled water connected to a vacuum pump. The time spent under vacuum depended on the permeability of the rock. Sandstone samples were left for 12 hours while basalt samples were left for 24 hours. Crab Orchard sandstone however, due to its low permeability and porosity, was also left for 24 hours prior to experimentation. Such times are overestimates of the time needed to fully saturate the samples; however, since stress corrosion is an environment-dependent chemical process it was very important to ensure samples were fully saturated. To this end, they were also left overnight inside the vessel under the relevant experimental conditions (usually a confining pressure of 50 MPa and a pore pressure of 20 MPa) before the experiment was started. This way, the pore pressure intensifier/pore volumometer would guarantee complete saturation.

5.2.5 Heat treating samples

Some samples were heat-treated for use in the uniaxial compression apparatus. All heat-treated samples were heated in an insulated tube furnace at 1 °C/min up to a target temperature of 900°C, where samples were held for one hour to allow for thermal microcrack equilibration. Samples were then cooled back to room temperature at the same rate.

5.3 Hand specimen and optical and scanning electron microscope analysis

5.3.1 Darley Dale sandstone

DDS is a brown-yellow, well-indurated, feldspathic sandstone from Derbyshire, England. It is widely used in rock physics due to excellent experiment reproducibility. In hand specimen, DDS appears poorly sorted containing homogeneously distributed white (feldspar) and dark brown/black (mica) speckling (~1 mm in diameter). There is no distinct layering or lamination.

The modal composition of DDS consists of 69% quartz, 26% feldspar, 3% mica and 2% clay. Optical microscopy and scanning electron microscope (SEM) analysis demonstrated that the grains are angular to sub-angular, vary between 100-800 μm in diameter and show no discernable preferential alignment (Fig. 5.2). The quartz grains are colourless in plane-polarized light (PPL) and exhibit low 1st order interference colours in cross-polarized light (XPL) (Fig. 5.2a). Feldspars can be clearly distinguished from the quartz in PPL by their cloudy, brownish appearance (Fig. 5.2b). The SEM image for DDS shows that most grains contain some clay overgrowth (Fig. 5.2c).

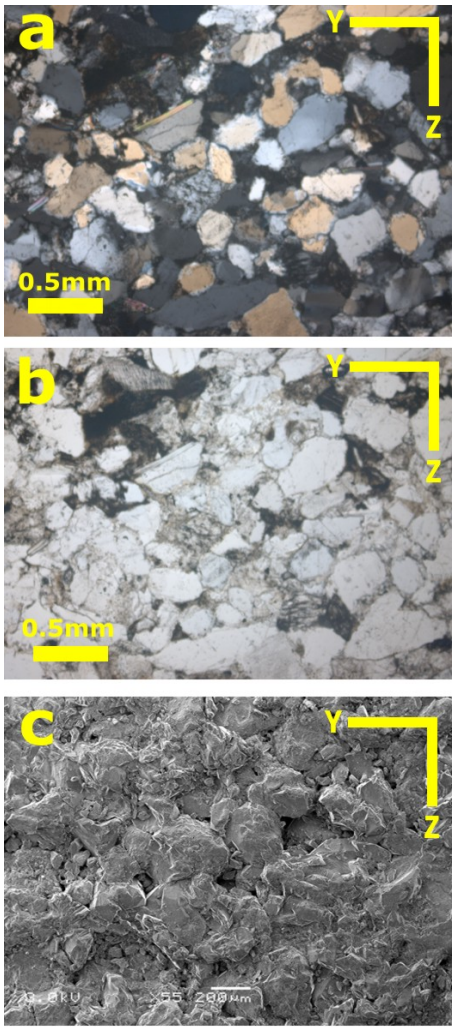

Figure 5.2. (a) Photomicrograph of undeformed DDS under cross-polarized light. (b) Photomicrograph of undeformed Darley Dale sandstone under plane-polarized light. (c) SEM image of an uncoated sample of undeformed Darley Dale sandstone at x55 magnification.

5.3.2 Etna basalt

EB is a porphyritic alkali basalt [Tanguy *et al.*, 1997] from Mount Etna, Italy. The EB used in this study was collected from the location indicated in Fig. 5.3. In hand specimen, EB is light-grey and contains many dark grey, angular, randomly distributed phenocrysts. EB is composed of a groundmass of fine-

grain matrix (~60%) that includes crystals of feldspar (25%), pyroxene (8.5%) and olivine (4%) (Figs. 5.4a and 5.4b).

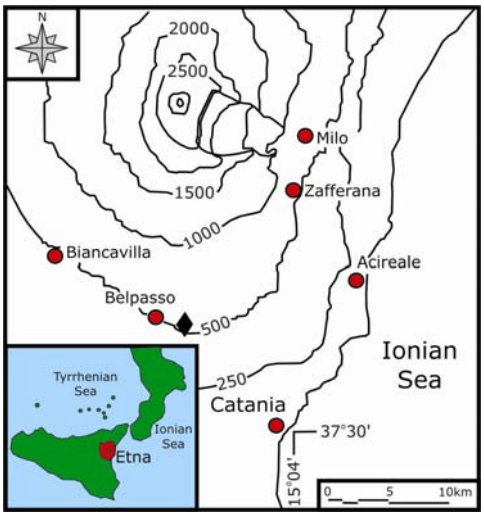

Figure 5.3. Location map of Mt. Etna showing main towns and morphological features. The solid diamond indicates the position of the quarry from which the EB test material was collected.

From optical microscopy and SEM analysis, EB contains a fine-grained matrix embedded with large phenocrysts of plagioclase, olivine and pyroxene varying from 200-2500 µm in diameter and show no discernable preferential alignment (Fig. 5.4). The plagioclase (low 1st order interference colours in XPL) is mostly rectangular in shape and regularly displays albite twinning. The olivine can be easily recognized by its high relief and high birefringence in XPL (high 2nd and 3rd order interference colours). Olivine grains are heavily traversed by randomly orientated microcracks. The pyroxene show yellow-brown interference colours in XPL. The fine-grained matrix is composed of the same minerals together with small, angular crystals of magnetite that can be easily identified as the only opaque mineral (black specks in PPL) (see Figs. 5.4a and 5.4b).

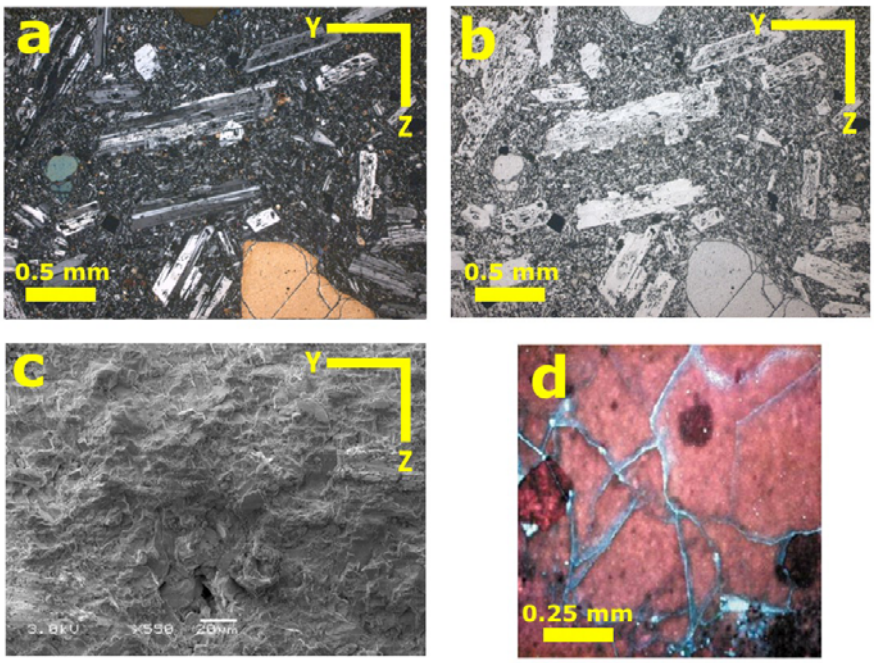

Figure 5.4. (a) Photomicrograph of undeformed EB under cross-polarized light. (b) Photomicrograph of undeformed EB under polarized light. (c) SEM image of an uncoated sample of undeformed EB at x55 magnification. (d) SEM image of a polished thin section of undeformed EB impregnated with UV fluorescent dye highlighting essentially randomly orientated thermal microcracks (taken from [Benson *et al.*, 2006]).

5.4 Porosity calculation

Porosity (ϕ) has been calculated using the Archimedes technique and was implemented on all samples immediately prior to experimentation. Firstly, the dry mass (M_{dry}), the vacuum-saturated (see *5.2.4 Saturating samples)* wet mass (M_{wet}) and the submersed mass (M_{arch}) were determined for each of the 40mm diameter cores. Porosity could then be calculated using the following equation:

$$\phi = \frac{M_{wet} - M_{dry}}{M_{wet} - M_{arch}} \qquad [5.1]$$

Complete representations of the variability of each of the two rock types, including the porosities calculated for this study, are listed in Tables 5.1 and 5.2. Using a helium pycnometer, EB was found to contain a connected porosity of 4.4% and a total porosity of 4.8% (courtesy of S. Vinciguerra).

5.4.1 Darley Dale sandstone

Author	Porosity (%)
This study	13.3 ± 0.8
Vinciguerra et al. [2004]	13
Baud et al. [2000]	13
Wu et al. [1997; 2000]	13.4
Wong et al. [1997]	14.5
Baud and Meredith [1997]	12-14
Ismail and Murrell [1976]	12
Ayling et al. [1994]	12

Table 5.1. Porosity variation in DDS.

5.4.2 Etna basalt

Author	Porosity (%)
This study	4.3 ± 0.2
Benson et al. [2007]	3.8
Vinciguerra et al. [2005]	2.1
Stanchits et al. [2005]	2.1 ± 0.1

Table 5.2. Porosity variation in EB.

5.5 Benchtop ultrasonic wave velocity analysis

5.5.1 Introduction

The knowledge and understanding of P- and S-wave velocities in rock physics is of paramount importance. It allows the calculation of velocity anisotropy, dynamic elastic moduli and is often used as a method for estimating the physical properties of rock due to the dependence of ultrasonic velocity on rock microstructure.

5.5.2 Methodology

Benchtop (room pressure and temperature) P- and S-wave velocity measurements were made using an Agilent Technologies 1.5GHz 'Infiniium' digital storage oscilloscope, a JSR DPR300 35MHz ultrasonic pulser/receiver and two custom-built sample assembly jigs that contain P- and S-wave transducers respectively (Fig. 5.5). Depending on the jig in use, the pulse generator applies a square wave voltage signal to either a P- or S-wave transducer (Panametrics V103 P-wave and V153 S-wave transducers with 1MHz resonance frequency and 0.5 inch diameter piezoelectric elements), which is then received by a second transducer after it has passed through the sample. At the same time, the pulse generator also sends a trigger signal directly to the oscilloscope to trigger the start of the timebase. The received signal is then amplified and sent to the oscilloscope. From this, the exact seismic travel time can be measured and recorded using a magnified image of the start of the received signal displayed on the oscilloscope (Fig. 5.6). The starts of the waveforms were picked by eye by looking for the first point at which the waveform deviated from the zero position (indicated by orange crosshair on Fig. 5.6a). Each of the custom-built sample assembly jigs (Fig. 5.5) allow the sample to be rotated in 10° increments.

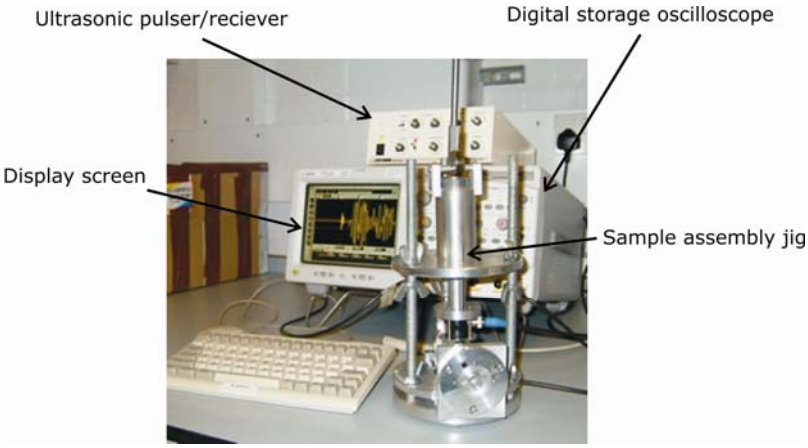

Figure 5.5. Photograph of the benchtop ultrasonic velocity analysis setup showing the main components.

A new reading was taken for each 10° increment the sample was rotated in the sample clamp assembly to provide a complete analysis of the ultrasonic wave velocity anisotropy within the sample. The process described above been completed for multiple 25 mm diameter by 75 mm long core samples of the two main rock types used in this study. Measurements were performed on both oven-dry and water-saturated samples (see *5.2.4 Saturating samples*) and in the XY, XZ and YZ planes (see Fig. 5.1). The measured ultrasonic velocity variation can be used to calculate the bulk experimental elastic anisotropy (A_{exp}), where V is the experimentally measured ultrasonic velocity, as defined by:

$$A_{\exp} = 100 \times \left[\frac{V_{\max} - V_{\min}}{V_{mean}} \right] \qquad [5.2]$$

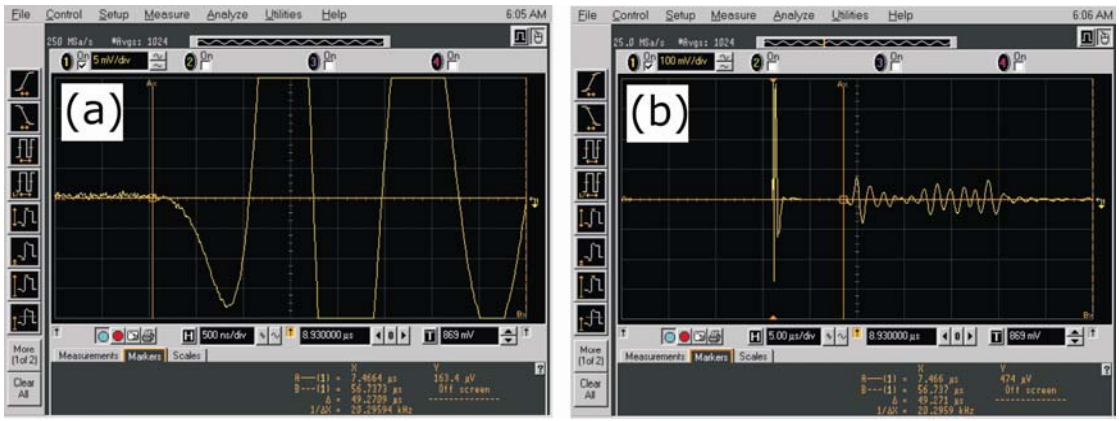

Figure 5.6. Oscilloscope images showing (a) magnified view for arrival picking and (b) enlarged view of the generated and received P-wave signal through a sample of Bentheim sandstone. Orange crosshair denotes start of the received signal.

5.5.3 Results

5.5.3.1 Darley Dale sandstone

The benchtop ultrasonic velocity variation with azimuth for DDS is shown in Fig. 5.7 and Table 5.3. DDS exhibits a systematic P- and S- wave variation with azimuth for all orientations. Planes XZ and YZ show the greatest variation with azimuth and have a ultrasonic velocity maximum at approximately 90° and minimum and both 0° and 180°. The XY plane shows the least variation and has a maximum at 140° and minimum at 40°.

Saturating the samples results in an increase in P-wave velocity of approximately 7% for all orientations (Fig. 5.7a) while S-wave velocity remains approximately the same (Fig. 5.7b). The calculated anisotropy parameters confirm that for both P- and S-wave anisotropy is greatest in the XZ and YZ planes and least in the XY plane, at approximately 9% and 4.5% respectively (Table 5.3).

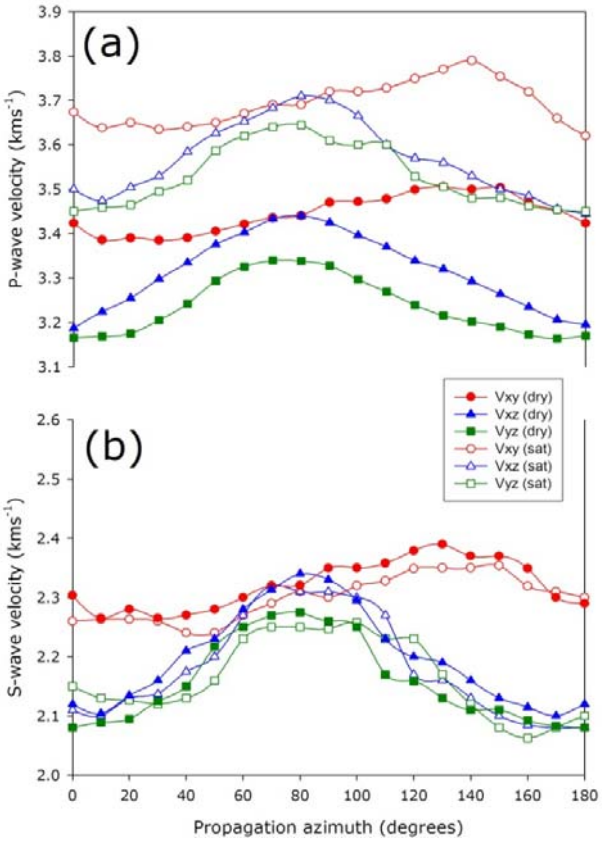

Figure 5.7. (a) P-wave and (b) S-wave velocities for DDS under oven-dry (filled shapes) and water-saturated (unfilled shapes) conditions.

		Velocity (kms^{-1})		Anisotropy parameter (%)		
		Average	Std. Dev.	YZ plane	XZ plane	XY plane
Dry	**Vp**	3.332	0.173	5.45	7.43	3.49
	Vs	2.236	0.164	9.04	10.92	5.39
Saturated	**Vp**	3.596	0.193	5.52	7.42	4.60
	Vs	2.215	0.139	8.22	11.00	4.95

Table 5.3. Ultrasonic wave velocity data summary for DDS.

5.5.3.2 Etna basalt

The benchtop ultrasonic velocity variation with azimuth for EB is shown in Fig. 5.8 and Table 5.4. EB shows no variation of P- or S-wave velocity with azimuth for both dry and saturated conditions, therefore, EB is perfectly isotropic.

P-wave velocity increases only very modestly on saturation, due to its low porosity (Fig. 5.8a). S-wave velocity is again unaffected (Fig. 5.8b). The calculated anisotropy parameters confirm that EB demonstrates an ultrasonic velocity isotropy (Table 5.4).

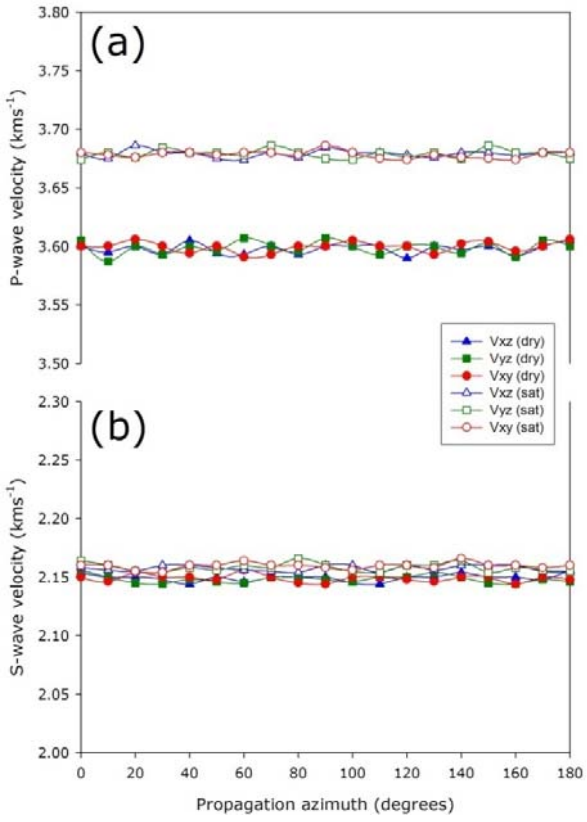

Figure 5.8. (a) P-wave and (b) S-wave velocities for EB under oven-dry (filled shapes) and water-saturated (unfilled shapes) conditions.

		Velocity (kms^{-1})		Anisotropy parameter (%)		
				YZ plane	XZ plane	XY plane
		Average	Std. Dev.			
Dry	**Vp**	3.599	0.008	0.417	0.445	0.361
	Vs	2.145	0.007	0.464	0.465	0.558
Saturated	**Vp**	3.679	0.007	0.321	0.345	0.326
	Vs	2.158	0.004	0.347	0.336	0.273

Table 5.4. Ultrasonic wave velocity data summary for EB.

5.6 Anisotropy of Magnetic Susceptibility (AMS) analysis

5.6.1 Introduction

Typically, AMS has mainly been used to determine the magnetic anisotropy of a dry rock matrix (mAMS). More recently [Pfleiderer and Halls, 1990; 1994; Hrouda *et al.*, 2000; Benson *et al*., 2003; 2005; Baud *et al.*, 2005] this method has been adapted to measure the void space anisotropy (pAMS) together with the mAMS (defined as the tAMS) by vacuum-saturating samples in a highly susceptible magnetic fluid or 'ferrofluid'. In this way we can accurately investigate the bulk pore space volume, shape and alignment.

5.6.2 Preparation of samples

The use of perfectly spherical samples is the most effective way to assess the anisotropy of a physical property of a rock in the laboratory [Vickers and Thill, 1969; Hrouda *et al*., 1993]. Unfortunately, owing

to the difficulty in producing spherical samples, cylindrical cores most accurately represent a sphere are used. The samples used were 25 mm in diameter and 22 mm in length, equating to a length/diameter ratio of 0.88 (Fig. 5.9). This is the standard geometry used in palaeomagnetic studies as it minimizes the shape dependent demagnetizing effect observed in samples with high intensity magnetization [Pfleiderer and Halls, 1990; Tarling and Hrouda, 1993].

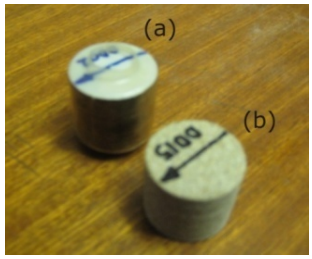

Figure 5.9. Photograph of samples of DDS prepared for AMS analysis (a) ferrofluid saturated sample (b) dry sample.

Multiple 25 mm diameter cores were taken from each of the orientated sample blocks. All of the coring took place along the Z-axis (see Fig. 5.1), since, after rotating resultant vectors into a common reference plane, principle pAMS directions show no direction dependence [Benson *et al*., 2003]. The cores were then cut to a 22mm length using a specially designed saw consisting of dual diamond impregnated circular saws with a 22mm separation between them. Each of the samples was carefully marked up with respect to their orientation to the block (Fig. 5.9b). After the dry mAMS measurements had been taken, the samples were then vacuum-saturated for 12 hours for DDS and 24 hours for EB with a highly susceptible ferrofluid EMG-905, comprising of a colloidal suspension of nano-particles (10 nm mean diameter) of magnetite in a light mineral oil carrier fluid. The nano-particles are coated with a stabilizing agent to prevent agglomeration and remain in suspension via Brownian motion. Due to their high porosities and low initial bulk susceptibilities, the ferrofluid used to saturate DDS was further diluted using additional carrier fluid to the ratio of one part ferrofluid to five parts carrier fluid. Thus keeping the

bulk susceptibility within a measurable range and minimising demagnetization effects. For EB no dilution was necessary owing to its low porosity and high initial bulk susceptibility.

It is of paramount importance to ensure that the ferrofluid remains in the pore space during the measurement process. Not only to produce the most accurate dataset possible but any contamination of the ferrofluid into the KLY-2 susceptibility bridge would be potentially very detrimental to future measurements. Firstly, each sample was wrapped in cling film immediately after removal from the vacuum bell jar. Secondly, 25mm diameter thin plastic discs were placed on both ends of the sample. The discs were correctly marked up to maintain the orientation of the sample. Finally, the sample was placed inside clear plastic heat shrink tubing which was shrink-fitted onto the sample using a heat gun (Fig. 5.9a).

5.6.3 Methodology

Magnetic susceptibility measurements were performed on a KappaBridge KLY-2 (AGICO Instruments) using the automated computer program Aniskly2. First, the KappaBridge was calibrated using the calibration stick ETALON 140 and the susceptibility of the sample holder measured and entered into Aniskly2 in order to nullify its contribution. Each sample was then measured in 15 different orientations allowing the statistical evaluation of errors in the three principle orientations (Fig. 5.10). To calculate the principal susceptibility axes, Aniskly2 used a least-squares method to fit a magnetic susceptibility ellipsoid to the data [Jelinek, 1978].

Samples were measured dry first to obtain the mAMS and then measured after ferrofluid saturation to obtain tAMS, the pAMS simply calculated by subtracting the mAMS from the tAMS. For DDS this process

is unnecessary since mAMS values are several orders of magnitude lower than the standard deviation of the tAMS values, in this case mAMS values can be neglected [Benson *et al.*, 2003].

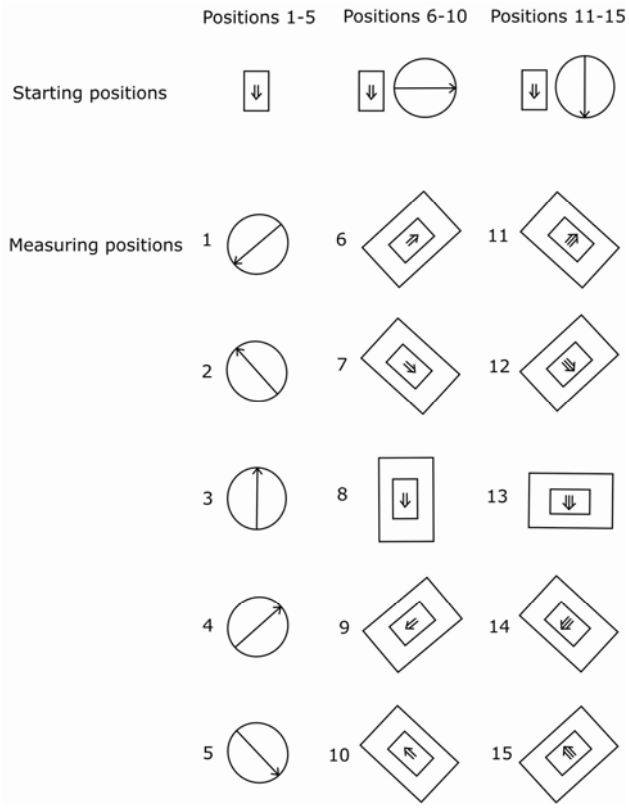

Figure 5.10. Diagram showing the 15 different sample orientations used during the measurement of each sample.

5.6.4 Results

The average mAMS and tAMS values, and resultant pAMS value for EB, for the two rock types are presented in Table 5.5. The mAMS values are much higher in EB than DDS due to the numerous magnetic minerals present within the matrix. As expected, the values for the tAMS are higher than the

mAMS in each case due to the incorporation of magnetic ferrofluid into the pores and cracks present within the rock.

Rock type	Bulk susceptibility of dry matrix (mAMS) (χ), x 10^{-6} SI	Bulk susceptibility of ferrofluid saturated sample (tAMS) (χ), x 10^{-6} SI	Bulk susceptibility of void space (pAMS) (χ), x 10^{-6} SI
Darley Dale sandstone	38.75 ± 1.55	45558 ± 8683	45558
Etna basalt	48964 ± 5745	103990 ± 10842	55026

Table 5.5. Average mAMS, tAMS and pAMS values for DDS and EB. pAMS values for DDS are deemed unnecessary since mAMS values are several orders of magnitude lower than the standard deviation of the tAMS values (see text and [Benson *et al.*, 2003] for details).

5.6.4.1 Darley Dale sandstone

The mAMS and tAMS principal directions obtained from AMS measurements on DDS are shown in Fig. 5.11. In this case, due to the very low initial magnetic susceptibility of the matrix, tAMS is assumed to be approximately equal to pAMS. The mAMS plot in Fig. 5.11a shows that, apart from the minimum direction forming a tight cluster aligned along the Z-axis of the co-ordinate frame, there are no distinct populations within the data. This is likely to be due to the very low bulk susceptibility of the dry matrix. However, observable relationships between the principal directions become more prominent in the tAMS plot (Fig. 5.11b). The minimum direction forms a very tight cluster for the tAMS measurements and aligns along the Z-axis of the co-ordinate frame (see Fig. 5.1). The maximum and intermediate directions are orientated approximately at 90° to each other and are within the same plane; they also lie at approximately 90° to the tAMS minimum direction.

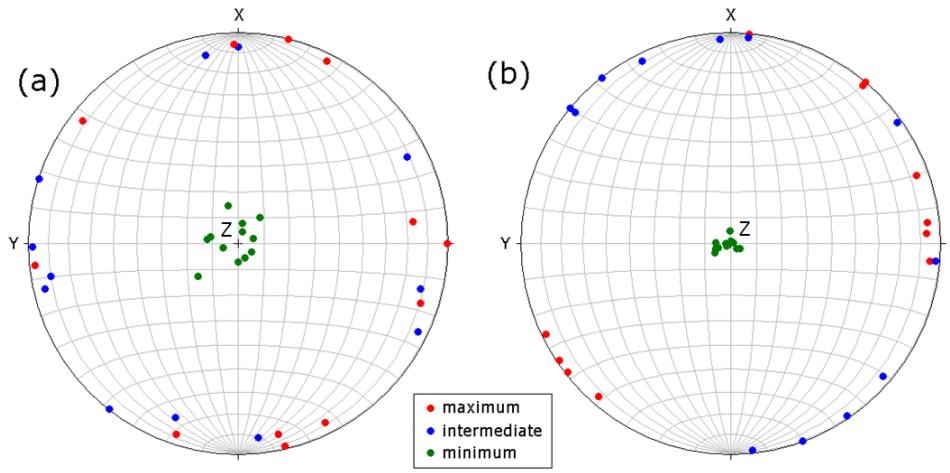

Figure 5.11. Stereographic projections of the principal ellipsoid directions for (a) mAMS and (b) tAMS for DDS.

The pore fabric anisotropy data can be presented graphically on a Flinn plot [1962] (Fig. 5.12). This allows the relationship between the lineation (*L*) and the foliation (*F*) to be observed allowing the shape of the pore space to be determined. Lineation is defined as the ratio of the maximum to the intermediate principal axis, and foliation is defined as the ratio of the intermediate to the minimum principal axis. For ellipsoids, the values of lineation and foliation reflect the extent to which the overall shape of the void space is oblate or prolate. Fig. 5.12 shows that the lineation vs. foliation data form a tight cluster within the oblate fabric field, the fabric expected for a sedimentary rock formed by the settling of grains in suspension. An anisotropy factor can be derived from the AMS data in the same way as for the anisotropy of ultrasonic wave velocity measurements (Equation [5.2]) and is presented in Table 5.6. The average anisotropy for DDS, calculated from AMS data, is 3.92% and 2.66% for mAMS and tAMS respectively.

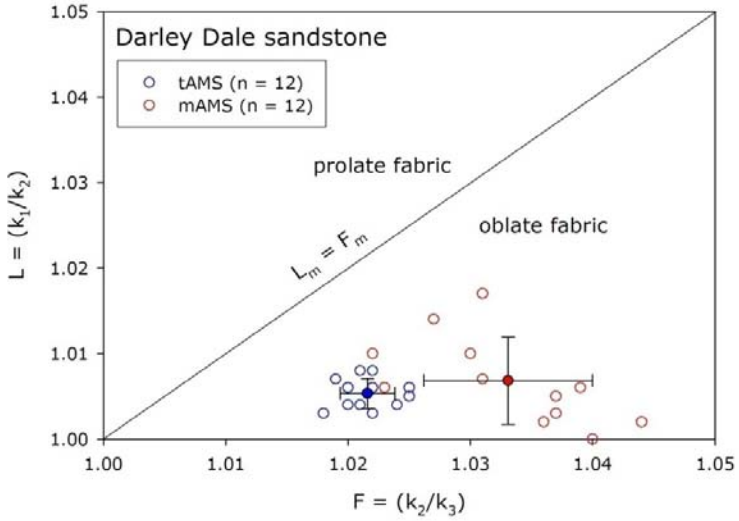

Figure 5.12. Flinn plot of lineation vs. foliation for both tAMS (blue open circles) and mAMS (red open circles) measurements for DDS. Solid circles represent the mean lineation and foliation for each type of measurement, with associated error.

	Bulk susceptibility (χ), x 10^{-6} SI	Principal axis length (normalized bulk susceptibility)			Anisotropy parameters		
		Max	Int	Min	F	L	(A %)
mAMS							
Average	37.75	1.015	1.008	0.976	1.033	1.007	3.92
Standard deviation	1.55	0.003	0.004	0.004	0.007	0.005	0.53
Minimum	35.21	1.011	1.004	0.973	1.022	1.000	2.80
Maximum	39.88	1.022	1.013	0.983	1.044	1.017	4.79
pAMS							
Average	45558	1.011	1.005	0.984	1.022	1.005	2.66
Standard deviation	8683	0.002	0.001	0.002	0.002	0.002	0.30
Minimum	31370	1.008	1.004	0.982	1.018	1.003	2.41
Maximum	58270	1.012	1.007	0.988	1.025	1.008	3.06

Table 5.6. Summary of the AMS data for DDS that includes an average, standard deviation, minimum and maximum for the bulk susceptibility, principal axis lengths and anisotropy factors.

4.6.4.2 Etna basalt

The mAMS and tAMS principal directions obtained from AMS measurements on EB are shown in Fig. 5.13. The mAMS plot in Fig. 5.13a shows that the minimum, intermediate and maximum directions form tight clusters. This is likely to be due to the flow orientation of the magnetic particles in the lava as it cooled. However, there are no observable relationships between the principal directions in the tAMS plot (Fig. 5.13b). The flow orientation relationship has been completely overprinted by the undiluted ferrofluid that now resides in the pre-existing network of thermal cracks in the rock [Vinciguerra *et al.*, 2005]. This cracking has been shown to be almost perfectly isotropic in the presented ultrasonic velocity data (see **5.5 Benchtop ultrasonic wave velocity analysis**) and by Vinciguerra *et al.* [2005]. The lack of any relationship in the tAMS data here (Fig. 5.13b) agrees with this hypothesis.

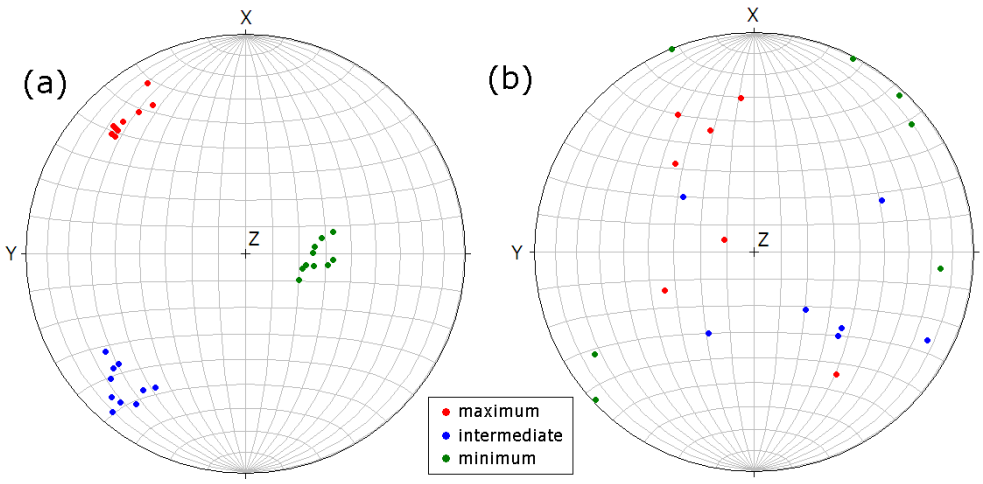

Figure 5.13. Stereographic projections of the principal ellipsoid directions for (a) mAMS and (b) tAMS for EB.

The pore fabric anisotropy data can be presented graphically on a Flinn plot [1962] (Fig. 5.14). The mAMS data all lie within the oblate fabric field, showing the shape of the magnetic grains that exist within the rock. The average for the tAMS data lies almost on the lineation equals foliation line

confirming that the void space, the network of thermal cracks [Vinciguerra *et al.*, 2005], is isotropic. The anisotropy factor derived from the AMS data, (using Equation [5.2]) is presented in Table 5.7. The average anisotropy for EB, calculated from AMS data, is 2.02% and 2.57% for mAMS and tAMS respectively.

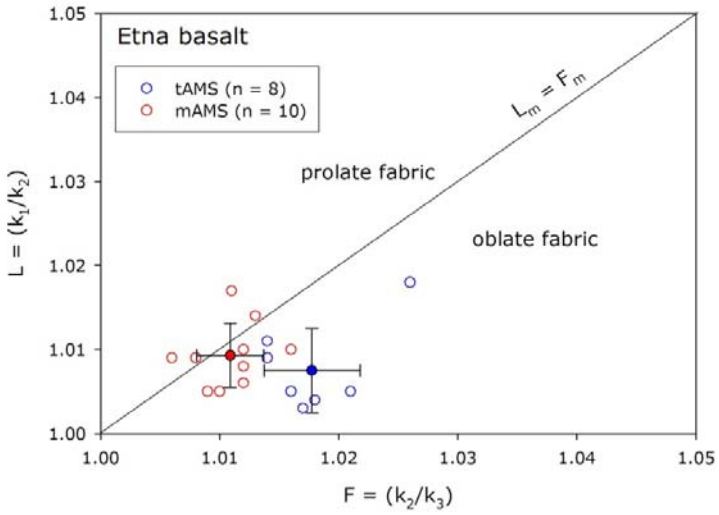

Figure 5.14. Flinn plot of lineation vs. foliation for both tAMS and mAMS measurements for Etna basalt. Solid symbols represent the mean lineation and foliation for each type of measurement, with associated error.

	Bulk susceptibility (χ), x 10^{-6} SI	**Principal axis length (normalized bulk susceptibility)**			**Anisotropy parameters**		
		Max	**Int**	**Min**	**F**	**L**	**(A %)**
mAMS							
Average	48964	1.010	1.001	0.990	1.011	1.009	2.02
Standard deviation	5745	0.003	0.001	0.002	0.003	0.004	0.52
Minimum	41920	1.007	0.998	0.987	1.006	1.005	1.49
Maximum	56230	1.015	1.002	0.992	1.016	1.017	2.84
pAMS							
Average	103990	1.011	1.003	0.986	1.018	1.008	2.57
Standard deviation	10842	0.004	0.002	0.004	0.004	0.005	0.80
Minimum	92370	1.008	1.002	0.985	1.014	1.003	2.07
Maximum	120400	1.020	1.005	0.988	1.026	1.018	4.34

Table 5.7. Summary of the AMS data for EB that includes an average, standard deviation, minimum and maximum for the bulk susceptibility, principal axis lengths and anisotropy factors.

5.7 Comparison of ultrasonic velocity measurements and AMS measurements

The two sets of data can be directly compared by converting azimuthal ultrasonic wave velocity data to an ellipsoid using a least-squares method [as in Benson *et al.*, 2005]. This calculation has been performed for the azimuthal P-wave velocities on dry samples only. The data is presented in Table 5.8 and has been plotted alongside tAMS data on stereographic projections in Fig. 5.15. Fig. 5.15 shows that the principal ellipsoid directions for both the tAMS and ultrasonic velocity data are in good agreement. From these data, the anisotropy has been calculated (using Equation [5.2]) to be 9.34 and 0.07 for DDS and EB respectively.

		Average principal anisotropy axes		
		Velocity kms^{-1}	**Trend degrees**	**Plunge degrees**
Darley Dale sandstone	**Maximum**	3.484	28.8	0.1
	Intermediate	3.356	241.2	5.3
	Minimum	3.173	60.2	84.7
Etna basalt	**Maximum**	3.600	87.1	63.1
	Intermediate	3.598	359.2	1.1
	Minimum	3.597	90.3	26.9

Table 5.8. Summary of the principal anisotropy axes for dry P-wave velocity ellipsoids of both DDS and EB (courtesy of P. Benson).

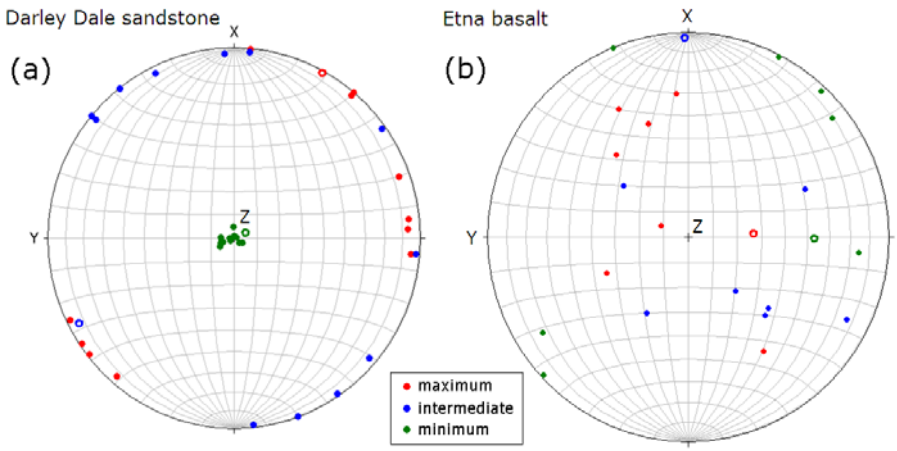

Figure 5.15. Stereographic projections of the tAMS principal ellipsoid directions (filled circles) and dry P-wave velocity principal ellipsoids (hollow circles) for (a) DDS and (b) EB.

5.8 Brief characterization of other rock types used in this study

5.8.1 Bentheim sandstone

Bentheim sandstone (BHS) is a white-yellow, quartz-rich sandstone (quartz arenite) from a well-known outcrop near the village of Bentheim, north-west Germany. In outcrop, BHS contains large-scale bedding (Fig. 5.16d). However, in hand specimen it appears very homogeneous and there is no distinct layering or lamination. The mineralogy of BHS, obtained by X-ray diffraction, consists of 95% quartz, 3% kaolinite and 2% orthoclase feldspar [Klein *et al.*, 2001]. The quartz grains are colourless in PPL and exhibit low 1st order interference colours in XPL (Figs. 5.16a and 5.16b). The porosity of the BHS used in this study, measured using the method outlined in **5.4 Porosity calculation**, is 24.3 ± 1.2%.

Optical and SEM analysis demonstrated that the grains are round to sub-round and are 50-500 µm in diameter (Figs. 5.16a, 5.16b and 5.16c). BHS is well sorted, moderately compacted in places (since some

quartz grains have been welded to their neighbours or even penetrate them slightly) and has no discernable preferred alignment of grains (Figs. 5.16a, 5.16b and 5.16c). The sediment is poorly-cemented so that a substantial pore space remains and grains are easily identifiable and contain very little clay overgrowth (Fig. 5.16c). Even in an undeformed state, intragranular microcracks (present as fluid inclusion planes) can be seen in some quartz grains and others exhibit moderate undulose extinction.

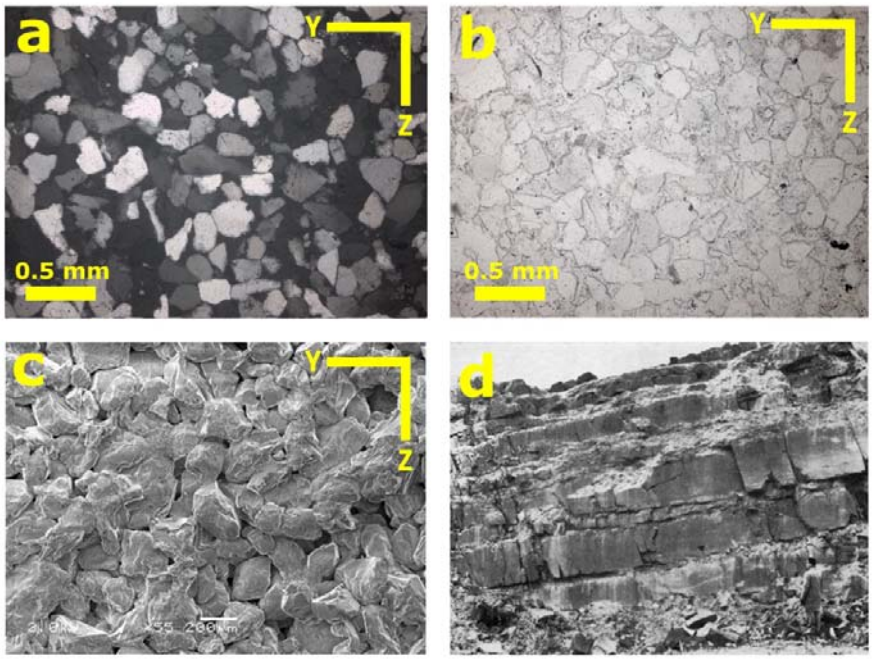

Figure 5.16. (a) Photomicrograph of undeformed Bentheim sandstone under cross-polarized light (b) Photomicrograph of undeformed Bentheim sandstone under plane-polarized light (c) SEM image of an uncoated sample of undeformed Bentheim sandstone at x55 magnification (d) Photograph from the quarry in Germany showing the large-scale bedding in Bentheim sandstone. Man for scale [taken from Kemper, 1976].

The benchtop ultrasonic velocity variation with azimuth for BHS is shown in Fig. 5.17 and Table 5.9. BHS exhibits a systematic P- and S- wave variation with azimuth for all orientations, this has been observed in previous studies on BHS [Louis *et al.*, 2003]. Planes XZ and YZ show the greatest variation with azimuth

and have a ultrasonic velocity maximum at approximately 90° and minimum and both 0° and 180°. The XY plane shows the least variation and displays the opposite maximum and minimum trend to the XZ and YZ planes. Saturating the samples results in an increase in P-wave velocity of approximately 10% for all orientations (Fig. 5.17b). The saturated S-wave velocity shows very little change due to the fact that liquids do not support shear mode displacement (Fig. 5.17b). The calculated anisotropy parameters confirm that for both P- and S-wave anisotropy is greatest in the XZ and YZ planes and least in the XY plane (Table 5.9).

		Velocity (kms^{-1})		Anisotropy parameter (%)		
				YZ plane	XZ plane	XY plane
		Average	Std. Dev.			
Dry	**Vp**	3.327	0.118	5.44	4.95	2.51
	Vs	2.165	0.034	4.37	3.74	2.50
Saturated	**Vp**	3.627	0.175	4.71	4.56	2.98
	Vs	2.201	0.056	3.49	4.84	2.42

Table 5.9. Ultrasonic wave velocity data summary for BHS.

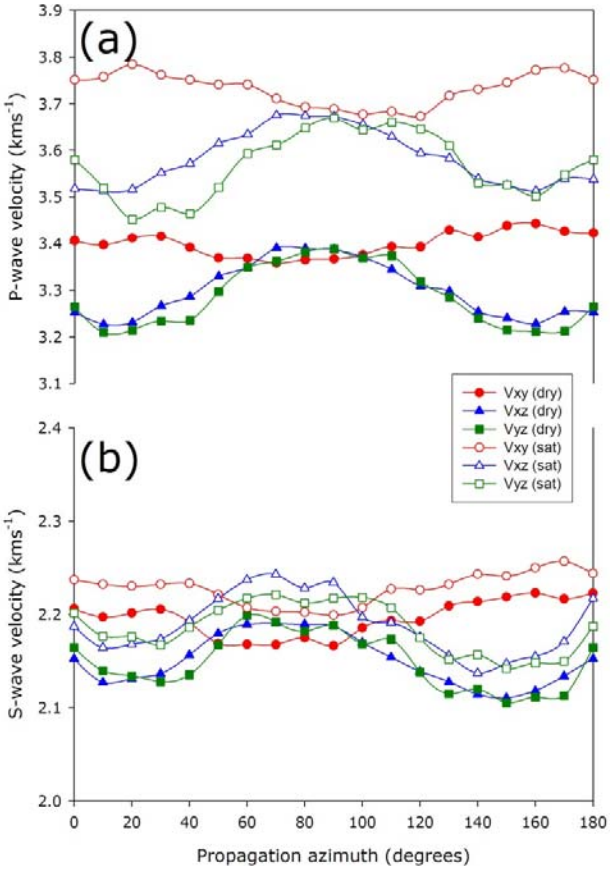

Figure 5.17. Benchtop (a) P-wave and (b) S-wave velocities for BHS under oven-dry (filled shapes) and water-saturated (unfilled shapes) conditions.

5.8.2 Crab Orchard sandstone

Crab Orchard sandstone (COS) is a white-pink, fine-grained fluvial sandstone from the Cumberland Plateau, Tennessee (USA). COS contains very distinct pink and orange layering in hand specimen and consists of 85% quartz with feldspar (10%) and iron-rich clays (5%). The cement of sericitic clay and mica is abundant and has significantly reduced the original porosity (Fig. 5.18c). The porosity of the COS used in this study, measured using the method outlined in **5.4 Porosity calculation**, is 3.3 ± 0.17%. The quartz grains are colourless in PPL and exhibit low 1st order interference colours in XPL (Figs. 5.18a and 5.18b).

Optical and SEM analysis demonstrated that the grains are generally sub-rounded and are on average 300 µm in diameter (Figs. 5.18a, 5.18b and 5.18c).

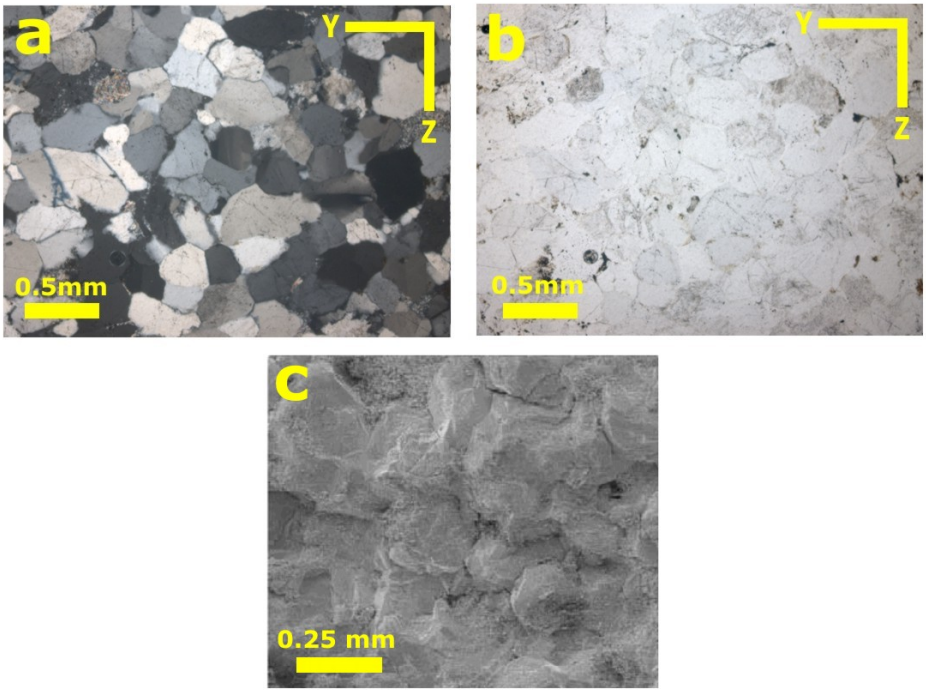

Figure 5.18. (a) Photomicrograph of undeformed COS under cross-polarized light. (b) Photomicrograph of undeformed Crab Orchard sandstone under plane-polarized light. (c) SEM image of a sample of undeformed Crab Orchard sandstone (taken from [Benson *et al.*, 2005]).

The benchtop ultrasonic velocity variation with azimuth for COS is shown in Fig. 5.19 and Table 5.10. COS exhibits a strong systematic P- and S- wave variation with azimuth for all orientations. Planes XZ and YZ show the greatest variation with azimuth and have a ultrasonic velocity maximum at approximately 90° and minimum and both 0° and 180°. The XY plane shows the least variation and displays the opposite maximum and minimum trend to the XZ and YZ planes. Saturating the samples results in an increase in P-wave velocity of approximately 10% for all orientations (Fig. 5.19b). The saturated S-wave velocity shows very little change due to the fact that liquids do not support shear mode displacement

(Fig. 5.19b). The calculated anisotropy parameters confirm that for both P- and S-wave anisotropy is greatest in the XZ and YZ planes and least in the XY plane (Table 5.10).

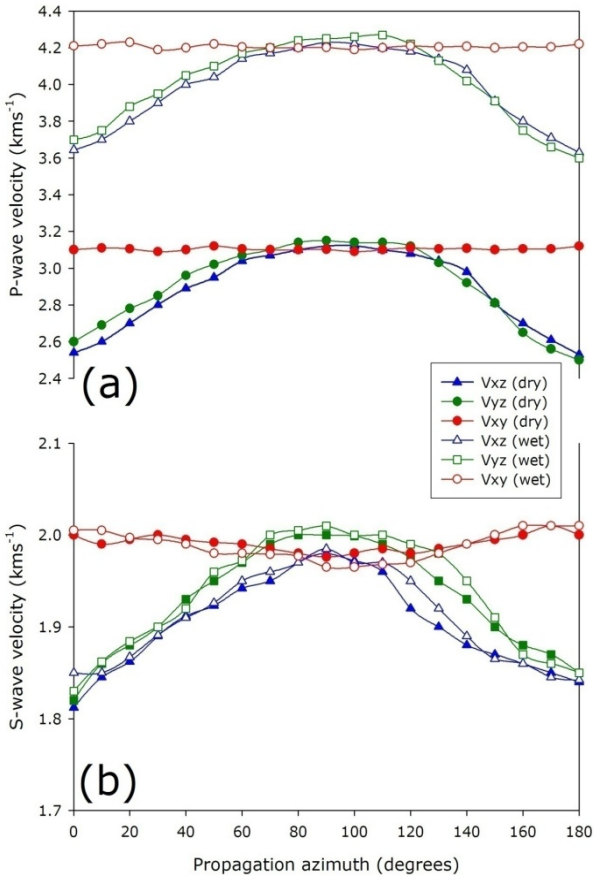

Figure 5.19. Benchtop (a) P-wave and (b) S-wave velocities for COS under oven-dry (filled shapes) and water-saturated (unfilled shapes) conditions.

		Velocity (kms^{-1})		Anisotropy parameter (%)		
		Average	Std. Dev.	YZ plane	XZ plane	XY plane
Dry	**Vp**	2.965	0.148	22.36	20.53	0.97
	Vs	1.941	0.039	8.83	9.33	1.71
Saturated	**Vp**	4.065	0.150	16.73	15.06	0.95
	Vs	1.944	0.043	7.49	9.05	2.01

Table 5.10. Ultrasonic wave velocity data summary for COS.

5.8.3 Stromboli basalt

Stromboli basalt (SB) from Mt. Stromboli, Italy, is light-grey and contains many dark grey and white, angular randomly distributed phenocrysts. The samples are from the most-recent Neostromboli lava flow unit [see Fig. 2 in Apuani *et al.*, 2005]. From optical microscopy, SB contains a fine-grained matrix embedded with large phenocrysts of plagioclase, olivine and pyroxene varying from 200-2500 μm in diameter that show no discernable preferential alignment (Fig. 5.20). SB is composed of a groundmass of fine-grain matrix (~50%) that includes crystals of feldspar (35%), pyroxene (10%) and olivine (5%) (Figs. 5.20a and b). The plagioclase (low 1^{st} order interference colours in XPL) is mostly rectangular in shape and regularly displays albite twinning. The olivine can be easily recognized by its high relief and high birefringence in XPL (high 2^{nd} and 3^{rd} order interference colours). Olivine grains are heavily traversed by randomly orientated microcracks. The pyroxene show yellow-brown interference colours in XPL. The porosity of the SB used in this study, measured using the method outlined in **5.4 Porosity calculation**, is 3.7 ± 0.26%. Unfortunately, due to the limited availability of sample material, a comprehensive ultrasonic velocity analysis could not be undertaken. To prevent direct comparisons

between complete and incomplete datasets, the ultrasonic velocity data from SB will not be presented in tabular form. It is clear however that SB does exhibit a seismic anisotropy and, in the XZ plane only, exhibits an average dry P- and S-wave velocity of 4.44 and 3.42 kms^{-1} respectively (Fig. 5.21).

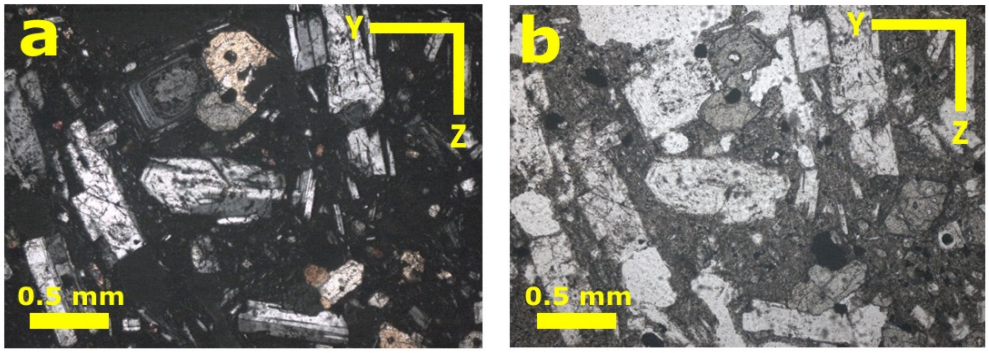

Figure 5.20. (a) Photomicrograph of undeformed Stromboli basalt under cross-polarized light. (b) Photomicrograph of undeformed Stromboli basalt under plane-polarized light.

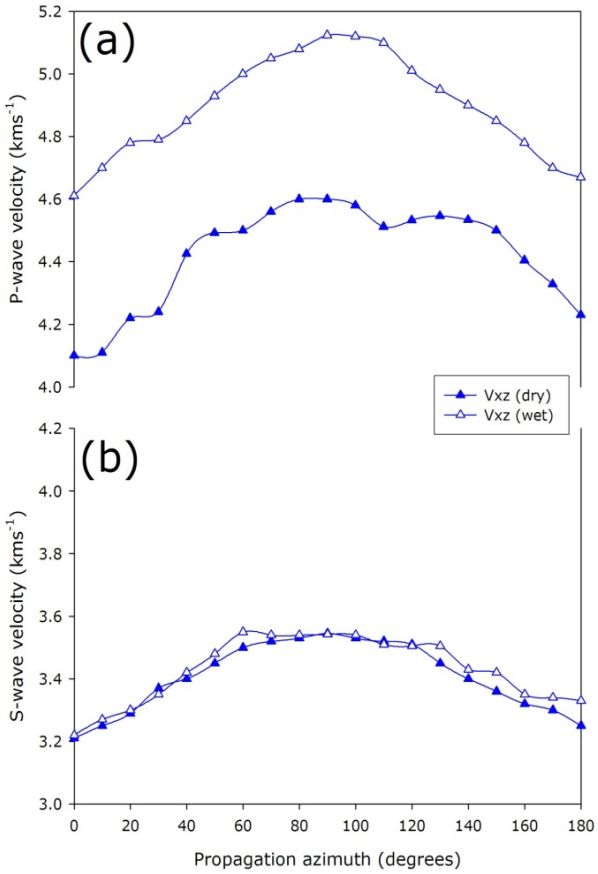

Figure 5.21. Benchtop (a) P-wave and (b) S-wave velocities for SB under oven-dry (filled shapes) and water-saturated (unfilled shapes) conditions.

5.9 Summary

A summary of the rock characterization is given in Table 5.11.

Rock type	Bentheim sandstone	Darley Dale sandstone	Crab Orchard sandstone	Etna basalt	Stromboli basalt
Modal composition	95% quartz, 3% kaolinite, 2 % orthoclase feldspar	69% quartz, 26% feldspar, 3% clay, 2% mica	85% quartz, 10% feldspar and 5% clay	Fine-grained matrix (~60%) that includes crystals of feldspar (25%), pyroxene (8.5%) and olivine (4%)	Fine-grained matrix (~50%) that includes crystals of feldspar (35%), pyroxene (10%) and olivine (5%)
Porosity (%)	23.4 ± 1.2	13.3 ± 0.8	3.3 ± 0.17	4.3 ± 0.20	6.7 ± 0.26
Grain size (µm)	50-500	100-800	100-500	Fine-grained matrix with large phenocrysts (200-2500)	Fine-grained matrix with large phenocrysts (200-2500)
Mean P-wave velocity (kms^{-1})	3.33 (dry) 3.63 (wet)	3.32 (dry) 3.60 (wet)	2.97 (dry) 4.07 (wet)	3.60 (dry) 3.68 (wet)	4.44 (dry and in XZ plane only)
Mean S-wave velocity (kms^{-1})	2.18	2.23	1.94	2.15	3.42 (in XZ plane only)
Maximum Vp anisotropy factor	5.44	7.43	22.36	0.45	10.59 (dry and in XZ plane only)

Table 5.11. Summary of the rock characterization for all the rock types used in this study.

Chapter six

6. The influence of crack damage on rock caused by stress-cycling

6.1 Introduction

This chapter presents results from a suite of increasing-amplitude, stress-cycling experiments performed on four different rock types. The experiments were devised to investigate: (1) the influence of an increasing level of microcrack damage on the evolution of static elastic moduli, and (2) to observe the acoustic emission (AE) output behaviour of rock during stress-cycling. The chapter first introduces the experiments materials and methods. The mechanical data from both constant strain rate and stress-cycling experiments are then presented, together with microstructural observations of the deformed samples.

6.2 Materials investigated

The main rock types investigated in this part of the study are Etna basalt (EB) and Darley Dale sandstone (DDS). However, for the purposes of comparison, another extrusive lava flow basalt from Mt. Stromboli, Italy (SB) and a quartz-rich, high-porosity sandstone from Bentheim, Germany (BHS) were also studied. Details on the characterization of all the rock types used in this study can be found in Chapter Five.

6.3 Experimental methodology

All experiments were performed on the uniaxial compression apparatus (for details see Chapter Four, section **4.2 The uniaxial compression apparatus**) situated in the Rock & Ice Physics Laboratory (RIPL), University College London. All samples were prepared for use in the uniaxial compression apparatus and water-saturated/oven-dried as outlined in **5.2 Rock sample preparation**. During experimentation, axial and radial strains were continuously monitored throughout each experiment using LVDT displacement

transducers (see Chapter Four, section *4.2.3 Sample assembly and auxiliary measurements*). AE hits and energy were recorded by a piezoelectric transducer located inside the bottom anvil using the MISTRAS-2001 recording system (see Chapter Four, section *4.4.2 AE data recording systems and logging software*).

Before stress-cycling experiments could be performed a series of constant strain rate experiments on both DDS and EB were untaken in order to establish their short-term, unconfined compressive strength (UCS). The average UCS for both EB and DDS were taken into account to devise the number and amplitude of the cycles that would be feasible during experimentation. Oven-dry (hereafter referred to as 'dry') and water-saturated (hereafter referred to as 'wet') samples of each rock type were loaded under a constant strain rate of 7.0×10^{-6} s^{-1} until failure. The strain rate, which is slightly slower than that of a conventional constant strain rate experiment (1.0×10^{-5} s^{-1}), was selected so that it was the same as that planned for the stress-cycling experiments. It is foreseen that, during stress-cycling experiments, a slower strain rate would allow the rock microstructure more time to equilibrate at the peak of each cycle. This strain rate is however not slow enough to make the experiments unfeasible on laboratory timescales.

Increasing-amplitude stress-cycling experiments were then performed on both dry and wet samples of DDS and EB, and also on dry samples of SB and BHS. In the first loading cycle, samples were loaded to a maximum stress of 20 MPa at a controlled strain rate of 7.0×10^{-6} s^{-1}, and then unloaded at the same rate to 8 MPa. In each subsequent cycle the maximum stress was increased by 10 MPa, and samples again unloaded to 8 MPa. Stress-cycling was continued in this way until samples eventually failed. After experimentation, each of the unloading portions of the stress-strain curves was separated and fitted with a third-order polynomial (Fig. 6.1). This polynomial was then differentiated, thus allowing the

gradient of the curve i.e. static Young's modulus to be calculated for each data point. The quasi-linear elastic portion, from where elastic moduli can be determined, was defined as the portion of the unloading stress-strain curve where the calculated gradients remained approximately constant for the longest duration (cross-hatched area, Fig. 6.1). The Young's modulus was then calculated as the gradient of this portion of the stress-strain curve. As a final check, *perfect elasticity* [see Heap and Faulkner, 2008] was monitored by comparing the gradients of the loading and unloading curves of a single cycle at the same stress interval. Where the gradients were the same, elasticity was assumed [see Heap and Faulkner, 2008 for more details] (shaded area, Fig. 6.1). Static Poisson's ratios were calculated from the axial and radial strains from exactly the same position as for the Young's modulus on each of the curves. A result of the outlined methodology is that the elastic moduli will be calculated for each of the curves at varying levels of differential stress, therefore an indication of the stress level at which each were calculated will be provided on the appropriate figures.

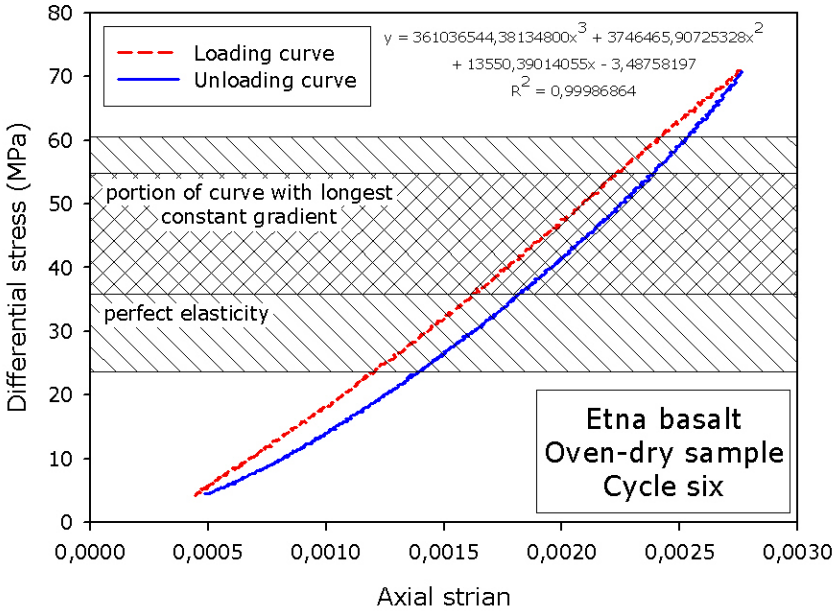

Figure 6.1. The loading (red dashed line) and unloading (blue solid line) curves for cycle six in an increasing-amplitude stress-cycling experiment on an oven-dry sample of EB (failed on the 13th cycle). The third-order polynomial fit for the unloading curve is shown in the top right of the figure. Shaded area – zone of *perfect elasticity* [see Heap and Faulkner, 2008] i.e. where the gradients of the loading and unloading curves are almost equal. Cross-hatched area – zone where the gradient of the unloading curve remained constant for the longest duration.

6.4 Results

6.4.1 Etna basalt experiments

6.4.1.1 Constant strain rate experiments

Fig. 6.2 shows representative stress-strain curves for curves for dry (Fig. 6.2a) and wet (Fig. 6.2b) samples of EB deformed at a constant strain rate until failure. The average UCS was 140 ± 6 and 120 ± 7 MPa for samples of dry and wet EB respectively. The reduction in UCS between dry and wet samples is

on the order of about 15%. The position of C', the departure from linear elastic behaviour, for both dry and wet samples was at approximately 36 MPa (Fig. 6.2).

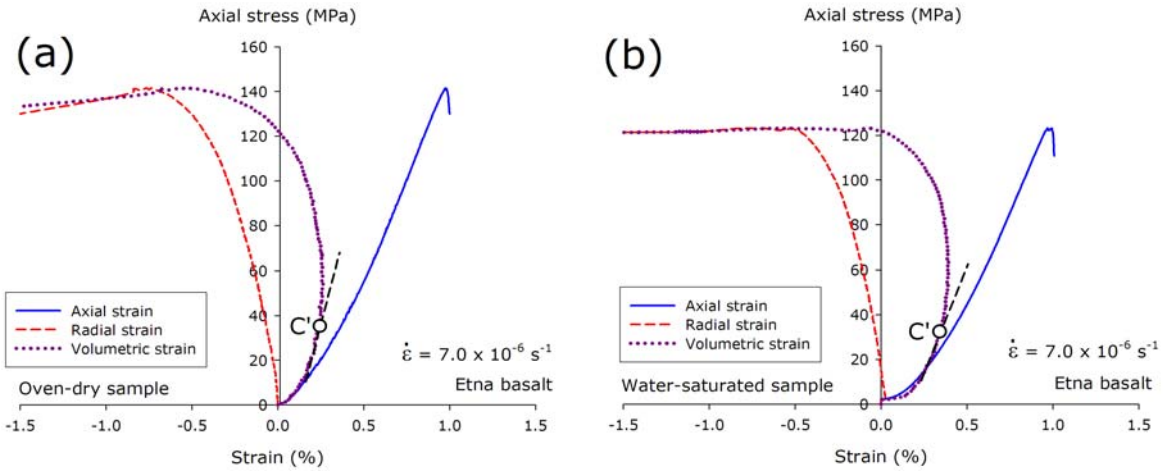

Figure 6.2. Stress-strain curves for constant strain rate experiments on (a) oven-dry EB [sample EB-25-09] and (b) water-saturated EB [sample EB-25-10] taken to failure under uniaxial compression. The strain rate for the experiment is indicated on the figure. The positions of C' are marked by the white circles.

6.4.1.2 Increasing-amplitude stress-cycling experiments

Fig. 6.3 shows representative stress-strain curves for dry (Fig. 6.3a) and wet (Fig. 6.3b) samples of EB that have undergone increasing-amplitude stress-cycling. It is apparent that the stress-strain response of the rock varies between loading cycles and is most easily seen in the radial strain curves. The rock becomes progressively more compliant in each cycle due to the increase in crack damage that leads to increasing amounts of irrecoverable strain.

Eventually the samples failed, generally by axial splitting as shown in Fig. 6.3c. In these experiments, the peak stress achieved did not change from dry to wet samples of EB; the peak stress for each of the

experiments shown (Fig. 6.3) was about 140 MPa, approximately the same as the UCS from a constant strain rate experiment on dry EB (Fig. 6.2a).

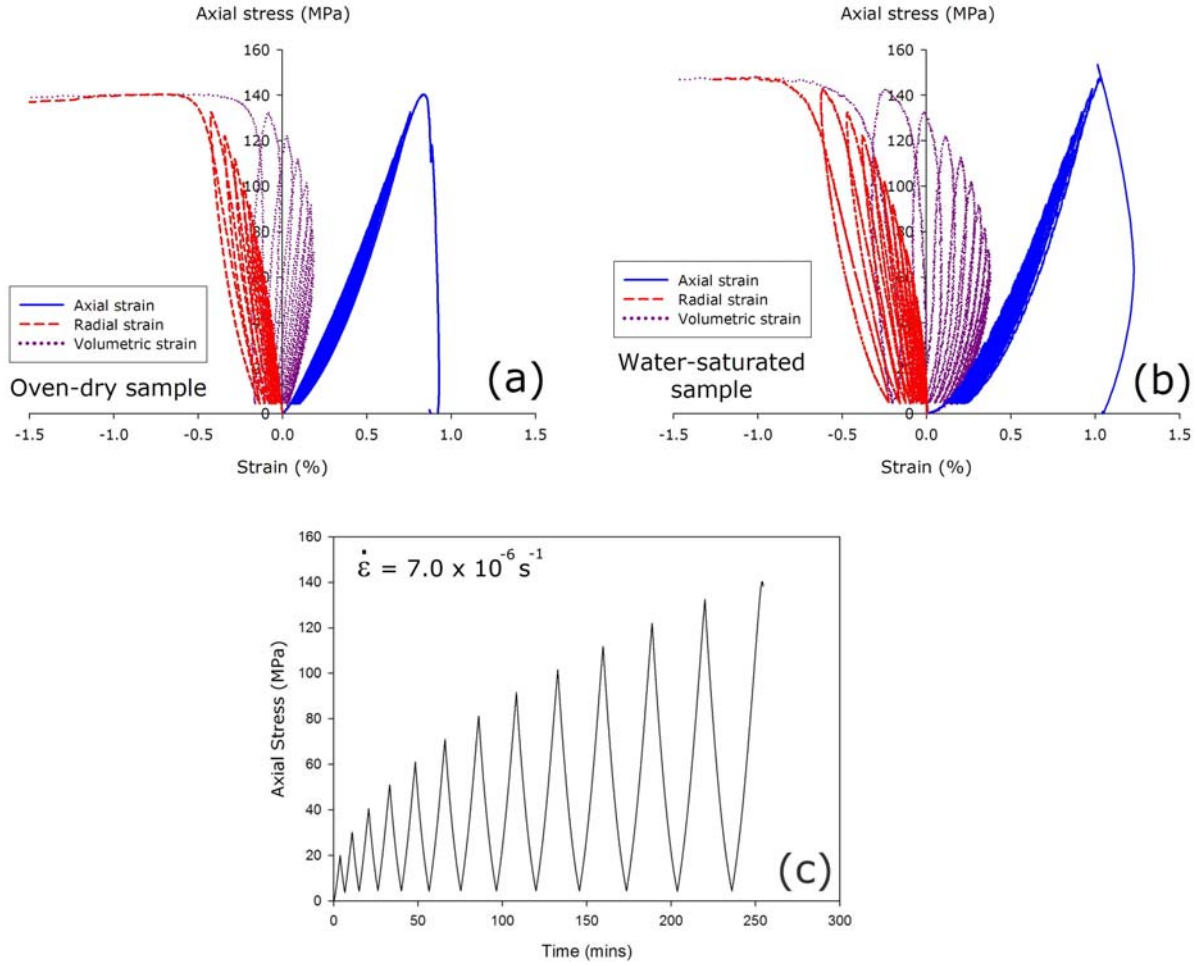

Figure 6.3. Representative axial and radial stress-strain curves for (a) oven dry and (b) water-saturated sample of EB under increasing-amplitude stress-cycling [samples EB-25-02 and EB-25-03] (c) Example of a loading path from an increasing-amplitude, stress-cycling experiment on a dry sample of EB that failed during the 13th loading cycle. The strain rate used during experimentation is indicated on the figure.

Fig. 6.4 shows the calculated values of Young's modulus and Poisson's ratio plotted against cycle number. The elastic response to cyclic stressing is similar for dry and wet samples of EB. In both cases,

Young's modulus is seen to decrease by about 30%, with Poisson's ratio increasing by 0.29. This corresponds to a Poisson's ratio increase by a factor of 2.5 and 3.0 for dry and wet samples respectively, due to their somewhat different starting values. Subsequent

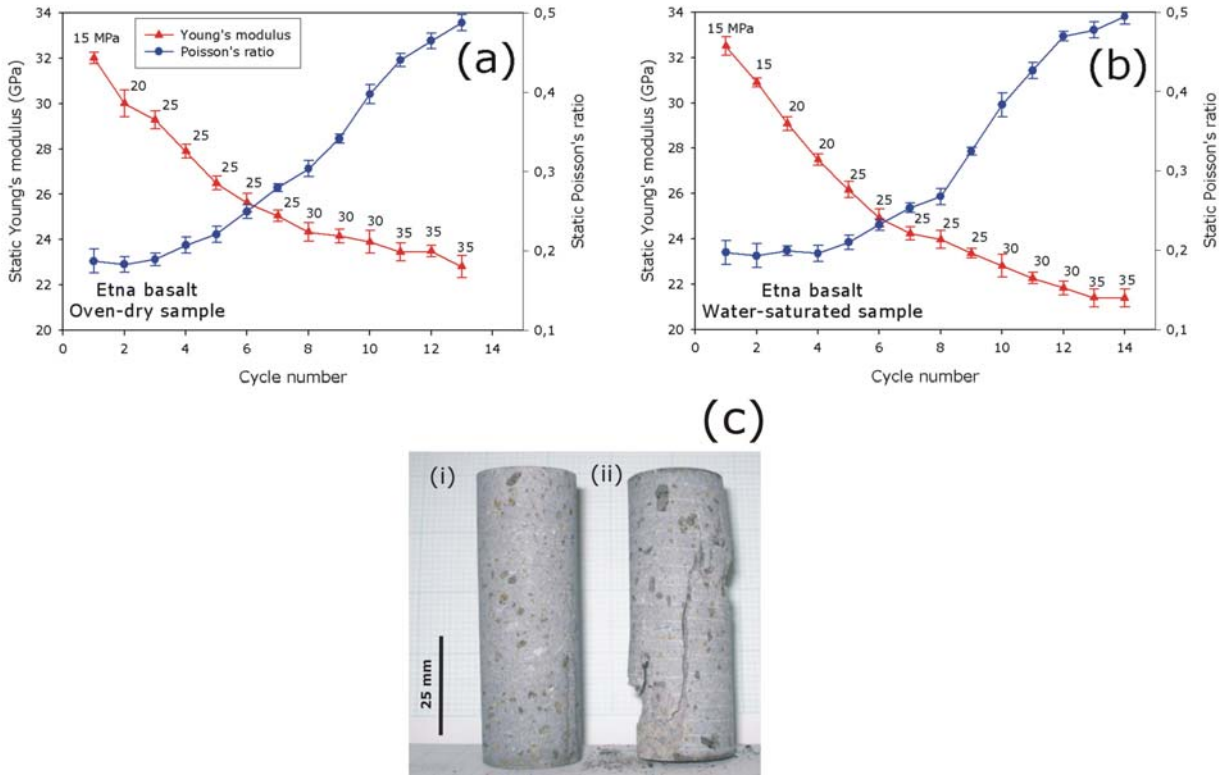

Figure 6.4. Static elastic moduli evolution with increasing cycles from increasing-amplitude stress-cycling experiments on (a) dry and (b) wet EB [samples EB-25-02 and EB-25-03] (c) Photographs of (i) an undeformed EB sample and (ii) a EB sample that failed by axial splitting after 14 cycles during an increasing-amplitude stress-cycling experiment [sample EB-25-02]. Values on each data point in (a) and (b) give an indication of the level of stress from where the static elastic moduli were calculated on the unloading curve of each cycle. Error bars indicate the variation in elastic moduli within the determined elastic portion of the unloading curves.

The position of C' can also be monitored during increasing-amplitude stress-cycling experiments (Fig. 6.5). The positions of C' were defined by the departure from linear elastic behaviour in the volumetric strain curves for each cycle (Fig. 6.5a). Fig. 6.5b demonstrates that, for a dry sample of EB, the position

of C’ remains roughly constant throughout the stress-cycling. The average position of C’ was found to be about 35 MPa, almost identical to that found during constant strain rate experiments (see Fig. 6.2).

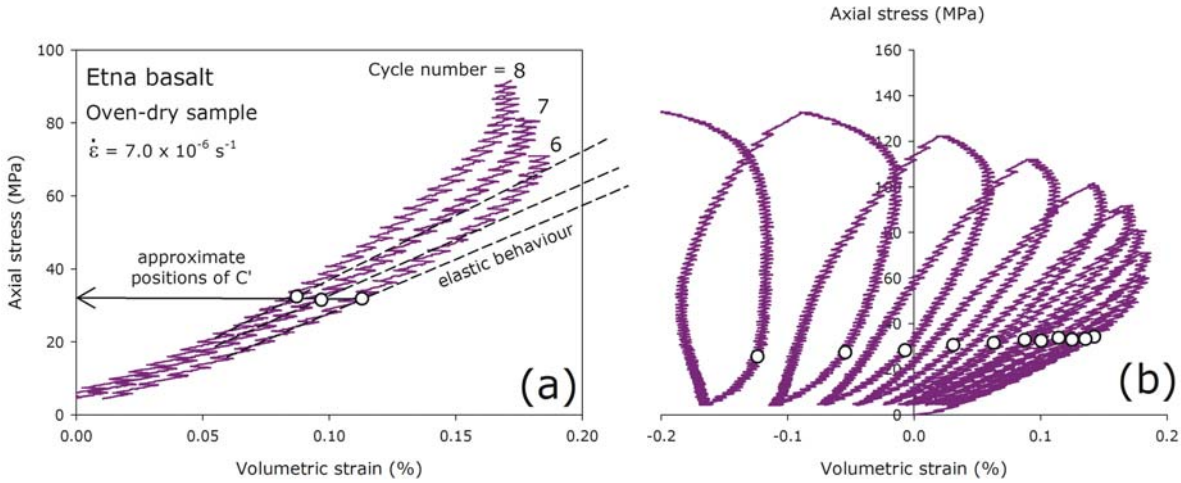

Figure 6.5. (a) Close inspection of how C’ were determined for each cycle. (b) The evolution of C’ during an increasing-amplitude stress-cycling experiment on a dry sample of EB. The position of C’ is marked for each cycle by a white circle.

The AE output from both of the dry and wet experiments shown in Fig. 6.3 are shown in Fig. 6.6, with both AE energy (Fig. 6.6a and 6.6b) and AE hits (Fig. 6.6c and 6.6d) plotted against stress and time. During most cycles, AE output is observed to commence just prior to the maximum stress on the previous cycle. In general, AE output re-commences during any loading cycle at the same level of stress that it ceased during the unloading portion of the previous cycle. It must be noted that the amount of AE energy emitted during the final loading cycle, where microcracks link and coalesce to produce the type of macroscopic failure shown in Fig. 6.4c, is much greater than for any of the preceding cycles. The AE output for the stress-cycling experiments on wet and dry EB show an identical trend (Fig. 6.6).

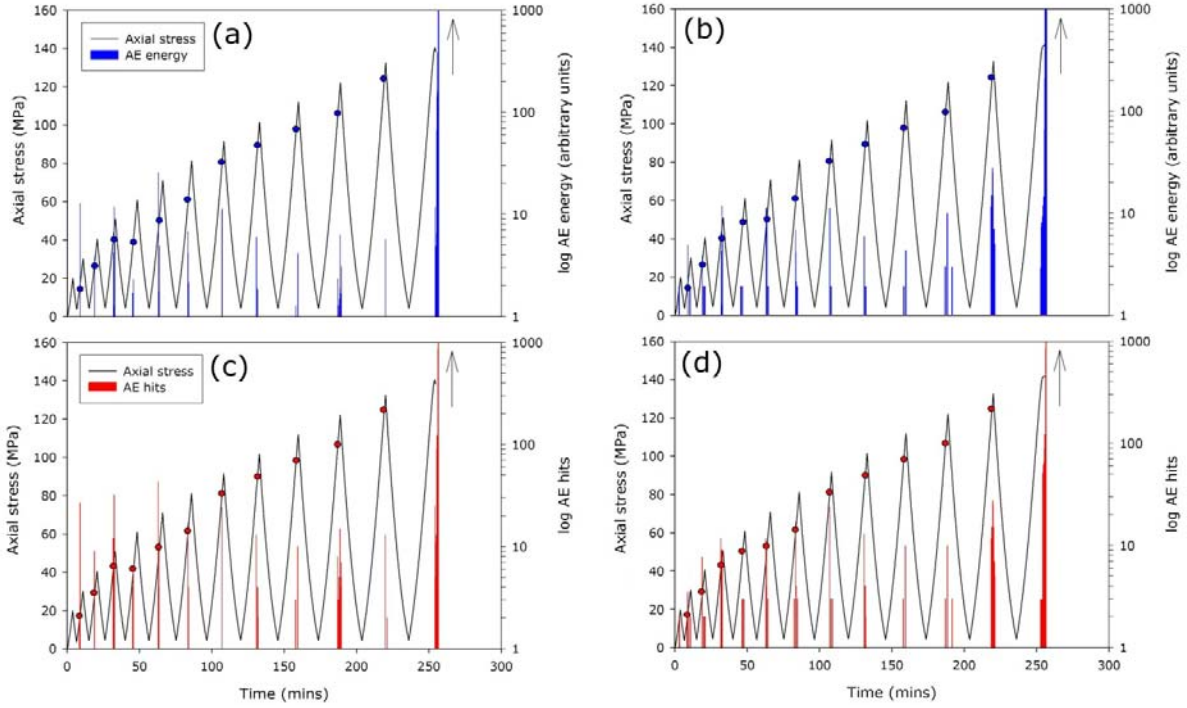

Figure 6.6. Acoustic emission (AE) activity during the stress-cycling of EB. The output of AE energy for a dry sample (a) and a wet sample of EB (b) and the number of AE hits for a dry sample (c) and a wet sample of EB (d), as a function of stress and time, from increasing-amplitude, stress-cycling experiments. Solid circles indicate the points at which AE output recommenced on each loading cycle. Arrows indicate the position where AE energy and hits has increased beyond the scale displayed [samples EB-25-02 and EB-25-03].

Although the presence of AE output signifies the inclusion of further microcrack damage within a particular sample and that experiments have demonstrated that elastic moduli changes are brought about during cycles that are commensurate with AE output, microstructural analysis is still required to confirm their existence in the deformed samples. Fig. 6.7 shows photomicrographs of a dry sample of EB that had failed after 13 increasing-amplitude stress cycles. Together with a large number of intragranular microcracks (Fig. 6.7d), there are also numerous, very large transgranular microcracks present within the sample (Figs. 6.7a-c). Many of these larger cracks, similar to those shown in Figs. 6.7a and 6.7b, show a preferred axial (Z-axis) orientation (for details on directional information see Chapter

Five, section *5.2.2 Orientation of samples*). The preferred axial orientation of microcracks is likely to be due to the absence of confinement during deformation; axial cracks are a much more common feature during uniaxial compression.

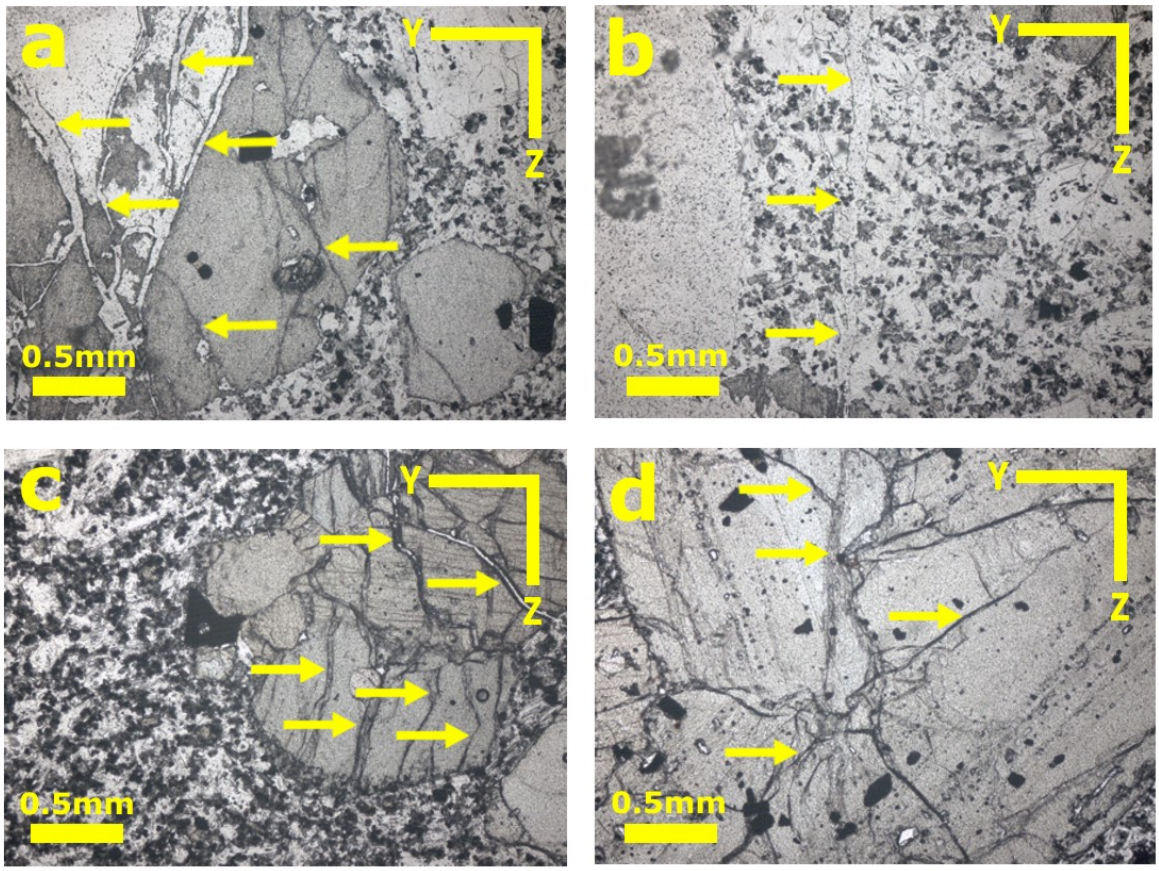

Figure 6.7. Photomicrographs of a dry sample of EB that has been cyclically stressed until failure, all photomicrographs are under PPL. (a-c) Photomicrographs showing large open transgranular microcracks (indicated with arrows). (d) Photomicrograph showing highly stressed grains of olivine that have been crushed into one another; the microcracks present here are only intragranular. All photomicrographs are taken within the same YZ plane, the Z-axis is normal to the axial loading direction (for details on directional information see *5.2.2 Orientation of samples*) [sample EB-25-02].

6.4.2 Darley Dale sandstone experiments

6.4.2.1 Constant strain rate experiments

Fig. 6.8 shows representative stress-strain curves for curves for dry (Fig. 6.8a) and wet (Fig. 6.8b) samples of DDS deformed at a constant strain rate until failure. The average UCS was 55 ± 7 and 40 ± 6 MPa for samples of dry and wet DDS respectively. The influence of water-saturation on the UCS in samples of DDS is much more pronounced than for EB. In DDS, a reduction of about 28% is seen, compared to a reduction of about 15% in EB. The position of C', the departure from linear elastic behaviour, for dry and wet samples was approximately 17 and 7 MPa respectively (Fig. 6.8).

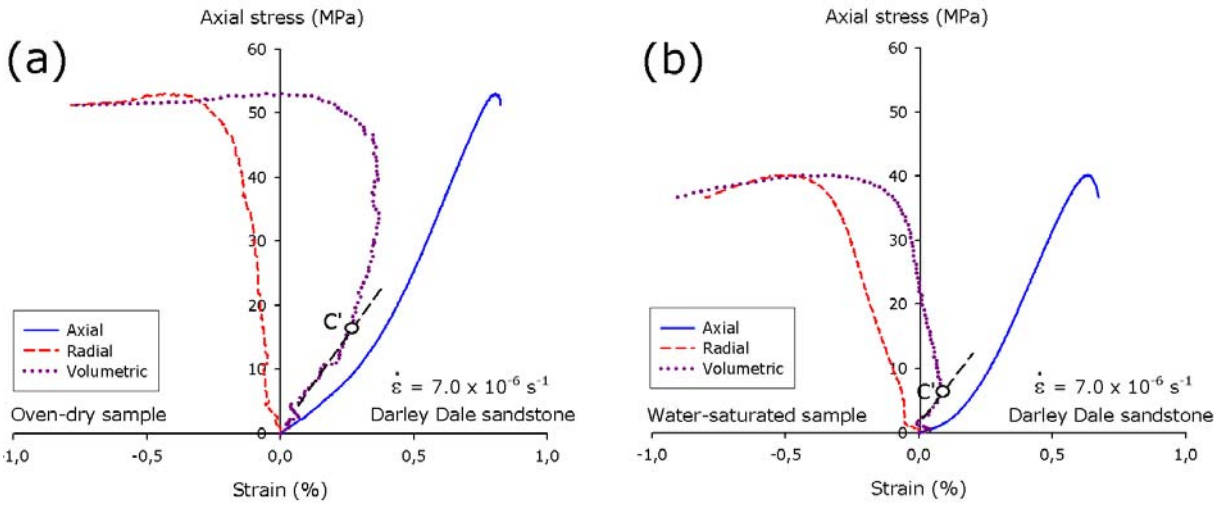

Figure 6.8. Stress-strain curves for constant strain rate experiments on (a) a dry sample of DDS [sample DDS-25-06Z] and (b) a wet sample of DDS [sample DD-25-08Z] taken to failure under uniaxial compression. The strain rate for the experiment is indicated on the figure. The positions of C' are marked by the white circles.

6.4.2.2 Increasing-amplitude stress-cycling experiments

Fig. 6.9 shows a representative stress-strain curve from a stress-cycling experiment on a dry (Fig. 6.9a) and a wet (Fig. 6.9b) sample of DDS. The experimental loading curves for each of the experiments are shown in Fig. 6.9c and 6.9d. It is apparent that the stress-strain response of the rock varies between loading cycles and is most easily seen in the radial strain curves, as per experiments on EB. The rock becomes progressively more compliant in each cycle due to the increase in crack damage that leads to increasing amounts of irrecoverable strain.

Eventually the samples failed, generally by axial splitting as shown in Fig. 6.10c. However, the stress-strain response to the wet sample is markedly different to that of the dry sample (failed on the 3rd cycle as opposed to the 6th cycle); this was not observed in experiments on EB. In fact, the peak stresses from the increasing-amplitude stress-cycling experiments on DDS (Fig. 6.9) bear close resemblance to the values for the UCS derived from constant strain rate experiments on DDS (Fig. 6.8).

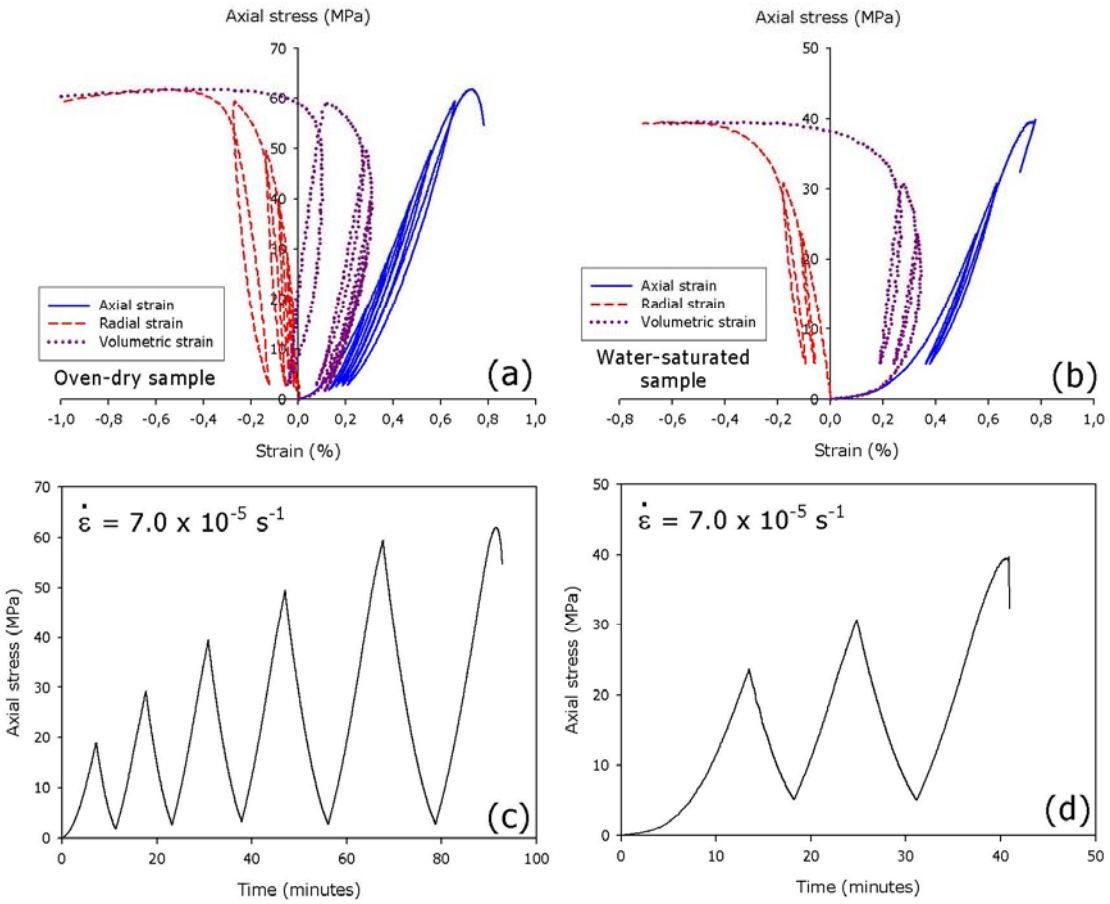

Figure 6.9. Representative axial and radial stress-strain curves for (a) dry and (b) wet sample of DDS under increasing-amplitude stress-cycling. (c) The loading path from an increasing-amplitude, stress-cycling experiment on a dry sample of DDS, showing sample failure during the 6th loading cycle. (d) The loading path from an increasing-amplitude, stress-cycling experiment on a wet sample of DDS, showing sample failure during the 3rd loading cycle [samples DDS-25-04Z and DDS-25-05Z]. The strain rates used during experimentation is indicated on the figure.

Fig. 6.10 shows the calculated values of Young's modulus and Poisson's ratio plotted against cycle number. The elastic response to stress-cycling is similar for dry and wet samples of DDS; however, the change in elastic moduli is achieved much quicker in the wet sample (i.e. 3 cycles compared to 6 in the dry sample). Young's modulus is seen to decrease by about 15% and 17% for dry and wet samples respectively, considerably less than the change seen in EB. Poisson's ratio increases by 0.35 for the dry

sample and by 0.29 for the wet sample; this corresponds to a Poisson's ratio increase by a factor of 6.0 and 3.7 for dry and wet samples respectively.

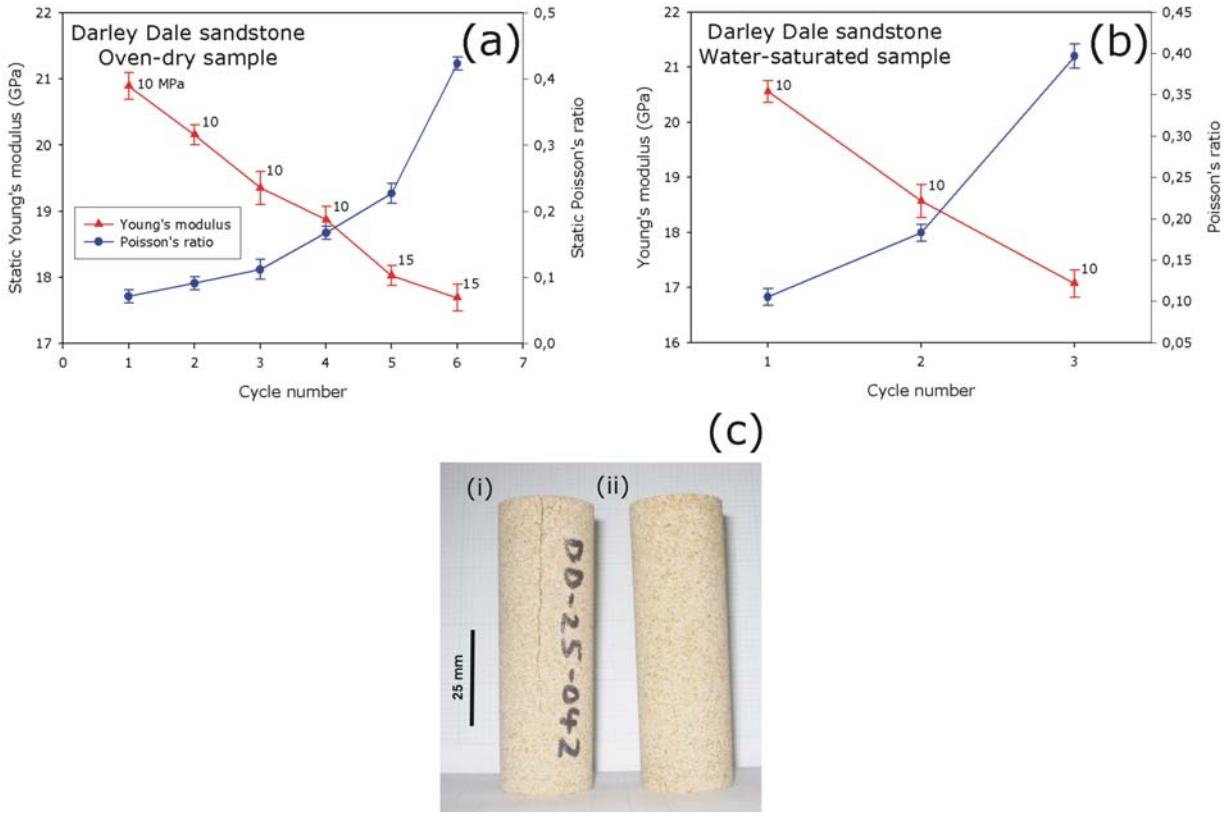

Figure 6.10. Static elastic moduli evolution with increasing cycles from increasing-amplitude stress-cycling experiments on (a) dry and (b) wet DDS [samples DDS-25-04Z and DDS-25-05Z] (c) Photographs of (i) a DDS sample that failed by axial splitting after 6 cycles during an increasing-amplitude cyclic stressing experiment [sample DDS-25-04Z] and (ii) an undeformed DDS sample. Values on each data point in (a) and (b) give an indication of the level of stress from where the static elastic moduli were calculated on the unloading curve of each cycle. Error bars indicate the variation in elastic moduli within the determined elastic portion of the unloading curves.

The position of C' can also be monitored during increasing-amplitude stress-cycling experiments (Fig. 6.11). The positions of C' were defined by the departure from linear elastic behaviour in the volumetric strain curves for each cycle (Fig. 6.5a). Fig. 6.11 demonstrates that, for a dry sample of DDS, the position

of C' remains roughly constant throughout the stress-cycling. The average position of C' was found to be about 17 MPa, almost identical to that found during constant strain rate experiments (see Fig. 6.8a).

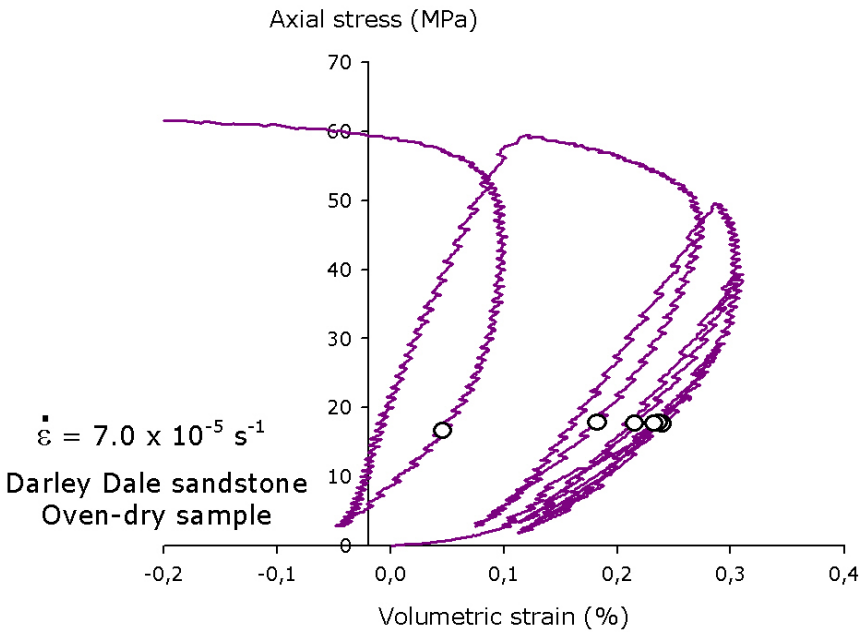

Figure 6.11. The evolution of C' during an increasing-amplitude stress-cycling experiment on a dry sample of DDS. The position of C' is marked for each cycle by a white circle.

AE output from both dry and wet experiments shown in Fig. 6.9 are shown in Fig. 6.12. Both AE energy (Fig. 6.12a and 6.12b) and AE hits (Fig. 6.12c and 6.12d) are plotted against stress and time. During most cycles, AE output is observed to commence just prior to the maximum stress on the previous cycle, similar to the behaviour observed in EB. Also, the amount of AE energy emitted during the final loading cycle, where microcracks link and coalesce to produce the type of macroscopic failure shown in Fig. 6.10c, is much greater than for any of the preceding cycles.

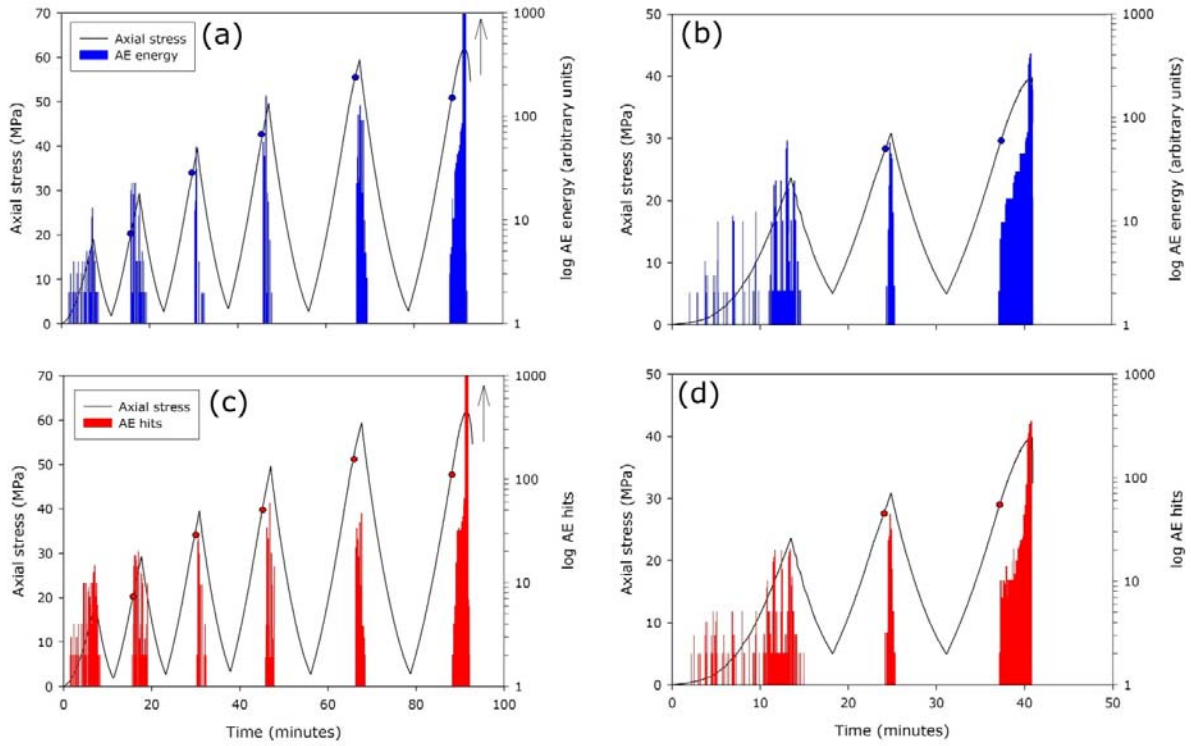

Figure 6.12. Acoustic emission (AE) activity during the stress-cycling of DDS. The output of AE energy for a dry sample (a) and a wet sample of DDS (b) and the number of AE hits for a dry sample (c) and a wet sample of DDS (d), as a function of stress and time, from increasing-amplitude, cyclic-stressing experiments. Solid circles indicate the points at which AE output recommenced on each loading cycle. Arrows indicate the position where AE energy and hits has increased beyond the scale displayed.

Fig. 6.13 shows photomicrographs of a dry sample of DDS that had failed after six increasing-amplitude stress cycles showing a number of intragranular microcracks (Fig. 6.13). Many of these cracks show a preferred axial (Z-axis) orientation (for details on directional information see *5.2.2 Orientation of samples*). The preferred axial orientation of microcracks is likely to be due to the absence of confinement during deformation; axial cracks are a much more common feature during uniaxial compression.

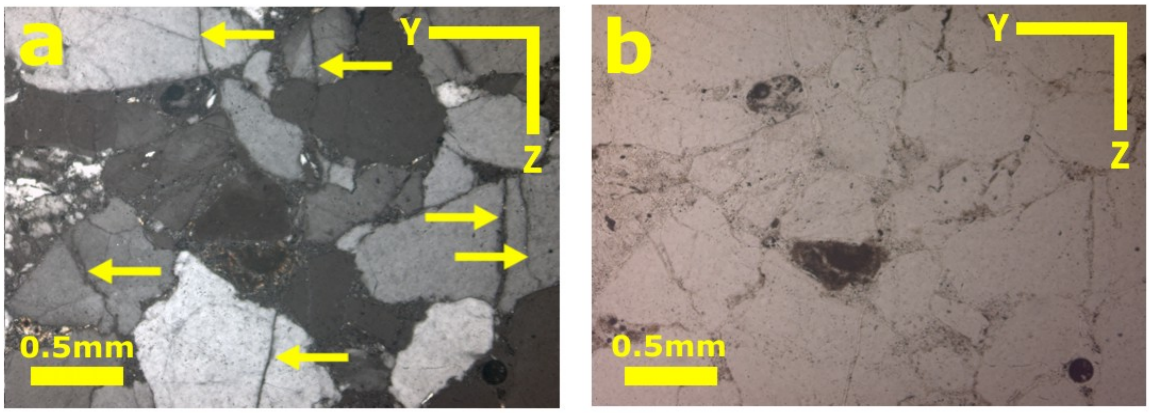

Figure 6.13. Photomicrographs of a dry sample of DDS that have been cyclically stressed until failure under (a) XPL and (b) PPL. Arrows indicate the position of large intragranular microcracks. All photomicrographs are taken within the same YZ plane, the Z-axis is normal to the axial loading direction (for details on directional information see *5.2.2 Orientation of samples*) [sample DD-25-04Z].

6.4.3 Other rock types

6.4.3.1 Stromboli basalt experiments

Fig. 6.14a shows a representative stress-strain curve from a stress-cycling experiment on a dry sample of SB. Similar to the other extrusive basalt, EB, it is apparent that the stress-strain response of the rock varies between loading cycles, and this is most easily seen in the radial strain curves. The rock becomes progressively more compliant in each cycle due to the increase in crack damage that leads to increasing amounts of irrecoverable strain. Eventually the samples failed by axial splitting as shown in Fig. 6.14c. Fig. 6.14b shows the calculated values of Young's modulus and Poisson's ratio plotted against cycle number. The elastic response to stress-cycling is almost identical to those for dry and wet samples of EB. In the case of SB, the Young's modulus is seen to decrease by about 30%, with Poisson's ratio increasing

by a factor of almost 5. Again, the position of C' (calculated as in Fig. 6.5a) remained roughly constant during stress-cycling (Fig. 6.14a).

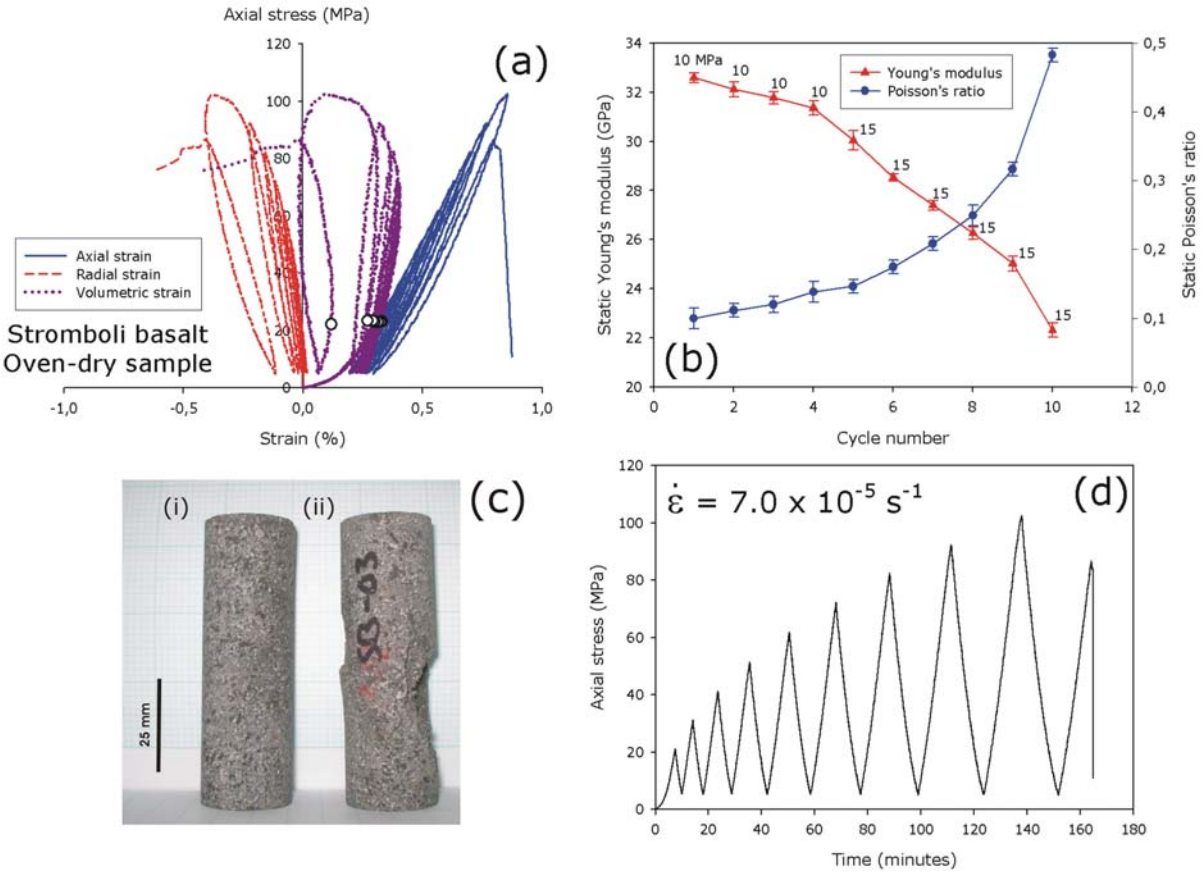

Figure. 6.14. (a) Representative axial and radial stress-strain curves from a stress-cycling experiment on a dry sample of SB (b) the evolution of elastic moduli during the experiment (c) (i) undeformed sample of SB and (ii) a SB sample that failed by axial splitting after 10 cycles during an increasing-amplitude stress-cycling experiment (d) Example of a loading path from an increasing-amplitude, stress-cycling experiment on a dry sample of SB that failed during the 10th loading cycle. The position of C' in (a) is marked for each cycle by a white circle. Values on each data point in (b) give an indication of the level of stress from where the static elastic moduli were calculated on the unloading curve of each cycle. Error bars in (b) indicate the variation in elastic moduli within the determined elastic portion of the unloading curves. The strain rate used during experimentation is indicated on the figure [sample SB-25-03Z].

AE output from one of the experiments on a dry sample of SB is shown in Fig. 6.15, plotted against stress and time. Similar to EB, AE output generally re-commences on any loading cycle at the same level of stress that it ceased during the unloading portion of the previous cycle (to avoid repeating information, further details can be found in *6.4.1 Etna basalt experiments*), with the exception of the final cycle in which the sample failed. Another difference between the two extrusive rock types is that much more AE output was observed for SB during the loading portion of the first cycle. AE output during this portion of a stress-strain curve is typically attributed to the closure of microcracks and other porosity. SB does contain a higher porosity, although it must also be noted that EB contains an extensive network of pre-existing microcracks [Vinciguerra *et al.*, 2005]. In general, AE activity between the two extrusive rock types is very similar.

An interesting feature of the experiment shown is that the sample failed far below the stress-peak of the penultimate cycle, this is most easily seen in the loading curve for the experiment (Fig. 6.14d). At the stress-peak of the penultimate cycle the sample was very close to failure, but was unloaded before microcracks could coalesce and cause catastrophic sample failure by axial splitting. This explains the much more substantial AE output (Fig. 6.15) and the dramatic changes in elastic moduli (Fig. 6.14b) calculated for the penultimate cycle. Therefore, only a very small amount of further microcrack damage would be required to result in sample failure. However, during the last cycle, AE output re-commenced at a very early stage of the cycle, far below the position expected from where AE output ceased on the previous cycle. It is possible that the stress at this point was not sufficient to initiate new microcracks, but was sufficient to re-open large, pre-existing axial cracks that could coalesce and cause sample failure.

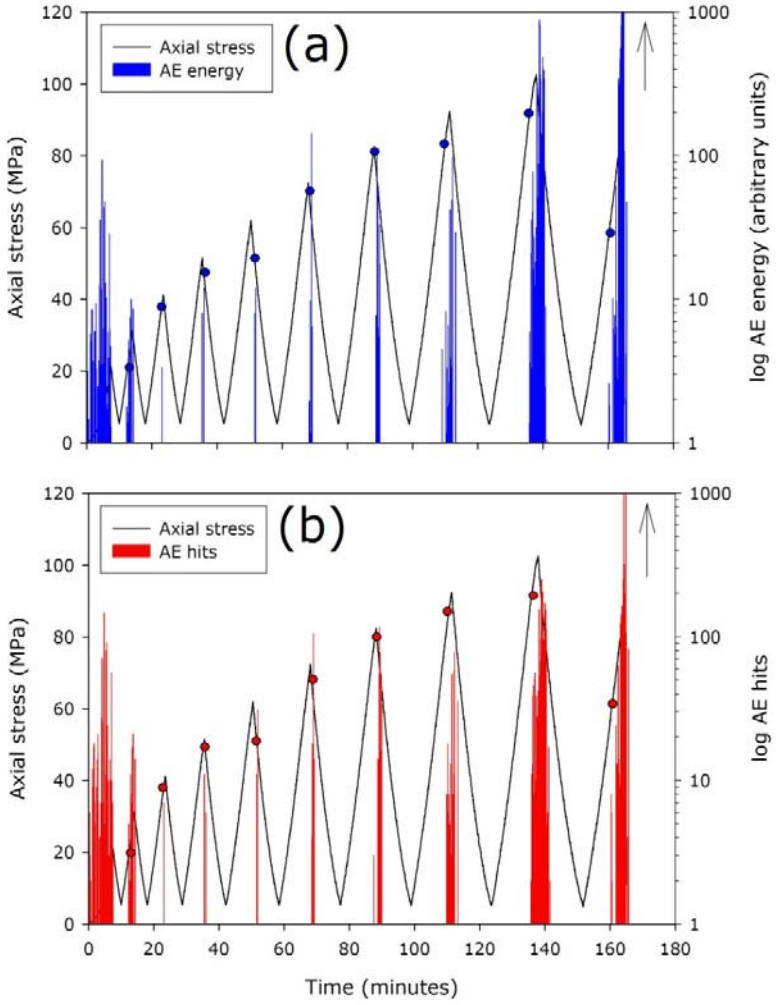

Figure 6.15. Acoustic emission (AE) activity during the stress-cycling of SB. (a) Output of AE energy and (b) output of AE hits for an increasing-amplitude stress-cycling experiment a dry sample of SB, as a function of stress and time. Solid circles indicate the points at which AE output recommenced on each loading cycle. Arrows indicate the position where AE energy and hits has increased beyond the scale displayed [sample SB-25-03Z].

Similar to EB, large transgranular microcracks could also be found within samples of SB that had undergone increasing-amplitude stress-cycling (Fig. 6.16). The large microcracks present in SB also show a preferred axial (Z-axis) orientation (for details on directional information see *5.2.2 Orientation of samples*).

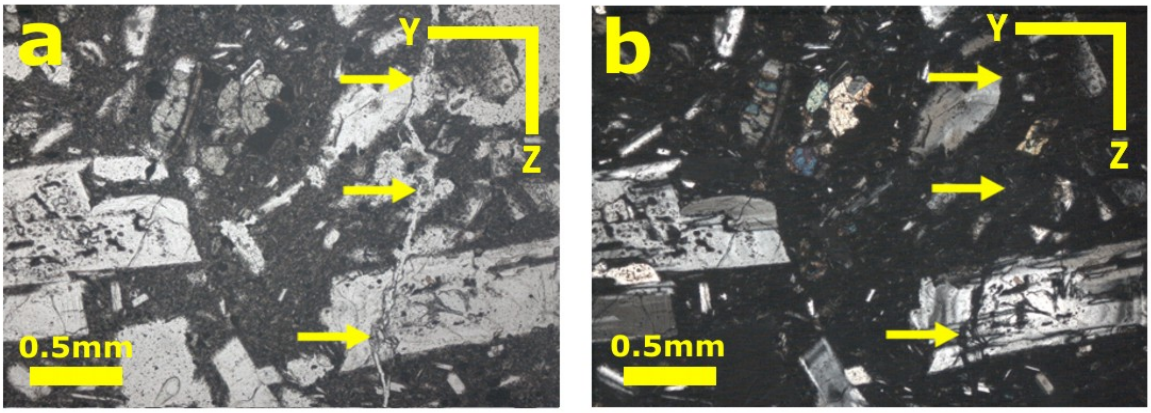

Figure 6.16. Photomicrographs of a sample of SB that have been cyclically stressed until failure under (a) XPL and (b) PPL. Arrows indicate the position of a large open transgranular microcrack. All photomicrographs are taken within the same YZ plane, the Z-axis is normal to the axial loading direction (for details on directional information see *5.2.2 Orientation of samples*) [sample SB-25-03Z].

6.4.3.2 Bentheim sandstone experiments

Fig. 6.17a shows a representative stress-strain curve from a stress-cycling experiment on a dry sample of BHS. Similar to the other rock types studied, it is apparent that the stress-strain response of the rock varies between loading cycles, and this is most easily seen in the radial strain curves. The rock becomes progressively more compliant in each cycle due to the increase in crack damage that leads to increasing amounts of irrecoverable strain and eventually the samples failed by axial splitting (Fig. 6.17c).

Fig. 6.17b shows the calculated values of Young's modulus and Poisson's ratio plotted against cycle number. The Young's modulus is seen to decrease by about 12%, a change similar to that seen in experiments on DDS, i.e. much less than the observed change in both extrusive basalts. The Poisson's ratio is seen to increase by a factor of about 4. In general, the changes in elastic moduli in BHS are

similar to those seen for DDS despite the lower number of cycles. The position of C' (calculated as in Fig. 6.5a) remained roughly constant during stress-cycling (Fig. 6.17a).

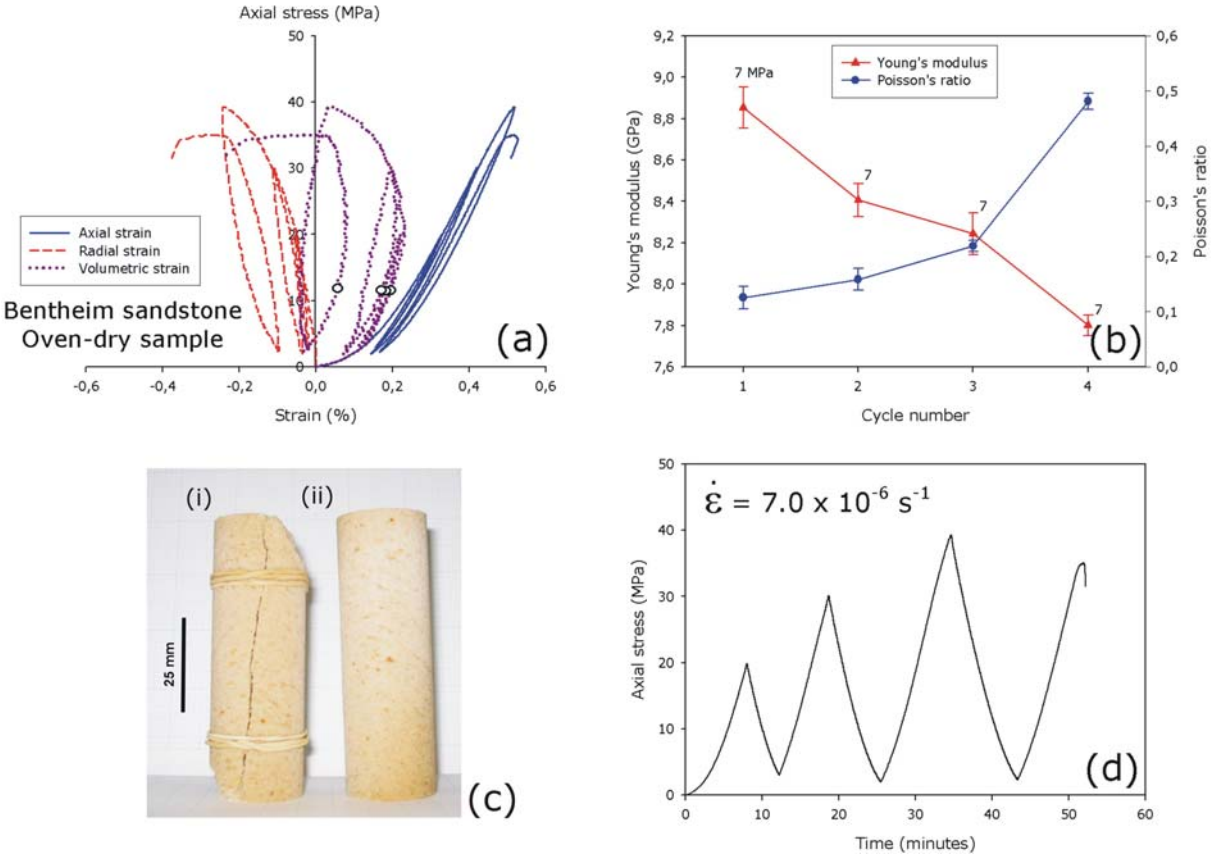

Figure. 6.17. (a) Representative axial and radial stress-strain curves from a stress-cycling experiment on a dry sample of BHS (b) the evolution of elastic moduli during the experiment. (c) (i) A BHS sample that failed by axial splitting after 4 cycles during an increasing-amplitude stress-cycling experiment and (ii) an undeformed sample of BHS. (d) Example of a loading path from an increasing-amplitude, stress-cycling experiment on a dry sample of BHS that failed during the 10th loading cycle. The position of C' in (a) is marked for each cycle by a white circle. Values on each data point in (b) give an indication of the level of stress from where the static elastic moduli were calculated on the unloading curve of each cycle. Error bars in (b) indicate the variation in elastic moduli within the determined elastic portion of the unloading curves. The strain rate used during experimentation is indicated on the figure [sample BH-25-04Z].

AE output from one of the experiments on a dry sample of BHS is shown in Fig. 6.18, plotted against stress and time. As per the other rock types, AE output generally re-commences on any loading cycle at the same level of stress that it ceased during the unloading portion of the previous cycle. Similar to SB, the experiment shown for BHS failed below the stress-peak for the penultimate cycle (see Fig. 6.14d). Again, substantial AE output (Fig. 6.18) and dramatic changes in elastic moduli (Fig. 6.17) are seen for the penultimate cycle.

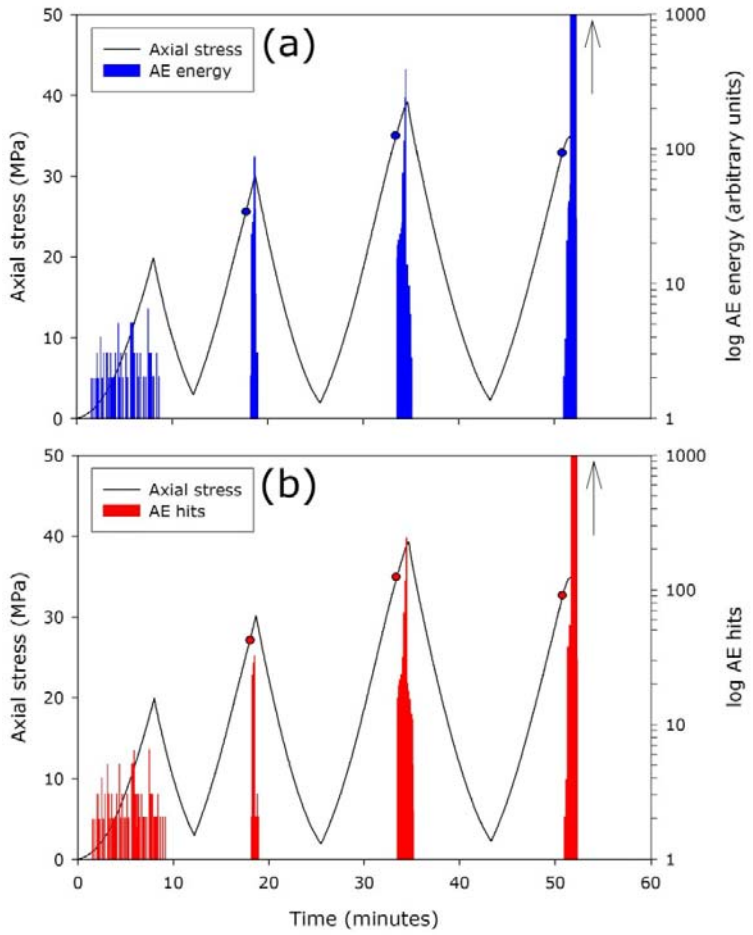

Figure 6.18. Acoustic emission (AE) activity during the stress-cycling of BHS. (a) Output of AE energy and (b) output of AE hits for an increasing-amplitude stress-cycling experiment a dry sample of BHS, as a function of stress and time. Solid circles indicate the points at which AE output recommenced on each loading cycle. Arrows indicate the position where AE energy and hits has increased beyond the scale displayed [sample BH-25-04Z].

Optical microscope analysis showed the BHS sample to have large intragranular microcracks after it had undergone increasing-amplitude stress-cycling (Fig. 6.19). The large microcracks present in BHS also show a preferred axial (Z-axis) orientation (for details on directional information see *5.2.2 Orientation of samples*).

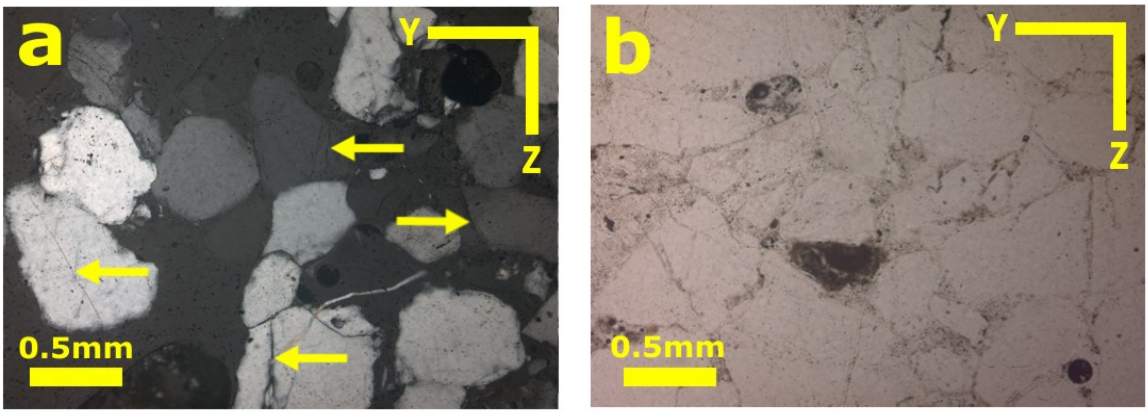

Figure 6.19. Photomicrographs of a dry sample of BHS that have been cyclically stressed until failure under (a) XPL and (b) PPL. Arrows indicate the position of large intragranular microcracks. All photomicrographs are taken within the same YZ plane, the Z-axis is normal to the axial loading direction (for details on directional information see *5.2.2 Orientation of samples*) [sample BH-25-04Z].

6.6 Summary

1. Constant strain rate (7.0 x 10^{-6} s^{-1}) experiments on both wet and dry samples of EB and DDS demonstrated that the presence of water reduces the UCS. A reduction of about 15% and 28% is seen in EB and DDS respectively.
2. The data demonstrates that cyclic-stressing significantly affects the static elastic moduli in all of the rock types studied. The rock becomes progressively more compliant in each cycle due to the increase in crack damage that leads to increasing amounts of irrecoverable strain and eventually

the samples failed by axial splitting. All rock types exhibit a decrease in Young's modulus and a significant increase in Poisson' ratio. In general, the decrease in Young's modulus was greater in the extrusive basalts (EB and SB) than in the porous sandstones (DDS and BHS). These data are summarized in Table 6.1.

3. In all cases, apart from the penultimate cycles in SB and BHS, AE output re-commences on any loading cycle at the same level of stress that it ceased during the unloading portion of the previous cycle.
4. Optical microscopy has shown that samples that have undergone increasing-amplitude stress-cycling contain many intragranular, and in some cases large transgranular, microcracks. The majority of these microcracks are orientated normal to the axial loading direction (Z-axis, see *5.2.2 Orientation of samples*).

Rock type	Percentage change in Young's modulus (%)	Percentage change in Poisson's ratio (%)
Etna basalt (dry)	-29	+250
Etna basalt (wet)	-34	+260
Darley Dale sandstone (dry)	-15	+600
Darley Dale sandstone (wet)	-17	+370
Stromboli basalt	-32	+485
Bentheim sandstone	-12	+380

Table 6.1. Summary of the total change in static elastic moduli as a result of increasing-amplitude stress-cycling for all investigated rock types.

Chapter seven

7. Discussion of the Influence of Crack Damage on Rock Caused by Stress-cycling

7.1 Introduction

This chapter discusses the results of the influence of microcrack damage on rock caused by stress-cycling data presented in Chapter Six. It is organized into six sections: discussion of (1) the evolution of static elastic moduli with increasing crack damage; (2) the analysis of AE output during the stress-cycling of rock; (3) the influence of thermal cracking on the elastic moduli evolution of EB; (4) the use of elastic moduli in deformation models; (5) the role of confining pressure in the evolution of elastic moduli and (6) potential avenues for future research.

7.2 The evolution of elastic moduli with increasing crack damage

The progressive degradation of sample stiffness that results in the Young's modulus reduction and Poisson's ratio increase (see Chapter Six, Figs. 6.4, 6.10, 6.14 and 6.17) is primarily attributed to an increase in the level of crack damage within the samples; either the extension of favourably-oriented, pre-existing cracks, the propagation of new cracks, or some combination of both. Each cycle that loads the sample to a higher stress imparts an additional increment of crack damage to the sample, leading to increasing amounts of irrecoverable strain. It was also found that C', the onset of dilatant microcracking and permanent strain, remained roughly constant during increasing-amplitude stress-cycling. This is true for all of the rock samples tested.

The evolution of both Young's modulus and Poisson's ratio for all samples with increasing damage level is qualitatively similar to the pattern previously reported by Heap and Faulkner [2008] from stress-cycling experiments on Westerly granite. However, they found that Young's modulus for their granite samples decreased by a total of about 11%, and Poisson's ratio increased by a factor of about 1.7 over

the total duration of their uniaxial stress-cycling experiments. The increase in Poisson's ratio is considerably less than that observed for the samples tested in this study. However, changes in Young's modulus for their Westerly granite samples are similar to those seen for the sandstones tested during this study. A summary of the static elastic changes during stress-cycling for all the rocks tested this study, including the data from Heap and Faulkner [2008], is presented in Table 7.1 and Fig. 7.1.

Rock type	Percentage change in Young's modulus (%)	Percentage change in Poisson's ratio (%)	Change in Poisson's ratio
Etna basalt (dry)	-29	+250	0.29
Etna basalt (wet)	-34	+260	0.29
Etna basalt (thermally-stressed)	-30	+375	0.33
Darley Dale sandstone (dry)	-15	+600	0.35
Darley Dale sandstone (wet)	-17	+370	0.29
Stromboli basalt	-32	+485	0.38
Bentheim sandstone	-12	+380	0.36
Westerly granite [Heap and Faulkner, 2008]	-11	+72	0.20

Table 7.1. Summary of the influence of increasing-amplitude stress-cycling on the elastic moduli of all the rock types tested in this study and those from Heap and Faulkner [2008]. The presented values represent total changes in elastic moduli during the course of complete experiments. Details on the thermally-stressed Etna basalt experiment can be found later in the text.

It is likely that the rock types in this study (Fig. 7.1 and Table 7.1) exhibit a greater increase in Poisson's ratio than Westerly granite [in Heap and Faulkner, 2008] due to its high initial Poisson's ratio; the result of a very low initial crack density [Hadley, 1976]. All of the rock types used in this study contain a much greater porosity (see Chapter Five for rock descriptions) than Westerly granite [see Brace, 1978 for example], and EB in particular contains a high degree of pre-existing microcrack damage present within the rock [Vinciguerra *et al*., 2005; Benson *et al*., 2006]. In general, a higher porosity (e.g. DDS, BHS and SB) or level of pre-existing crack damage (e.g. EB) results in a lower initial Poisson's ratio. Since all rock types reach approximately the same value on the cycle immediately prior to failure (just short of 0.5),

the percentage change in Poisson's ratio for the Westerly granite is comparatively low. The opposite is true for the sandstones, explaining their significant percentage increase in Poisson's ratio.

The results demonstrate that when the level of crack damage through stress-cycling increases, the Poisson's ratio also increases. This appears to be a contradiction, but it is not. The pre-existing crack damage in EB for example is known to be isotropically distributed [Vinciguerra *et al*., 2005; Benson *et al*., 2006], and the other rock types have been shown to only exhibit a mild ultrasonic velocity anisotropy (see Chapter Five). Therefore, radial cracks oriented sub-normal to the direction of the applied stress are easily closed when that stress is first applied. This leads to a relatively low radial strain and a low initial Poisson's ratio. By contrast, when the stress is high enough to generate new cracks, these are preferentially oriented parallel to the applied stress (i.e. axially). They therefore open easily when stress is re-applied on the next loading cycle, leading to a high radial strain and a high Poisson's ratio. This is evidenced by the preferred axial spitting failure mode of samples that had undergone increasing-amplitude, stress-cycling (see Chapter Six, Figs. 6.4c, 6.10c, 6.14c and 6.17c). The same conclusion was drawn by Heap and Faulkner [2008] in their study of stress-cycling of Westerly granite.

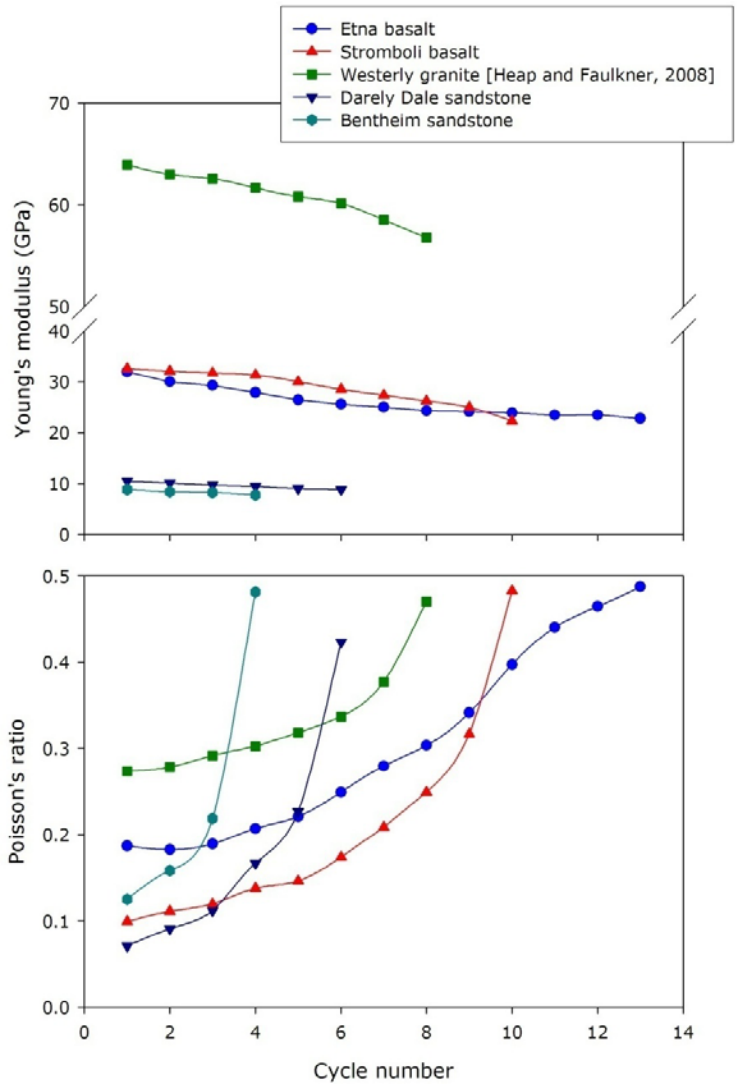

Figure 7.1. The evolution of (a) static Young's moduli and (b) static Poisson's ratio with increasing number of increasing-amplitude stress cycles for dry samples of Etna basalt (blue circles), Stromboli basalt (red triangles), Westerly granite from Heap and Faulkner [2008] (green squares), Darley Dale sandstone (dark blue inverted triangles) and Bentheim sandstone (cyan diamonds). Note that, for improved clarity, there is an axis break between 40-50 GPa in (a).

During UCS experiments on both EB and DDS it was found that the UCS of the rock was lower for wet samples compared to those that were dry. A reduction of about 15% and 28% is seen in EB and DDS respectively. Previous experimental studies have shown that the presence of the most common fluid phase, water, acts to reduce the brittle strength of porous rock [Rutter and Mainprice, 1978; Chester

and Logan, 1986; Hadizadeh and Law, 1991; Dewers and Hajash, 1995; Zang *et al.*, 1996; Masuda, 2001; Baud *et al.*, 2000], and even low-porosity crystalline rock [Lajtai *et al.*, 1987; Dennis and Atkinson, 1982].

However, the peak stresses for both wet and dry samples during increasing-amplitude stress-cycling experiments on DDS were the same as those derived from the wet and dry constant strain rate experiments i.e. no further weakening was observed due to the stress-cycling alone. This is a contrast to the stress-cycling experiments performed by Li *et al.* [2003] who saw an 18% decrease in peak stress in water-saturated sandstone from conventional constant strain rate loading to cyclic loading. No further reduction in peak stress was also observed in the stress-cycling experiments on EB. In fact, both wet and dry samples of EB taken to failure during stress-cycling experiments failed at the same peak stress as found for the dry constant strain rate experiments on EB. A 25% reduction in peak stress from constant strain rate loading to stress-cycling has been previously observed in low-porosity granites [Roa and Ramana, 1992]; not a basic rock, but a better analogue than the study on sandstone discussed previously.

Despite this, no significant difference in the evolution of static elastic moduli with increasing stress-cycling damage is observed between dry and wet samples of EB and DDS (Table 7.1). Bearing in mind that the percentage changes in the Poisson's ratio can be fairly misleading, as explained earlier. Wet samples are however considered to be more relevant to field observations [Vinciguerra *et al*., 2006] where rocks are expected to be saturated in the sub-surface. Furthermore, it is well-known that the values of dynamic elastic moduli are frequency dependent [e.g. Vinciguerra *et al*., 2006]. Therefore, fluid saturation has a significant influence on dynamic elastic moduli measured at ultrasonic frequencies [Winkler and Murphy, 1995; Vinciguerra *et al*., 2006], due to rapid energy dissipative mechanisms such as 'fluid squirt'. However, the experiments presented in this study, have yielded static elastic moduli at a

frequency some nine orders of magnitude lower than ultrasonic frequencies, it would only be expected that water-saturation affects the mechanical/elastic behaviour of the rock through the law of effective stress. However, that law has no effect on the results of the experiments in this study because they were conducted at atmospheric pressure without a pressurized pore fluid.

The changes in static elastic moduli observed during the experiments presented in this study are large. However, large changes in elastic wave velocities are also observed in volcanic rocks upon the introduction of new crack damage [Vinciguerra *et al*., 2005; Stanchits *et al*., 2006]. For example, Vinciguerra *et al*. [2005] report a 40% decrease in the P-wave velocity of initially undamaged Seljadur basalt (from Iceland) after thermal stressing to 900°C. The variation in static elastic moduli is currently unknown for volcanic edifices, since in-situ measurements are inevitably dynamic values derived from seismic wave velocities, and it has long been recognized that such elastic moduli values are frequency dependent [Simmons and Brace, 1965; Cheng and Johnston, 1981; Eissa and Kazi, 1989; Ciccotti and Mulargia, 2004; Ciccotti et al., 2004] due to intrinsic anelasticity. However, it is likely that static moduli are more representative than dynamic moduli in modelling the deformation of volcanic edifices, because the pre-eruptive deformation of such edifices proceeds quasi-statically rather than dynamically [e.g. Kilburn, 2003]. Furthermore, the static moduli measurements are made on laboratory samples that are extensively damaged during the experiments. Hence, the measurements are characteristic of the whole sample. By contrast, dynamic measurements calculated from elastic wave velocities through volcanic edifices are average values for the whole edifice. Since only a small proportion of the total volume of the edifice is likely to be damaged by new crack growth during any pressurization cycle, only commensurately smaller changes in the average dynamic moduli would be expected. It must also be noted that our results exhibit very similar trends to those previously published by Heap and Faulkner [2008] and Eberhardt *et al*. [1999] who used similar techniques.

Elastic moduli are the key parameters for defining relationships between stress and strain. They determine the distribution and magnitude of sub-yield stresses, the propagation velocity of elastic (seismic) waves and can be used to relate strain measurements to in situ stresses within the Earth's crust. In volcanic regions for example, reliable estimates of mechanical properties and their degradation under multiple episodes of stressing are crucial to the accurate modelling of routinely monitored data such as ground deformation, and the calibration of damage-mechanics criteria for the weakening of rocks forming volcanic edifices.

Activity on Mt Etna volcano, for example, may be divided into (1) persistent activity with episodic paroxysmal events, which generally occurs at or near the summit and is not preceded by seismic precursors [e.g. Lombardo and Cardaci, 1994], and (2) cycles of hazardous flank eruptions [Guest, 1982], which are preceded by intense seismic activity [Castellano *et al.*, 1997; Vinciguerra *et al.*, 2001], often including shallow destructive earthquakes [Azzaro *et al.*, 2000], which indicates the acceleration of brittle failure mechanisms [Patanè *et al.*, 2004]. Over the last 20 years, new technological developments and denser monitoring networks at Mt Etna volcano have provided one of the highest quality volcanological, geophysical and geochemical data sets for any volcano in the world [Bonaccorso, 2004]. Following the 1991-1993 eruption, the largest effusive eruption of the 20th century [Patanè *et al.*, 1996], the volcano has experienced a cycle of intense activity [Allard *et al.*, 2006; Carbone and Greco, 2007 and references therein]. The cycles evolve from initial recharging of the plumbing system and inflation, followed by powerful summit eruptions [Behncke and Neri, 2003; Andronico *et al.*, 2004] and slow spreading of the eastern to southern flanks, to a sequence of flank eruptions accompanied by accelerated flank displacement [Burton *et al.*, 2005]. In this framework, pre-eruptive patterns defined from seismic fault plane solutions and deformation events [Bonaccorso *et al.*, 1996; Patanè *et al.*, 2003; Patanè *et al.*, 2006] indicated that magma intruded along tensional gashes, within a strongly anisotropic state of stress, which induced strike-slip faulting. Importantly, a number of field and monitoring based studies revealed that, before

eruptive episodes at Mt Etna volcano, magma did not actively trigger the opening of eruptive fissure, but intruded after the development of the fracture system [Branca *et al.*, 2003; Alparone *et al.*, 2004; Carbone and Greco, 2007]. Taken together, these observations suggest that repeated episodes of deformation can lead, through brittle mechanisms, to an increase in the level of crack damage within the rocks of the edifice, and hence to changes in their elastic moduli.

The most representative basalt from Mt Etna volcano, a porphyritic alkali lava flow basalt (EB) [see Tanguy *et al.*, 1997], has been the subject of a number of mechanical studies in the last few years. Quantitative investigations of lava flow fracturing dynamics have been pursued through mechanical tests in both tension [Balme *et al.*, 2004] and compression [Rocchi *et al.*, 2004] at high temperatures and low pressures. Under compression, Etna basalt exhibits a typical strength of around 100 MPa that varies little with confining pressure and a low Young's modulus around 40 GPa at temperature up to 600°C. Above this temperature both strength and elastic modulus are observed to decrease even further [Rocchi *et al.*, 2004]. The physical properties of Etna basalt have also been investigated, yielding unexpectedly low ultrasonic wave velocities and unexpectedly high fluid permeability. Both observations have been attributed to the presence of a high level of connected pre-existing microcrack damage [Vinciguerra *et al.*, 2005]. Such microcracks are interpreted as being of thermal origin, since values of physical properties are not affected by further thermal stressing [Vinciguerra *et al.*, 2005]. These observations are entirely consistent with the low dynamic Young's modulus reported for Etna basalt by Rocchi *et al.* [2004]. However, these results were strongly influenced by the rock type investigated. High values were found for the denser, crystallized core of the 1983 lava flow whilst low values were found for the more porous, glass-rich crust [Rocchi *et al.*, 2004]. Furthermore, the lava pile at Mt Etna has formed over Miocene flysch sediments to the NW and argillaceous Pleistocene formations to the SE [Brusca *et al.*, 2001]. Many of the large faults that offset the lava pile reach down into the sedimentary

rocks, its deformation, by repeated cyclic deformation behaviour, could influence flank stability [see Allard *et al.*, 2006].

7.3 Analysis of AE output during stress-cycling

Previous AE studies of cracking in rocks have demonstrated that, in general, new microcrack damage is generated only once the previous maximum stress has been exceeded during stress-cycling. This phenomenon was first reported in metals [Kaiser, 1953] and is now known as the Kaiser 'stress-memory' effect. Rocks have been shown to also exhibit this behaviour [see Li and Nordlund, 1993; Holcomb, 1993; Lockner, 1993; and Lavrov, 2003]. However, all of the experiments in this study demonstrate that AE output re-commenced during any loading cycle at the same level of stress that it ceased during the unloading portion of the previous cycle (see Chapter Six, Figs. 6.6, 6.12, 6.15 and 6.18). Therefore, the classical manifestation of the Kaiser stress-memory effect is not observed. Since the samples were not held at the maximum stress on any cycle for any extended period of time, crack damage did not have time to equilibrate to the level of applied stress. Consequently, time-dependent subcritical cracking continues during a small portion of the unloading part of that cycle. If samples were held at the stress peak of each cycle until AE activity had stopped, or if the strain rate of the loading/unloading was decreased somewhat, then it is likely that the classic manifestation of the Kaiser effect would be observed.

However, during the complex pattern of stressing that can act over extended time within volcanic edifices, for example, the stress acting on the rock during any loading/pressurization cycle may not necessarily exceed that during the previous cycle. Under these circumstances, the Kaiser effect would predict that no further crack damage would be generated in those cycles where the stress did not

exceed the previous maximum. A further stress-cycling experiment was therefore performed on EB in which the maximum stress in each cycle has been randomly selected to be either higher or lower than that of the previous cycle, in order to gain a better understanding of this more realistic scenario. In this case a more complex manifestation of the Kaiser effect is observed, as expected, where significant AE output in any cycle was only observed when the stress in that cycle exceeded the maximum stress on any previous cycle (as shown in Fig. 7.2b and 7.2d). It must be noted that the single hits recorded during the cycles that do not exceed the previous maximum stress (Fig. 7.2d) do not register any AE energy (Fig. 7.2b).

The evolution of the elastic moduli for this experiment, calculated exactly as previously described, is shown in Fig. 7.2c. It is clear that changes in the elastic moduli are only observed during cycles that are accompanied by AE output, and in which the maximum stress exceeded that on any previous cycle. It can therefore be suggested that, in nature, only those stress episodes that are accompanied by volcano-seismicity will result in extra damage to the edifice and lead to changes in elastic moduli and seismic velocities; the same is likely to be true for the seismic activity at a fault zone. A number of specific mechanisms have been proposed for the origin of volcano-tectonic earthquakes [e.g. Hill, 1977; Ukawa and Tsukahara, 1996; Roman and Cashman, 2006]. However, this interpretation is consistent with all of these, and also with detailed seismological studies at Mt. Etna volcano over many years which demonstrate that volcano-tectonic events occur before and during flank eruptions, involving fracturing and dyke propagation [Bonaccorso *et al.*, 1996; 2004], but that no volcano-tectonic events are observed before and during summit eruptions, which occur along open conduits [Lombardo and Cardaci, 1994].

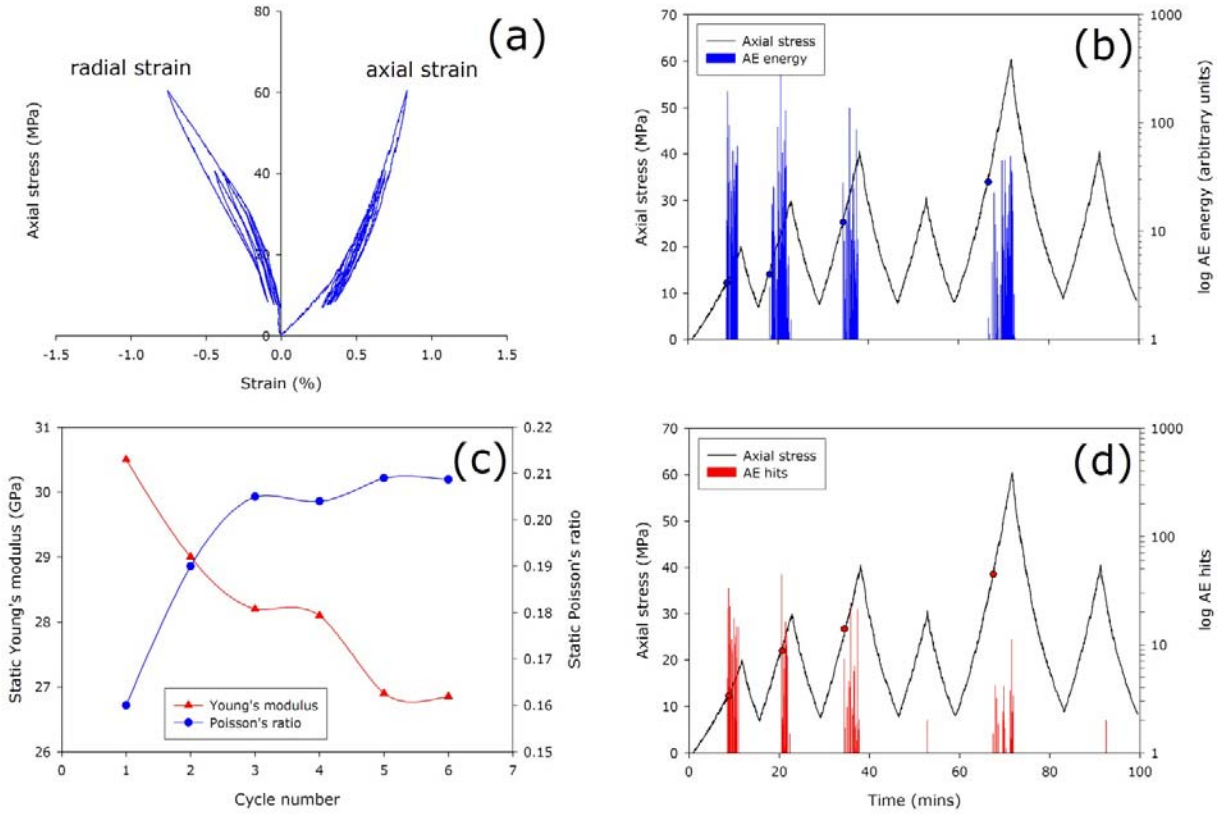

Figure 7.2. Results from a cyclic stressing experiment on a dry sample of EB in which the maximum stress in each cycle has been randomly selected to be either higher or lower than that of the previous cycle. (a) The stress-strain curve, (b) the output of AE energy, (c) the evolution of elastic moduli and (d) the number of AE hits for the experiment.

7.4 The influence of thermal cracking on the evolution of elastic moduli in Etna basalt

The brittle response of the volcanic edifice to the stress induced by dyke propagation also needs to take account of any elevated temperature and/or temperature fluctuation linked to magma intrusion. However, previous work on EB [Vinciguerra *et al.*, 2005] have concluded that thermal stressing did not lead to the creation of further crack damage if the temperature did not exceed that already experienced by the rock during the process of cooling from a lava flow. Data from this study has also demonstrated this observation (Fig. 7.3). Indeed, Vinciguerra *et al.* [2005] reported no significant change from ambient

temperature values of P-wave velocity, S-wave velocity or fluid permeability in samples of EB that were thermally stressed to 300°, 600° and 900°C. This is, in essence, a manifestation of the thermal equivalent of the Kaiser effect seen in mechanical stressing.

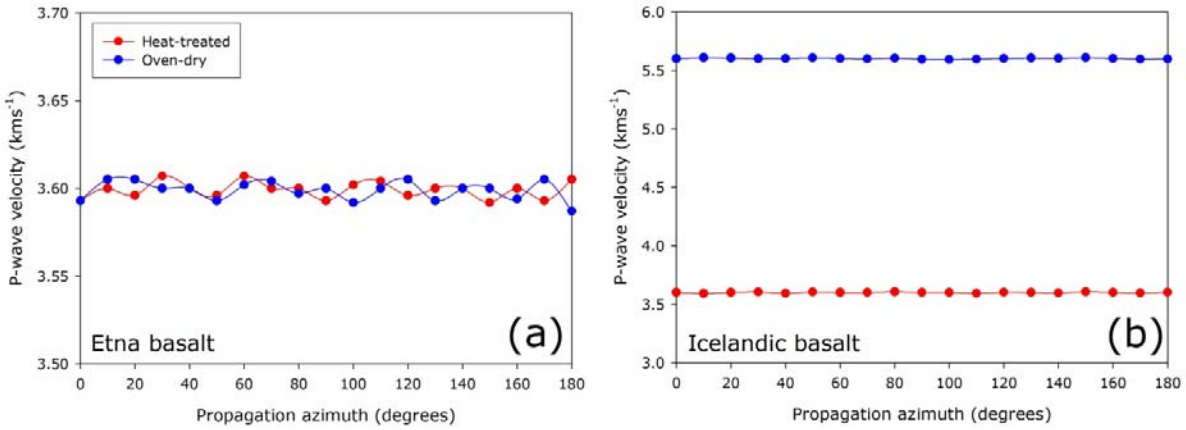

Figure 7.3. The influence of heat-treating samples of Etna basalt and Icelandic basalt on P-wave velocity. See *5.2.5 Heat treating samples* for details on the heat-treatment process. Note that, while the P-wave velocity of EB remains unchanged, the P-wave velocity of Seljadur basalt (from Iceland) falls by about 2 kms^{-1}. The Icelandic basalt used here is from the same block as used by Vinciguerra *et al*. [2005].

Nevertheless, increasing-amplitude stress-cycling experiments were performed on thermally-stressed samples of EB in order to ascertain if the above observation for physical and transport properties also holds for mechanical and elastic properties. Samples were heated in a tube furnace at a constant rate of 1°C/min to 900°C, held at that temperature for one hour to equilibrate, and then cooled to ambient temperature at the same rate (see **5.2 Rock sample preparation**). Results from a cyclic-stressing experiment on a heat-treated sample of EB are shown in Fig. 7.4, and should be compared with the data of Figs. 6.3 and 6.4. Overall, the results are very similar; both in the absolute values of the Young's modulus and Poisson's ratio and in their changes during stress cycling. For example, over 13 stress cycles the Young's modulus of the heat-treated sample decreased by 30%; the same change observed for the

untreated samples (Fig. 6.4). During the same experiment, the Poisson's ratio of the heat-treated sample increased by 0.33; a little more than the increase of 0.29 observed for the non-heat-treated samples, and likely due to the slightly lower starting value of Poisson's ratio for the heat-treated sample. The results from this experiment have been included in Table 7.1 for ease of comparison with the previous stress-cycling experiments on EB.

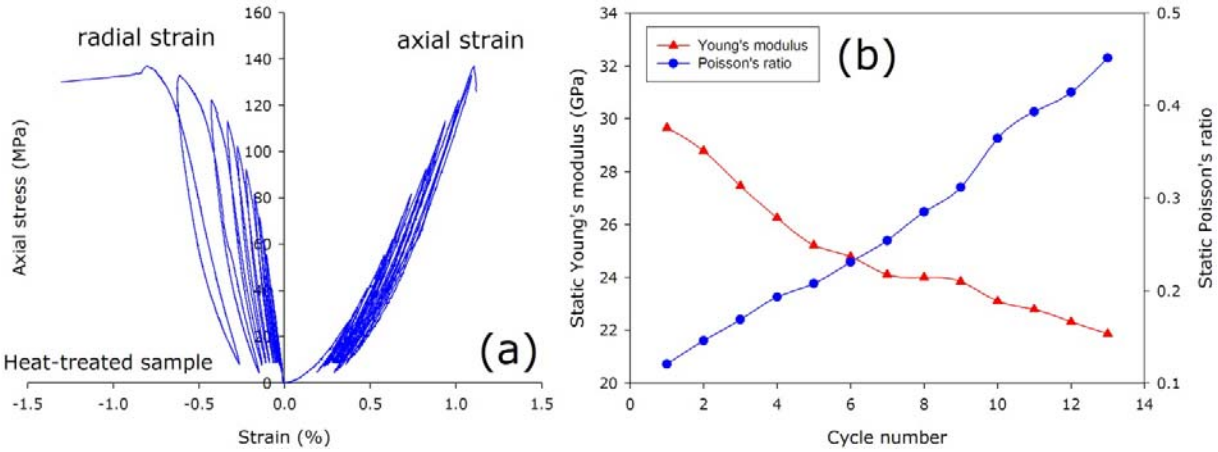

Figure 7.4. (a) The stress strain curve and (b) the evolution of static elastic moduli during an increasing-amplitude, cyclic stressing experiment on a sample of EB thermally stressed to 900°C.

Overall, the observations of changes in elastic moduli during cyclic-stressing of heat-treated EB samples are in agreement with the observations of changes in physical and transport properties reported by Vinciguerra *et al.* [2005]. That is, that thermal stressing up to 900°C does not induce any new crack damage into samples of EB, and hence does not induce any significant change in the response to mechanical loading. This is consistent with the observation that during the final stages of dyke intrusion (higher temperatures and lower pressures), only low magnitude earthquakes occur, while during the early stages of intrusion (lower temperatures and higher pressures) activation of focal volumes and brittle deformation of the volcanic pile is observed, indicated by higher magnitude volcano-tectonic

events [Patanè *et al.*, 2004 and references therein]. It should be noted, however, that during extended periods of volcano quiescence, elevated temperatures could lead to time-dependent healing of some of the microcrack damage caused by the stress-cycling, and thus at least partially re-set the clock [see e.g., Hickman and Evans, 1987].

7.5 The use of elastic moduli in deformation models

Quantifying the mechanical properties, such as the elastic moduli and strength, of the rocks constituting Mt Etna volcano's edifice is of key importance in establishing the reliability of modelled deformation sources. Elastic deformation models have proved an extremely useful tool for examining surface deformation related to the movement of magma within an active volcanic edifice and it is generally accepted that volcanic eruptions are preceded by the movement and intrusion of magma at depth [Sigurdsson and Sparks, 1978]. The most widely used is the classic model by Mogi [1958] that uses point dilatation in an elastic half-space to model deformation at the surface. However, it does not incorporate the influence of topography [Mogi, 1958]. Ground deformation models have subsequently been improved to incorporate two-dimensional topographic effects [McTigue and Segall, 1988] and finally three-dimensional topographic effects [Cayol and Cornet, 1998; Williams and Wadge, 1998; 2000]. Such models, however, require the precise knowledge of the elastic moduli of the rocks that comprise the volcanic edifice. Recent studies have suggested that the elastic heterogeneities of the medium significantly alter the position of the inferred source, not the topography [Trasatti *et al.*, 2008]. Previous studies at Mt Etna, Italy, assume values of Young's modulus ranging from 50-100 GPa and a Poisson's ratio between 0.21-0.3 [Cayol and Cornet, 1998; Bonaccorso and Davis, 1999; Obrizzo *et al.*, 1994; Lungarini *et al.*, 2005]. Therefore, accurately quantifying the mechanical properties, such as the elastic moduli and peak stress, for the rocks constituting a volcanic edifice is a crucial goal for the reliability of

the modelling inversions of deformation patterns. It has been shown that there is an underestimation of the source depth and volume change for the migration and accumulation of magma beneath volcanoes due to the interpretation of geodetic data using homogeneous models [Manconi *et al.*, 2007]. Results from this study suggest that it is important to consider that elastic moduli do not remain constant and heavily depend on the level of crack damage in a rock.

7.6 The role of confining pressure in the evolution of elastic moduli

For the most part, rocks contained within the Earth's brittle upper lithosphere are under 'all-round-compression' i.e. they experience an effective confining pressure (P_{eff}). A uniaxial method has been employed in this part of the study so that the behaviour rock in the immediate sub-surface (couple of tens of metres) can be investigated. This scenario is indeed true for the volcanic edifice setting discussed. However, this is not generally applicable and uniaxial experiments are often prone for criticism [e.g. Healy, 2008], since most rock in the Earth's crust is subject to an effective confining pressure that can greatly influence rock physical properties. Despite this, Ayling *et al.* [1995] measured dynamic moduli during the triaxial deformation of DDS and found very similar trends in their evolution with damage to those reported here for static moduli (Fig. 7.5).

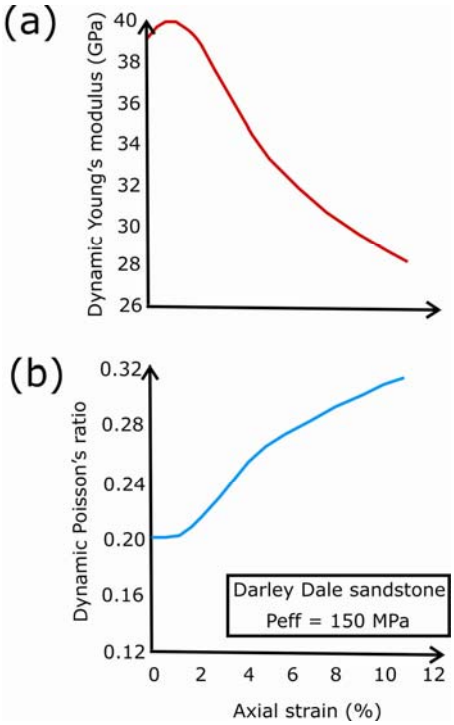

Figure 7.5. Calculated effective dynamic (a) Young's modulus and (b) Poisson's ratio for DDS at an effective confining pressure of 150 MPa using the method of [Soga *et al.*, 1978]. Note that experiments were performed on dry samples [taken from Ayling *et al.*, 1994].

The data from Ayling et al. [1994] are not derived from stress-cycling experiments however. To this end an increasing-amplitude stress-cycling experiment has been performed on DDS under triaxial conditions. The experiment was conducted under a 30 MPa P_{eff} (50 MPa confining pressure (P_c) and a 20 MPa pore fluid (distilled water) pressure (P_p)) and at 20°C. It must be noted that triaxial experiments use a larger sample size of 100 mm by 40 mm diameter (samples were prepared for triaxial experimentation as outlined in **5.2 Rock sample preparation**). The radial strain was calculated using the pore volumetry and therefore describes an average radial strain across the sample. In the uniaxial experiments performed in this study, together with the majority of previous studies, the radial strain was measured across the middle of the sample, where the greatest change in radial strain is seen due to sample barrelling and

edge effects. It can be argued that using the pore volumetry is a more accurate method; however, the data presented here from pore volumetry should be treated as somewhat of a minimum effect.

The stress-strain curve for the experiment, shown in Fig. 7.6a, demonstrates that the response to stress-cycling in rock under triaxial conditions is very similar to that for uniaxial compression. The rock becomes progressively more compliant in each cycle due to the increase in crack damage that leads to increasing amounts of irrecoverable strain; this can be most easily observed in the axial strain curves. However, due to the confinement, the mode of failure changed from axial splitting to shear faulting as in Figs. 8.11 and 8.12 (see Chapter Eight). The peak stress for the experiment was about 130 MPa, a reduction from the short-term peak stress (σ_p) stress calculated to be 155 MPa (see Chapter Eight, Fig. 8.6). Fig. 7.6b shows the calculated values of Young's modulus and Poisson's ratio plotted against cycle number. The Young's modulus shows a similar trend, albeit more modest, compared to the uniaxial experiments shown in Fig. 6.10. The initial Poisson's ratio is much higher, probably due to the 30 MPa P_{eff} closing up pores and cracks. However it is first seen to decrease before increasing after the third cycle up to about 0.44 (a similar value reached during uniaxial experiments). This result can be explained in much the same way as the uniaxial experiments. The first three cycles are likely to have imparted distributed, isotropic crack damage that has resulted in a decrease in Poisson's ratio. Beyond this point, commensurate with entering a deformation regime dominated by dilatancy (see Chapter Eight, Fig. 8.6), an anisotropic crack network starts to build as deformation becomes more localized. Such cracks are preferentially oriented parallel to the applied stress (i.e. axially). They therefore open easily when stress is re-applied on the next loading cycle, leading to a high radial strain and therefore an increase in Poisson's ratio.

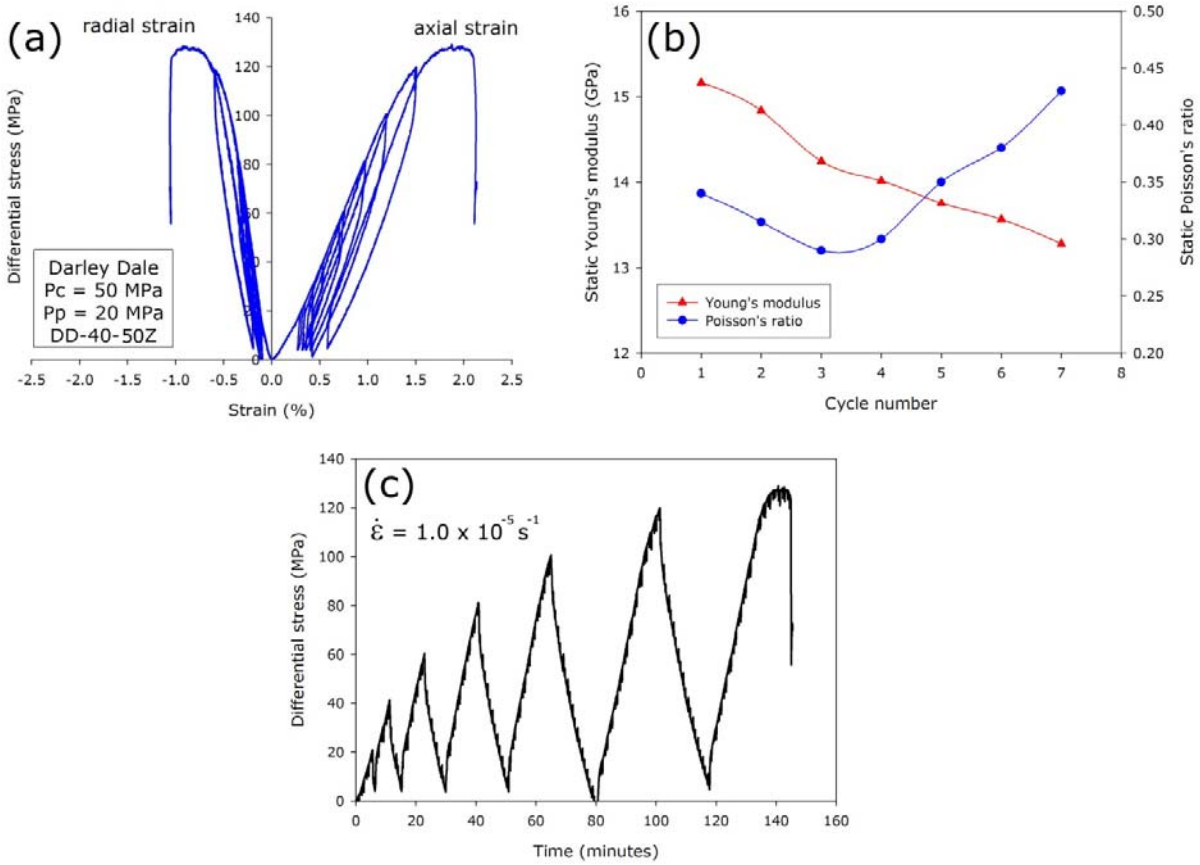

Figure 7.6. (a) Representative axial and radial stress-strain curves for a sample of DDS under increasing-amplitude stress-cycling [sample DD-40-50Z]. Volumetric strain has been excluded for clarity. Experimental conditions are indicated on the figure. P_c – confining pressure; P_p – pore fluid pressure. (b) Static elastic moduli evolution with increasing cycles from an increasing-amplitude cyclic stressing experiment on DDS. (c) Example of a loading path from an increasing-amplitude, stress-cycling experiment on a sample of DDS that failed during the 7th loading cycle. The strain rate used during experimentation is indicated on the figure.

7.7 Avenues for future research

The obvious direction for this research is to delve into stress-cycling experiments performed under a confining pressure. To the author's knowledge, no studies have investigated the evolution of static elastic moduli with increasing crack damage caused by stress-cycling under triaxial stress conditions. A more systematic study is required in order to confirm that the same trends are observed under a variety of effective confining pressures.

The data can also be used to model stress rotations [Faulkner *et al.*, 2006]. It has been shown that, for crystalline rock, damage-induced changes to elastic moduli can provide the necessary stress rotation to allow fault weakening without the occurrence of hydrofracture i.e. the pore pressure can remain high [Faulkner *et al.*, 2006]. Damage-induced elastic changes in both the rock comprising the volcanic edifice and underlying sedimentary rock at Mt. Etna, caused by pressurization/depressurization cycles, could therefore result in stress rotations near faults that traverse both the edifice and sedimentary rocks and potentially influence flank stability [Allard *et al.*, 2006].

Chapter eight

8. Time-dependent Deformation: Brittle Creep in Darley Dale Sandstone

8.1 Introduction

This chapter reports results from a systematic experimental study of brittle creep in Darley Dale sandstone under triaxial stress conditions. Firstly, the investigated material is introduced and experimental techniques explained. Benchmark results from a series of constant strain rate experiments and conventional brittle creep experiments are then presented. This is followed by results from stress-stepping experiments in which the influence of both effective confining pressure (P_{eff}) and pore fluid pressure (P_p) on brittle creep is investigated.

8.2 Sample material and experimental methodology

All experiments were performed at room temperature in the servo-controlled triaxial rock deformation apparatus (see Chapter Four, section **4.3 The triaxial deformation ensemble**) situated in the Rock & Ice Physics Laboratory (RIPL) at University College London. Axial strain was continuously monitored using LVDT displacement transducers, and porosity change was measured continuously by means of a servo-controlled pore fluid pressure intensifier and volumometer (see Chapter Four, section 4.3.5.1 Intensifiers/pore volumometers). Acoustic emission (AE) output was recorded and stored by a VALLEN AMSY-5 AE recording system (see Chapter Four, section *4.4.2 AE data recording systems and logging software)* using ten PZT-5A transducers mounted on steel inserts embedded within the rubber sample jacket (see Chapter Four, section 4.3.4.1 The jacketing system). For full details on the experimental set-up see Chapter Four. All experiments presented in this section were performed on DDS (for rock descriptions and characterization see Chapter Five) and were prepared for use in the triaxial ensemble as outlined in **5.2 Rock sample preparation**. During the experiments a significant P_p gradient is not

expected due to the high permeability of DDS of 5 x 10^{-15} m^2 at the implemented experimental pressure conditions [Zhu and Wong, 1997].

Prior to performing brittle creep experiments, a series of constant strain rate experiments were conducted at a strain rate of 1.0 x 10^{-5} s^{-1} and an P_{eff} of 30 MPa (50 MPa confining pressure (P_c) and P_p of 20 MPa) in order to establish the short-term failure characteristics of the test material. Once this had been established, a series of conventional brittle creep experiments were performed under the same P_{eff} conditions. In these latter experiments, samples of DDS were first loaded to a pre-determined percentage of the short-term peak stress (σ_p) or strength established during the constant strain rate experiments. Generally, this was in the range 80 to 90% of σ_p [see also Baud and Meredith, 1997]. Following this pre-loading, samples were allowed to deform under constant stress until failure. The evolution of crack damage was monitored throughout each experiment by measuring the damage proxies of axial strain, porosity change and output of AE energy. At the end of each experiment, creep strain rates were calculated from the secondary ('steady-state') phase of the creep curve (see Chapter Three, Fig. 3.17).

It must be noted as this point that all creep experiments in this study were performed under a constant force, since during deformation a change in sample length also corresponds to a change in sample cross-sectional area in contact with the actuator piston. This is an important consideration during ductile, high temperature experiments where strains can reach up to 30%; however, it is also sensible to compute the change in stress due to an increase in cross-sectional area for the constant strain rate experiments and creep experiments presented in this study. The change in cross-sectional area was calculated using the following formula, where A is the cross-sectional area, V is the sample volume and ℓ is the sample length:

$$\frac{\Delta A}{A} = \frac{\Delta V}{V} - \frac{\Delta \ell}{\ell} \qquad [8.1]$$

This change in cross-sectional area during deformation was then included into the calculation of stress. Fig. 8.1 shows the difference between the corrected and uncorrected stress values for constant strain rate experiments on both DDS (Fig. 8.1a) and EB (Fig. 8.1b). Fig. 8.1 demonstrates that, at a maximum axial strain between 2.0 and 2.5%, there is only a very modest change in the stress calculation. A decrease of 2 and 6 MPa is observed in the σ_p for DDS and EB respectively. Nevertheless, it will be corrected stress that will be computed for experimental throughout this study.

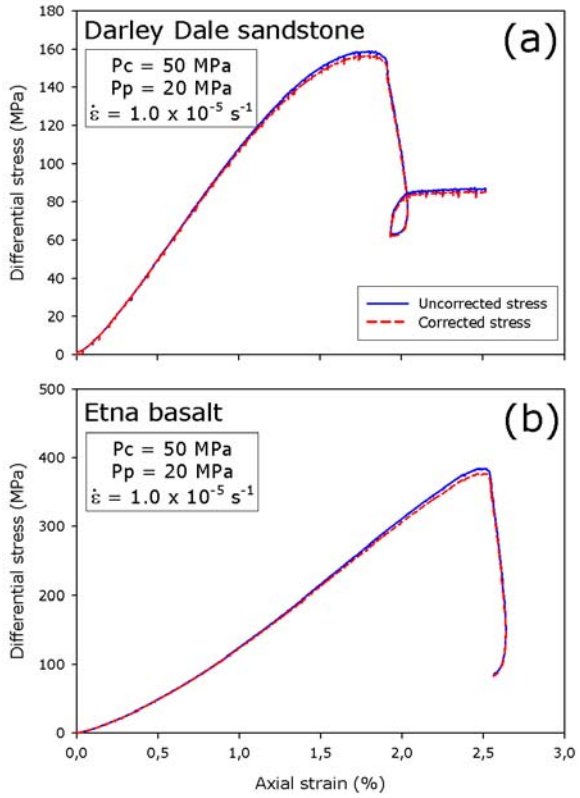

Figure 8.1. Conventional constant strain rate experiments on samples of (a) DDS and (b) EB showing the difference between the uncorrected stress (solid blue lines) and the stress corrected for the change in cross-sectional area during deformation (dashed red lines). P_c – confining pressure; P_p – pore fluid pressure.

The calculated stress during constant force creep experiments can also be corrected for the change in cross-sectional area. Fig. 8.2 shows the difference between the corrected and uncorrected stress values for a conventional creep experiment on DDS (Fig. 8.2a) and EB (Fig. 8.2b). Fig. 8.2 shows that there is a change of only about 0.1 to 0.3 MPa during a brittle creep experiment on DDS and EB respectively. This is less than 0.1% of the σ_p, approximately the same variation as in the load measurement (see Fig. 8.3c). This uncertainty in the applied differential stress will be shown on creep strain rate – differential stress plots by the size of the datapoint. From hereon, creep experiments will be described as being performed under a constant stress.

A key aspect of any study involving experiments running over extended periods of time is the stability of measurements over the maximum experiment duration. The stability of our experimental system was therefore determined by loading a sample of DDS to a low percentage (about 60%) of σ_p and holding this stress constant for a period of ten days. During this period, the servo-controlled parameters of axial load, confining pressure and P_p all remained essentially constant, and fluctuations in axial strain and pore volume change (converted to porosity change for the experiments in this study) were both less than 0.1% (Fig. 8.3). The maximum diurnal range in ambient laboratory temperature was ±2.5°C, but this reduced to ±0.3°C inside the deformation cell (Fig. 8.4), most likely due to the large thermal mass of the cell (approximately 1100 kg of nickel chrome alloy steel) and the significant volume of oil inside the vessel. This small temperature fluctuation did not significantly affect any of the other measured parameters (Fig. 8.3).

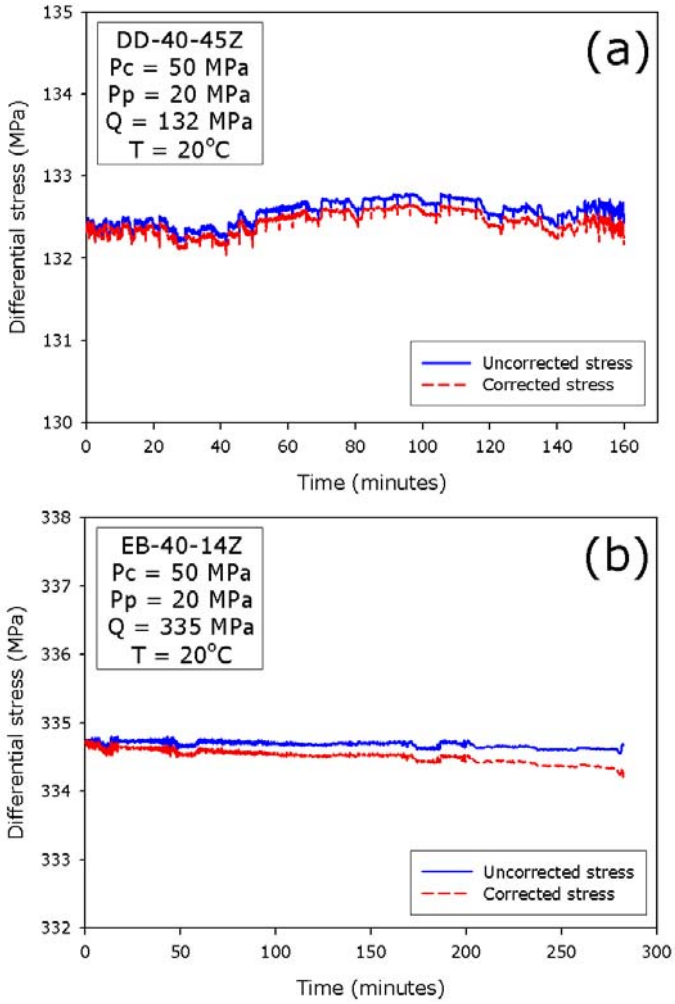

Figure 8.2. Conventional brittle creep experiments on samples of (a) DDS and (b) EB showing the difference between the uncorrected stress (solid blue lines) and the stress corrected for the change in cross-sectional area during creep (dashed red lines). P_c – confining pressure; P_p – pore fluid pressure.

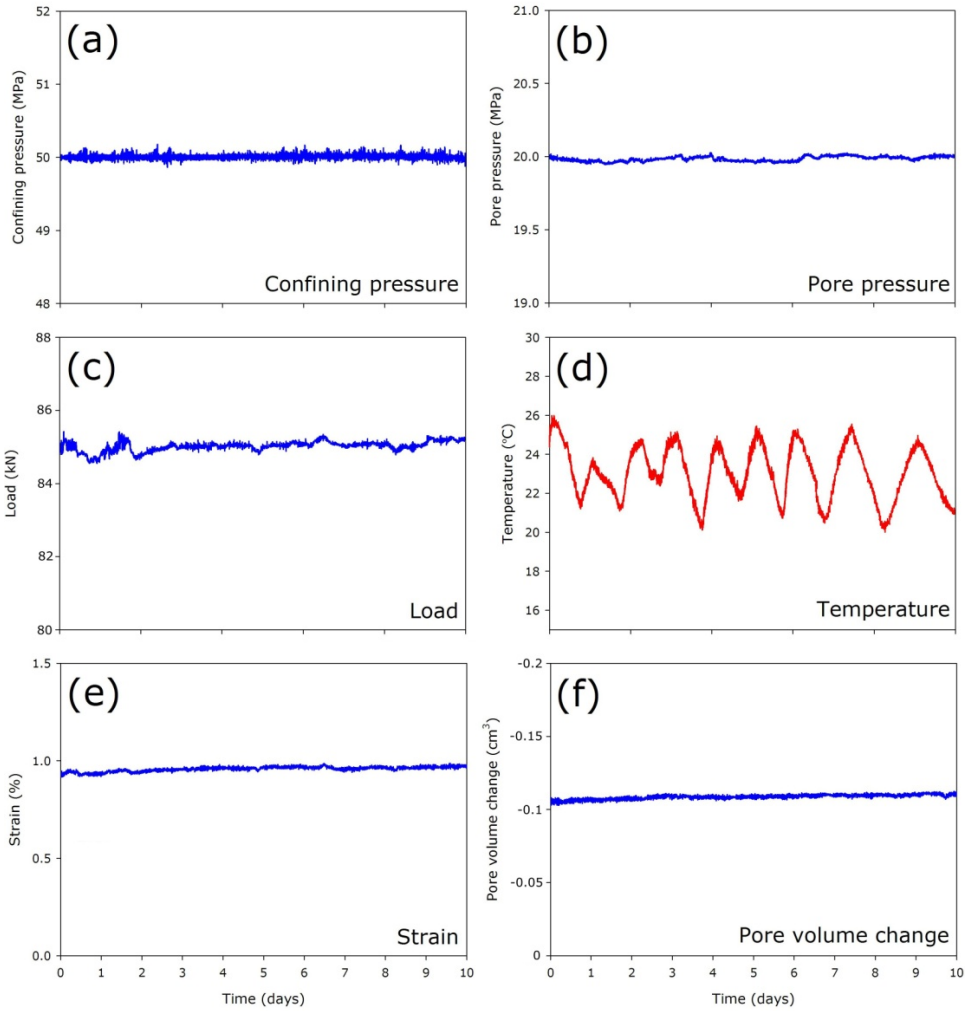

Figure 8.3. Graphs to demonstrate the stability of the experimental equipment over a ten day period during which a low load (approximately 60% of the short term peak stress) was maintained on a water-saturated sample of DDS (a) confining pressure (b) pore fluid pressure (c) load (d) ambient laboratory temperature measured next to the pressure vessel (e) strain and (f) pore volume change.

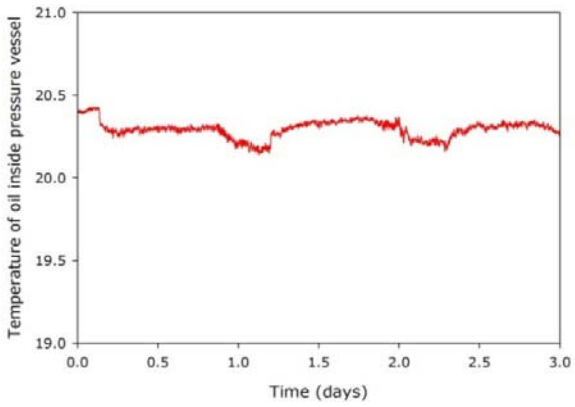

Figure 8.4. Temperature of the silicone oil measured inside the pressure vessel adjacent to the rock sample over a three day period. Graph demonstrates that the diurnal temperature range within the vessel was about ±0.2°C during experimentation.

Together with the conventional creep experiments, a number of focussed experiments were performed to investigate the spatial distribution and density of cracking at the onset of tertiary creep. During these experiments, samples of DDS were allowed to deform to the onset of tertiary creep at different but constant applied differential stresses that produced different creep strain rates. Once deformation reached the onset of tertiary creep, the samples were slowly unloaded; and P_c and P_p were decreased to ambient values. Samples were then removed from the apparatus, and epoxy-impregnated thin sections were prepared for microscopic analysis. Crack densities were determined using the same method as that reported by Wu *et al*. [2000] for measurements on DDS [see also, Underwood, 1970]. Linear crack densities and orientations were measured over a gridded area of 11 x 11 mm^2 from the same relative location within each sample (Fig. 8.5a). This was achieved by counting the number of crack intersections (P) with an array of 10 parallel grid lines (at 0.1 mm spacing) orientated both normal ($P_\perp$) and parallel ($P_\parallel$) to the axial loading direction (Fig. 8.5b).

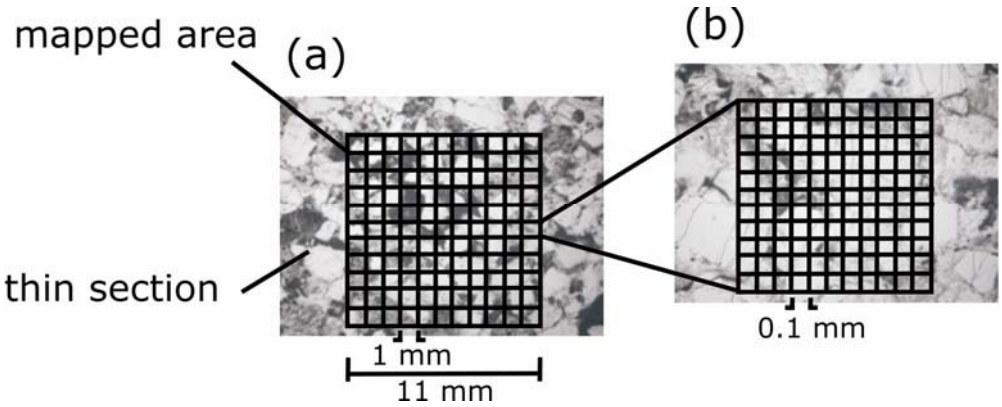

Figure 8.5. Schematic diagram of the crack counting method showing the (a) mapped area and the 121 sub-regions from where the measurements were taken and (b) the array of parallel grid lines orientated both normal and parallel to the axial loading direction. Photomicrographs are not to scale and are included for illustrative purposes only.

The crack densities per unit volume (P_v) can be inferred from the linear intercept measurements taken in the two orthogonal directions ($P_\perp$ and $P_\parallel$) using the following formula:

$$Pv = \left(\frac{\pi}{2}\right) P_\perp + \left(2 - \left(\frac{\pi}{2}\right)\right) P_\parallel \quad [8.2]$$

The anisotropy of the crack distribution (A_c), the ratio between the surface area of cracks parallel to σ_1 and the total crack surface area, can be determined using the following formula:

$$Ac = \frac{P_\perp - P_\parallel}{P_\perp + \left(\left(\frac{4}{\pi}\right) - 1\right) P_\parallel} \quad [8.3]$$

8.3 Results

8.3.1 Constant strain rate experiments

As noted above, a series of constant strain rate experiments were first undertaken on samples of DDS in order to establish its short-term deformation and failure characteristics. A key goal was to ascertain the reproducibility of the σ_p that would be used to guide the applied stress in later creep experiments. Fig. 8.6 shows the stress-strain curves and the damage proxies of porosity change and cumulative AE energy for two representative experiments conducted at a constant strain rate of 1.0 x 10^{-5} s^{-1} and a P_{eff} of 30 MPa (Fig. 8.6). The repeatability is excellent, and the small variation between the two sets of curves simply reflects the variability between natural rock samples. A series of experiments yielded a mean σ_p of 155 ± 6 MPa. Following an initial period of compaction, the onset of dilatancy, termed *C'* [see Chapter Two, Fig. 2.16; Wong *et al.*, 1997], occurs at differential stress of around 40 MPa and is marked on the differential stress versus volumetric strain curve presented as Fig. 8.7. As expected, this also corresponds to the onset of AE output around 0.5% axial strain as shown in Fig. 8.6c. The minimum in the porosity change curve (Fig. 8.6b) marks the transition from compaction-dominated deformation to dilatancy-dominated deformation, which is termed *D'*. This also corresponds to the maximum in the volumetric strain (Fig. 8.7), and occurs at a differential stress around 130 MPa.

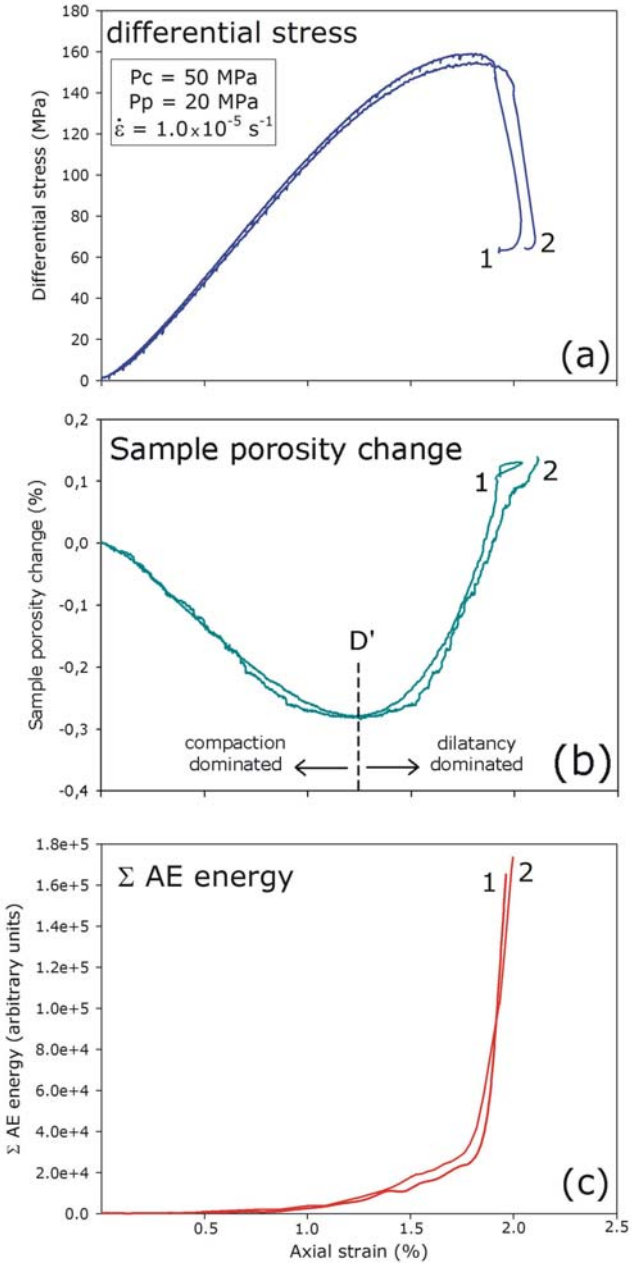

Figure 8.6. Two conventional constant strain rate experiments on water-saturated DDS showing variability in the three proxies for damage within the rock. (a) stress-strain curves, (b) the porosity change curves and (c) the AE energy output curves. Experimental conditions are indicated on the figure and *D'*, the stress at which a dilatant-dominated regime dominates, is indicated in (b). P_c – confining pressure; P_p – pore fluid pressure [DD-40-04Z and DD-40-05Z]. The experiments were both performed at 20°C.

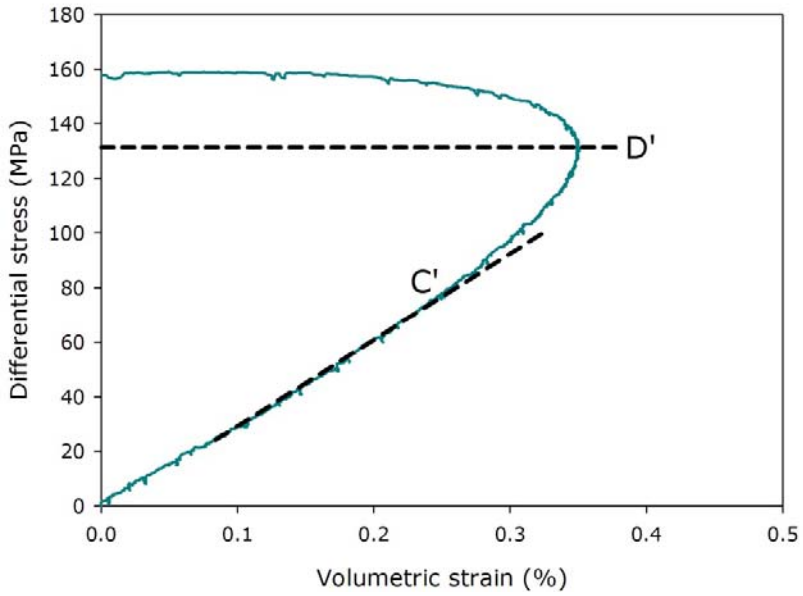

Figure 8.7. Volumetric strain against differential stress for a constant strain rate experiment on water-saturated DDS. Both *C'*, the stress at which the volumetric strain deviates from that observed from hydrostatic loading, and *D'*, the stress at which a dilatant-dominated regime dominates, are indicated [sample DD-40-04Z].

Fig. 8.8 shows the results from a series of experiments to investigate the influence of P_{eff} on the deformation of DDS at a constant strain rate of 1.0 x 10^{-5} s^{-1}. Increasing the P_{eff} results in significant increases in the σ_p (Fig. 8.8 and 8.9 and Table 8.1), the duration of the strain softening phase that precedes failure and the axial strain at dynamic failure (Fig. 8.8a). Similar observations in sandstone have been reported by [Wong *et al.*, 1997; Baud *et al.*, 2000]. Fig. 8.8b also shows pore volume variation is also strongly influenced by the P_{eff}. Indeed, the axial strain at which D' occurs increases significantly (see also, Table 8.1). Since the transition from compaction to dilatancy occurs later with increasing effective pressure, it is perhaps not surprising that the onset of significant AE output (Fig. 8.8c) also occurs later. However, the total output of AE energy does not vary significantly between experiments even though the rock strength increases by over 70%, from 103 MPa (P_{eff} = 10 MPa), to 152 MPa (P_{eff} = 30 MPa) and eventually to 178 MPa (P_{eff} = 50 MPa) (Fig. 8.8 and Table 8.1).

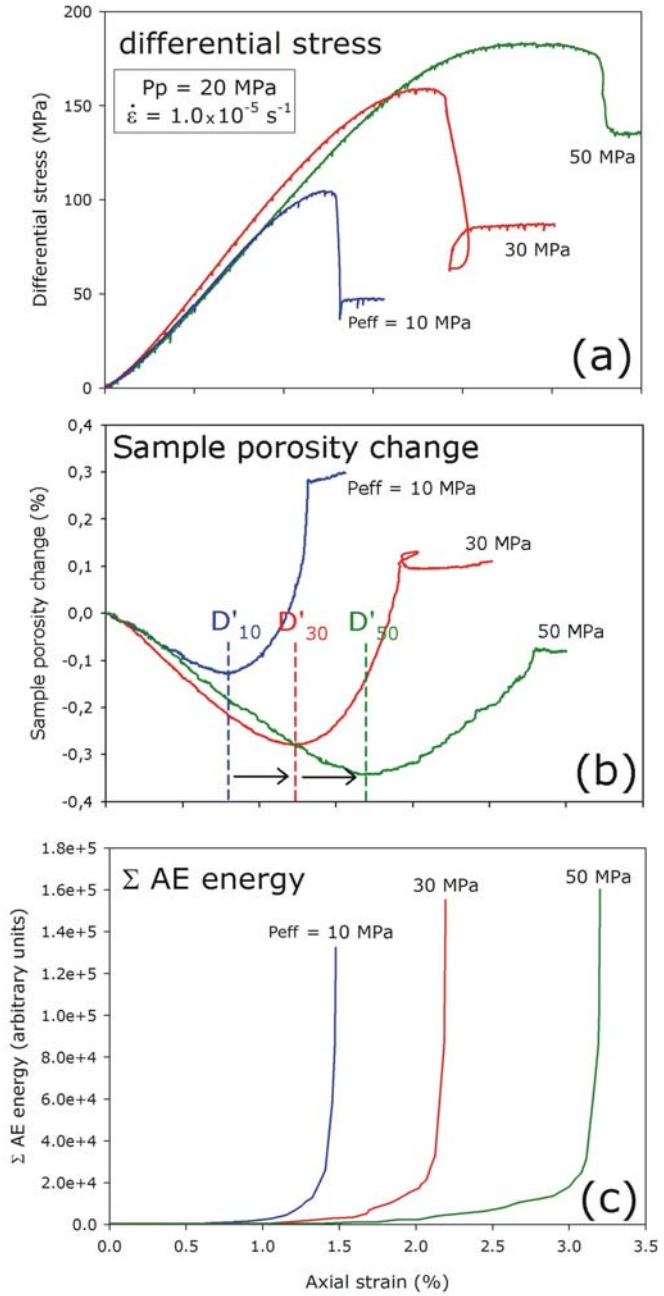

Figure 8.8. Conventional constant strain rate experiments on water-saturated DDS showing variability in (a) the stress-strain curves, (b) the porosity change curves and (c) the AE energy output curves for effective confining pressures of 10, 30 and 50 MPa, whilst maintaining a constant P_p of 20 MPa. Experimental conditions are indicated on the figure an the position of *D'*, and how it migrates with increasing P_{eff}, is indicated in (b). P_p – pore fluid pressure [samples DD-40-33Z, DD-40-05Z and DD-40-30Z]. The experiments were all performed at 20°C.

Sample	Effective confining pressure (MPa)	Confining pressure (MPa)	Pore fluid pressure (MPa)	Peak stress (MPa)	% strain at *D'*
DD-40-33Z	10	30	20	103	0.8
DD-40-05Z	30	50	20	152	1.25
DD-40-30Z	50	70	20	178	1.7

Table 8.1. Summary of the experimental conditions, peak stresses and % strain at *D'* for three experiments performed at effective confining pressure of 10, 30 and 50 MPa (same experiments as shown in Fig. 8.6).

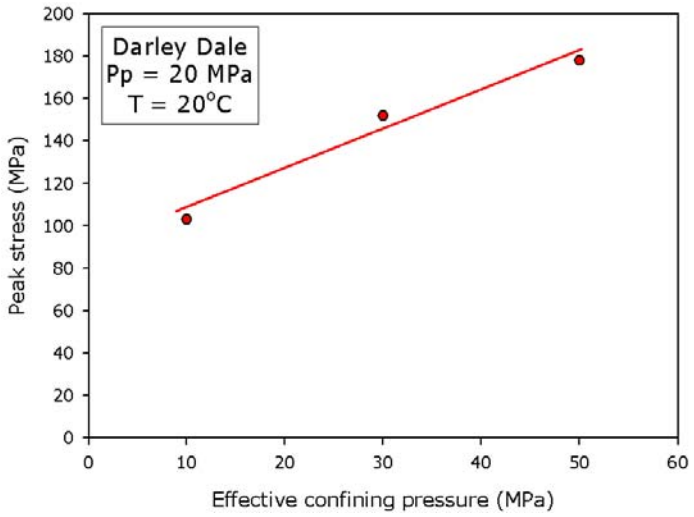

Figure 8.9. Graph of peak stress against effective confining pressure for three experiments performed at effective confining pressure of 10, 30 and 50 MPa (same experiments as shown in Fig. 8.8). Experimental conditions are indicated on the figure. P_p – pore fluid pressure; *T* – sample temperature [samples DD-40-33Z, DD-40-05Z and DD-40-30Z].

Fig. 8.10 shows the results from two experiments to investigate the influence of P_p on the deformation of DDS at a constant strain rate of 1.0 x 10^{-5} s^{-1}. In stark contrast to increasing the P_{eff}, a twofold increase in the P_p from 20 MPa to 40 MPa, whilst maintaining a constant P_{eff} of 30 MPa, exerts no influence on the mechanical properties of the sample during experimentation. This is expected as the gross mechanical behaviour of a porous rock sample is governed by the P_{eff} [Terzaghi, 1943; Jaeger *et al.*, 2007].

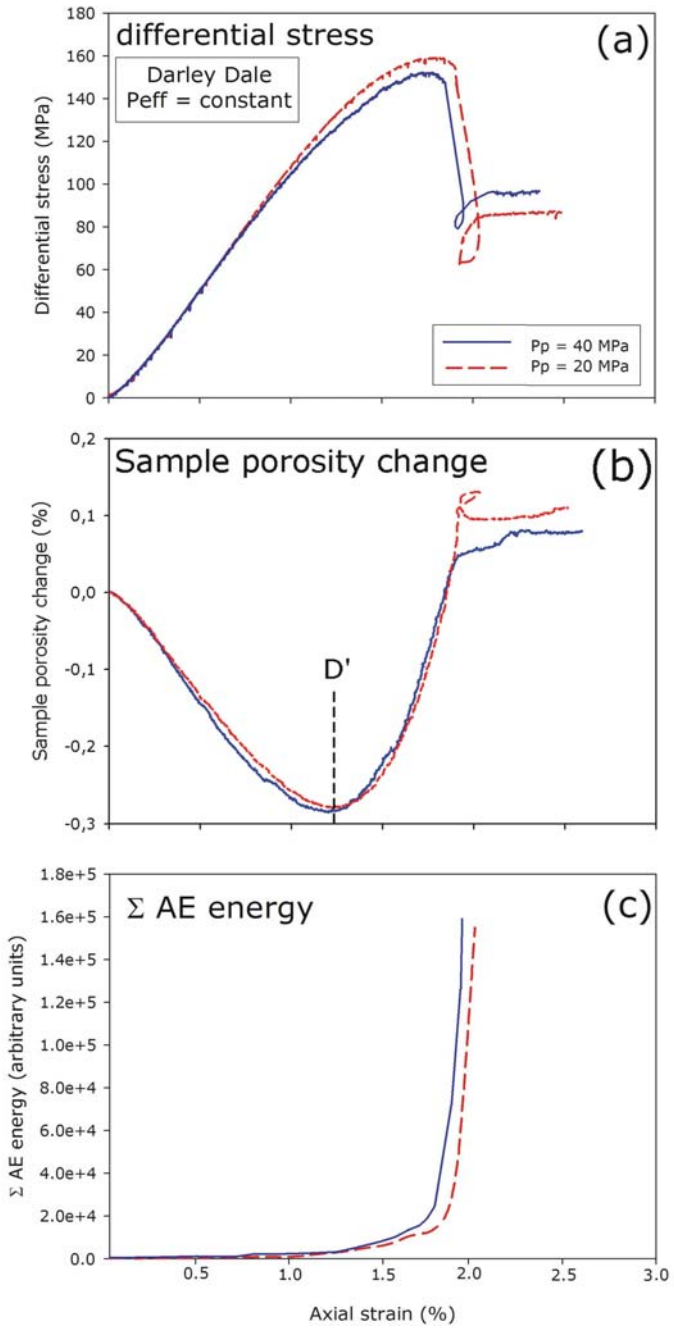

Figure 8.10. Conventional constant strain rate experiments on water-saturated DDS showing variability in (a) the stress-strain curves, (b) the porosity change curves and (c) the AE energy output curves for pore fluid pressures of 20 and 40 MPa, whilst maintaining a constant effective confining pressure of 30 MPa. Experimental conditions are indicated on the figure. P_{eff} – effective confining pressure; P_p – pore fluid pressure [samples DD-40-03Z and DD-40-37Z]. The experiments were both performed at 20°C.

All samples, under the range of tested conditions, failed by brittle shear faulting. The angle of the shear fracture was orientated approximately 30° to the direction of the maximum principal stress (Fig. 8.11). Photomicrographs of a sample of DDS deformed until failure under a constant strain rate are provided in Fig. 8.12 and show the localized shear band and extensive grain cracking adjacent to the shear band.

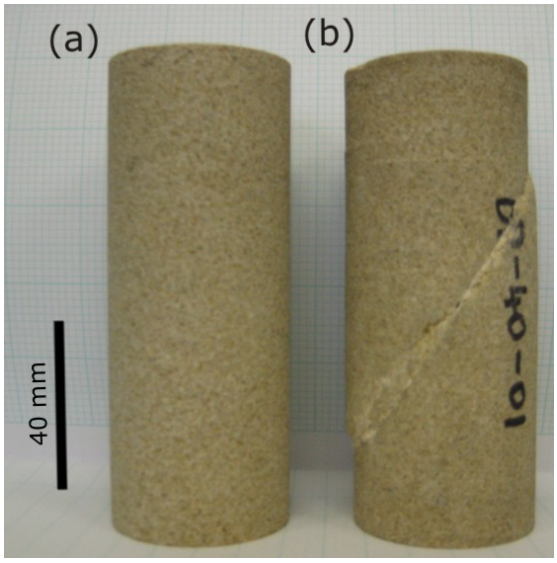

Figure 8.11. Photographs of (a) an undeformed sample of DDS, and (b) a sample of DDS that failed by shear faulting under a constant strain rate of 1.0 x 10^{-5} s^{-1} under the conditions of P_c = 50 MPa and P_p = 20 MPa (P_{eff} = 30 MPa) and a sample temperature of 20°C [sample DD-40-01Z].

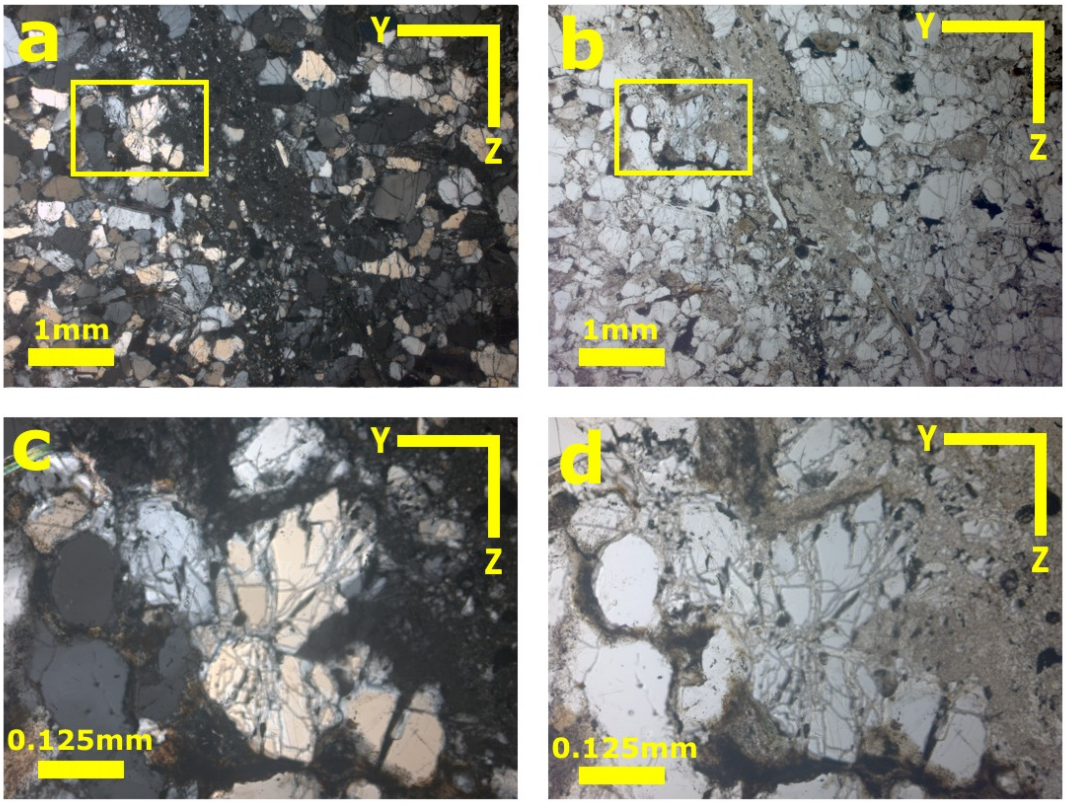

Figure 8.12. Photomicrographs of a sample of DDS deformed to failure under a constant strain rate of 1.0 x 10^{-5} s^{-1} (a) and (b) shear band within sample under both XPL and PPL (b) and (c) close inspection of the microcracks present within the grains adjacent to the shear band in both XPL and PPL. Zoomed in area is indicated on both (a) and (b). All photomicrographs are taken within the same YZ plane, the Z-axis is normal to the axial loading direction (for details on directional information see *5.2.2 Orientation of samples*). For photomicrographs of undeformed samples of DDS see Chapter Five, Fig. 5.2.

8.3.2 Conventional brittle creep experiments

Conventional creep experiments were performed on samples of DDS over a range of constant applied differential stress levels in order to yield times-to-failure and creep strain rates over several orders of magnitude. Following Baud and Meredith [1997], the levels of applied differential stress were selected to be greater than that corresponding to *C'*, but lower than the stress level that would generate very rapid failure within a few seconds or a few minutes. Such stress levels generally corresponded to between 80% and 90% of the σ_p. Fig. 8.13 shows the results from three such experiments conducted across this applied stress range. The three independent proxy measures of damage (axial strain, porosity change and cumulative AE energy) are shown plotted against time for each experiment.

All of the axial strain curves show the trimodal behaviour via which creep deformation is generally interpreted [Baud and Meredith, 1997; Main, 2000; see also Chapter Three, Fig. 3.17]. Each primary creep phase is characterized by an initially high strain rate that decreases with time to reach a quasi-linear secondary phase that is often interpreted as steady-state creep. After an extended period of time, a tertiary phase is entered, characterized by accelerating strain. This eventually results in macroscopic failure of the samples by propagation of a shear fault, similar to that shown in Fig. 8.11.

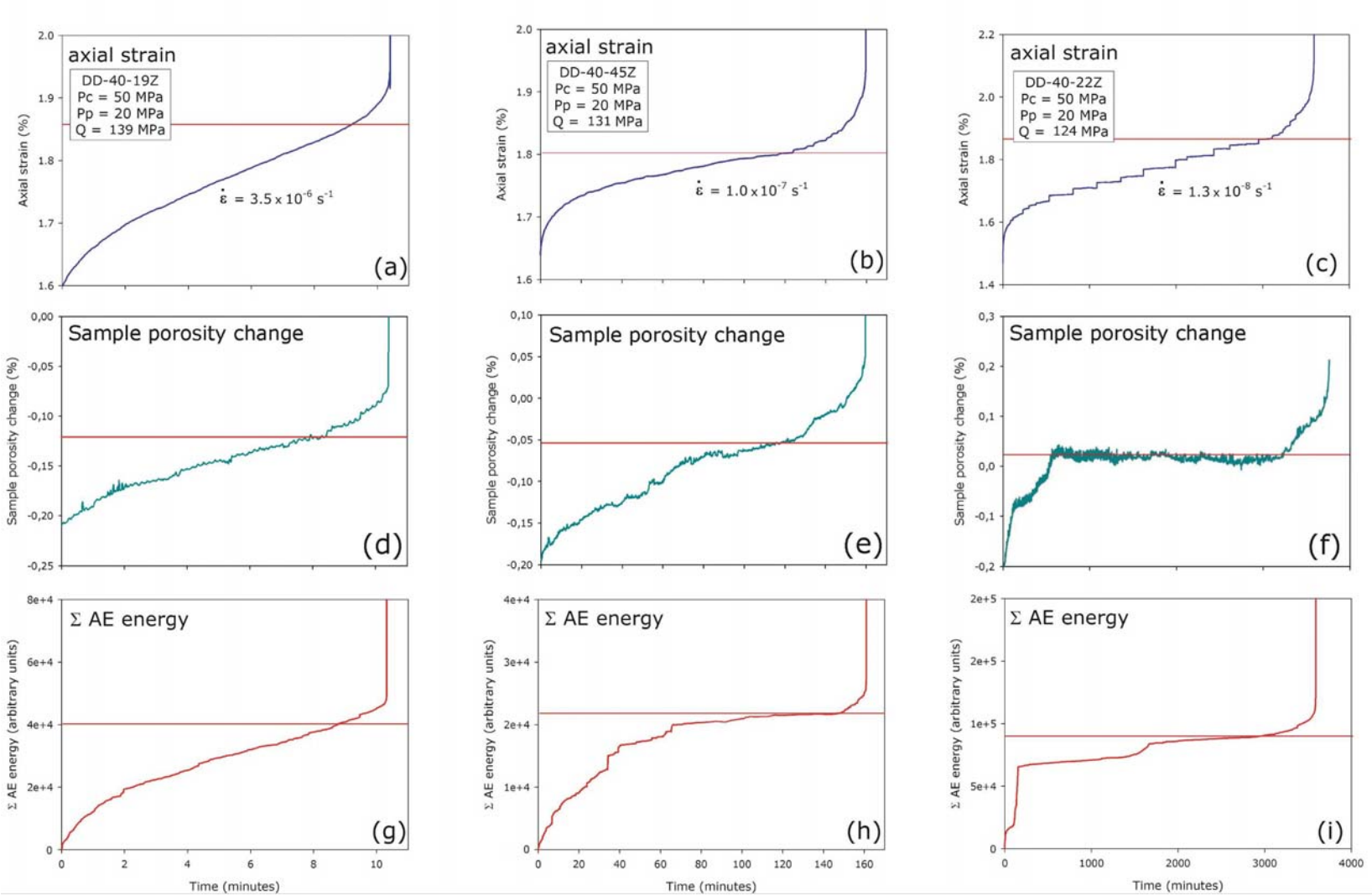

Figure 8.13. Damage proxies of axial strain, pore volume change and AE energy output for three conventional brittle creep experiments on DDS held at applied differential stresses that yielded creep strain rates over three orders of magnitude. Experimental conditions are indicated on the figure. P_c – confining pressure; P_p – pore fluid pressure; Q – applied differential stress [samples DD-40-19Z, DD-40-22Z and DD-40-45Z]. The experiments were all performed at 20°C.

Creep strain rates were calculated for each experiment from the quasi-linear portions of the strain-time curves. Quasi-linear behaviour was confirmed by plotting the first derivatives of the strain-time curves (i.e. strain rates against time); an example of one such plot is shown in Fig. 8.14a. Fig. 8.14a demonstrates that there is a large constant strain rate portion of the curve as evidenced by the plateau in the strain rate i.e. there is a real steady-state creep phase (indicated by the shaded region). The steady-state creep strain rate was calculated as the average strain rate of this portion of the strain-time creep curve. The error on the strain rate calculation, represented in subsequent figures using error bars, is simply the deviation of the data from the average creep strain rate calculated for this portion (see red line, Fig. 8.14a). The creep strain rates indicated on Fig. 8.13 are the calculated average values.

However, it is intuitive that, during the secondary creep phase, the sample microstructure will not remain constant and will be evolving i.e. maybe there is no steady-state. To emphasize any minor changes in gradient during the steady-state secondary creep phase, Fig. 8.14a was replotted using a log strain rate (Fig. 8.14b). Fig. 8.14b shows that, even with the strain rate plotted on a log axis, the portion of the curve from where the creep strain rate was calculated remains approximately linear. There is an enhanced curvature in the calculated fit at the extremes of the designated area (shaded portion, Fig. 8.14b). This is however incorporated into the calculated error in the creep strain rate measurements (see subsequent figures). Furthermore, the calculated creep strain rate does not invoke a particular mechanism and is simply the observed strain rate during the portion of a creep curve that is quasi-linear.

The data show that both the creep strain rate and the overall time-to-failure depend strongly and non-linearly on the level of applied differential stress. Even modest increases in applied stress can result in order of magnitude changes in times-to-failure and creep strain rates. At 139 MPa (90% of σ_p), the time-to-failure was approximately 10 minutes and the creep strain rate was 3.6×10^{-6} s^{-1}. At 131 MPa (85% of

σ_p), the time-to-failure increased to 160 minutes and the creep strain rate decreased to 1.0 x 10^{-7} s^{-1}. Finally, for 124 MPa (80% of σ_p), the time-to-failure was 3600 minutes and the creep strain rate was 1.3 x 10^{-8} s^{-1}. In summary, a 10% reduction in applied differential stress resulted in an increase in time-to-failure and a decrease in creep strain rate of approximately 2.5 orders of magnitude. A summary is given in Table 8.2.

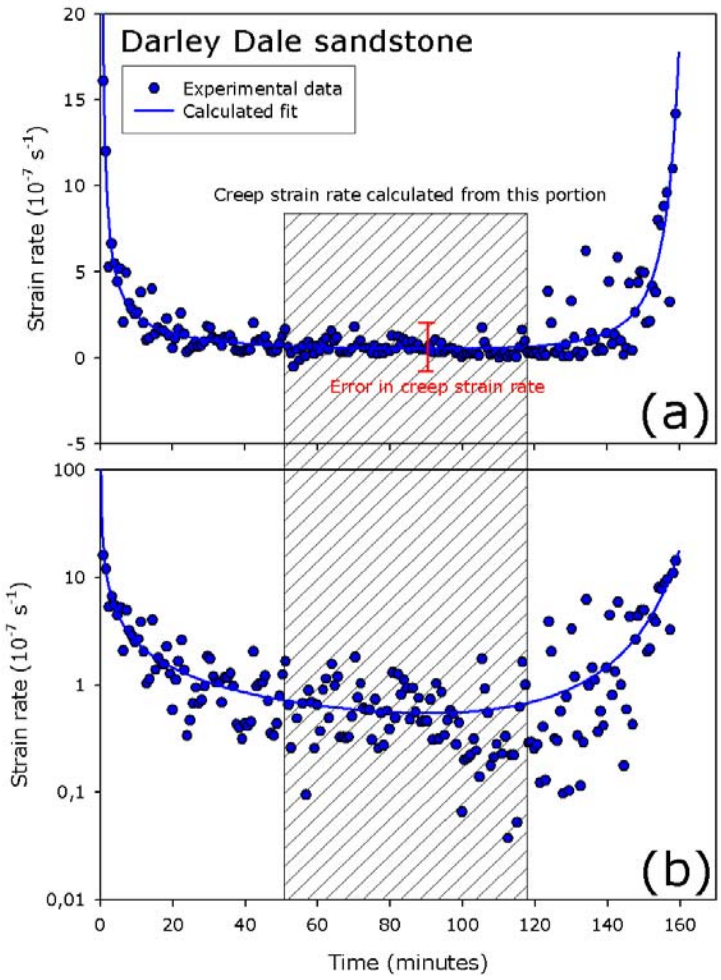

Figure 8.14. (a) Plot of the first derivative of the experimental strain data from a conventional creep experiment on DDS that yielded a creep strain rate of 1.0 x 10^{-7} s^{-1} against time. (b) Plot of the first derivative, as in (a), with creep strain rate plotted on a log axis. Experimental conditions are indicated on Fig. 8.11b [sample DD-40-45Z] (courtesy of S. Hunt).

Sample	Effective confining pressure (MPa)	Level of applied stress (% of σ_p)	Resultant creep strain rate (s^{-1})	Time-to-failure (minutes)
DD-40-40Z	30	75	3.7×10^{-9}	12960
DD-40-22Z	30	80	1.3×10^{-8}	3600
DD-40-45Z	30	85	1.0×10^{-7}	160
DD-40-19Z	30	90	3.5×10^{-6}	10

Table 8.2. Summary of the experimental conditions and resultant calculated creep strain rates and time-to-failure for a suite of conventional creep experiments on DDS (note that sample DD-40-40Z is explained later in the text). Other experiments are shown in Fig. 8.13.

Table 8.3 shows the relative durations spent in each of the three creep curve phases for the conventional creep experiments on DDS spanning creep strain rates of three orders of magnitude and shows that the percentage of time spent in each of the three phases remains remarkably similar, regardless of the applied differential stress and resultant creep strain rate and time-of-failure. For each experiment the duration of the primary creep phase is approximately 20% of the total time-to-failure, the duration of the secondary and tertiary creep phases are approximately 60 and 20% respectively (Table 8.3).

Sample	Resultant creep strain rate (s^{-1})	Time spend in primary creep phase		Proportion of time spend in secondary creep phase		Proportion of time spend in tertiary creep phase	
		(minutes)	(%)	(minutes)	(%)	(minutes)	(%)
DD-40-40Z	3.7×10^{-9}	1800	14	9000	69	2160	17
DD-40-22Z	1.3×10^{-8}	600	17	2400	67	600	17
DD-40-45Z	1.0×10^{-7}	30	19	90	56	40	25
DD-40-19Z	3.5×10^{-6}	2.5	25	6.5	65	1	10

Table 8.3. Summary of the time spent in each of the three creep curve phases for conventional creep experiments on DDS (note that sample DD-40-40Z is explained later in the text). Experiments are shown in Fig. 8.11. Percentages are rounded to the nearest percent.

The two other damage proxies of porosity change and cumulative AE energy also exhibit trimodal behaviour throughout, although the curves are visibly less smooth in some cases. This is particularly the

case for the porosity change and cumulative AE curves at the lowest applied stress (Q = 125 MPa; Figs. 8.13f and 8.13i). In this case, there is a much greater contribution to the total porosity change and cumulative AE energy during the primary creep phase than for the experiments at higher applied stresses. In fact, the porosity appears to remain essentially constant during the whole of the secondary creep phase.

In all cases, the tertiary creep phase is characterized by accelerations in all three proxies for damage (onset of tertiary creep phase is marked by red lines on Fig. 8.13). Furthermore, the value of each of the three proxy measures at the onset of tertiary creep is in a very narrow range, regardless of the different applied stresses and the very different lengths of time required to reach that point; an axial strain in the range of 1.80 to 1.88%, a porosity change in the range -0.12 to 0.02 %, and cumulative AE energy in the range of 10^4 units. This implies that the onset of tertiary creep occurs at a similar level of crack damage in all cases.

To explore the lower limit of the creep strain rate realistically achievable in the laboratory, a conventional creep experiment was also performed at approximately 75% of σ_p (Fig. 8.15). During this experiment, the axial strain demonstrated trimodal behaviour similar to the experiments shown in Fig. 8.13. However, throughout the duration of the primary and secondary creep phases, the porosity change steadily decreased up until very close to failure when a sudden and substantial increase was observed; this is likely to be the result of a small leak in the pore pressure system. Unfortunately, for this experiment, the output of AE energy was stored over several files, some of which became corrupted due to their very large file size. Quantitatively different behaviour is seen during conventional creep experiments at the lowest applied differential stresses (Fig. 8.13c and 8.15). At these low strain rates, the strain increases in a step-wise manner with extended periods of very slow strain rate punctuated by

short periods of very rapid deformation. At higher applied stresses, and therefore higher strain rates, this step-wise behaviour is not observed. Since the steps are not commensurate with any output of AE energy it would be wise to assume that they are not a result of the deforming sample but a product of stick-slip of the moving seal in the actuator piston.

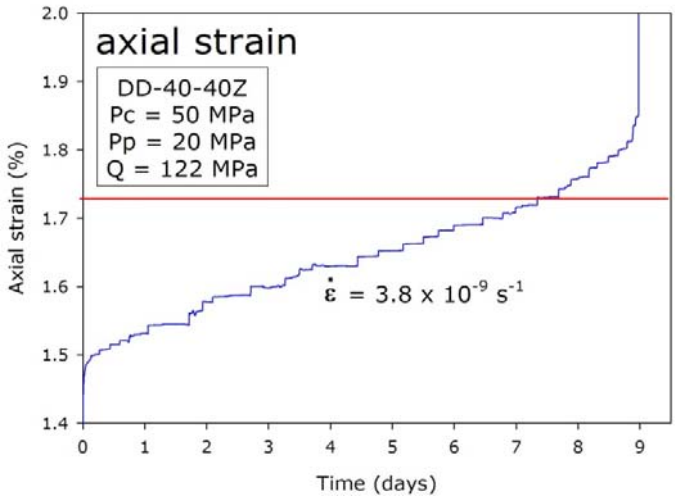

Figure 8.15. Creep curve for a conventional brittle creep experiment held at 75% of σ_p that yielded a creep strain rate of 3.8 x 10^{-9} s^{-1}. Experimental conditions are indicated on the figure. P_c – confining pressure; P_p – pore fluid pressure; Q – applied differential stress [sample DD-40-40Z].

Results from the two creep experiments that were stopped at the onset of tertiary creep in order to investigate the spatial distribution and density of microcracking are shown in Fig. 8.16. These experiments were conducted at applied differential stresses of 137 MPa and 131 MPa, resulting in creep strain rates of 1.4 x 10^{-6} s^{-1} and 1.7 x 10^{-7} s^{-1}, respectively. The linear crack densities from these two samples, together with those from an undeformed sample and a sample taken to failure (but measured away from the localized shear band) for comparison, are displayed in Table 8.4, together with their anisotropies. Fig. 8.17 shows photomicrographs of the two samples taken to the onset of tertiary creep (Fig. 8.17a and 8.17b), together with the shear band in the post-failure sample (Fig. 8.17c) and

microcracking in the failed sample (Fig. 8.17d). A micrograph of an undeformed sample, at the same scale, can be seen in Chapter Five, Fig. 5.2. The results of the microstructural analysis (Table 8.4) show that the linear crack densities ($P_{\perp}$ and $P_{\parallel}$) and the crack area per unit volume all increase from the values for the undeformed state for both samples taken to the onset of tertiary creep, and increase markedly more for the sample taken to failure. While the increases for the samples taken to the onset of tertiary creep are modest (11 to 44%), the increase for the sample taken to failure is much greater (300 to 700%). This can also be clearly seen in the photomicrographs of Fig. 8.17. Similar trends are seen in the crack anisotropy, with the crack fabric for the sample taken to failure dominated by axial microcracks.

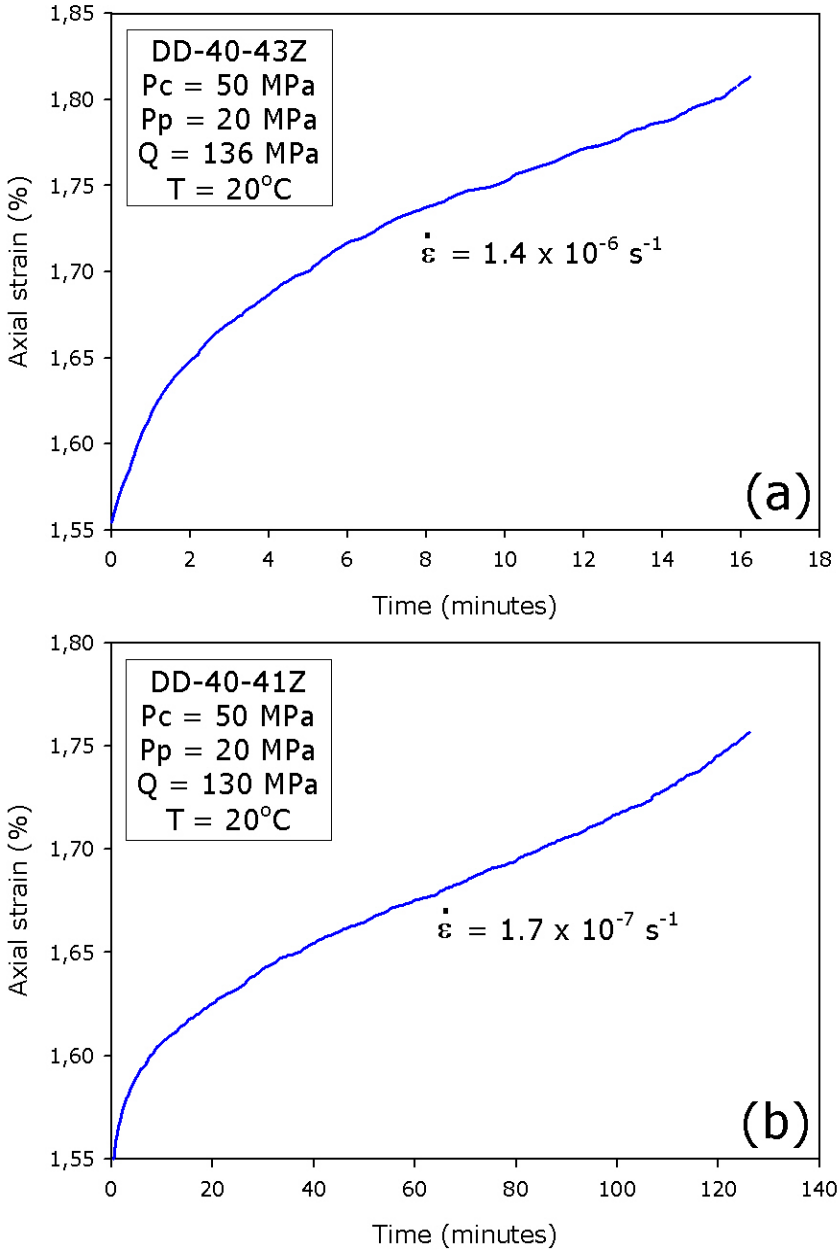

Figure 8.16. Axial strain against time for the two experiments designed to investigate the rock microstructure at the onset of accelerating tertiary creep at (a) 1.4 x 10^{-6} and (b) 1.7 x 10^{-7} s^{-1}. Experimental conditions are displayed on the figure. P_c – confining pressure; P_p – pore fluid pressure; Q – applied differential stress; T – sample temperature [samples DD-40-41Z and DD-40-43Z].

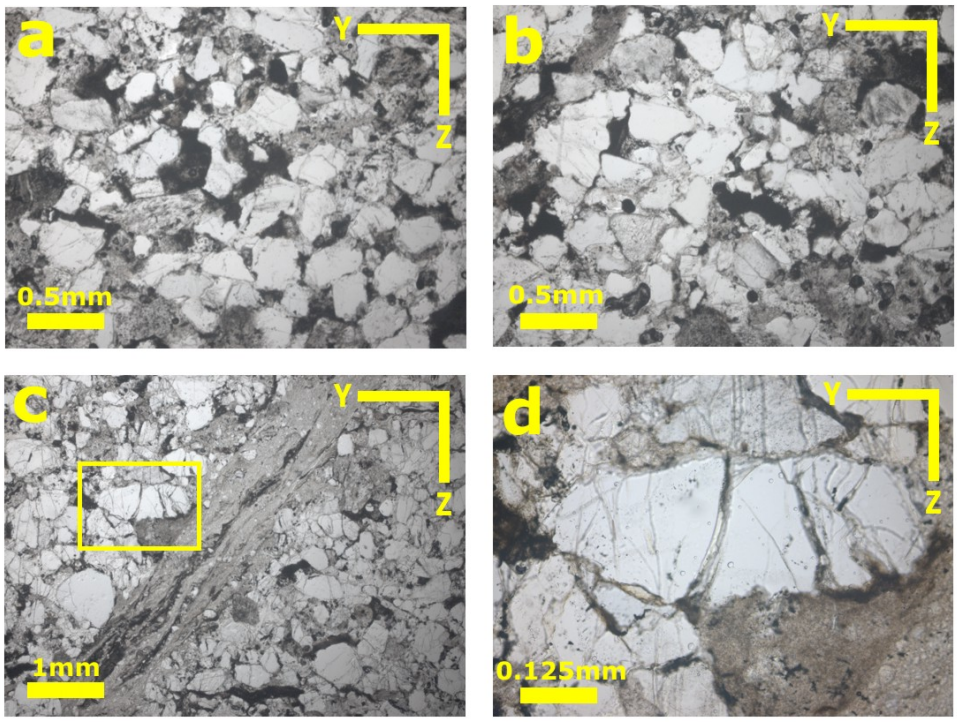

Figure 8.17. Photomicrographs of samples of DDS under plane polarized light used for the investigation into the spatial distribution and density of microcracks. (a) sample taken to the onset of accelerating tertiary creep at 10^{-6} s^{-1} (see Fig. 8.15a) (b) sample taken to the onset of accelerating tertiary creep at 10^{-7} s^{-1} (see Fig. 8.15b) (c) shear band within sample taken to failure in a conventional brittle creep experiment (d) close inspection of the microcracks present within the grains in the same sample as in (c). All photomicrographs are taken within the same YZ plane, the Z-axis is normal to the axial loading direction (for details on directional information see Chapter Five, section *5.2.2 Orientation of samples*). For photomicrographs of undeformed samples of DDS see Chapter Five.

Sample conditions	**Crack density for linear intercepts normal to σ_1 $P_\perp$ (mm^{-1})**	**Crack density for linear intercepts parallel to σ_1 $P_\parallel$ (mm^{-1})**	**Crack area per unit volume P_v (mm^{-1})**	**Crack anisotropy A_c**
Undeformed	0.41	0.38	0.81	0.08
Onset of tertiary creep at 1.7 x 10^{-7} s^{-1}	0.59	0.45	1.11	0.27
Onset of tertiary creep at 1.4 x 10^{-6} s^{-1}	0.53	0.42	1.00	0.24
Post-failure	2.97	1.46	5.29	0.68

Table 8.4. Quantitative microstructural data from optical microscopy analysis on an undeformed sample, samples taken to the onset of the tertiary creep phase under different creep strain rates and a post-failure sample. See text for details on measurement technique.

The relation between applied differential stress and creep strain rate (calculated for the quasi-linear portions of trimodal creep curves, as defined by the plateau in Fig. 8.14 for example) is plotted on semi-log axes in Fig. 8.18. For the range of stresses applied and strain rates measured in the presented experiments, the relation can be adequately described by either a power law or exponential function (Chapter Three, Equations [3.6] and [3.7]) with the parameters listed in Table 8.5. Because the relation is so non-linear and stress sensitive, any variation in the initial state of damage within test samples becomes very important. This is a significant problem when using natural materials such as porous rocks, because there is inevitably variation in porosity and crack density between different samples even when cored form the same block of material. This problem was partially circumvented by measuring the porosity, bulk density and elastic wave velocities of all our samples prior to testing, and rejecting samples where these measures fell outside a very narrow range. This inevitably led to considerable sample wastage. However, the consequence of not pursuing such a rigorous approach is illustrated by the solid square in Fig. 8.18, which shows data for a sample with a marginally higher porosity and lower bulk density than our main suite of samples. An anomalously high strain rate was achieved with only a modest applied stress. The likely cause is that the sample had a higher level of initial damage than our main suite of samples. The same problem has previously been reported in Baud and Meredith [1997]. In order to circumvent the problem of sample variability, a methodology of stress-stepping in which multiple brittle creep experiments can be conducted on a single sample was adopted.

The relation between the time-to-failure and the creep strain rate is plotted on semi-log axes in Fig. 8.19. The relation is again very stress sensitive and only a small change in applied differential stress results in a dramatic change in the time-to-failure (Fig. 8.19). The relationship between time-to-failure and the creep strain rate can be adequately described by both a power law and exponential function (see Fig. 8.19 for details).

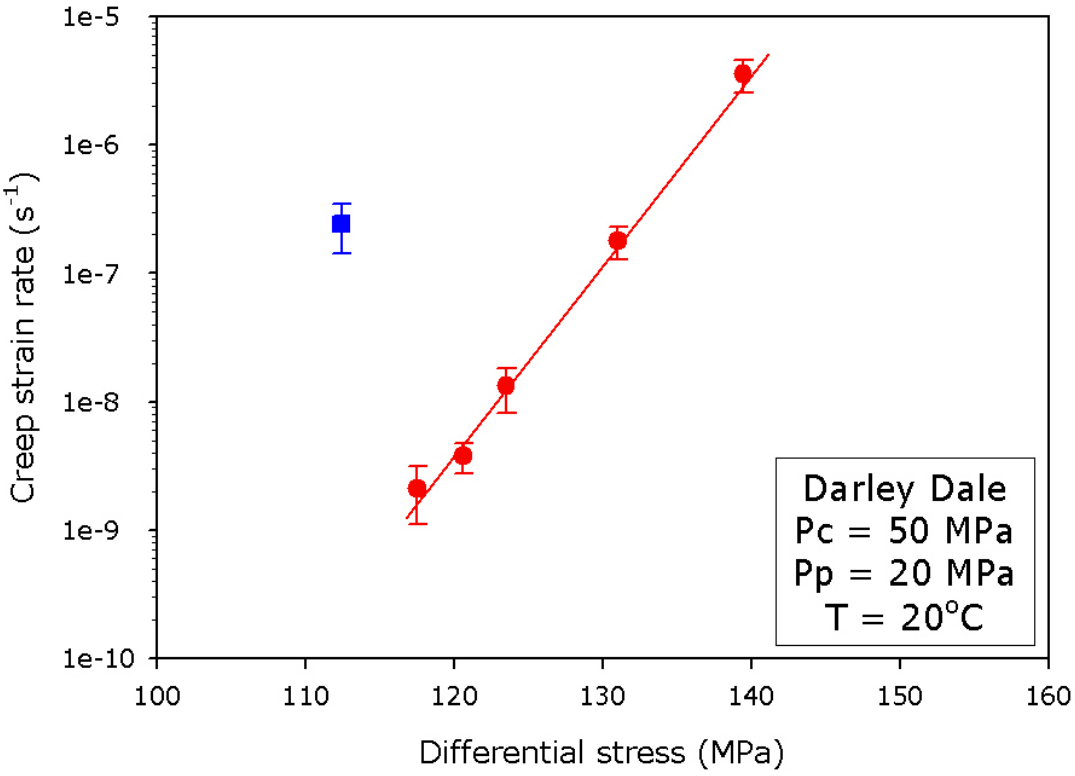

Figure 8.18. Creep strain rate data from multiple conventional brittle creep experiments on water-saturated DDS plotted on a log scale against applied differential stress (red circles). The blue square represents a conventional brittle creep experiment that highlights the problem associated with sample variability during conventional brittle creep experiments (see text for details). Error in the creep strain rate measurements are denoted by the error bars, error in the differential stress values are represented by the size of the datapoints. P_c – confining pressure; P_p – pore fluid pressure; T – sample temperature.

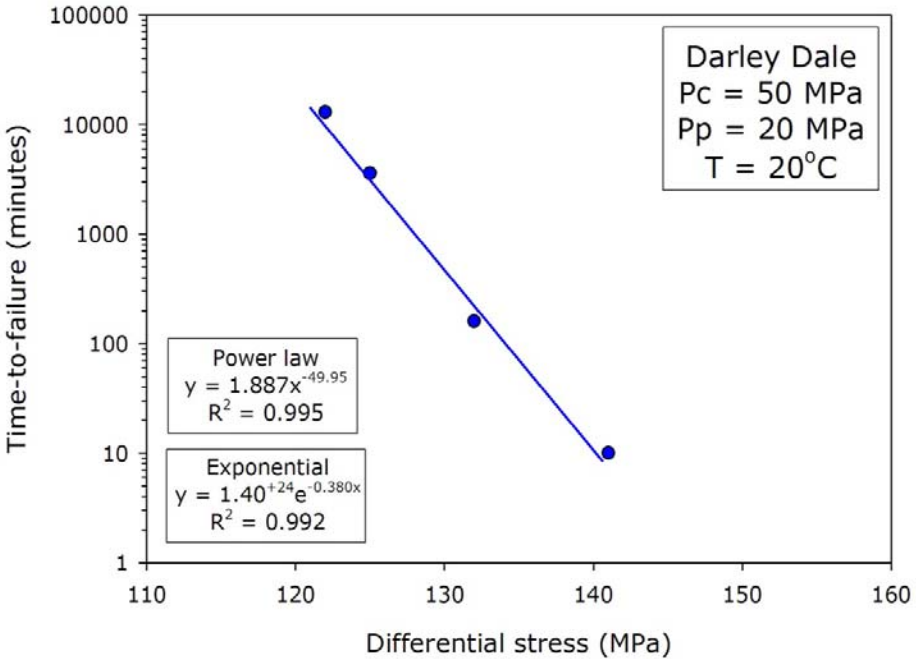

Figure 8.19. Time-to-failure data from multiple conventional brittle creep experiments on water-saturated DDS plotted on a log scale against applied differential stress. Experimental conditions are indicated on the figure. Power law and exponential function fits are also shown on the figure. P_c – confining pressure; P_p – pore fluid pressure; T – sample temperature (data in Table 8.2).

Sample number	Confining pressure (MPa)	Pore fluid pressure (MPa)	Effective confining pressure (MPa)	Temperature (°C)	Power law gradient function (η)	Exponential gradient function (β)	Power law R^2 value	Exponential R^2 value
DD-40-15Z	50	20	30	20	45.73	0.342	0.996	0.997
DD-40-44Z	50	20	30	20	44.59	0.331	0.997	0.999
DD-40-45Z	50	20	30	20	44.00	0.344	0.994	0.996
DD-40-28Z	30	20	10	20	52.68	0.691	0.988	0.984
DD-40-32Z	70	20	50	20	37.24	0.210	0.988	0.989
DD-40-35Z	70	40	30	20	45.48	0.325	0.994	0.992
Conventional creep experiments	50	20	30	20	44.53	0.347	0.995	0.997

Table 8.5. Experimental conditions, power law and exponential function gradient coefficients and results of regression analysis for a number of stress-stepping creep experiments (for more information see the next section) and the series of conventional creep experiments shown in Fig. 8.18. Power law and exponential function fits are calculated using Equations [3.6] and [3.7].

8.3.3 Stress-stepping brittle creep experiments

The overall aim of using the stress-stepping methodology is to be able to capture the type of data shown in Fig. 8.18 using a single sample, so that the problem of sample variability is confidently eliminated. In turn, this would allow the effect of other experimental variables of interest to be quantified in a more sample and time efficient manner. The stress-stepping approach has previously been used and has shown to provide reliable data by [Lockner, 1993; Maranini and Brignoli, 1999; Ngwenya *et al.*, 2001, among others].

A key point before starting any stress-stepping creep experiments is to determine the level of differential stress to be applied in the first stress step. Since the exact strength of any particular sample cannot be known prior to the experiment due to sample variability, a pre-determined percentage of the peak stress cannot be simply used, as explained at the end of the previous section. It is also clear that sample will not creep if stress levels are set below those required for the onset of dilatant cracking (*C'*). However, whilst *C'* can be determined relatively easily from the volumetric strain curve after an experiment, it is extremely difficult to determine in real time during an experiment. Therefore, *D'* (the transition from compaction-dominated deformation to dilatancy-dominated deformation as seen on porosity change curves, see Figs. 8.6 and 8.7) has been chosen as the starting point for the presented stress-stepping experiments. This has several advantages: (1) it is relatively easy to determine in real time during experiments because it is a minimum, (2) it is likely to represent a reproducible state of damage within the material and (3) because it marks the onset of dilatancy dominated deformation, it is likely to induce a measurable creep strain rate. Therefore, during stress-stepping experiments, samples were first loaded at a constant strain rate of 1.0×10^{-5} s^{-1} to *D'* (monitored from the porosity change curve and regardless of the level of applied stress required to reach this point). At this point, the applied

differential stress was held constant to allow the sample to go through primary creep and into secondary creep. Once the sample had undergone approximately 0.15 mm of axial shortening during secondary creep, the stress was stepped up by a small increment (usually in the range 5 to 7 MPa). It was found that about 0.15 mm of axial shortening was enough to allow an accurate creep strain rate to be determined. This cycle was then repeated sequentially until the sample eventually failed, usually after about 10 to 14 days. The methodology is illustrated in Fig. 8.20, which shows the last two stress steps imposed during the final day of a ten day experiment.

Creep stain rates were determined as outlined previously in this chapter; however, during stress-stepping creep experiments it could be possible to investigate the evolution of creep strain rate with respect to differential stress as a function of constant permanent strain i.e. under a constant microstructure. This can be achieved by plotting the first derivative of the entire strain – time curve for a stress-stepping experiment. However, the secondary creep phase has been shown to exhibit a very constant creep strain rate (Fig. 8.14), and when the first derivative is plotted for a stress-stepping experiment the creep strain rates were still within the range of the calculated error bars. Furthermore, such methods involve measuring creep strain rates on extrapolated experimental data curves; indeed a few of the stress steps will be extrapolated to a permanent strain at which the sample is likely to fail. Although this is an interesting concept, and has its merits (e.g. for the computation of a creep flow law), it has not been employed within this study.

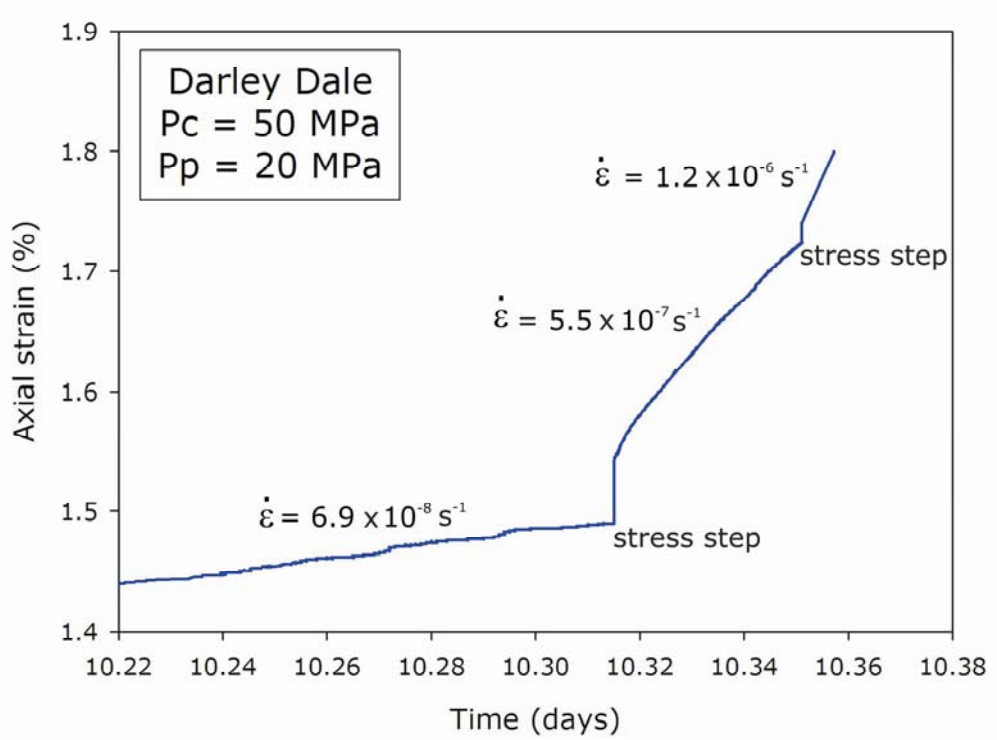

Figure 8.20. Graph of axial strain against time to demonstrate the methodology behind the stress-stepping brittle creep experiments. The figure shows the stress steps and from where the creep strain rates were calculated. The sample in this experiment failed after approximately 10.36 days. Experimental conditions are displayed on the figure. P_c – confining pressure; P_p – pore fluid pressure. This experiment was performed at 20°C.

In order to verify this methodology, a number of stress-stepping creep experiments were performed on samples of DDS under the same experimental conditions (Fig. 8.21), and these results were then compared with those from conventional creep experiments (Fig. 8.22). Fig. 8.22 shows the creep strain rates from a set of conventional experiments and a single stress-stepping experiment, all run at a P_{eff} of 30 MPa. It must be noted that the trends observed in the stress dependence of the creep train rates is virtually identical, but that the curves are somewhat offset. This offset is attributed to the problem of natural sample variability noted above. As before, the creep strain rate data collected from stress-stepping experiments under the outlined conditions can be adequately described by either a power law or exponential function (Table 8.5).

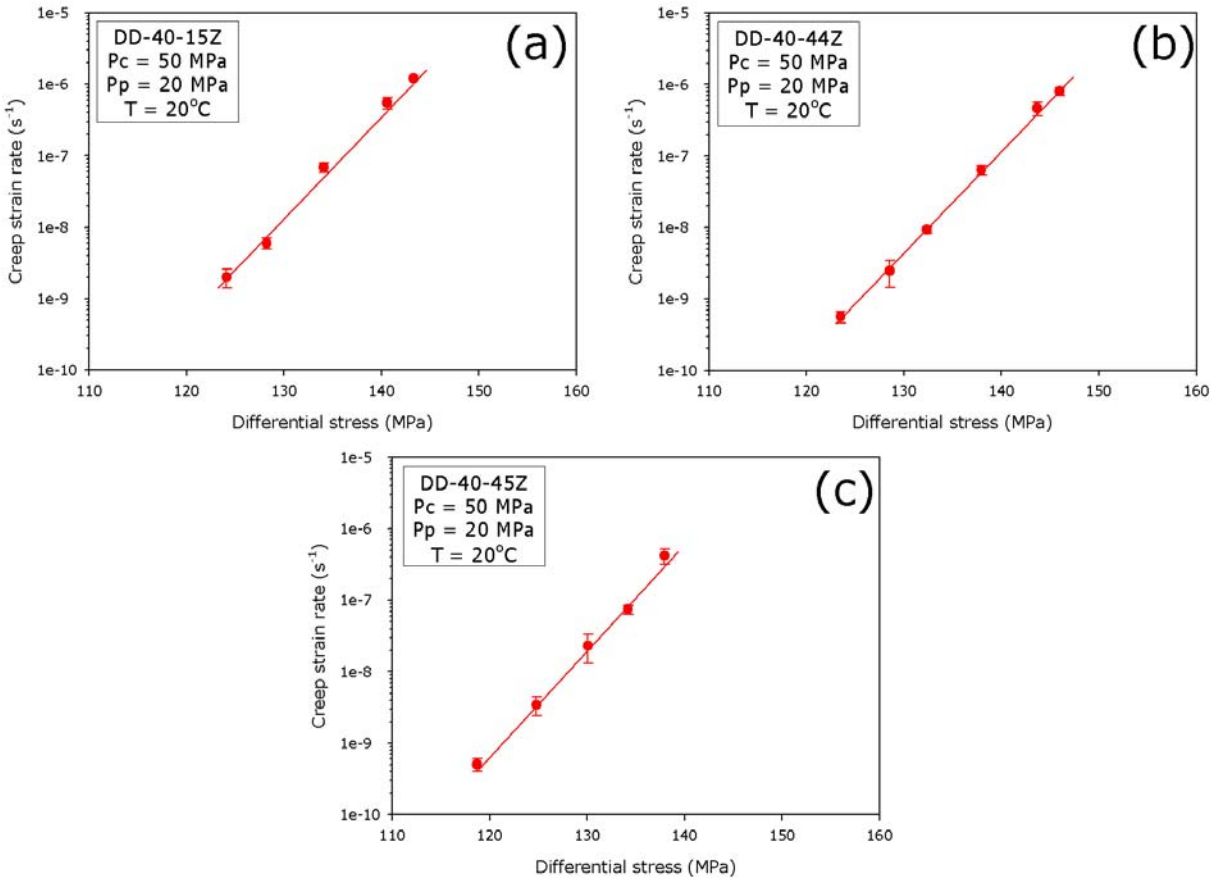

Figure 8.21. Creep strain rate data from three stress-stepping brittle creep experiments on water-saturated DDS. Creep strain rate data is plotted on a log scale against applied differential stress. Experimental conditions are displayed on the figure. Error in the creep strain rate measurements are denoted by the error bars, error in the differential stress values are represented by the size of the datapoints. P_c – confining pressure; P_p – pore fluid pressure; T – sample temperature [samples DD-40-15Z, DD-40-44Z and DD-40-45Z]. The fits to these curves are summarized in Table 8.5.

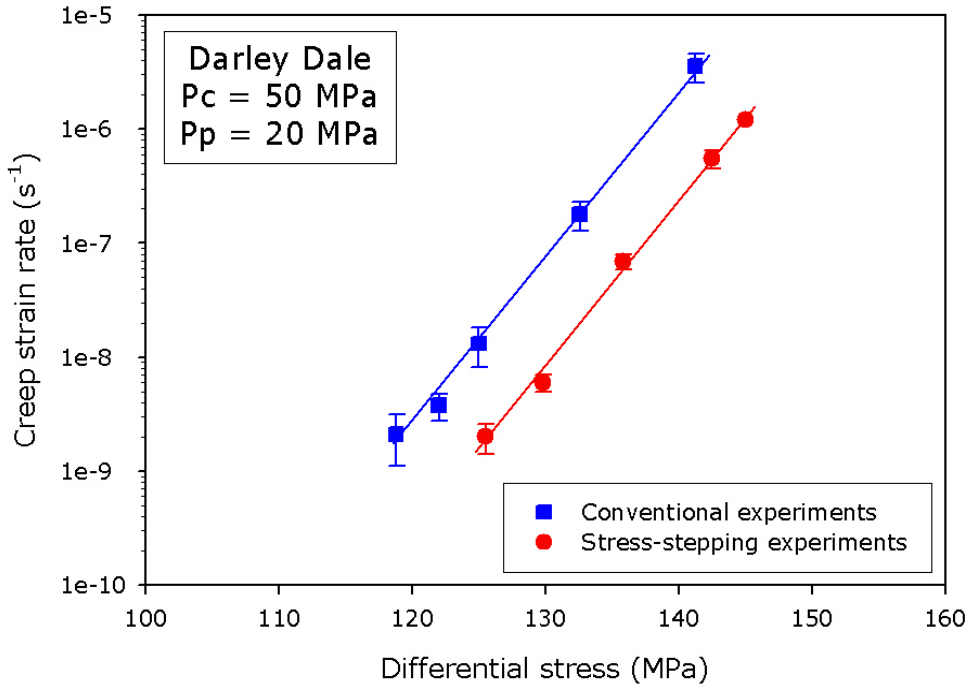

Figure 8.22. Creep strain rate data from a stress-stepping brittle creep experiment on water-saturated DDS (red circles) plotted side-by-side with those data derived from a suite of conventional brittle creep experiments (blue squares). Creep strain rate data is plotted on a log scale against applied differential stress. The horizontal shift in the experimental curves is due to initial sample variability (see text for details). Error in the creep strain rate measurements are denoted by the error bars, error in the differential stress values are represented by the size of the datapoints. Stress-stepping experimental data – sample DD-40-15Z (see Table 8.5). Experimental conditions are displayed on the figure. P_c – confining pressure; P_p – pore fluid pressure; T – sample temperature.

Having demonstrated that the stress-stepping technique can replicate the creep strain rate dependence on differential stress, the new methodology was then used to investigate the influence of P_{eff} on brittle creep at effective confining pressures of 10, 30 and 50 MPa (whilst maintaining a constant P_p of 20 MPa). The results are given in Fig. 8.23, which shows that varying the P_{eff}, even over this modest range, has a profound influence on creep strain rates. Firstly, the strain rates are shifted to dramatically lower values for the same differential stress as P_{eff} is increased. This appears consistent with the results from constant strain rate experiments showing that DDS is stronger at higher P_{eff} (Fig. 8.8). However, the

increase in strength seen in constant strain rate experiments as confining pressure is increased from 10 to 50 MPa is about 70% (plotted as unfilled shapes in Fig. 8.23), while the decrease in creep strain rate over the same interval is many orders of magnitude. Secondly, the gradient of the curves on Fig. 8.23 describing the relation between creep strain rate and differential stress decrease significantly as P_{eff} is increased (see Table 8.5 and Fig. 8.24).

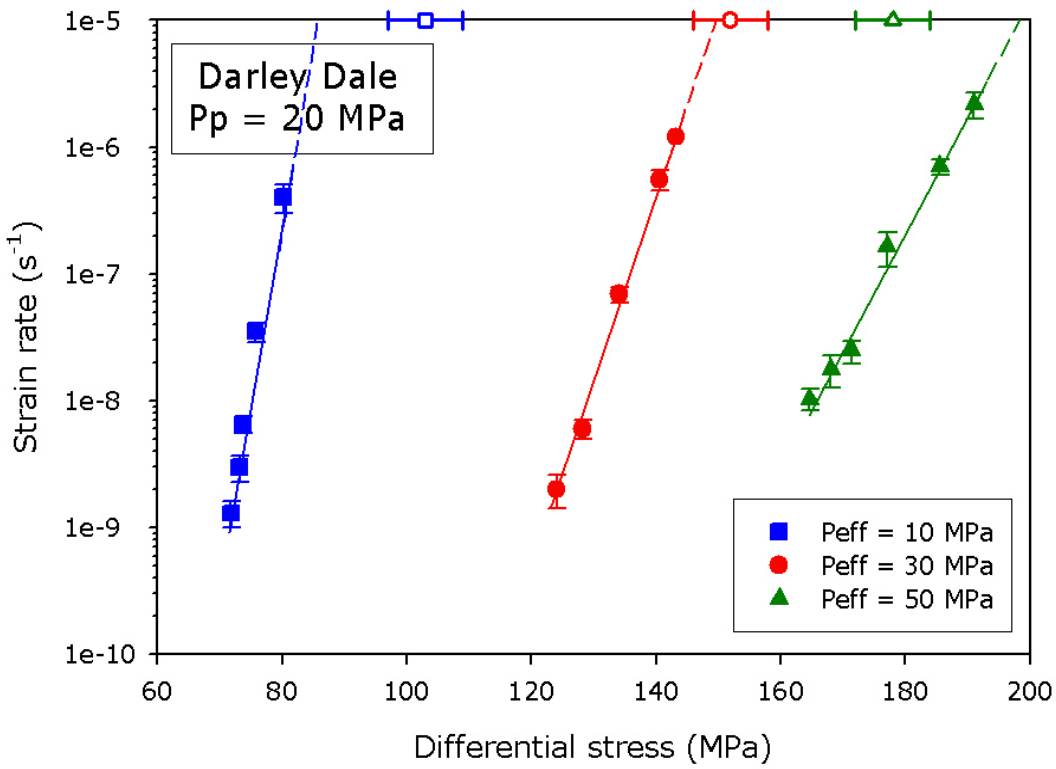

Figure 8.23. Creep strain rate data from stress-stepping brittle creep experiments performed at 10 (squares), 30 (circles) and 50 MPa (triangles) effective confining pressures on water-saturated DDS, whilst maintaining a constant pore fluid pressure of 20 MPa. Creep strain rate data is plotted on a log scale against applied differential stress. Short-term peak stress data from constant strain rate (1.0×10^{-5} s^{-1}) experiments are plotted as unfilled shapes. Error in the creep strain rate measurements are denoted by the error bars, error in the differential stress values are represented by the size of the datapoints. 10 MPa effective confining pressure – sample DD-40-28Z; 30 MPa effective confining pressure – sample DD-40-15Z; 50 MPa effective confining pressure – sample DD-40-32Z (see Table 8.5). P_{eff} – effective confining pressure; P_p – pore fluid pressure; T – sample temperature. The fits to these curves are summarized in Table 8.5.

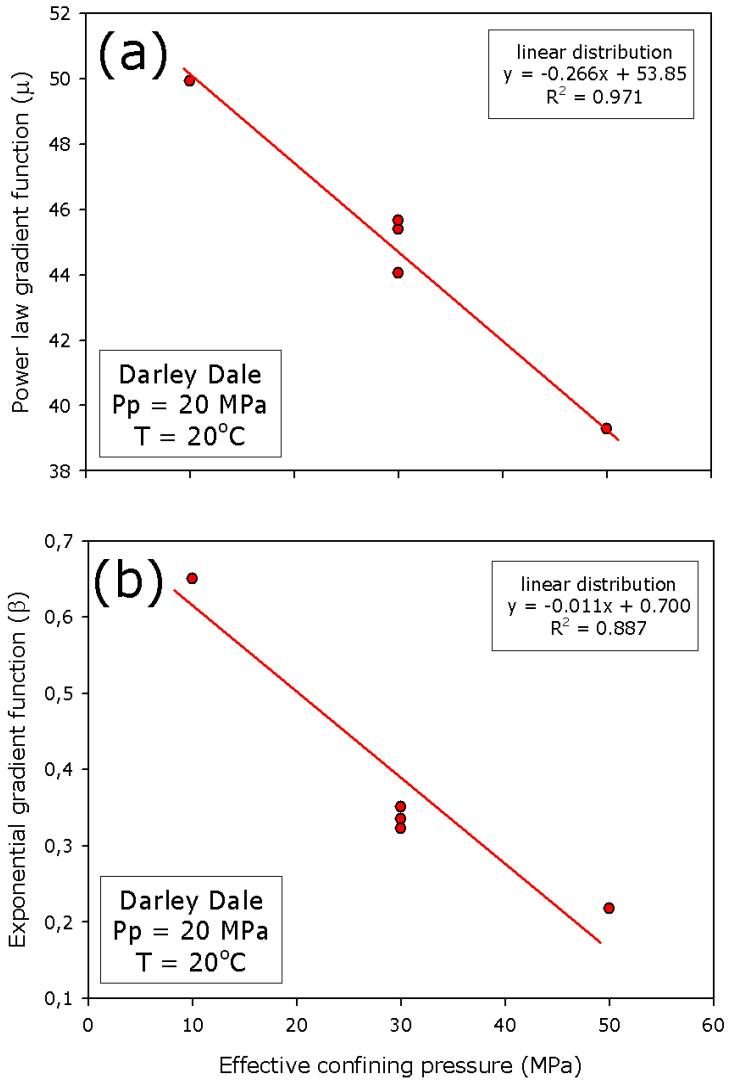

Figure 8.24. Graphs of the effective confining pressure dependence of the (a) power law gradient function, η and (b) the exponential gradient function, β (see also Table 8.5) in DDS using data derived from stress-stepping creep experiments. Experimental conditions are indicated on the figure. Power law and linear distribution fits are also shown on the figure; the curve fit shown on each figure is the one that best describes the data. P_p – pore fluid pressure; T – sample temperature.

Since it is possible that an increased presence of water molecules may influence the rate of stress corrosion reactions, stress-stepping methodology was also used to investigate the possible influence of P_p on brittle creep at constant P_{eff}. Experiments were run at a fixed P_{eff} of 30 MPa, but with a P_p of 20 and 40 MPa. The results are presented in Fig. 8.25. The two creep curves are very close and there is no

difference in their gradients; furthermore, the creep strain rates at a P_p of 40 MPa are lower than those at 20 MPa. The small offset between the two creep curves is however within the range expected from sample variability and therefore it is unwise to state, from the limited data, whether doubling the P_p has any influence on the creep rate or not. As before, the creep strain rate data presented in Fig. 8.25 can be adequately described by either a power law or exponential function (Table 8.5).

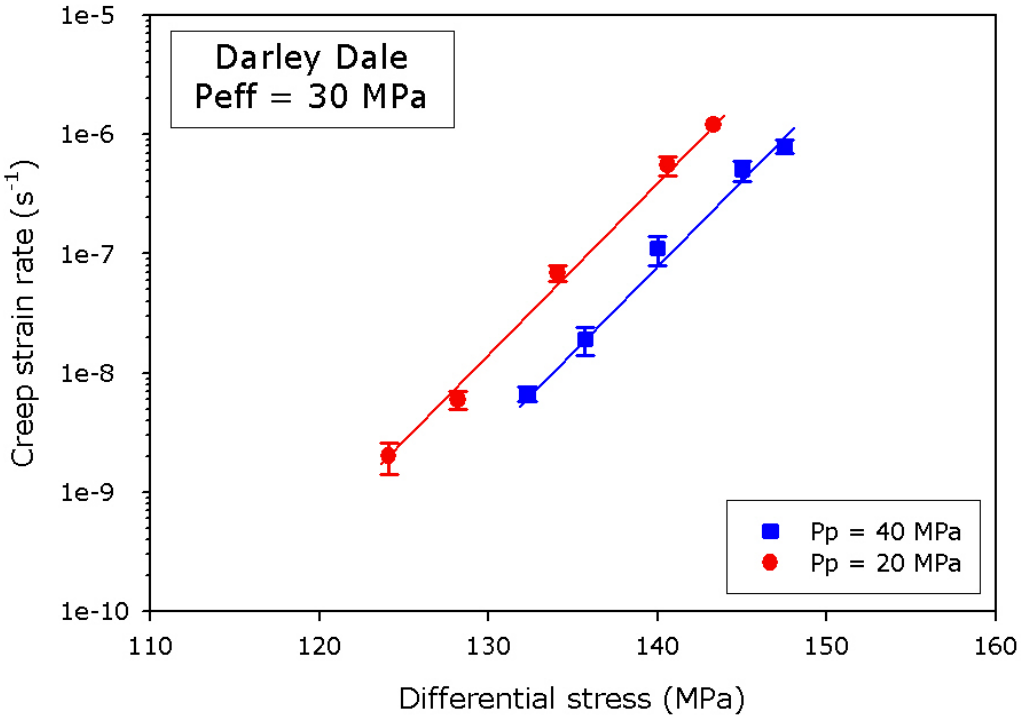

Figure 8.25. Creep strain rate data from stress-stepping brittle creep experiments on water-saturated DDS performed at 20 (circles) and 40 MPa (squares) pore fluid (distilled water) pressure, whilst maintaining a constant 30 MPa effective confining pressure. Creep strain rate data is plotted on a log scale against applied differential stress. Error in the creep strain rate measurements are denoted by the error bars, error in the differential stress values are represented by the size of the datapoints. 20 MPa pore fluid pressure – sample DD-40-15Z; 40 MPa pore fluid pressure – sample DD-40-35Z (see Table 8.5). P_{eff} – effective confining pressure; P_p – pore fluid pressure; T – sample temperature.

8.4 Conclusions

1. Constant strain rate experiments have shown that the experimental reproducibility of DDS under the same conditions is very good. They have also shown that peak stress is increased when the P_{eff} on the sample during deformation is increased. An increase from 10 MPa to 50 MPa P_{eff} results in an 80% increase in the peak stress. Doubling the P_p from 20 MPa to 40 MPa, whilst maintaining a constant P_{eff}, has no discernable effect on the mechanical behaviour, as anticipated by the law of effective stress.
2. Conventional brittle creep experiments have shown that applied differential stress exerts a crucial influence on both creep strain rate and time-to-failure. They have also demonstrated that the independent proxies for damage are approximately similar at the onset of the tertiary creep phase. It is also shown that, regardless of creep stain rate, the relative proportions of the durations of each of the creep phases remains the same. Detailed microstructural analysis has shown that crack densities at the onset of the tertiary creep phase are relatively low (compared with a sample taken to failure) and that crack densities and anisotropy are similar for samples taken to this point under creep strain rates that differ by an order of magnitude.
3. Stress-stepping creep experiments have been shown to accurately replicate the trends derived from a suite of conventional creep experiments. This has circumvented the problems associated with sample variability and has allowed the variables of effective confining pressure and pore fluid pressure to be studied. An increase in P_{eff} has been shown to affect the creep strain rates in a way not expected from purely mechanical processes; however, doubling the P_p (whilst maintaining a constant P_{eff}) has no discernable influence on the creep strain rates.

Chapter nine

9. Time-dependent Deformation: the Influence Temperature on Brittle Creep in Sandstones

9.1 Introduction

This chapter presents results from a systematic experimental study on the influence of an elevated temperature on creep strain rate in a suite of sandstones under triaxial stress conditions. The investigated materials are introduced and the experimental techniques explained. The influence of temperature on the short-term peak stress (σ_p) is first investigated, before its influence on the chemically-driven time-dependent process of stress corrosion is revealed from stress-stepping brittle creep experiments.

9.2 Sample material and experimental methodology

All experiments were performed in the servo-controlled triaxial rock deformation apparatus (see Chapter Four, section **4.3 The triaxial deformation ensemble**) situated in the Rock & Ice Physics Laboratory (RIPL) at University College London. Axial strain was continuously monitored using LVDT displacement transducers, and porosity change was measured continuously by means of a servo-controlled pore fluid pressure intensifier and volumometer (see Chapter Four, section 4.3.5.1 Intensifiers/pore volumometers). Acoustic emission (AE) output was recorded and stored by a VALLEN AMSY-5 AE recording system (see Chapter Four, section *4.4.2 AE data recording systems and logging software)* using ten PZT-5A transducers mounted on steel inserts embedded within the rubber sample jacket (see Chapter Four, section 4.3.4.1 The jacketing system). For full details on the experimental set-up see Chapter Four. Experiments presented in this chapter were performed on DDS, BHS and COS (for rock descriptions and characterization see Chapter Five) and were prepared for use in the triaxial ensemble as outlined in **5.2 Rock sample preparation**.

A series of conventional constant strain rate experiments at elevated temperature were untaken prior to any stress-stepping creep experiments. This was to simply ascertain the effect of temperature on the σ_p; also, so that data from stress-stepping experiments performed at elevated temperatures can be normalized with respect to the newly determined σ_p. Constant strain rate experiments (1.0×10^{-5} s^{-1}) were performed on samples of DDS, BHS and COS at temperatures of 20 and 75°C until failure. Stress-stepping creep experiments (performed to the methodology outlined in Chapter Eight) were performed on samples of DDS, BHS and COS at both 20 and 75°C. The elevated temperatures during experimentation were achieved using the internal electric furnace (see Chapter Four, section *4.3.6 The furnace* for details). The evolution of crack damage was monitored throughout each experiment by measuring the damage proxies of axial strain, porosity change and output of AE energy. All experiments in this chapter were performed under the conditions of a confining pressure (P_c) of 50 MPa and a pore fluid pressure (P_p) of 20 MPa (effective confining pressure (P_{eff}) of 30 MPa)

9.3 Results

9.3.1 Constant strain rate experiments at elevated temperature

A series of constant strain rate (1.0×10^{-5} s^{-1}) experiments at both 20 and 75 °C were performed on samples of DDS, BHS and COS. For each experiment, the three independent proxies for damage of strain, porosity change and output of AE energy were measured and recorded (Fig. 9.1). A summary of the influence of temperature in the constant strain rate experiments shown is given in Table 9.1.

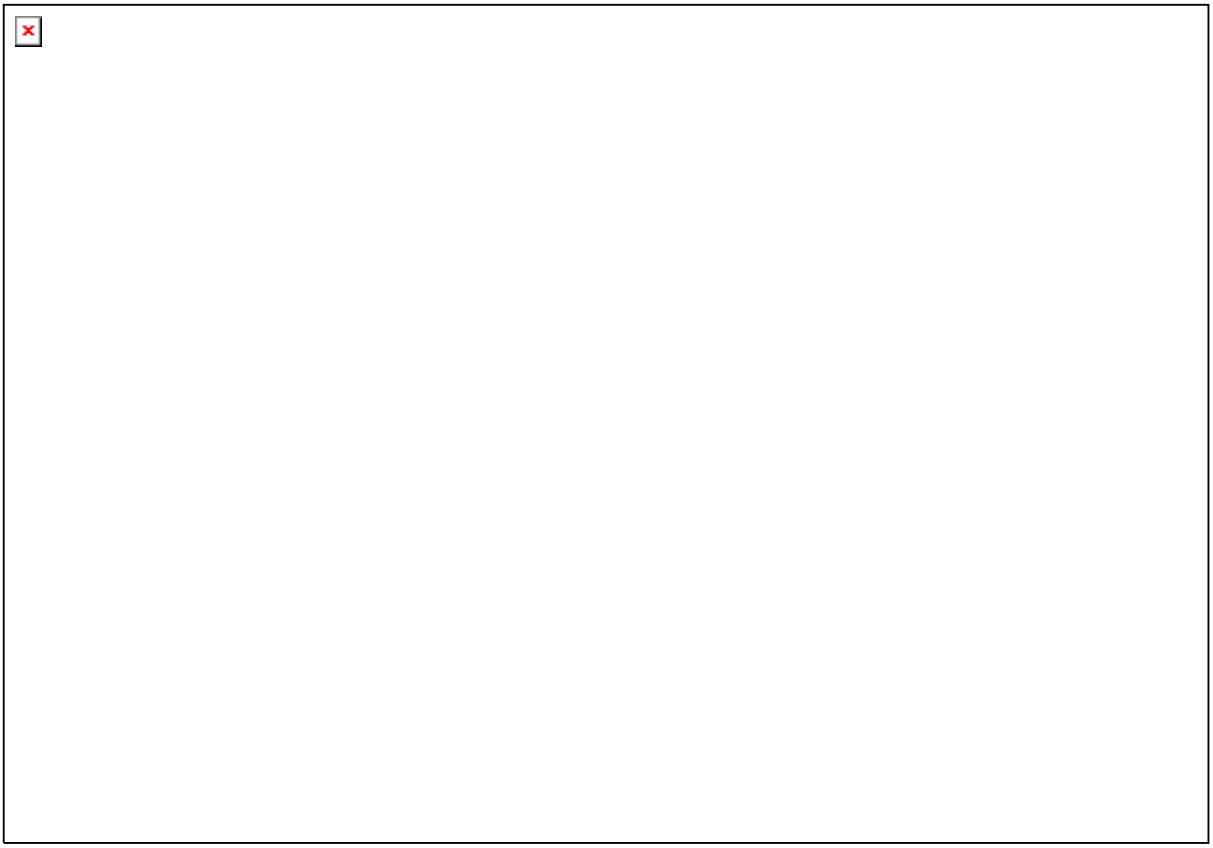

Figure 9.1. Conventional constant strain rate (1.0 x 10^{-5} s^{-1}) experiments on DDS, BHS and COS at both 20 and 75 °C showing the three independent proxies for damage: (a-c) strain, (d-f) porosity change and (g-i) output of AE energy. Experimental conditions are indicated on the figure. P_c – confining pressure; P_p – pore fluid pressure.

Rock type	Confining pressure (MPa)	Pore fluid pressure (MPa)	Peak stress at 20°C (MPa)	Peak stress at 70°C (MPa)	Percentage decrease in peak stress	% strain at D' at 20°C	% strain at D' at 75°C
Darley Dale sandstone	50	20	155	146	9	20	1.35
Bentheim sandstone	50	20	136	130	9	20	1.7
Crab Orchard sandstone	50	20	398	384	10	20	2.0

Table 9.1. Peak stresses of DDS, BHS and COS from constant strain rate (1.0 x 10^{-5} s^{-1}) experiments under the conditions of a P_{eff} = 30 MPa (P_c = 50 MPa and P_p = 20 MPa) at both 20°C and 75°C.

In general, the short-term mechanical deformation behaviour is quite similar between 20°C and 75°C, especially when you consider the normal variability of samples under the same pressure and temperature conditions. However, both Fig. 9.1 and Table 9.1 show that there is a modest reduction (by 4-6%) in σ_p from 20°C to 75°C. The modest reduction in σ_p is systematic and is observed in all three rock types. Also, the % axial strain at which the samples enter dilatancy-dominated deformation behaviour, termed *D'* (see Chapter Eight for more information on *D'*), is slightly reduced (Table 9.1).

9.3.2 Conventional creep experiment at elevated temperature

A conventional creep experiment was performed on DDS in order to investigate the influence of an elevated temperature on a complete brittle creep curve (Fig. 9.2). The experiment was performed at a constant creep stress of 129 MPa and yielded a steady-state (secondary) creep strain rate of 5.5×10^{-6} s^{-1}. Fig. 9.2 confirms that, at an elevated temperature of 75°C, the creep curve exhibits a qualitatively similar three-stage brittle creep curve as that observed at ambient temperature (see Chapter Eight).

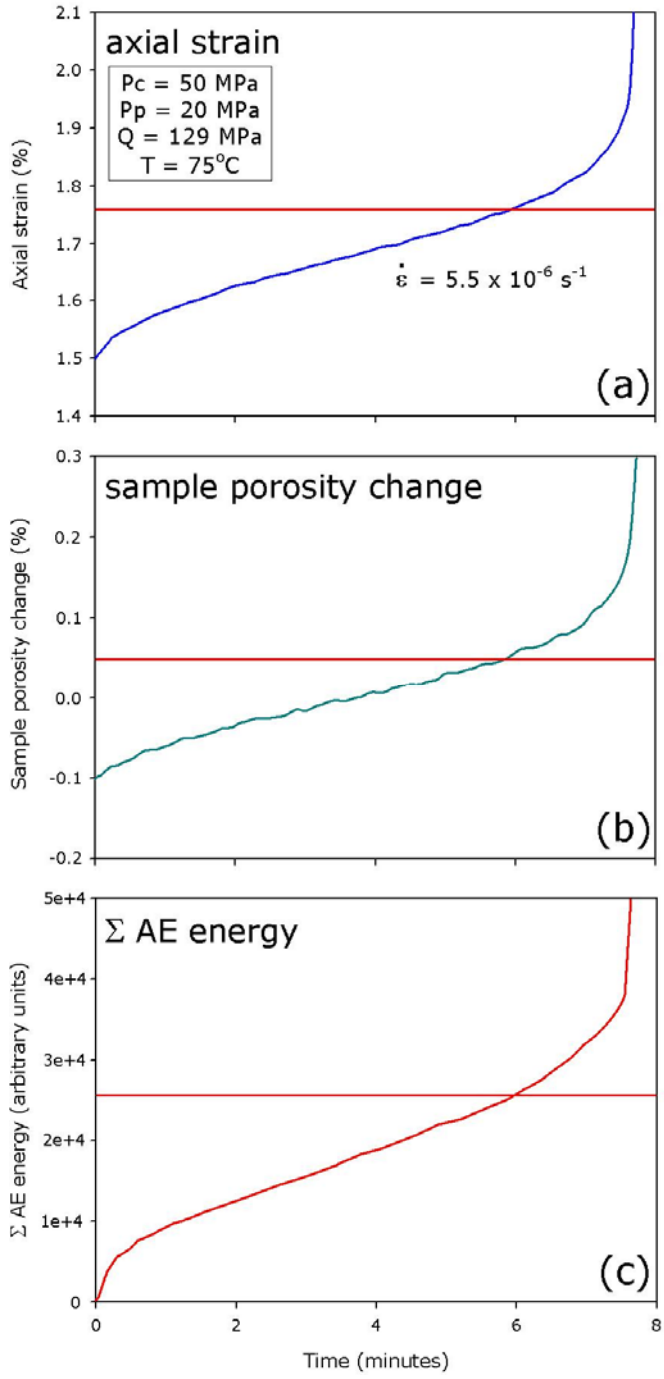

Figure 9.2. Conventional brittle creep experiment on a water-saturated sample of Darley Dale sandstone showing the evolution over time of the three proxies for damage (a) axial strain, (b) porosity change and (c) cumulative AE energy under a constant creep stress of 129 MPa. Experimental conditions are shown on the figure. Pc – confining pressure; Pp – pore fluid pressure; Q – applied differential stress; T – sample temperature. Calculated creep strain rate for the steady-state secondary creep phase is indicated in (a). Red lines indicate the estimated positions at which the sample enters accelerating tertiary creep.

9.3.3 Stress-stepping creep experiments at elevated temperature

The relation between differential stress and steady-state creep strain rate at both 20° and 75°C for the three rock types was investigated via stress-stepping creep experiments. The results are plotted on semi-log axes in Fig. 9.3 and show that the creep behaviour of the three sandstones is qualitatively similar. In all cases, the steady-state creep strain rate increases significantly and non-linearly with increasing differential stress. The creep strain rate from the conventional creep experiment performed on DDS at a temperature of 75°C (as in Fig. 9.2) is also plotted on Fig. 9.3b as on open triangle. Fig. 9.2b shows that there is a very good correlation between the conventional experiment and the stress-stepping experiment.

The effect of increasing the temperature from 20° to 75°C, for a given differential stress, is to increase all the creep strain rates by multiple orders of magnitude (Fig. 9.3). For example, at a constant creep stress of 125 MPa, the creep strain rates in BHS and DDS are increased by approximately 3 orders of magnitude (Figs. 9.3a and 9.3b). For COS, the creep strain rate is increased by approximately 2 orders of magnitude over the same temperature interval at a creep stress of 383 MPa. Therefore, the applied differential stress required to achieve a particular creep strain rate is reduced. To achieve a creep strain rate of 1.0×10^{-7} s^{-1}, the applied differential stress required is reduced from 136, 128 and 394 MPa to 109, 98 and 369 MPa for DDS, BHS and COS respectively between 20 and 75°C.

Furthermore, not only does an increase in temperature shift the strain rate-differential stress curves to higher strain rates, but it also results in a decrease in the gradient of the curves (see Table 9.2). At higher temperatures the gradients of the curves are shallower; this means that a greater increment of applied differential stress is needed to produce the same increase in creep strain rate. The change in gradient is

most pronounced in BHS and least in COS. For the range of stresses applied and strain rates measured in our experiments, the relation can be adequately described by either a power law or an exponential function (Chapter Three, Equations [3.6] and [3.7]) with the parameters listed in Table 9.2.

Sample number	Confining pressure (MPa)	Pore fluid pressure (MPa)	Effective confining pressure (MPa)	Temperature (°C)	Power law gradient function (β)	Exponential gradient function (μ)	Power law R^2 value	Exponential R^2 value
DD-40-15Z	50	20	30	20	45.57	0.342	0.996	0.997
DD-40-53Z	50	20	30	75	19.07	0.169	0.993	0.992
BH-40-05Z	50	20	30	20	62.37	0.498	0.999	0.998
BH-40-10Z	50	20	30	75	19.70	0.198	0.997	0.995
COS-40-03Z	50	20	30	20	74.47	0.194	0.981	0.980
COS-40-04Z	50	20	30	75	55.58	0.151	0.992	0.992

Table 9.2. Experimental conditions from stress-stepping creep experiments on DDS, BHS and COS performed at both 20 and 75°C and the results of regression analysis of power law and exponential function fits to the data.

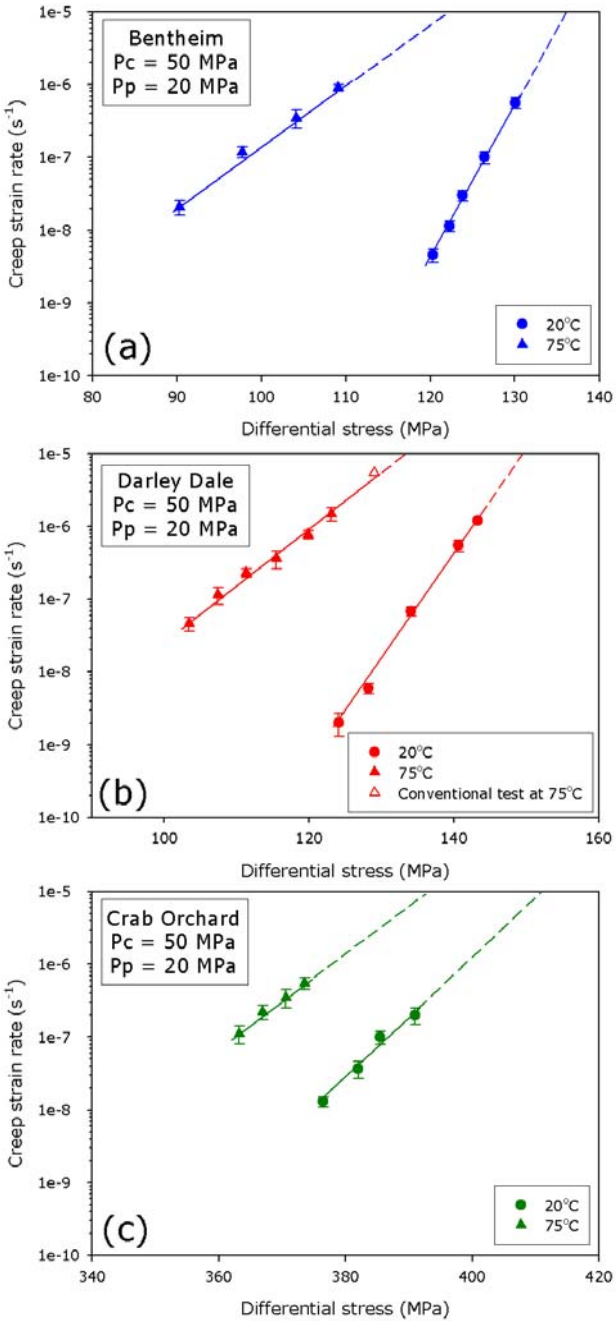

Figure 9.3. Creep strain rate data from stress-stepping brittle creep experiments on water-saturated samples of (a) Bentheim, (b) Darley Dale and (c) Crab Orchard sandstone at both 20° (filled circles) and 75°C (filled triangles). Creep strain rate data is plotted on a log scale against applied differential stress. Unfilled triangle in (b) represents the single conventional creep experiment on DDS (see Fig. 9.2). Experimental conditions are shown on the figures. Error bars indicate level of uncertainty in the calculated creep strain rates and the size of the symbols represents the uncertainty in the values of constant differential stress. Pc – confining pressure; Pp – pore fluid pressure.

In order to compare the data more easily, all stress-stepping creep data at elevated temperature were also plotted against normalized short-term peak stress (Fig. 9.4). The data were normalized with respect to the σ_p derived from conventional constant strain rate (1.0 x 10^{-5} s^{-1}) experiments and both 20 and 75°C (see Fig. 9.1). The data demonstrates that DDS and BHS both have a very similar response to the increase in temperature, as noted earlier. Fig. 9.4 shows that, to achieve a creep strain rate of. 1.0 x 10^{-7} s^{-1} for example, the proportion of the σ_p (normalized with respect to the peak stresses found during a constant strain rate experiments, see Fig. 9.1 and Table 9.1) required is reduced from 0.88, 0.86 and 0.97 to 0.76, 0.75 and 0.94 for DDS, BHS and COS respectively between 20 and 75°C. Furthermore, the gradients of the DDS and BHS curves at 75°C are now very similar; at room temperature gradients were markedly different (see Figs. 9.3 and 9.4).

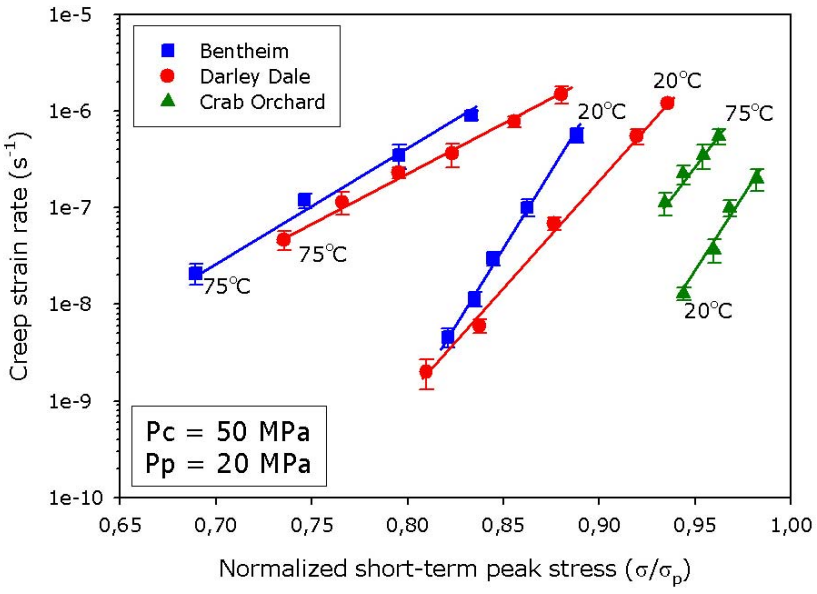

Figure 9.4. Creep strain rate data from stress-stepping creep experiments at elevated temperatures on DDS, BHS and COS plotted on a log scale against failure stress, normalized with respect to the short-term peak stress derived from conventional constant strain rate (1.0 x 10^{-5} s^{-1}) experiments. Experimental conditions are indicated on the figure. P_c – confining pressure; P_p – pore fluid pressure. Error bars indicate level of uncertainty in the calculated creep strain rates and the size of the symbols represents the uncertainty in the values of constant differential stress.

9.4 Conclusions

1. Constant strain rate (1.0×10^{-5} s^{-1}) experiments performed at an elevated temperature resulted in a very minor, but systematic across the three rock types, reduction (between 9-10%) of the σ_p for all three sandstones.
2. Stress-stepping creep experiments at an elevated temperature showed that the creep strain rate is dramatically influenced by temperature. Experiments on both DDS and BHS reported creep strain rates that were approximately 3 orders of magnitude faster at 75°C compared to room temperature data, for a given applied differential stress. COS displayed an increase of 2 orders of magnitude for the same temperature increase.

Chapter ten

10. Time-dependent Deformation: Brittle Creep in Etna Basalt

10.1 Introduction

This chapter reports results from a systematic experimental study of brittle creep in Etna basalt under triaxial stress conditions. Firstly, the investigated material is introduced and experimental techniques explained. Results from a series of constant strain rate experiments and conventional brittle creep experiments are then presented. This is followed by results from stress-stepping experiments in which the influence of both effective confining pressure (P_{eff}) and temperature on brittle creep is investigated.

10.2 Sample material and experimental methodology

All experiments were performed in the servo-controlled triaxial rock deformation apparatus (for details see Chapter Four, section **4.3 The triaxial ensemble**) situated in the Rock & Ice Physics Laboratory (RIPL) at University College London. Axial strain was continuously monitored using LVDT displacement transducers, and porosity was measured continuously by means of a servo-controlled pore fluid pressure intensifier and volumometer (see 4.3.5.1 Intensifiers/pore volumometers). Acoustic emission (AE) output was recorded and stored by a VALLEN AMSY-5 AE recording system (see Chapter Four, section *4.4.2 AE data recording systems and logging software)* using PZT-5A transducers mounted on steel inserts embedded within the rubber sample jacket (see Chapter Four, section 4.3.4.1 The jacketing system). For full details on the experimental set-up see Chapter Four. Experiments presented in this chapter were all performed on samples of EB (for rock descriptions and characterization see Chapter Five) and were prepared for use in the triaxial ensemble as outlined in **5.2 Rock sample preparation**.

A series of constant strain rate experiments on samples of EB were untaken prior to performing any creep experiments in order to ascertain the short-term peak stress (σ_p) and associated failure

characteristics. Constant strain rate experiments (1.0 x 10^{-5} s^{-1}) were performed at both 20°C and 75°C under the conditions of a 50 MPa confining pressure (P_c) and a 20 MPa pore fluid pressure (P_p) (P_{eff} = 30 MPa) until failure. Constant strain rate experiments were also performed at 20°C under effective confining pressures of 10, 30 and 50 MPa (whilst maintaining a constant P_p of 20 MPa).

Once the σ_p had been established, a series of conventional brittle creep experiments were performed at 20°C under the conditions of a P_c = 50 MPa and a P_p = 20 MPa (i.e. the same conditions used for the conventional creep experiments on DDS in Chapter Eight). Samples of EB were first loaded to a pre-determined percentage of the σ_p (or strength) established during the constant strain rate experiments. Generally, this was in the range 80 to 95% of the σ_p [see Chapter Eight; Baud and Meredith, 1997]. Stress-stepping brittle creep experiments (performed to the methodology outlined in Chapter Eight), again under the same P_{eff} conditions, were also conducted on samples of EB. To study the influence of P_{eff} on brittle creep in EB, stress-stepping creep experiments were also performed at effective confining stresses of 10, 30 and 50 MPa (whilst maintaining a constant P_p = 20 MPa). Stress-stepping creep experiments performed at 75°C investigated the influence of an elevated temperature using the internal electric furnace (see Chapter Four, section *4.3.6 The furnace* and Chapter Nine for more details). The influence of an elevated P_p, whilst maintaining a constant P_{eff} of 30 MPa, was not investigated in this case. Previous experiments on DDS (see Chapter Eight) demonstrated that doubling the P_p (with a constant P_{eff} of 30 MPa) yielded no measureable effect on the creep strain rate. The evolution of crack damage was monitored throughout each experiment by measuring the damage proxies of axial strain, porosity change and output of AE energy.

A number of focussed conventional brittle creep experiments were performed to investigate the degree of cracking and any changes in crack morphology caused by stress corrosion cracking during the

secondary creep phase. During these experiments, samples of EB were allowed to deform under the same constant applied differential stress to the onset of secondary creep and after a significant proportion of the secondary creep phase, with care taken to stop the experiment prior to the onset of acceleration to failure (calculated using complete curves of similar creep strain rates) (Fig. 10.1, numbers 2 and 3 respectively).

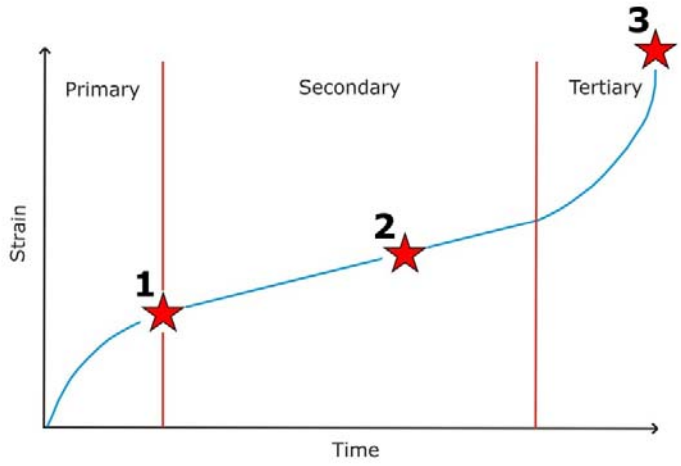

Figure 10.1. Schematic creep curve showing the positions (numbered red stars) where the microstructurally-focussed conventional creep experiments on EB were stopped and carefully unloaded.

Once the targeted level of deformation had been achieved, the samples were slowly unloaded; and P_c and P_p were decreased to ambient values. Samples were then removed from the apparatus, and epoxy-impregnated thin sections were prepared for microscopic analysis. Thin sections of a sample that had failed under a similar constant applied differential stress and therefore resulted in a similar creep strain rate were also prepared for microscopic analysis (Fig. 10.1, number 3).

10.3 Results

10.3.1 Constant strain rate experiments

Fig. 10.2 shows the stress-strain curves and the damage proxies of pore volume change and cumulative AE energy for two experiments conducted at a constant strain rate of 1.0 x 10^{-5} s^{-1} and a P_{eff} of 30 MPa (Fig. 10.2). The repeatability is excellent, and the small variation between the two sets of curves simply reflects the variability between natural rock samples. The experiments yielded a mean σ_p of 387 ± 5 MPa. Following an initial period of compaction, the onset of dilatancy, termed *C'* [see Chapter Two, Fig. 2.16; Wong *et al.*, 1997], occurs at differential stress of around 50 MPa and is marked on the differential stress versus volumetric strain curve presented as Fig. 10.3. The minimum in the porosity change curve (Fig. 10.2b) marks the transition from compaction-dominated deformation to dilatancy-dominated deformation, which we term *D'* (see Chapter Eight for more information on *D'*). This also corresponds to the maximum in the volumetric strain (Fig. 10.3), and occurs at a differential stress around 250 MPa.

Fig. 10.4 shows the results from a series of experiments to investigate the influence of effective confining pressure on the deformation of EB at a constant strain rate of 1.0 x 10^{-5} s^{-1}. Increasing the P_{eff} results in significant increases in the σ_p (Fig. 10.4 and 10.5 and Table 10.1), the duration of the strain softening phase that precedes failure and the axial strain at dynamic failure (Fig. 10.4a). Similar observations in sandstone have been reported by [Wong *et al.*, 1997; Baud *et al.*, 2000; see also Chapter Seven]. EB does however remain very brittle, even at P_{eff} = 50 MPa. Fig. 10.4b also shows that the axial strain at which *D'* occurs increases significantly with increasing P_{eff} (see also, Table 10.1). Since the transition from compaction to dilatancy occurs later with increasing P_{eff}, it is perhaps not surprising that the onset of significant AE output (Fig. 10.4c) also occurs later. However, the total output of AE energy

does not vary significantly between experiments even though the rock strength increases by about 75%, from 291 MPa (P_{eff} = 10 MPa), to 387 MPa (P_{eff} = 30 MPa) and eventually to 504 MPa (P_{eff} = 50 MPa) (Fig. 10.4).

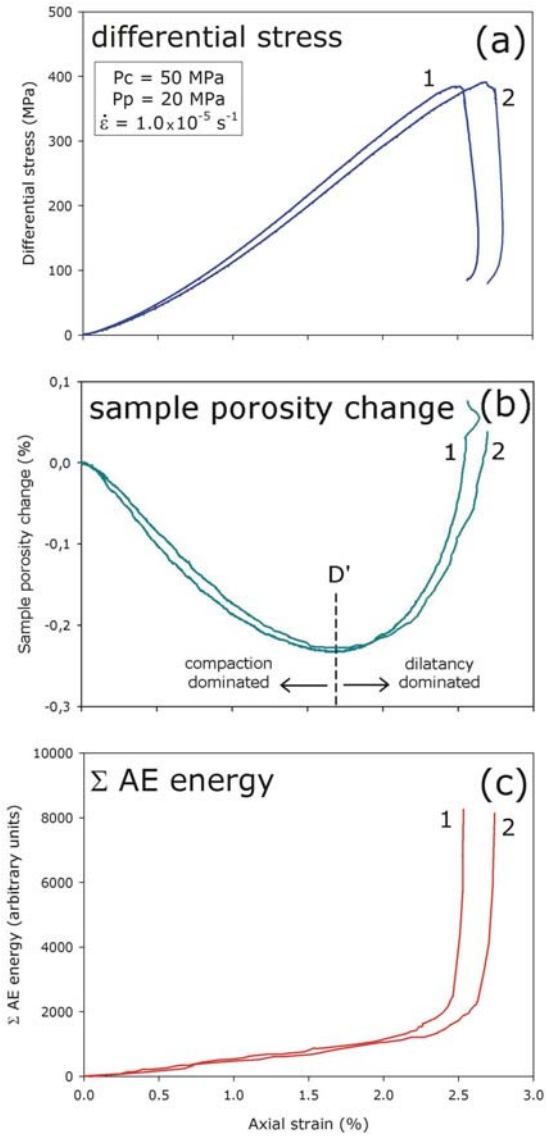

Figure 10.2. Two conventional constant strain rate experiments on water-saturated EB showing variability in the three proxies for damage within the rock: (a) stress-strain curves, (b) the porosity change curves and (c) the AE energy output curves. Experimental conditions are indicated on the figure. *D'*, the stress at which a dilatant-dominated regime dominates, is indicated in (b). P_c – confining pressure; P_p – pore fluid pressure [samples EB-40-02Z and EB-40-03Z].

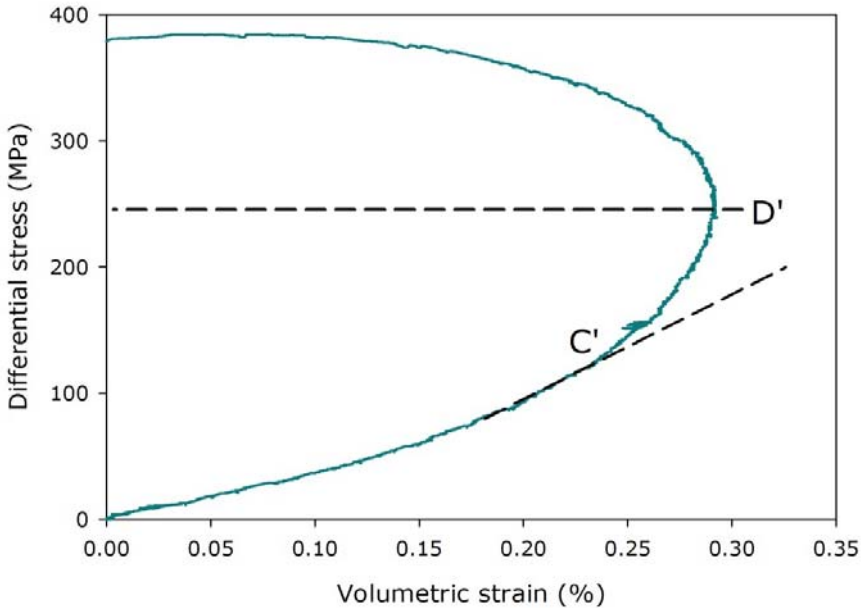

Figure 10.3. Volumetric strain against differential stress for a constant strain rate experiment on water-saturated EB. Both *C'*, the stress at which the volumetric strain deviates from that observed from hydrostatic loading, and *D'*, the stress at which a dilatant-dominated regime dominates, are indicated [sample EB-40-02Z].

Sample	Effective confining pressure (MPa)	Confining pressure (MPa)	Pore fluid pressure (MPa)	Peak stress (MPa)	Temperature (°C)	% strain at D'
EB-40-07Z	10	30	20	291	20	1.35
EB-40-02Z	30	50	20	387	20	1.7
EB-40-08Z	50	70	20	504	20	2.0
EB-40-24Z	30	50	20	362	75	1.5

Table 10.1. Summary of the experimental conditions, peak stresses and % strain at *D'* for three experiments performed at effective confining pressure of 10, 30 and 50 MPa (same experiments as shown in Fig. 10.4). The constant strain rate experiment performed at an elevated temperature of 75°C is also summarized here; this experiment is explained later in this chapter.

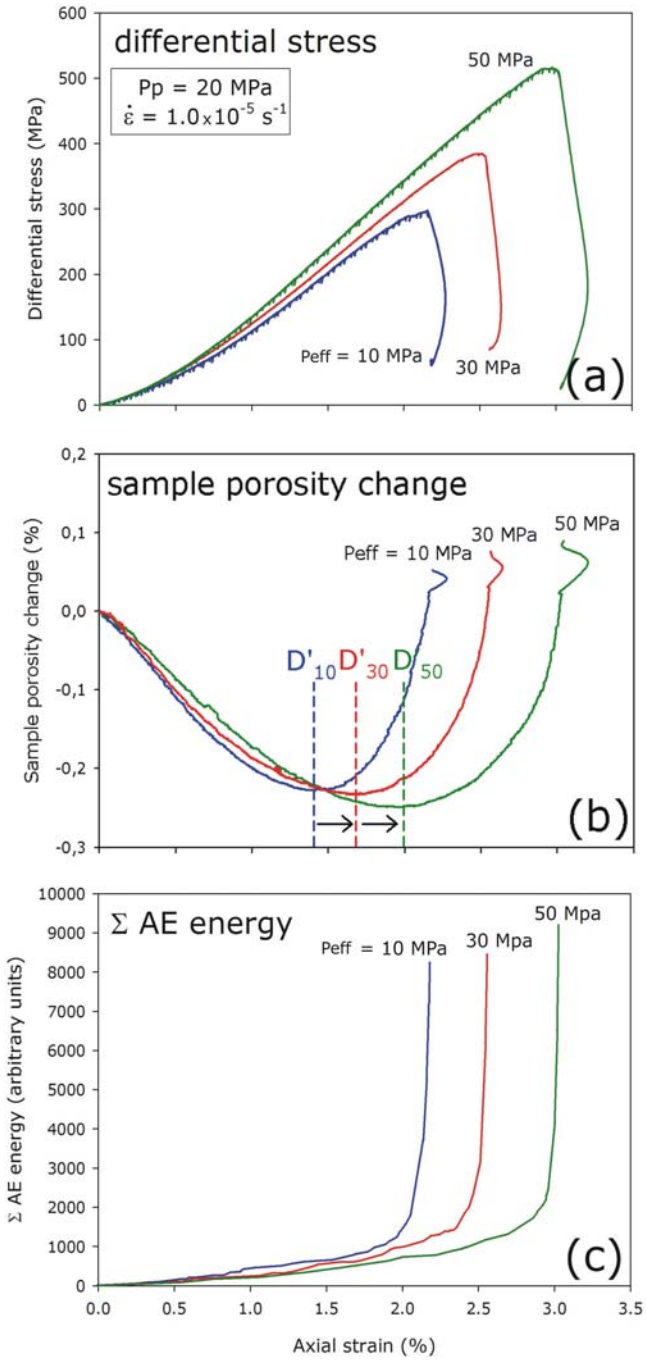

Figure 10.4. Conventional constant strain rate experiments on water-saturated EB showing variability in (a) the stress-strain curves, (b) the porosity change curves and (c) the AE energy output curves for effective confining pressures of 10, 30 and 50 MPa, whilst maintaining a constant P_p of 20 MPa. Experimental conditions are indicated on the figure. The position of *D'*, and how it migrates with increasing P_{eff}, is indicated in (b). P_c – confining pressure; P_p – pore fluid pressure [samples EB-40-02Z, EB-40-07Z and EB-40-08Z].

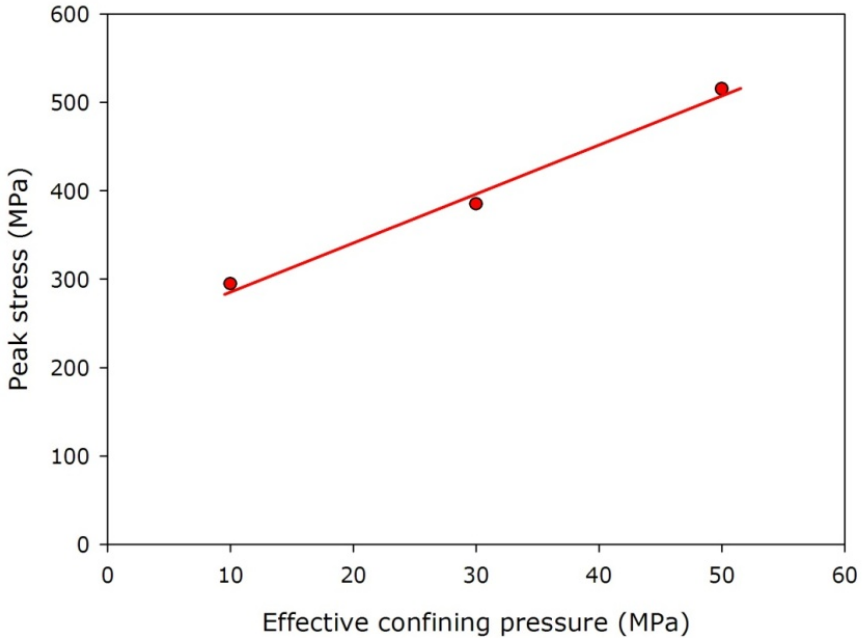

Figure 10.5. Graph of peak stress against effective confining pressure for three experiments performed at effective confining pressures of 10, 30 and 50 MPa (same experiments as shown in Fig. 10.4).

Fig. 10.6 shows the results from an experiment designed to investigate the influence of an elevated temperature of 75°C on the deformation of EB at a constant strain rate of 1.0 x 10^{-5} s^{-1}. In general, the short-term mechanical deformation behaviour is quite similar between 20°C and 75°C, especially when you consider the normal variability of samples under the same pressure and temperature conditions. However, as Table 10.1 demonstrates, the σ_p is reduced by about 9% (from 387 to 362 MPa) and the position of *D'* is reduced from 1.7% to 1.5% axial strain. This is beyond the observed natural variability seen between samples (typical variability in the σ_p was on the order of ±5 MPa; see also Fig. 10.2). A similar response to an elevated temperature was observed in constant strain rate experiments performed on sandstones (see Chapter Nine, Fig. 9.1).

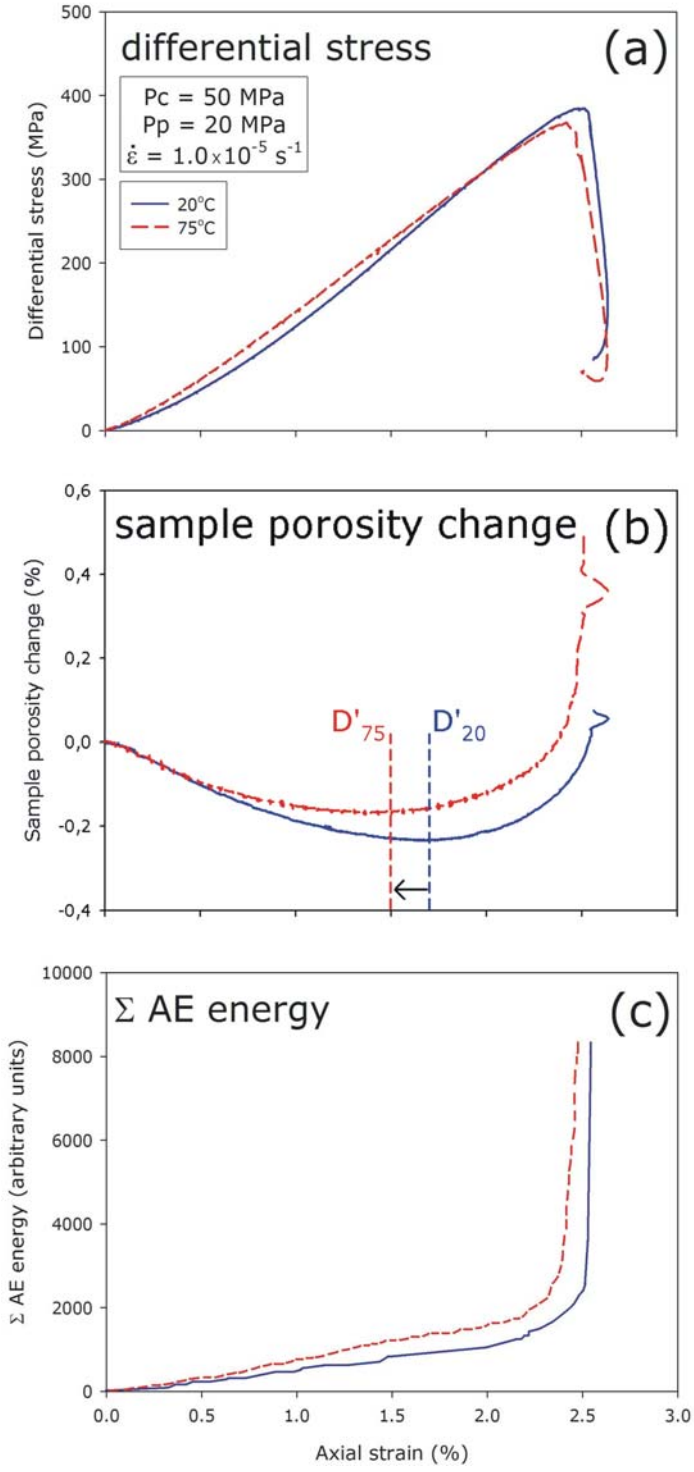

Figure 10.6. Conventional constant strain rate (1.0 x 10^{-5} s^{-1}) experiments on EB at both 20 and 75 °C showing the three independent proxies for damage: (a) strain, (b) porosity change and (c) output of AE energy. Experimental conditions are indicated on the figure. P_c – confining pressure; P_p – pore fluid pressure [samples EB-40-02Z and EB-40-24Z].

All samples, under the range of tested conditions, failed by brittle shear faulting. The angle of the shear fracture was orientated approximately 30° to the direction of the maximum principal stress (Fig. 10.7). Photomicrographs of samples of EB deformed to failure under a constant strain rate are presented in Fig. 10.8 and demonstrate the high degree of grain cracking (Fig. 10.8a) and the shear fault (Fig. 10.8b).

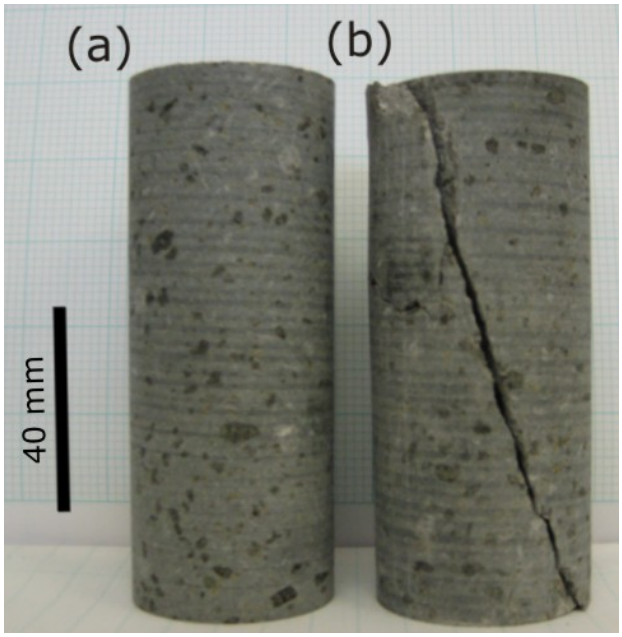

Figure 10.7. Photographs of (a) an undeformed sample of EB, and (b) a sample of EB that failed by shear faulting under a constant strain rate of 1.0 x 10^{-5} s^{-1} under the conditions of a P_c = 50 MPa and a P_p = 20 MPa pore fluid pressure (P_{eff} = 30 MPa) [sample EB-40-02Z].

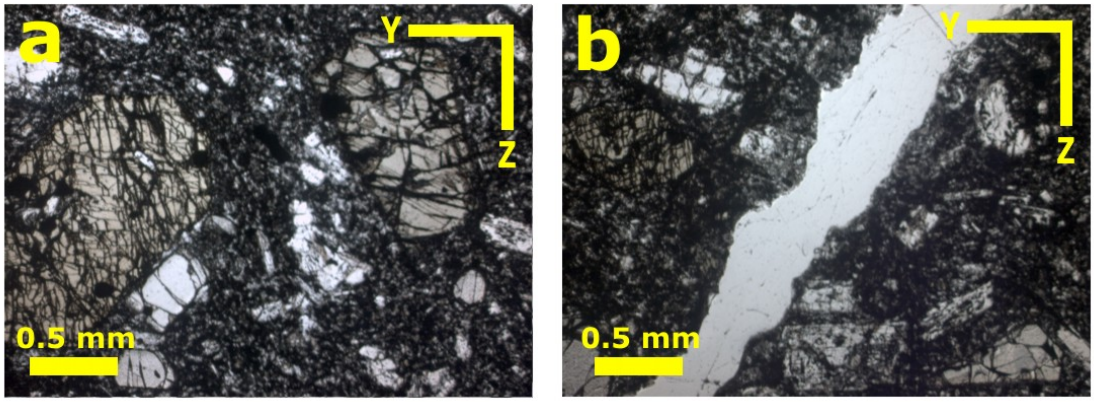

Figure 10.8. Photomicrographs of a sample of EB deformed to failure under a constant strain rate of 1.0 x 10^{-5} s^{-1} under XPL. (a) Close inspection of the microcracks present within the grains adjacent to the shear band. (b) The shear fault that ruptured the sample. All photomicrographs are taken within the same YZ plane, the Z-axis is normal to the axial loading direction (for details on directional information see *5.2.2 Orientation of samples*). For photomicrographs of undeformed samples of EB see Chapter Five, Fig. 5.3 [sample EB-40-02Z].

10.3.2 Conventional brittle creep experiments

Conventional brittle creep experiments were performed at 20°C on samples of EB at applied differential stress levels that have yielded times-to-failure and creep strain rates over four orders of magnitude (Fig. 10.9). Fig. 10.9 shows, for each experiment, the three sets of measured independent damage proxies (axial strain, pore volume change and output of AE energy). All of the axial strain curves show the trimodal behaviour via which creep deformation is generally interpreted [Baud and Meredith, 1997; Main, 2000; see also Chapter Eight, Fig. 8.13] (Fig. 10.9 a-d). Each primary creep phase is characterized by an initially high strain rate that decreases with time to reach a quasi-linear secondary phase that is often interpreted as steady-state creep. After an extended period of time, a tertiary phase is entered, characterized by accelerating strain. This eventually results in macroscopic failure of the samples by propagation of a shear fault.

Creep strain rates were calculated for each experiment from the quasi-linear portions of the strain-time curves in the same manner as outlined in Chapter Eight. Again, quasi-linear behaviour was first confirmed by plotting the first derivative (strain rate) of the strain data against time (e.g. Fig. 10.10). As for the experiments on DDS, there is a distinctive plateau in the strain rate curves confirming 'steady-state' behaviour (Fig. 10.10). The data show that both the creep strain rate and the overall time-to-failure depend strongly and non-linearly on the level of applied differential stress. Even modest increases in applied stress can result in order of magnitude changes in times-to-failure and creep strain rates. At 375 MPa (approximately 97.5% of σ_p), the time-to-failure was approximately 4.5 minutes and the creep strain rate was 2.7 x 10^{-6} s^{-1}. At 357 MPa (95% of σ_p), the time-to-failure increased to 25 minutes and the creep strain rate decreased to 4.1 x 10^{-7} s^{-1}. For 329 MPa (92.5% of σ_p), the time-to-failure was 270 minutes and the creep strain rate was 4.0 x 10^{-8} s^{-1} and, finally, at 304 MPa (90% of σ_p) the time-to-failure increased to 4500 minutes and the creep strain rate reduced to 2.4 x 10^{-9} s^{-1} (see Table 10.2 for summary). In summary, less than a 10% reduction in applied differential stress resulted in an increase in time-to-failure and a decrease in creep strain rate of approximately 3.5 orders of magnitude.

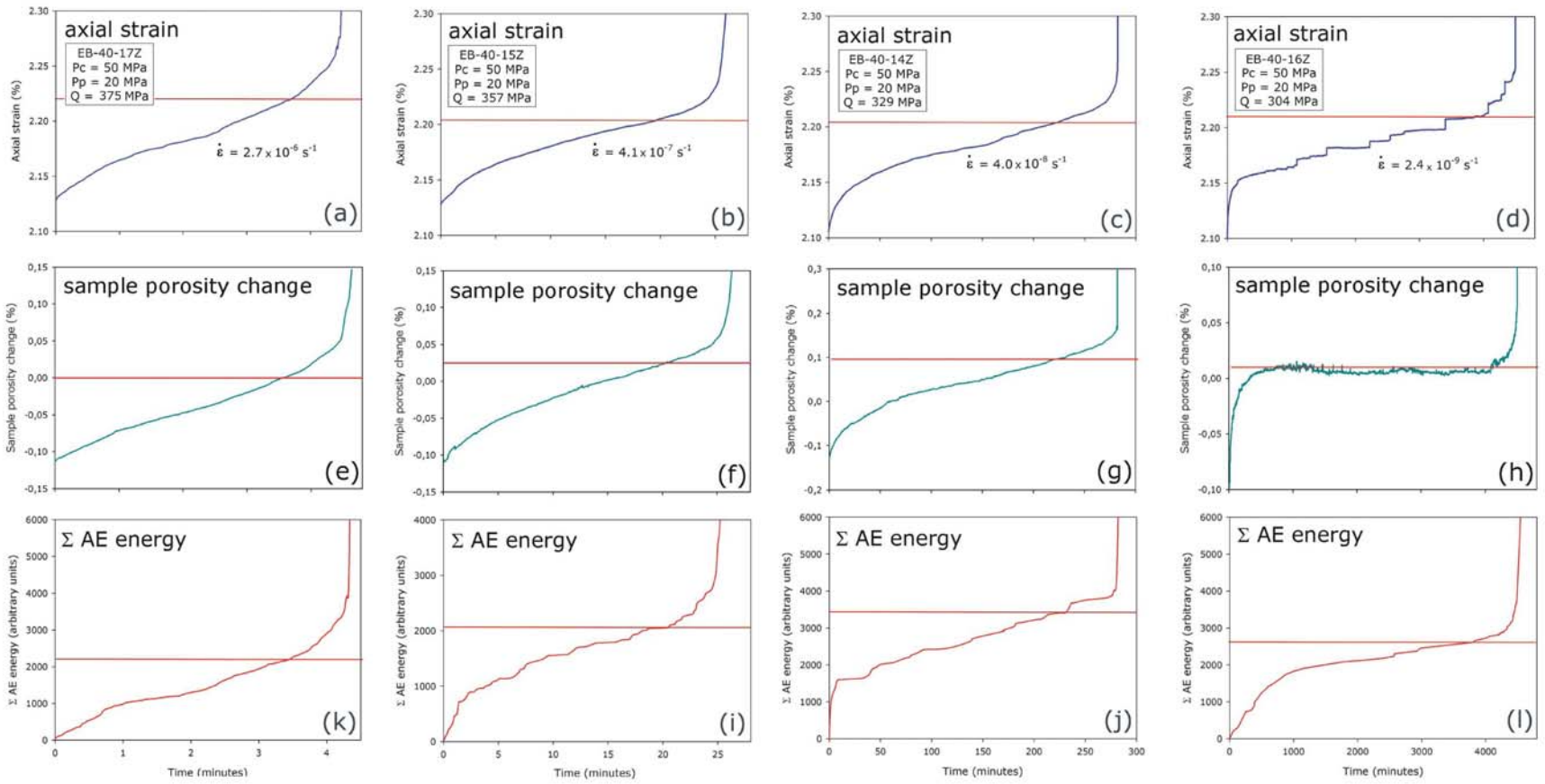

Figure 10.9. Graphs of the three damage proxies for four conventional brittle creep experiments on water-saturated EB that have yielded creep strain rates over three orders of magnitude: 2.4 x 10^{-9}, 4.0 x 10^{-8}, 4.1 x 10^{-7} and 2.7 x 10^{-6} s^{-1}. (a)-(d) time-strain (creep) curves (e)-(h) porosity change curves and (i)-(l) output of AE energy for the three experiments. The position of the onset of accelerating tertiary creep is indicated in each figure by a horizontal line. Experimental conditions are indicated on the figures. P_c – confining pressure; P_p – pore fluid pressure; Q – applied differential stress [samples EB-40-14Z, EB-40-15Z, EB-40-16Z and EB-40-17Z]. The experiments were all performed at 20°C.

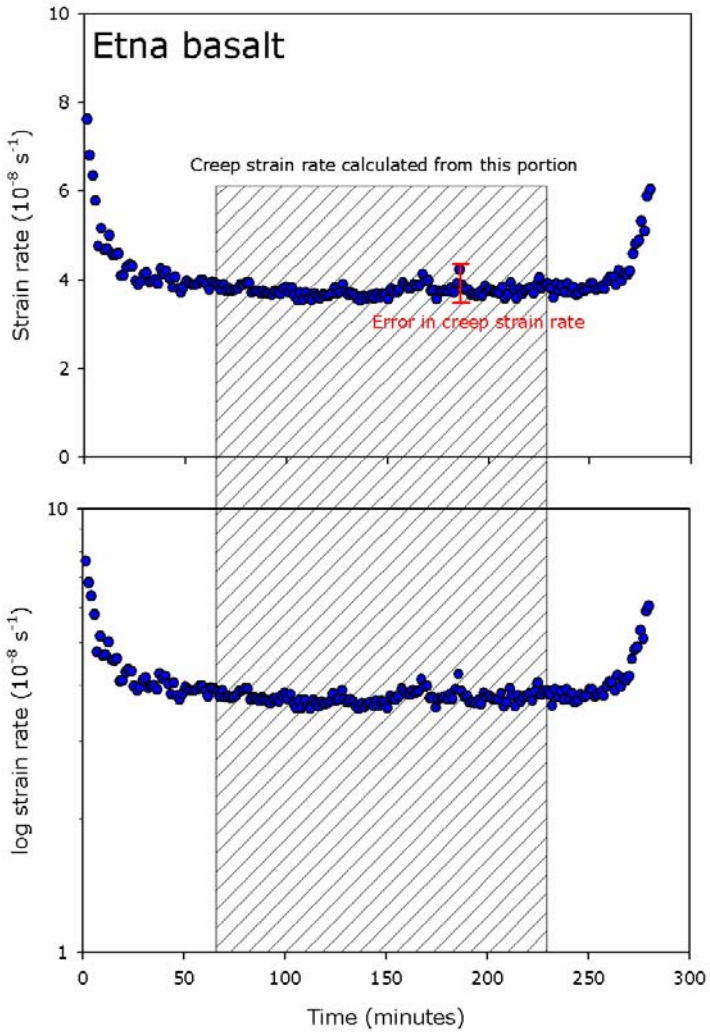

Figure 10.10. (a) Plot of the first derivative of the experimental strain data from a conventional creep experiment on EB that yielded a creep strain rate of 4.0 x 10^{-8} s^{-1} against time. (b) Plot of the first derivative, as in (a), with creep strain rate plotted on a log axis. Experimental conditions are indicated on Fig. 10.9c [sample DD-40-14Z] (courtesy of S. Hunt).

Sample	Effective confining pressure (MPa)	Level of applied stress (% of σ_p)	Resultant creep strain rate (s^{-1})	Time-to-failure (minutes)
EB-40-16Z	30	90	2.4 x 10^{-9}	4500
EB-40-14Z	30	92.5	4.0 x 10^{-8}	270
EB-40-15Z	30	95	4.1 x 10^{-7}	25
EB-40-17Z	30	97.5	2.7 x 10^{-6}	4.5

Table 10.2. Summary of the experimental conditions and resultant calculated creep strain rates and time-to-failure for a suite of conventional creep experiments on EB. Experiments are shown in Fig. 10.9.

Table 10.3 shows the relative durations spent in each of the three creep curve phases for the conventional creep experiments on EB spanning creep strain rates of three orders of magnitude. Table 10.3 shows that the percentage of time spent in each of the three phases remains remarkably similar, as observed in experiments on DDS (Chapter Eight, Table 8.3). As before, samples spend approximately 20, 60 and 20% of their total time-to-failure duration in primary, secondary and tertiary creep phases respectively.

Sample	**Resultant creep strain rate (s^{-1})**	Time spend in primary creep phase		Proportion of time spend in secondary creep phase		Proportion of time spend in tertiary creep phase	
		(minutes)	(%)	(minutes)	(%)	(minutes)	(%)
EB-40-16Z	2.4×10^{-9}	1000	22	2700	60	800	18
EB-40-14Z	4.0×10^{-8}	60	17	165	61	45	17
EB-40-15Z	4.1×10^{-7}	5	20	15	60	5	20
EB-40-17Z	2.7×10^{-6}	0.9	20	2.8	62	0.8	18

Table 10.3. Summary of the time spent in each of the three creep curve phases for conventional creep experiments on EB. Experiments are shown in Fig. 10.9. Times are calculated by eye from the axial strain against time curves (creep curves). Percentages are rounded to the nearest percent.

Similar to creep in DDS (Chapter Eight, Figs. 8.13c and 8.15), quantitatively different behaviour is observed in the strain curve at the lowest applied stresses (Fig. 10.9d). At this lowest strain rate, the strain increases in a step-wise manner with extended periods of very low strain rate punctuated by short periods of very rapid deformation. At higher applied stresses, and therefore higher strain rates, the step-wise behaviour is not observed. Since the steps are not commensurate with any output of AE energy it would be wise to assume that they are not a result of the deforming sample but a product of stick-slip of the moving seal in the actuator piston.

The two other damage proxies of pore volume change and cumulative AE energy also exhibit trimodal behaviour throughout, although the curves are visibly less smooth in some cases. This is particularly the

case for the porosity change and cumulative AE curves at the lowest applied stress (Q = 304 MPa; Figs. 10.9h and 10.9). In this case, there is a much greater contribution to the total porosity change and cumulative AE energy during the primary creep phase than for the experiments at higher applied stresses. In fact, the porosity appears to remain essentially constant during the whole of the secondary creep phase.

In all cases, the tertiary creep phase is characterized by accelerations in all three proxies for damage (onset of tertiary creep phase is marked by red lines on Fig. 10.9). Furthermore, the value of each of the three proxy measures at the onset of tertiary creep is in a very narrow range, regardless of the different applied stresses and the very different lengths of time required to reach that point; an axial strain in the range of 2.20 to 2.22%, a porosity change in the range 0.00 to 0.10%, and cumulative AE energy in the range of 2000-3500 units. This implies that the onset of tertiary creep occurs at a similar level of crack damage in all cases.

The relation between applied differential stress and creep strain rate (calculated for the quasi-linear portions of trimodal creep curves) is plotted on semi-log axes in Fig. 10.11. For the range of stresses applied and strain rates measured in our experiments, obtained, the relation can be adequately described by either a power law or an exponential law (see Chapter Three, Equations [3.6] and [3.7]) with the parameters listed in Table 10.4. Because the relation is so non-linear and stress sensitive, any variation in the initial state of damage within test samples becomes very important. This is a significant problem when using natural materials such as porous rocks (see Chapter Eight), because of the inevitable variation in porosity and crack density between different samples, even when cored form the same block of material. However, it was found that repeatability between samples of EB was much superior to DDS. Nevertheless, in order to circumvent the problem of performing a large number of

experiments to investigate the potential influence of variables such as P_{eff} and temperature, and due to the fact that stress-stepping has been shown to be reliable (see Chapter Eight), stress-stepping creep experiments were employed on samples of EB.

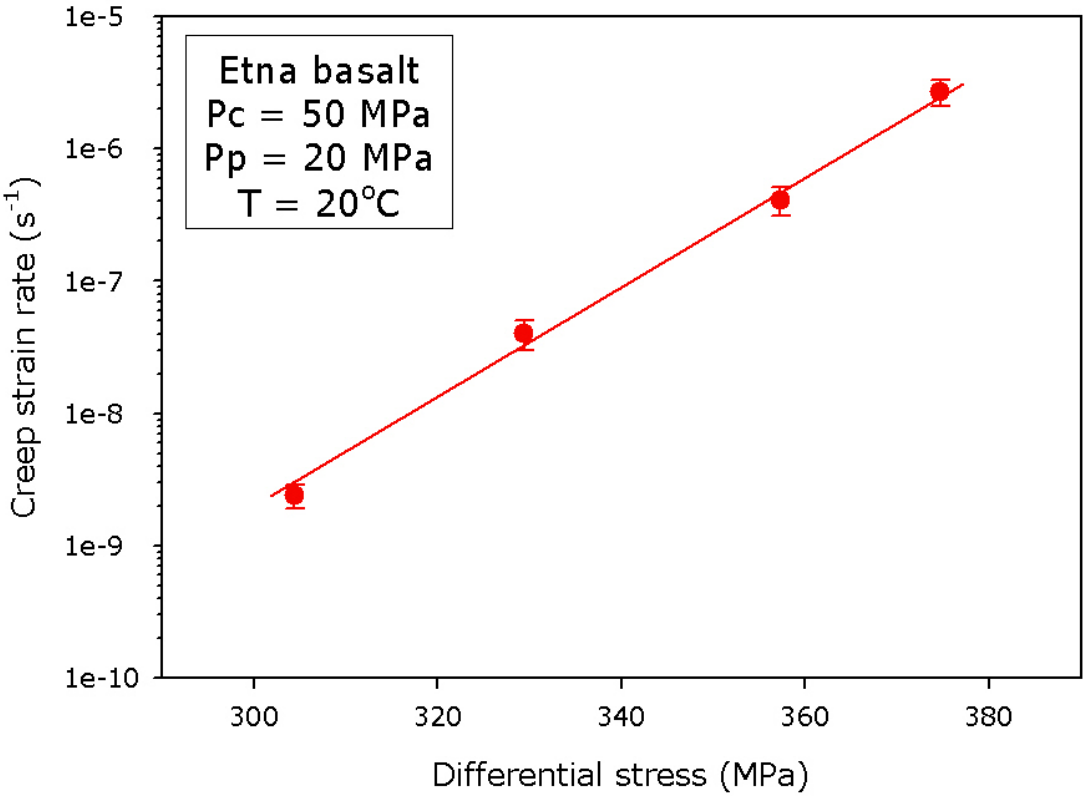

Figure 10.11. Creep strain rate data from multiple conventional brittle creep experiments on water-saturated EB plotted on a log scale against applied differential stress. Experimental conditions are indicated on the figure. P_c – confining pressure; P_p – pore fluid pressure; T – sample temperature [samples EB-40-14Z, EB-40-15Z, EB-40-16Z and EB-40-17Z].

The relation between the time-to-failure and the creep strain rate is plotted on semi-log axes in Fig. 10.12. The relation is again very stress sensitive and only a small change in applied differential stress results in a dramatic change in the time-to-failure (Fig. 10.13). The relationship between time-to-failure and the creep strain rate can be adequately described by both a power law and exponential function (see Fig. 10.12 for details).

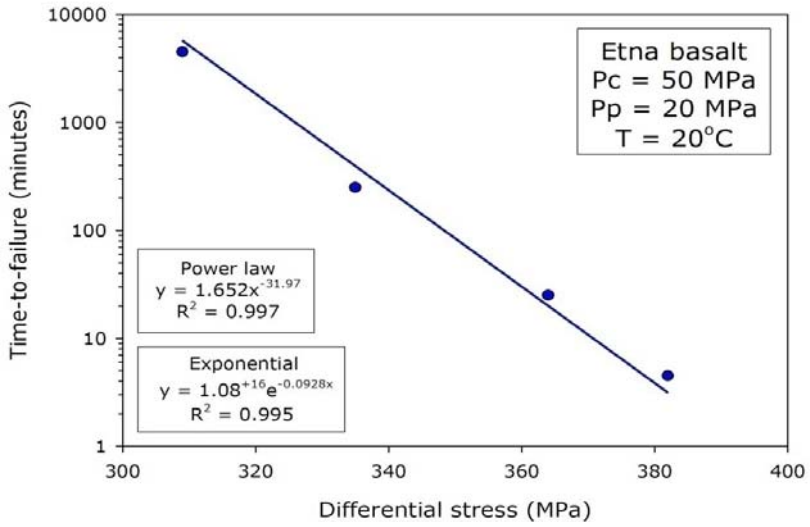

Figure 10.12. Time-to-failure data from multiple conventional brittle creep experiments on water-saturated EB plotted on a log scale against applied differential stress. Experimental conditions are indicated on the figure. Power law and exponential function fits are also shown on the figure. P_c – confining pressure; P_p – pore fluid pressure; T – sample temperature [samples EB-40-14Z, EB-40-15Z, EB-40-16Z and EB-40-17Z] (data in Table 10.2).

Sample number	Confining pressure (MPa)	Pore fluid pressure (MPa)	Effective confining pressure (MPa)	Temperature (°C)	Power law gradient function (η)	Exponential gradient function (β)	Power law R^2 value	Exponential R^2 value
EB-40-04	50	20	30	20	29.19	0.0886	0.995	0.994
EB-40-05	50	20	30	20	32,04	0.1024	0.999	0.997
EB-40-06	50	20	30	20	31.09	0.0958	0.999	0.998
EB-40-10	30	20	10	20	60.56	0.2400	0.992	0.992
EB-40-11	70	20	50	20	25.65	0.0590	0.996	0.997
EB-40-23	50	20	30	75	27.28	0.0827	0.993	0.995
Conventional creep experiments	50	20	30	20	33.09	0.0978	0.997	0.996

Table 10.4. Experimental conditions, power law and exponential function gradient coefficients and results of regression analysis for a number of stress-stepping creep experiments (for more information see the next section) and the series of conventional creep experiments shown in Fig. 10.9.

The results of the conventional creep experiments devised to investigate microstructural observations during the secondary creep phase are presented in Fig. 10.13. These experiments were both conducted at applied differential stress of 316 MPa; for the experiment devised to be stopped after a significant portion of the secondary creep phase this resulted in a creep strain rate of 1.4 x 10^{-8} s^{-1} (Fig. 10.13b).

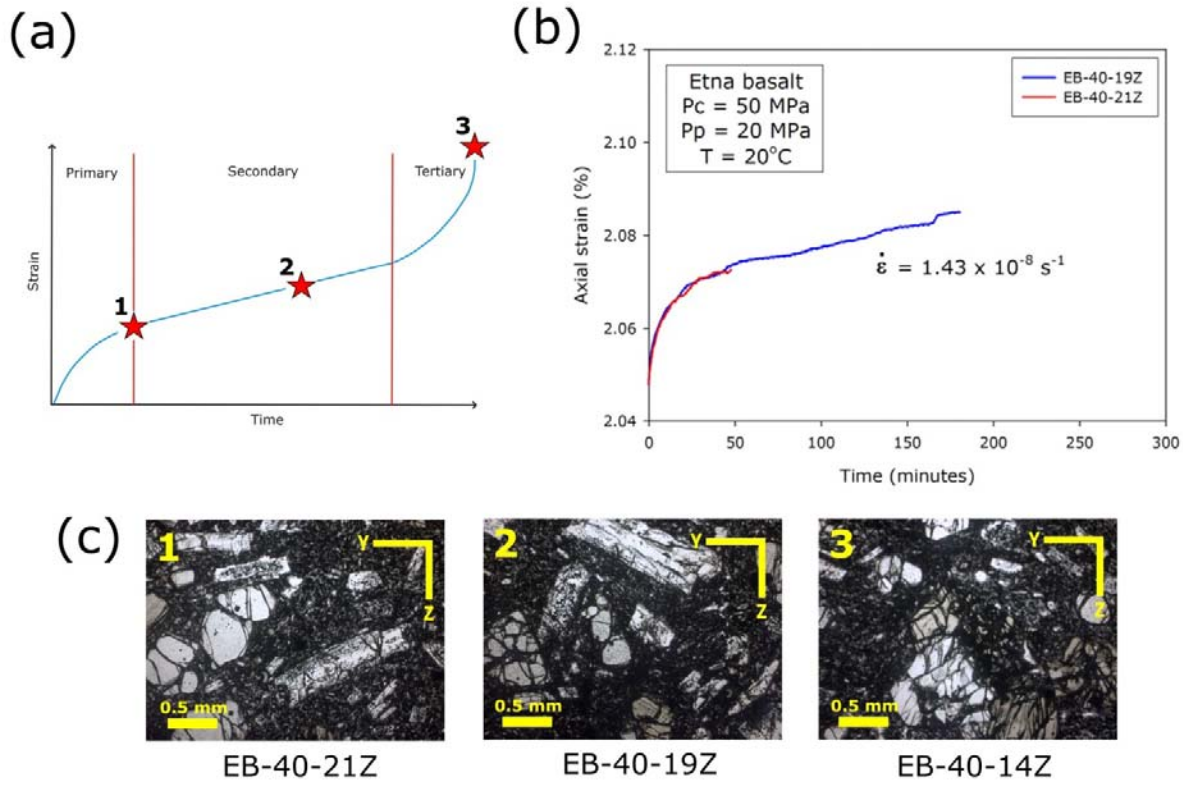

Figure 10.13. Microstructural analysis of stress corrosion cracking in EB during the secondary creep phase. (a) Schematic creep curve showing the positions where the microstructurally-focussed conventional creep experiments on EB were stopped and carefully unloaded. (b) The axial strain data from experiments devised to reach the points on the creep curve marked 1 and 2 shown in (a). (c) Photomicrographs for each of the three positions marked 1, 2 and 3 in (a).

Optical microscopy has demonstrated that the level of microcrack damage present within the sample taken to failure (sample EB-40-14Z) is markedly more significant than both the sample taken to the onset of the secondary creep phase (sample EB-40-21Z) and the sample stopped after a significant

portion of the secondary creep phase (sample EB-40-19Z) (Fig. 10.13c). Also, samples EB-40-21Z and EB-40-19Z do not show any signs of damage localization; however, they clearly contain a greater amount of damage than those from the undeformed state (Chapter Five, Fig. 5.4). It is difficult to distinguish any crack morphological differences between the samples taken to points 1 and 2 on the creep curve in Fig. 10.13a using optical microscopy. A more rigorous SEM study would be required to investigate this further.

10.3.3 Stress-stepping brittle creep experiments

In order to further verify the stress-stepping methodology, a number of stress-stepping creep experiments were performed on samples of EB under the same experimental conditions as in Fig. 10.9 (Fig. 10.14), and these results were then compared with those from conventional creep experiments (see Fig. 10.15). Fig. 10.15 shows the creep strain rates from a set of conventional experiments and a single stress-stepping experiment, all run at an effective confining pressure of 30 MPa. It must be noted that the trends observed in the stress dependence of the creep train rates is virtually identical. The natural variability between samples of EB is much less than that for DDS i.e. there is essentially no offset between the curves.

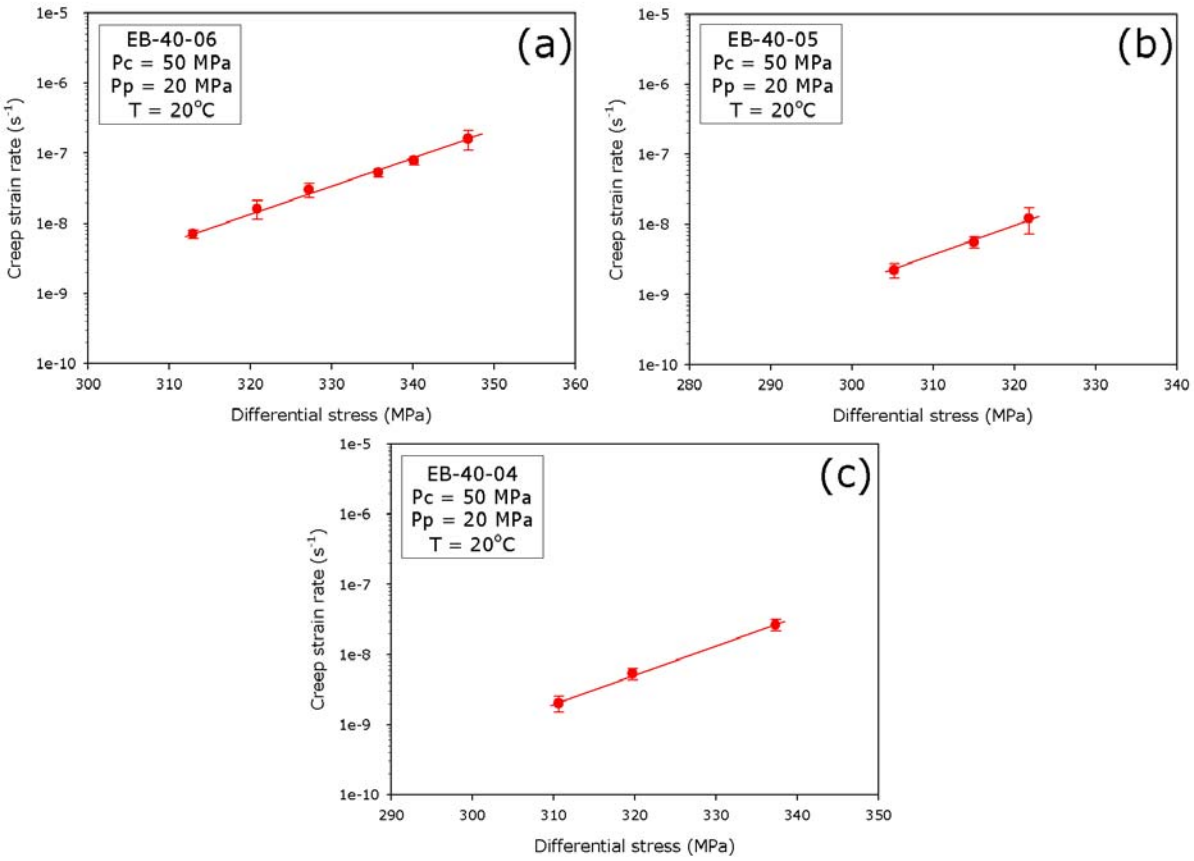

Figure 10.14. Creep strain rate data from three stress-stepping brittle creep experiments on water-saturated EB. Creep strain rate data is plotted on a log scale against applied differential stress. Experimental conditions are displayed on the figure. P_c – confining pressure; P_p – pore fluid pressure; T – sample temperature [samples EB-40-04Z, EB-40-05Z and EB-40-06Z]. Samples EB-40-04Z (c) and EB-40-05Z (b) only yielded three points each due to the unexpected very short duration of the secondary creep phases at higher applied differential stresses (much shorter than DDS). This was anticipated in EB-40-06Z (a) thus allowing more creep strain rate points to be collected. Error in the creep strain rate measurements are denoted by the error bars, error in the differential stress values are represented by the size of the datapoints. The fits to these curves are summarized in Table 10.4.

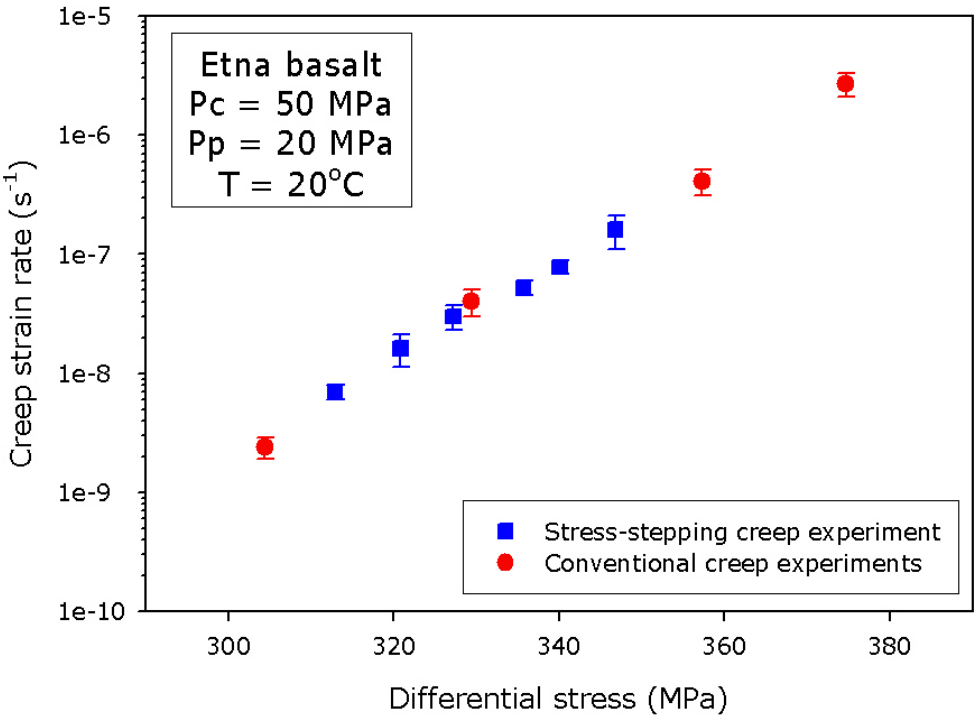

Figure 10.15. Creep strain rate data from a stress-stepping brittle creep experiment on water-saturated EB (red circles) plotted side-by-side with those data derived from a suite of conventional brittle creep experiments (blue squares). Creep strain rate data is plotted on a log scale against applied differential stress. Experimental conditions are displayed on the figure. Error in the creep strain rate measurements are denoted by the error bars, error in the differential stress values are represented by the size of the datapoints. P_c – confining pressure; P_p – pore fluid pressure; T – sample temperature. Stress-stepping experiment data – sample EB-40-06; conventional creep experiment data – samples EB-40-14Z, EB-40-15Z, EB-40-16Z and EB-40-17Z (see Table 10.4).

The influence of P_{eff} on brittle creep in EB was investigated at effective confining pressures of 10, 30 and 50 MPa (whilst maintaining a constant P_p of 20 MPa). The results are given in Fig. 10.16, which shows that varying the P_{eff}, even over this modest range, has a profound influence on creep strain rates. Firstly, the strain rates are shifted to dramatically lower values for the same differential stress as P_{eff} is increased. This appears consistent with the results from constant strain rate experiments showing that EB is stronger at a higher P_{eff} (Fig. 10.16). However, the increase in strength seen in constant strain rate

experiments as P_{eff} is increased from 10 to 50 MPa is about 75% (Fig. 10.4) (plotted as unfilled shapes on Fig. 10.16), while the decrease in creep strain rate over the same interval is many orders of magnitude. Secondly, the gradient of the curves on Fig. 10.16 describing the relation between creep strain rate and differential stress decrease significantly and systematically as P_{eff} is increased; a change that would not be expected from a purely mechanical process (see Table 10.4 and Fig. 10.17). This trend is identical to that observed in DDS (see Chapter Eight).

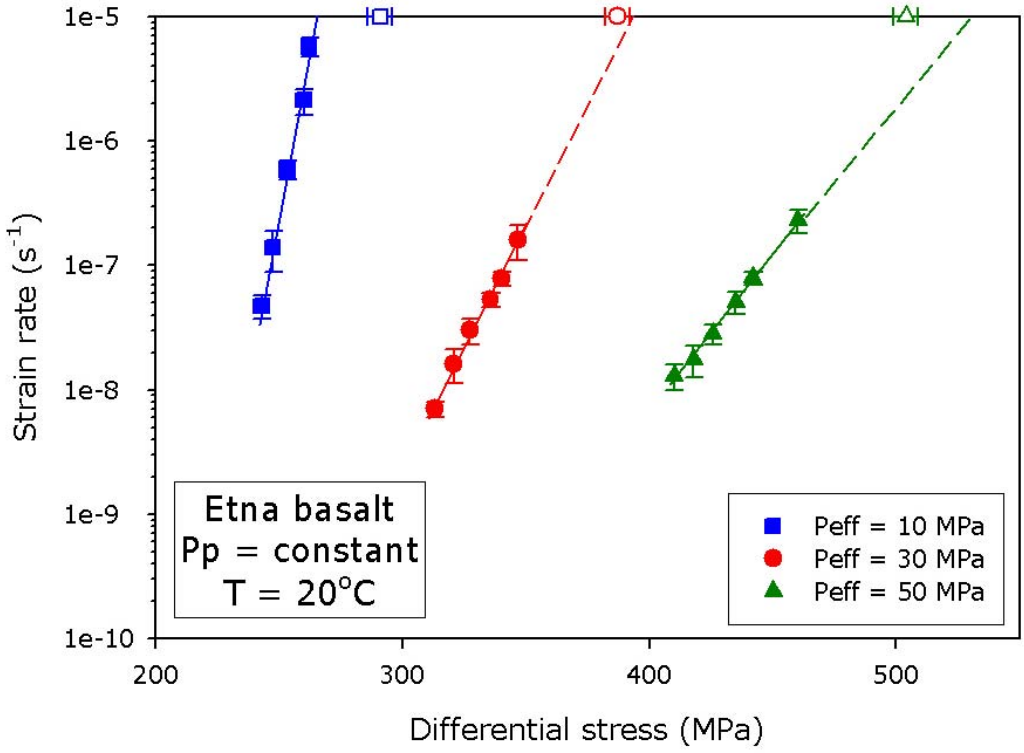

Figure 10.16. Creep strain rate data from stress-stepping brittle creep experiments performed at 10 (blue squares), 30 (red circles) and 50 MPa (green triangles) effective confining pressures on water-saturated EB, whilst maintaining a constant pore fluid pressure of 20 MPa. Creep strain rate data is plotted on a log scale against applied differential stress. 10 MPa effective confining pressure – sample EB-40-10Z; 30 MPa effective confining pressure – sample EB-40-06Z; 50 MPa effective confining pressure – sample EB-40-11Z. Experimental conditions are indicated on the figure. Short-term peak stress data from constant strain rate (1.0×10^{-5} s^{-1}) experiments are plotted as unfilled shapes. Error in the creep strain rate measurements are denoted by the error bars, error in the differential stress values are represented by the size of the datapoints. P_{eff} – effective confining pressure; P_p – pore fluid pressure; T – sample temperature. The fits to these curves are summarized in Table 10.4.

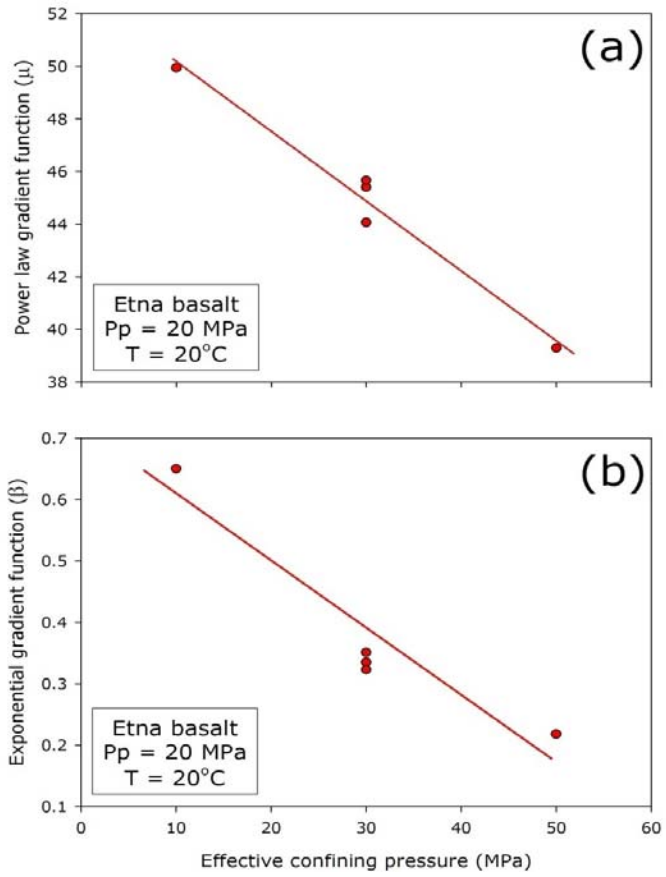

Figure 10.17. Graphs of the effective confining pressure dependence of the (a) power law gradient function, η and (b) the exponential gradient function, β (see also Table 10.4) in EB using data derived from stress-stepping creep experiments. Experimental conditions are indicated on the figure. Linear distribution fits are shown on the figure. P_p – pore fluid pressure; T – sample temperature [samples EB-40-04Z, EB-40-05Z, EB-40-06Z, EB-40-10Z and EB-40-11Z].

The influence of an elevated temperature on brittle creep in EB was investigated using temperatures of 20 and 75°C. The experiments were conducted under the conditions of P_c = 50 MPa and P_p = 20 MPa (P_{eff} = 30 MPa). Creep strain rates from the experiments (calculated from the quasi-linear portions of the trimodal creep curves) are plotted on semi-log axes against both applied differential stress and normalized failure stress in Fig. 10.18. The results demonstrate that increasing the temperature of the sample from 20 to 75°C induces only a very minor increase in the calculated creep strain rates for a given applied differential stress. The observed difference is, however, beyond the natural variability of

EB seen in previous experiments (e.g. see Figs. 10.14 and 10.15). Fig. 10.18a shows that a lower applied differential stress is required to yield the same creep strain rate at 75°C. To achieve a creep strain rate of 1.0×10^{-7} s^{-1} for example, the applied differential stress needed is reduced from 341 to 335 MPa between 20 to 75°C. Fig. 10.18b shows that, to achieve a creep strain rate of. 1.0×10^{-7} s^{-1} for example, the proportion of the σ_p (normalized with respect to the peak stresses found during a constant strain rate experiment performed at both 20 and 75°C) required is 0.875 and 0.925 for 20 and 75°C respectively. This is the opposite trend seen in the sandstones in identical experiments (see Chapter Nine).

An elevated temperature is not only seen to shift the creep strain rate curve towards lower stresses, but also alters the gradient of the curve. At 75°C the gradient of the creep strain rate curve becomes shallower, the same trend, albeit less pronounced, seen in the sandstones (see Chapter Nine). For the range of stresses applied and strain rates measured in our experiments, the relation can be adequately described by either a power law or an exponential function (see Chapter Three, Equations [3.6] and [3.7]) with the parameters listed in Table 10.4. In general, the response to an elevated temperature in EB is a stark contrast to the behaviour of the sandstones during identical experiments (see Chapter Nine). Here, at a constant applied differential stress level, the creep strain rate is merely doubled or trebled, the multiple orders of magnitude change seen in the sandstones is not observed here.

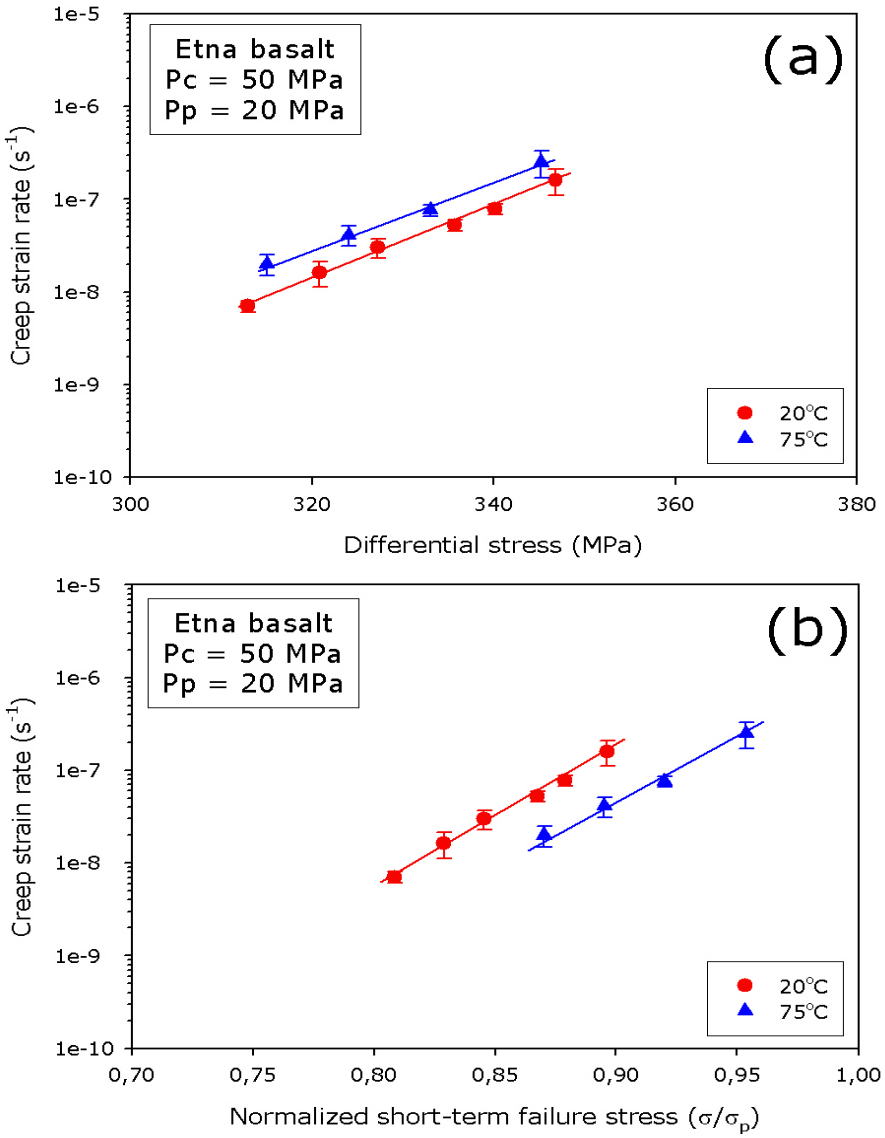

Figure 10.18. Creep strain rate data from stress-stepping creep experiments at elevated temperatures on samples of water-saturated EB plotted on a log scale against (a) differential stress and (b) normalized short-term failure stress (using peak stresses derived from experiments conducted under a constant strain rate at both 20 and 75°C, see Fig. 10.6). Experimental conditions are indicated on the figure. Error in the creep strain rate measurements are denoted by the error bars, error in the differential stress values are represented by the size of the datapoints. P_c – confining pressure; P_p – pore fluid pressure [samples EB-40-06Z and EB-40-23Z]. The fits to these curves are summarized in Table 10.4.

10.4 Conclusions

1. Constant strain rate experiments have shown that the experimental reproducibility of EB under the same conditions is excellent. They have also shown that σ_p is increased when the P_{eff} on the sample during deformation is increased. An increase from 10 MPa to 50 MPa P_{eff} results in about a 75% increase in the σ_p (from 291 to 504 MPa). Those performed at 75°C showed a 9% (from 387 to 362 MPa) decrease in σ_p.
2. Conventional brittle creep experiments have shown that applied differential stress exerts a crucial influence on both creep strain rate and time-to-failure. They have also demonstrated that the independent proxies for damage are approximately similar at the onset of the tertiary creep phase. It is also shown that, regardless of creep stain rate, the relative proportions of the durations of each of the creep phases remains the same.
3. Stress-stepping creep experiments have been shown to accurately replicate the trends derived from a suite of conventional creep experiments. Stress-stepping creep experiments on EB have also demonstrated that an increase in P_{eff} affects the creep strain rates in a way not expected from purely mechanical processes, in a similar way to the behaviour of DDS (see Chapter Eight). An increase in temperature from 20 to 75°C only produces a modest increase in the creep strain rates, especially when compared to the impact of an elevated temperature on the sandstones (see Chapter Nine).

Chapter eleven

11. Discussion of Time-dependent Brittle Creep in Rock

11.1 Introduction

This chapter discusses the results of the time-dependent brittle deformation data presented in Chapters Eight, Nine and Ten. It is organized into eight sections: (1) discussion on creep strain rates and damage levels; discussion on the influence of (2) mineralogical composition and microstructure (3) effective confining pressure (P_{eff}) and pore fluid pressure (P_p) and (4) temperature; (5) discussion on predicting rock failure under constant stress; (6) discussion on the fitting of macroscopic creep laws to the data; (7) consideration of a creep flow law; (8) the application of the data in understanding large-scale geophysical problems; (9) the importance of brittle creep with depth in the crust and (10) potential avenues for future research.

The range of brittle creep behaviour observed in this study is plotted in effective confining pressure – applied differential stress (Peff-Q) space in Fig. 11.1. As noted in Chapter Eight, in order to perform brittle creep experiments in a feasible laboratory time scale, only the range of Q between D' and σ_p was used. It is likely that brittle creep can occur at any Q above C'; however, brittle creep close to C' is likely to be extremely slow and therefore impracticable to study over any reasonable laboratory time scale. Given that C' marks the lower limit of dilatant cracking (and the lower limit of new damage accumulation) it is suggested that brittle creep is unlikely to occur below this limit (Fig. 11.1).

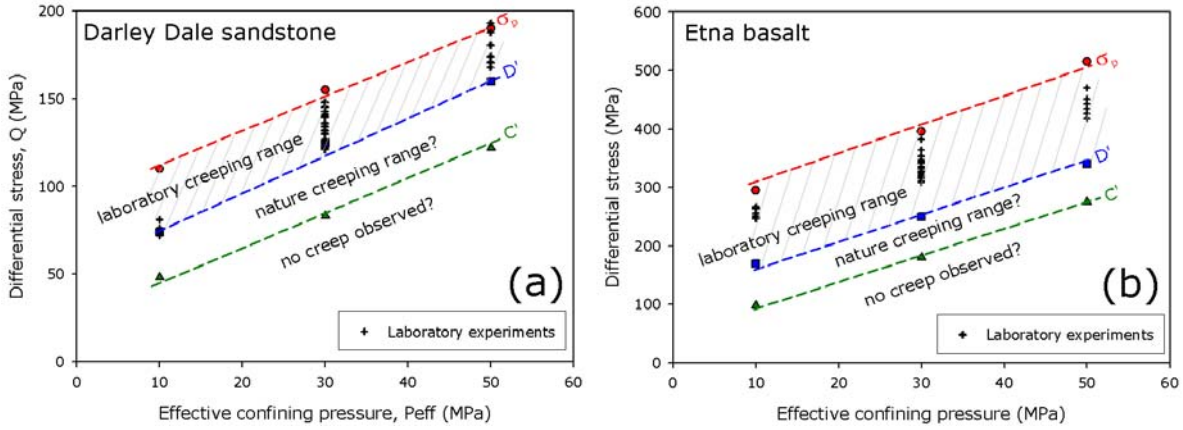

Figure 11.1. Pressure-stress (*PQ*) diagrams for the experimental creep data collected for (a) DDS and (b) EB during this study demonstrating, in *PQ* space, the laboratory creeping range, the potential natural creeping range and the range where no creep is likely to be observed. The figures include experimentally-derived values for the peak stress, *D'* and *C'* for P_{eff} = 10, 20 and 30 MPa from constant strain rate (1.0 x 10^{-5} s^{-1}) experiments. Experimental creep data from both conventional and stress-stepping experiments are included on the figures.

11.2 Creep strain rates and damage levels

The conventional brittle creep experiments on DDS (see Chapter Eight, Fig. 8.13) and EB (see Chapter Ten, Fig. 10.9) demonstrate that creep strain rate and time-to-failure in both porous sandstone and thermally-cracked basalt are strongly dependent on the applied differential stress; an observation previously noted for creep in sandstones [Baud and Meredith, 1997; Ngwenya *et al.*, 2001] and in crystalline rock [Kranz *et al.*, 1982]. A comparison between the DDS creep data from the conventional creep experiments from this study and those of Baud and Meredith [1997], under the same effective confining pressure conditions (P_{eff} = 30 MPa), is given in Fig. 11.2 and also in Table 11.1. The gradients of the two curves in Fig. 11.2 are remarkably similar (see Table 11.1) and, again, the slight offset can be explained by sample variability due to the fact that the samples were prepared from different blocks.

The conventional creep experiments on EB presented in this study (see Chapter Ten) represent the first performed on a basic rock sample.

Sample number	Confining pressure (MPa)	Pore fluid pressure (MPa)	Effective confining pressure (MPa)	Temperature (°C)	Power law gradient function (η)	Exponential gradient function (β)	Power law R^2 value	Exponential R^2 value
Conventional creep experiments [this study]	50	20	30	20	44.53	0.347	0.995	0.997
Conventional creep experiments [Baud and Meredith, 1997]	75	45	30	20	47.05	0.341	0.990	0.986

Table 11.1. Experimental conditions, power law and exponential function gradient coefficients and results of regression analysis for the series of conventional creep experiments on DDS shown in Fig. 8.11 and data from Baud and Meredith [1997].

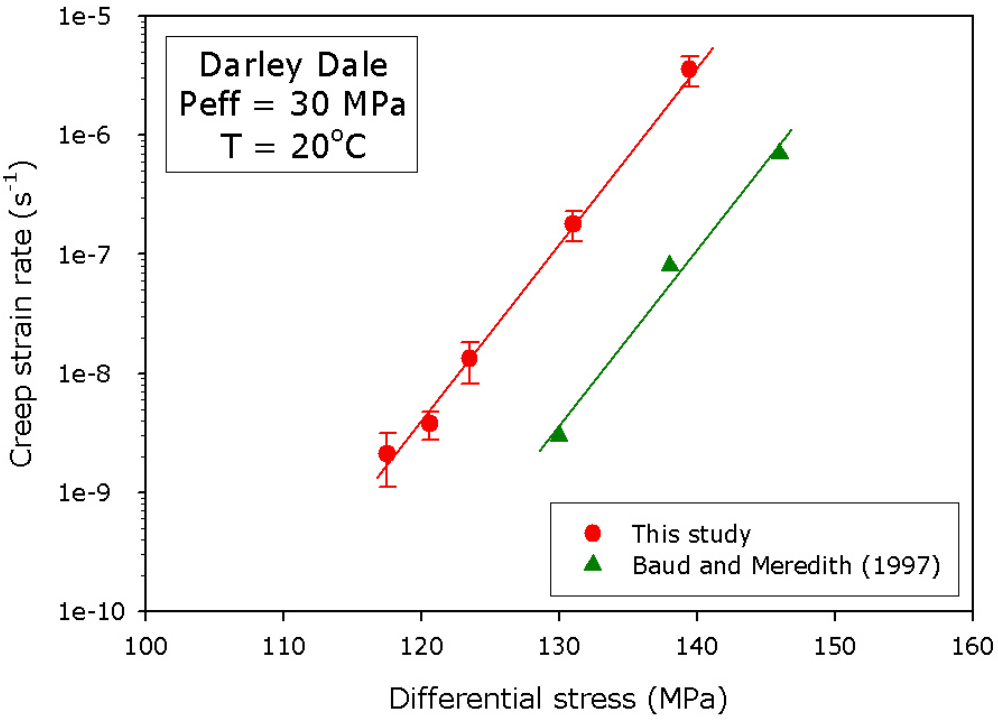

Figure 11.2. Creep strain rate data from a suite of conventional brittle creep experiments on water-saturated DDS at 30 MPa effective confining pressure from this study (red circles) and from conventional brittle creep experiments on water-saturated DDS at P_{eff} = 30 MPa from Baud and Meredith [1997] (green triangles). Creep strain rate data is plotted on a log scale against applied differential stress. Error in the creep strain rate measurements are denoted by the error bars, error in the differential stress values are represented by the size of the datapoints. Experimental conditions are indicated on the figure. P_{eff} – effective confining pressure; T – sample temperature.

Although both DDS and EB exhibit classic trimodal creep when held at a constant applied differential stress (Chapter Eight, Fig. 8.13 and Chapter Ten, Fig. 10.9), the times-to-failure at the same creep strain rate are much different. Time-to-failure is considerably less in EB than DDS (Table 11.2); for example, at a creep strain rate of 10^{-7} s^{-1} the time-to-failure is 3600 and 250 minutes for DDS and EB respectively. It is likely that this is due to the fact that EB requires a higher percentage of its short-term peak stress (σ_p) than DDS to creep at a given creep strain rate (Table 11.2). Therefore, samples of EB will be closer to failure and creeping at the same creep strain rate, thus the time-to-failure is reduced.

Sample	Effective confining pressure (MPa)	Level of applied stress (% of σ_p)	Resultant creep strain rate (s^{-1})	Time-to-failure (minutes)
DD-40-40Z	30	75	3.7×10^{-9}	12960
DD-40-22Z	30	80	1.3×10^{-8}	3600
DD-40-45Z	30	85	1.0×10^{-7}	160
DD-40-19Z	30	90	3.5×10^{-6}	10
EB-40-16Z	30	90	2.4×10^{-9}	4500
EB-40-14Z	30	92.5	4.0×10^{-8}	270
EB-40-15Z	30	95	4.1×10^{-7}	25
EB-40-17Z	30	97.5	2.7×10^{-6}	4.5

Table 11.2. Summary of the experimental conditions and resultant calculated creep strain rates and time-to-failure for a suite of conventional creep experiments on both DDS and EB. Confining pressure – 50 M Pa; Pore fluid pressure – 20 MPa; Sample temperature – 20°C.

The results from the conventional creep experiments presented for both DDS and EB in this study also demonstrate that the three measured proxies for crack damage (axial strain, pore volume change and output of AE energy) have approximately equal values at the transition from secondary to tertiary creep (marked by red horizontal lines in Chapter Eight, Fig. 8.13 and Chapter Ten, Fig. 10.9). This holds for all creep strain rates (measured during secondary creep) over the three orders of magnitude sampled. This suggests that there is a critical level of damage required before the onset of acceleration to failure. This observation of a critical damage threshold for the onset of tertiary creep has previously been reported from a number of experimental studies [e.g., Griggs, 1939;1940; Wawersik and Brown, 1973; Cruden, 1974; Kranz and Scholz, 1977; Baud and Meredith, 1997], and has also been predicted from modelling [Armitrano and Helmstetter, 2006]. In particular, Kranz and Scholz [1977] reported that tertiary creep only commenced when the rock had sustained a critical amount of inelastic volumetric strain. Baud and Meredith [1997] support this observation and reported that a critical level of volumetric strain (as measured by pore volume change) was required to induce tertiary creep. Furthermore, they demonstrated that a critical level was required in their other proxy measures of damage (axial strain and

output of AE energy) before the onset of tertiary creep (see Chapter Three, Fig. 3.18). They suggested that this point also marked the onset of localization of damage, leading to acceleration to failure on a localized fault zone regardless of the applied differential stress and the creep strain rate.

In order to address this point further, samples of DDS that were taken to the onset of tertiary creep and then unloaded and removed from the deformation apparatus for microstructural analysis have been investigated. Crack analysis of the samples taken to the onset of tertiary creep was then compared with the same analysis on undeformed samples and samples taken to failure. For all samples, linear crack densities ($P_{\perp}$ and $P_{\parallel}$) were determined by the technique described earlier, and the results are given in Table 8.3 together with measurements of crack area per unit volume (P_v) and crack anisotropy (A_c). All measures of crack density show an increase from the values for the initial, undeformed state in both samples taken to the onset of tertiary creep. For example, P_v increases by between 24 and 37% between the two states. While these increases are significant, more important is the increase in crack anisotropy. In the undeformed state the anisotropy is very low at 8%, while at the onset of tertiary there is a threefold increase to between 24 and 27%. This is strong evidence that the new damage induced during primary and secondary creep is dominated by the growth of axial cracks sub-parallel to the maximum principal stress [Lawn, 1993]. The crack densities and anisotropy for both samples have similar values in spite of the order of magnitude difference in creep strain rate. However, for the sample taken to failure, all the measures of crack density and the anisotropy increase substantially, as expected. Crack density values from both undeformed and post-failure samples in this study compare well with those previously published for DDS [Wu *et al.*, 2000]. The level of crack damage at the onset of tertiary creep is very similar to that for a sample taken to the pre-peak stress stage in a constant strain rate experiment presented by Wu *et al*. [2000]. This should not be surprising, since both conditions represent a point that is well into the phase of dilatant cracking but that precedes crack coalescence and damage

localization. Unfortunately, it is apparent that further SEM analysis is required in order to draw up firm conclusions on the morphology of microcracks during the secondary creep phase in EB.

To further investigate the time evolution and spatial distribution of cracking during brittle creep, the locations of AE hypocenters during conventional brittle creep experiments on DDS were determined at a P_{eff} of 30 MPa (P_c = 50 MPa and P_p = 20 MPa). The AE hypocentre location data for DDS were excellent and consistent; therefore, only experiments performed on DDS are presented and discussed here. Numerous previous studies have shown that AE output increases exponentially or supra-exponentially as stressed rock approaches macroscopic failure [e.g., Scholz, 1968b; Sammonds *et al.*, 1992; Cox and Meredith, 1993; Fortin *et al.*, 2006; Stanchits *et al.*, 2006], and multi-channel recording systems have been used to determine the location of AE hypocenters of the AE output within the sample [Lockner *et al.*, 1991;1992; Lockner and Byerlee, 1992; Lockner, 1993b; Zang *et al.*, 1996; Lei *et al.*, 2000; Lei *et al.*, 2004]. More recently, Giga-RAM recorders have been used to capture continuous AE waveforms during rock deformation experiments to allow even more sophisticated analysis [Thompson *et al.*, 2006; Benson *et al.*, 2007; Townend *et al.*, 2008].

For the experiments, an applied differential stress that produced a creep strain rate of approximately 10^{-7} s^{-1} was selected so that the secondary creep phase was long enough (about 150 minutes) to allow a sufficient number of AE hypocenters to follow the evolution of crack damage with time to be recorded. Fig. 11.3 shows the located AE events from one such experiment in which the strain rate during secondary creep was 1.4×10^{-7} s^{-1}. A total of 1877 AE hypocenters were located during the experiment, of which 592 occurred during the primary creep phase, 702 during secondary creep and 583 during tertiary creep. During primary creep (Fig. 11.3a) the AE hypocenters form two diffuse clusters in the upper and lower parts of the sample that cover the full sample diameter. During secondary creep the

hypocenter locations become more evenly distributed through the sample volume (Fig. 11.3b). During tertiary creep (Fig. 11.3c) the pattern becomes a little more complicated. Both a distributed pattern of hypocenters and, superimposed on this, a set of localized hypocenters that locate along the eventual fault plane is observed. The AE events that produce these localized hypocenters occurred during that latter part of tertiary creep as the fault propagated rapidly across the sample to produce dynamic, macroscopic failure. With the benefit of hindsight, it could be argued that there is some indication of localization in the locations determined during secondary creep, but this is only apparent after looking at the tertiary creep data. The total number of located AE hypocenters during all three phases is shown in Fig. 11.3d, with the orientation of the eventual shear failure plane superimposed. The pattern seen in Fig. 11.3 is characteristic of all our experiments in which AE hypocenter locations were investigated. In general, AE behaviour is (1) diffuse and distributed during primary creep, (2) distributed with some suggestion of localization or 'mixed mode' during secondary creep and (3) increasingly localized during tertiary creep.

The suggestion that AE clustering might commence during the latter part of secondary creep appears to conflict with the idea of a critical damage threshold for the onset of tertiary creep and localization of deformation [e.g. Baud and Meredith, 1997]. However, this may merely highlights the difficulty of defining the onset of tertiary creep from an emergent strain-time curve. It may well be that the transition would actually be better defined using all the available AE data (hit rate, energy rate and hypocenter locations). Whilst there have been a number of studies that have monitored AE output during brittle creep experiments on rock [e.g., Wu and Thomsen, 1975; Lockner and Byerlee, 1975; Ohnaka, 1983; Yanagidani *et al.*, 1985; Nishizawa *et al.*, 1984; Hirata *et al.*, 1987; Nishizawa and Noro, 1990; Baud and Meredith, 1997], only a few have used the location of AE hypocenters to investigate the transition from distributed to localized deformation as samples approach failure.

Furthermore, with the exception of Hirata *et al.* [1987], these have all been conducted on dry crystalline rock samples under uniaxial compression [Yanagidani *et al.*, 1985; Nishizawa *et al.*, 1984; Hirata *et al.*, 1987; Nishizawa and Noro, 1990]. Under such uniaxial conditions, localization of AE event hypocenters is reported to have commenced during secondary, or even primary [Yanagidani *et al.*, 1985], creep. This is as expected, since axial crack extension is not suppressed by the application of a confining pressure, and samples can fail by axial splitting rather than shear faulting associated with failure under triaxial compression [Paterson and Wong, 2005]. By contrast, Hirata *et al*. [1987] located AE hypocenters during brittle creep of dry granite under triaxial stress conditions. They calculated an evolving spatial fractal dimension of AE events by cross-correlation of hypocenter locations, and reported that their fractal dimension decreased as creep progressed. This indicates that clustering and localization increases as creep progresses, with the biggest changes occurring during the tertiary creep phase.

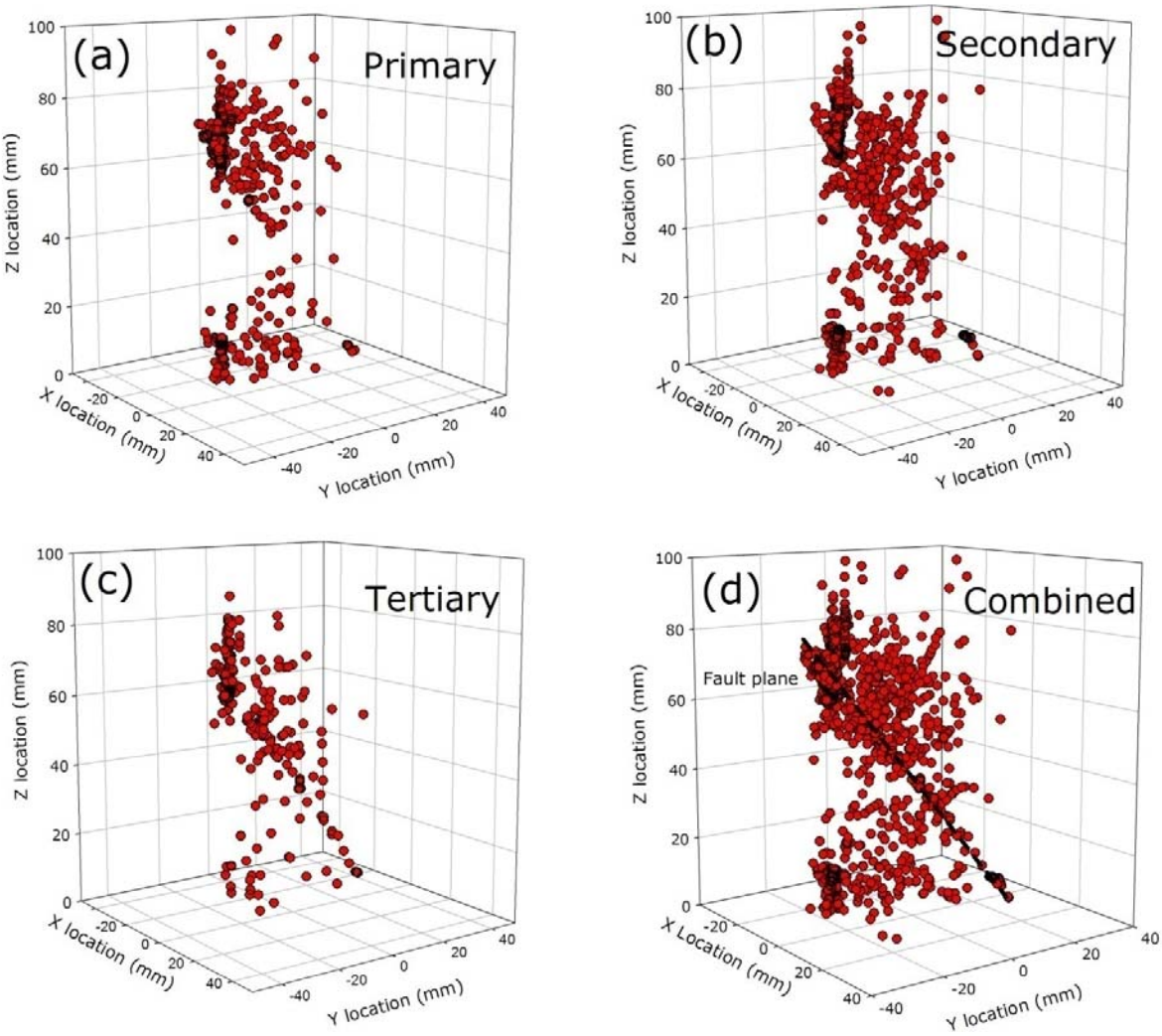

Figure 11.3. Plots of the calculated AE hypocentres for (a) primary creep, (b) secondary creep, (c) tertiary creep and (d) the total of all three of the creep phases for a conventional brittle creep experiment on DDS at a creep strain rate of 1.4×10^{-7} s^{-1}. The combined plot in (d) also shows the location of the eventual fault plane. Z-axis is normal to the axial loading direction.

11.3 The influence of mineralogical composition and microstructure on creep strain rates

All of the stress-stepping creep experiments performed in this study, regardless of rock type, have demonstrated that the applied differential stress exerts a crucial influence on creep strain rate (Fig. 11.4). Fig. 11.4 shows that the creep behaviour of the different rock types is remarkably similar, especially considering that the sandstones and basalt are essentially 'end-members' when their differences in mineralogical and microstructural properties are considered.

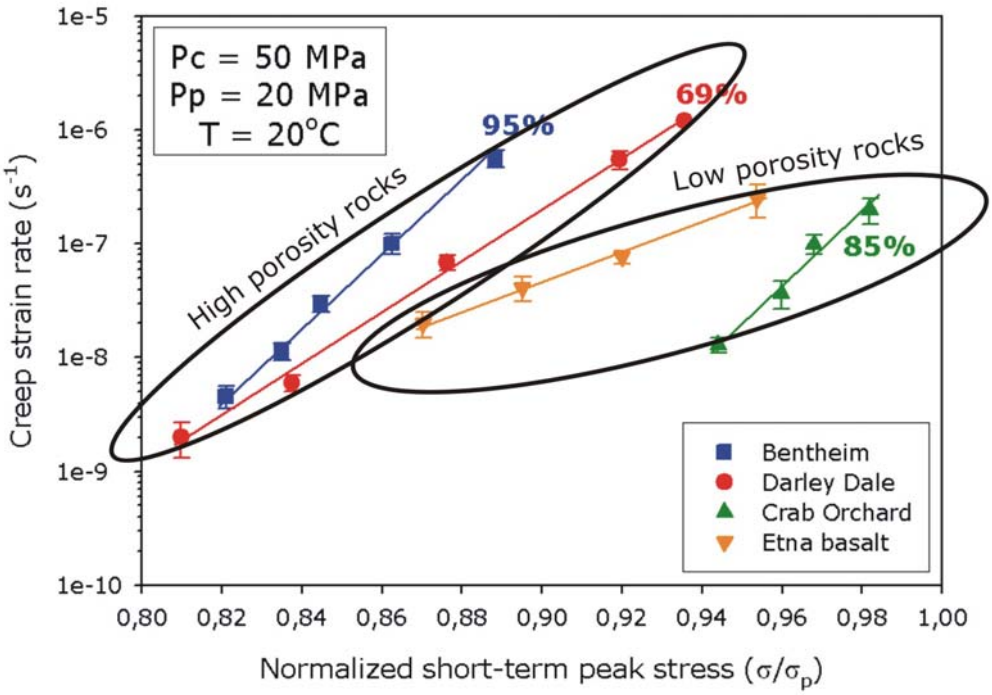

Figure 11.4. Creep strain rate data from stress-stepping brittle creep experiments on water-saturated samples of Darley Dale (red circles), Bentheim (blue squares), Crab Orchard sandstone (yellow diamonds) and Etna basalt (green triangles). Creep strain rate data is plotted on a semi-log scale against normalized σ_p (as determined from constant strain rate experiments performed under the same experimental conditions). Experimental conditions are shown on the figure. Error in the creep strain rate measurements are denoted by the error bars, error in the differential stress values are represented by the size of the datapoints. P_c – confining pressure; P_p – pore fluid pressure; T – sample temperature. Ellipses group rocks by their porosity (into 'high' and 'low') and percentages next to the sandstone curves indicate the proportion of quartz.

However, as Fig. 11.4 shows, there are slight differences in the creep strain rate curves in terms of gradient and position along the normalized σ_p stress axis. This variation will now be discussed in terms of the mineralogical and microstructural differences between the rock types. Previous studies on brittle creep in different sandstones have also shown that four sandstones of contrasting petrophysical properties (porosities ranging from 4% to 35%) yielded slightly different creep strain rate curves [Ngwenya *et al.*, 2001]. They found that creep deformation had a different sensitivity to the level of applied differential stress, depending on the initial state of damage represented by the porosity.

Stress-stepping creep experiments have demonstrated that the creep curve gradient for EB is much shallower than that for all three sandstones; this means that for a given increase in applied differential stress the increase on creep strain rate will be greater in all three of the sandstones than the basalt. This result corroborates the volume of data on stress corrosion cracking derived from DT experiments at room temperature (20°C in this case) (Fig. 11.5). Fig. 11.5 shows that, for a given normalized stress intensity factor of 0.4, crack velocity is at the very least 1.5 orders of magnitude lower in basic rocks than for quartz, the main constituent of the sandstone samples. In fact, quartz exhibits the fastest stress corrosion crack growth rates for a given stress intensity factor when compared to a number of other geological materials [see Fig. 11.5; Atkinson, 1984 for a review]. Also, data from Atkinson [1984] suggest that the more complex the microstructure, the lower the susceptibility to subcritical crack growth. This can adequately explain the comparatively larger differences seen in the creep strain rate curve gradients and therefore 'creep susceptibility' between the sandstones and the basalt. The more subtle differences between the behaviour in the sandstones can also be explained in this manner. The sandstone with the least quartz, DDS (69% quartz), requires a larger increase in applied differential stress to produce the same increase in creep strain rate than both quartz-rich BHS (95%) and COS (85%). It must be noted however that the creep strain rate curve gradient for COS is slightly steeper than that of BHS, even

though BHS contains a higher proportion of quartz. This may be due to the high degree of cementation in the COS 'blunting' cracks and preventing active species from reaching bridging bonds at the crack tips within the quartz grains.

It is not just the creep strain rate gradients that are different however. To deform at a given creep strain rate, EB must be held at a higher proportion of its normalized σ_p than both DDS and BHS; however, this relationship cannot be explained by the proportion of quartz in the rock samples, since COS requires even higher proportion of its normalized σ_p than EB. This relationship can however be explained in terms of sample porosity. The proportion of the normalized σ_p the rock type must be held at to achieve a creep strain rate of 1.0×10^{-7} s^{-1} for example is 0.86, 0.89, 0.92 and 0.96 for BHS (23.4% porosity), DDS (13.3%), EB (4.3%) and COS (3.3%) respectively (Fig. 11.4).

Theory predicts, in a silica-water system, that stress corrosion cracking requires a chemically-active pore fluid phase to reacts dissociatively with stress-supporting bridging bonds at crack tips. A greater porosity would not only suggest that the sample may contain more crack porosity are therefore more reaction sites, but there will be more reactive species available to react at such sites, thus facilitating stress corrosion cracking [see Michalske and Freiman, 1982;1983; Hadizadeh and Law, 1991]. An explanation of these data could also be that the low porosity rocks (both EB and COS; and therefore independent on rock type) require a greater degree of imposed crack porosity, the result of dilatancy during the initial loading curve, than the other more porous rocks (DDS and BHS) to creep at the same creep strain rate. This will in turn require that the low porosity rocks will be held at a high proportion of their σ_p than the high porosity rocks.

In summary, for the data presented in this study, the gradients of the creep strain rate curves are likely to be controlled by the mineralogy (the proportion of quartz in the rock) and the proportion of the σ_p at which a sample creeps at a given creep strain rate is likely to be controlled by the sample porosity.

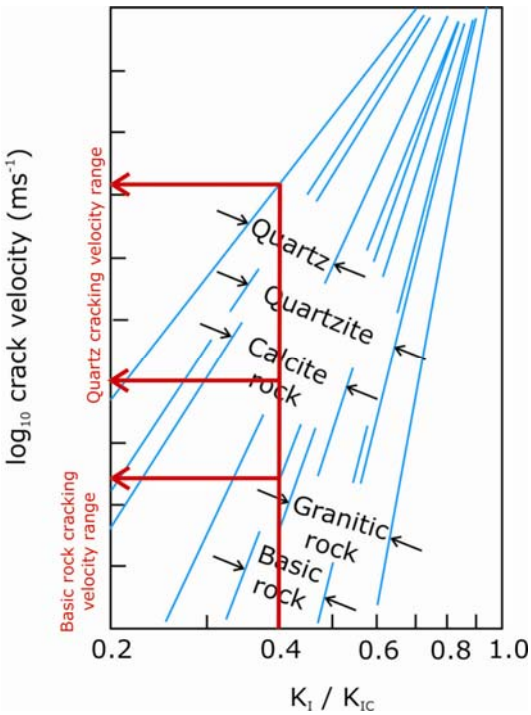

Figure 11.5. Schematic log-log diagram showing the variation in subcritical tensile crack growth behaviour for a number of geological materials. All data were obtained using the DT method at room temperature and in liquid water [from Atkinson, 1984]. Red lines indicate the position of the range of crack velocities for both quartz and basic rock for a given normalized stress intensity factor of 0.4.

11.4 The influence of confining pressure and pore fluid pressure on creep strain rates

Results from stress-stepping creep experiments on both DDS and EB have demonstrated that creep strain rates are dramatically reduced for the same level of differential stress when the P_{eff} is increased (Chapter Eight, Fig. 8.23 and Chapter Ten, Fig. 10.16). This is at least partially expected, since it well

known that rock strength increases with increasing P_{eff} [e.g., Paterson, 1958; Byerlee, 1967; Francois and Wilshaw, 1968; Rummel and Fairhurst, 1970; Wawersik and Brace, 1971; Ohnaka, 1973; Baud *et al.*, 2000]. For example, in the constant strain rate experiments on DDS (Chapter Eight, Fig. 8.6) an increase in strength of over 70% is seen (from 103 to 178 MPa) as P_{eff} is increased from 10 to 50 MPa. About a 75% increase in strength is seen (from 291 to 504 MPa) in EB during an identical suite of experiments (Chapter Ten, Fig. 10.4). These data are plotted as open symbols on Figs. 8.22 and 10.17.

However, the purely mechanical influence of the P_{eff} demonstrated by the open symbols is not sufficient to explain the orders of magnitude decreases that are observed in the creep strain rate over the same pressure interval (Chapter Eight, Fig. 8.23 and Chapter Ten, Fig. 10.16). It can therefore be suggested that the remainder of the observed shift is due to the chemical influence of water. Furthermore, the shifts in the strain rate curves appear to decrease with increasing Peff, suggesting that the chemically-driven process of stress corrosion cracking that drives brittle creep is therefore inhibited at a higher P_{eff} in both DDS and EB samples. This is entirely consistent with the suggestion that stress corrosion is inhibited at higher P_{eff} due to a decrease in water mobility (i.e. the diffusion of the reactive species to the bonds at crack tips) because of a reduction in crack aperture [Atkinson and Meredith, 1987].

Figs. 8.24 and 10.17 also show that stress corrosion in EB is affected more by the increase in P_{eff} than DDS over the experimental range. For example, η is reduced from 56.8 to 25.3 in EB while a change from 49.9 to 39.3 is observed in DDS over the pressure range investigated (from 10 to 50 MPa effective confining pressure). Such an P_{eff} dependence is not unexpected in EB since permeability studies have previously shown that a large proportion of the pre-existing cracks in EB close on the application of a modest confining pressure [Vinciguerra *et al.*, 2005; Benson *et al.*, 2006], and hence limiting the number of crack tip reactions (Fig. 11.6).

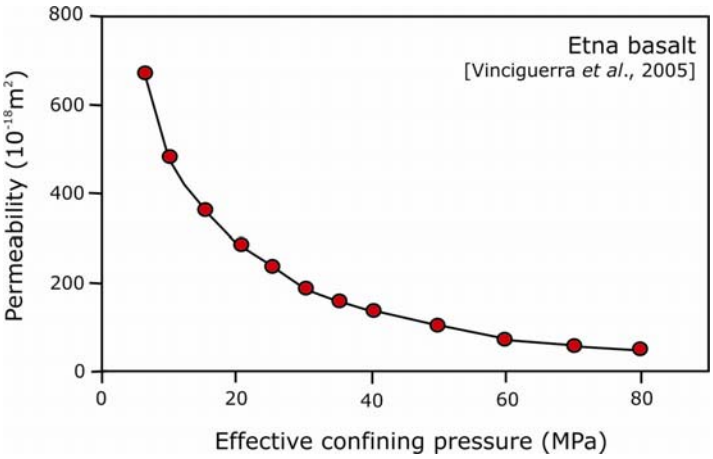

Figure 11.6. Evolution of permeability with increasing effective confining pressure for EB [from Vinciguerra *et al.*, 2005].

These observations are consistent with the results of the systematic study on the influence of P_{eff} on brittle creep in granite [Kranz, 1980], which showed that increasing the P_{eff} led to an increase in the overall time-to-failure (equivalent to a decrease in the strain rate). Kranz [1980] also postulated that the increase in P_{eff} led to a decrease in the rate at which corrosive chemical species could reach crack tips, and also to a decrease in the rate of crack interaction prior to the onset of tertiary creep. However, the study is limited by the fact that it was performed on air-dry samples in the absence of pressurized pore fluid.

Subsequent work has highlighted the importance of using wet samples [Kranz *et al.*, 1982; Meredith and Atkinson, 1983]. Other studies on the influence of effective stress on brittle creep can be found in Wawersik and Brown [1973] and Ngwenya *et al.* [2001]. Wawersik and Brown [1973] performed creep experiments on sandstone and granite at confining pressures of 7, 35 and 70 MPa and found that an increase in confining pressure resulted in a decrease in creep strain rates. Ngwenya *et al.* [2001] also performed stress-stepping brittle creep experiments, where multiple measurements are made on the

same rock sample. They found that the influence of increasing P_{eff} is to shift the individual curves of strain rate systematically towards higher differential stresses; in accordance with the law of effective stress. For Gyda sandstone, an increase in effective confining pressure from 17.2 MPa to 34.5 MPa shifted creep strain rate curves by about 45 MPa along the x-axis. This is approximately the same shift observed in the experiments presented in this study (55 MPa shift for an increase of 20 MPa effective confining pressure).

The creep strain rate curves at different P_{eff} (Chapter Eight, Fig. 8.23 and Chapter Ten, Fig. 10.16) can also be plotted with respect to a normalized σ_p (using experimentally-derived values from Chapter Eight, Table 8.1 and Chapter Ten, Table 10.1). Fig. 11.7 shows that as P_{eff} is decreased in experiments on DDS, the percentage of the normalized σ_p the rock creeps at a given strain rate is reduced. At 1.0×10^{-7} s^{-1} for example, the proportion of normalized σ_p is 0.74, 0.88 and 0.92 for a P_{eff} of 10, 30 and 50 MPa respectively. In the case of DDS (Fig. 11.7), the gradients of the creep strain rate curves decrease as P_{eff} is increased, as before (Chapter Eight, Fig. 8.23).

The trend observed for EB is more complex. Fig. 11.7 demonstrates that only until the P_{eff} is decreased to 10 MPa, does the percentage of the normalized σ_p the rock creeps at a given strain rate decrease. At 1.0×10^{-7} s^{-1} for example, the proportion of normalized σ_p is 0.85, 0.90 and 0.90 for a P_{eff} of 10, 30 and 50 MPa respectively. For EB, the gradients of the 30 and 50 MPa curves are virtually identical, whilst the gradient of the 10 MPa P_{eff} curve is much steeper by contrast. A possible explanation for this is that upon the application of fairly modest P_{eff}, drastic changes in permeability in EB are observed [Vinciguerra *et al.*, 2005]. For example, between 10 and 30 MPa the permeability is reduced from 700 to 200×10^{-18} m^2, whereas between 30 and 50 MPa only a further 100×10^{-18} m^2 decrease was observed [see Fig. 11.5 and Vinciguerra *et al.*, 2005]. A similar hypothesis can be applied to the DDS data. Since, when normalized to

σ_p, the 30 and 50 MPa P_{eff} DDS creep curves are much closer together than the 10 and 30 MPa curves (Fig. 11.7). This does however postulate that at even higher P_{eff} there will be little change in the creep strain rate curves for both rock types. This may suggest that, beyond a certain P_{eff}, the influence of P_{eff} on creep strain rates is negligible. Further experiments would be required to investigate this.

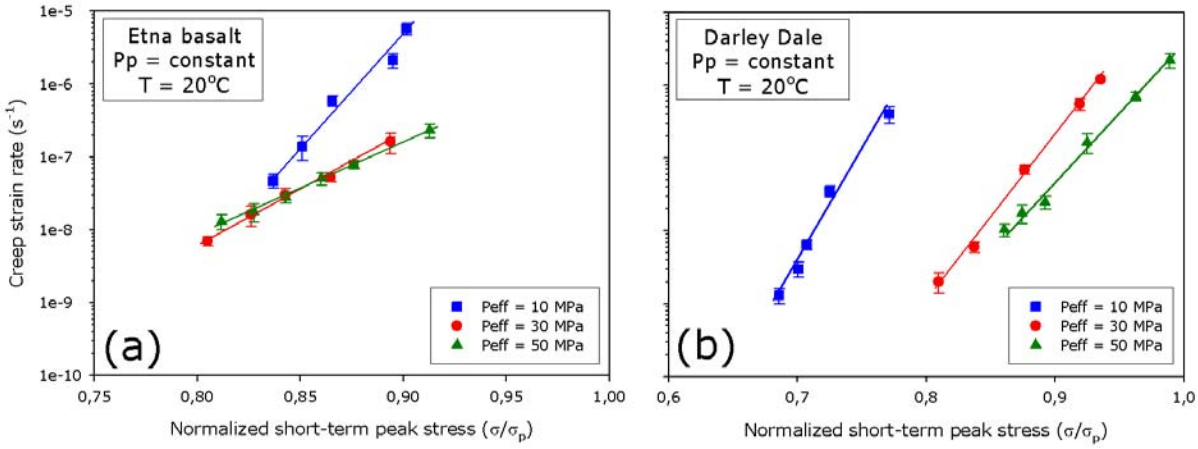

Figure 11.7. Creep strain rate data from stress-stepping brittle creep experiments performed at 10 (blue squares), 30 (red circles) and 50 MPa (green triangles) effective confining pressures on water-saturated samples of (a) DDS and (b) EB, whilst maintaining a constant pore fluid pressure of 20 MPa. Creep strain rate data is plotted on a log scale against normalized differential stress. Error in the creep strain rate measurements are denoted by the error bars, error in the differential stress values are represented by the size of the datapoints. 10 MPa effective confining pressure – sample EB-40-10Z; 30 MPa effective confining pressure – sample EB-40-06Z; 50 MPa effective confining pressure – sample EB-40-11Z. Experimental conditions are indicated on the figure. P_{eff} – effective confining pressure; P_p – pore fluid pressure; T – sample temperature.

In the data of Figs. 8.23 and 10.16, it must be noted that not only are the curves shifted to lower strain rates as P_{eff} is increased, but that they also appear to decrease in gradient. A gradient in the strain rate – Q curves is entirely as expected since it is known that rock strength increases with an increase in strain rate [Paterson and Wong, 2005]. However, it is not clear if this can explain the observed change in gradient, or if it is due to a combined mechanical and chemical effect. Unfortunately, it is hard to

discriminate between these two effects on the basis of the current data. This would require further measurements on both saturated and dry samples over a range of constant and creep strain rates. This change in gradient is emphasized by the log-linear nature of the plots (i.e. an exponential fit). However, it has previously been noted by Main [2000] that it is difficult to discriminate between exponential and power-law fits to brittle creep data given the relatively narrow range of experimental data currently available. For comparison, a log-log plot of the same data has been provided in Fig. 11.8 and the change in gradient is again evident (Fig. 11.8), albeit now less pronounced in the DDS curves. The comparison of exponential and power-law fits to the creep data is discussed in more detail in **11.7 Macroscopic creep laws**.

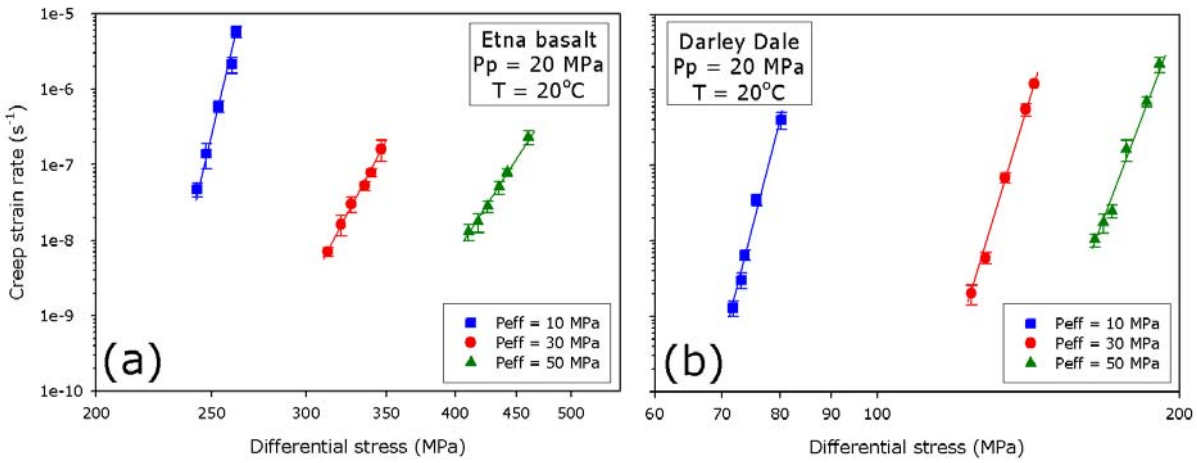

Figure 11.8. Creep strain rate data from stress-stepping brittle creep experiments performed at 10 (blue squares), 30 (red circles) and 50 MPa (green triangles) effective confining pressures on water-saturated (a) EB and (b) DDS, whilst maintaining a constant pore fluid pressure of 20 MPa. Creep strain rate data is plotted on a log-log scale against applied differential stress. Error in the creep strain rate measurements are denoted by the error bars, error in the differential stress values are represented by the size of the datapoints. 10 MPa effective confining pressure – sample DD-40-28Z and EB-40-10Z; 30 MPa effective confining pressure – sample DD-40-15Z and EB-40-06Z; 50 MPa effective confining pressure – sample DD-40-32Z and EB-40-11Z (see Tables 8.5 and 10.4). P_p – pore fluid pressure; T – sample temperature.x

The data shown in Fig. 11.8 can be extrapolated as in Fig. 11.9, assuming in fact that the data follow such trends at strain rates slower than those achievable in the laboratory. For EB, where the influence of P_{eff} on the gradients of the creep strain rate curves is more pronounced, the extrapolation results in the convergence of the three curves (Fig. 11.9a), at about 180 MPa and 9 x 10^{-13} s^{-1}. For DDS, such a convergence occurs at extremely low stresses and creep strain rates (Fig. 11.9b). The convergence of such curves would suggest that, at this point, the influence of P_{eff} on creep strain rate is negligible. Perhaps this point marks the lower limit of stress corrosion cracking. Interestingly, the value of differential stress at the point of convergence is consistent with the predicted area in *PQ* space in which brittle creep is unlikely to operate, i.e. below *C'* (see Fig. 11.1). However, it would be sensible to assume that from, or even prior to, this point that the curves would not continue on their projected paths.

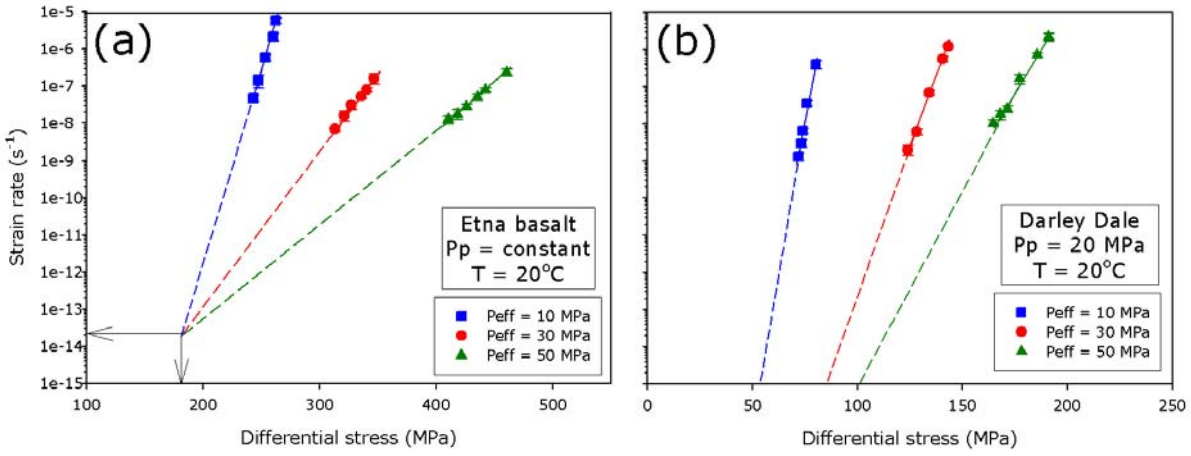

Figure 11.9. The extrapolation of creep strain rate data from stress-stepping brittle creep experiments performed at 10 (blue squares), 30 (red circles) and 50 MPa (green triangles) effective confining pressures on water-saturated (a) EB and (b) DDS, whilst maintaining a constant pore fluid pressure of 20 MPa. Creep strain rate data is plotted on a log scale against applied differential stress. Error in the creep strain rate measurements are denoted by the error bars, error in the differential stress values are represented by the size of the datapoints. 10 MPa effective confining pressure – sample DD-40-28Z and EB-40-10Z; 30 MPa effective confining pressure – sample DD-40-15Z and EB-40-06Z; 50 MPa effective confining pressure – sample DD-40-32Z and EB-40-11Z (see Tables 8.5 and 10.4). P_p – pore fluid pressure; *T* – sample temperature.

The chemical activity of water is enhanced by elevated pressure [Fyfe *et al.*, 1978]. Therefore, if chemically-enhanced stress corrosion cracking is the mechanism responsible for inducing brittle creep, it might be expected that creep rates would be enhanced at a higher P_p even when the Peff was held constant. This was investigated this in stress-stepping experiments and the data are shown in Chapter Eight, Fig. 8.25. However, as previously noted, the results suggest that doubling the P_p from 20 to 40 MPa, while maintaining the P_{eff} constant at 30 MPa, influenced creep strain rates within the range expected from natural sample variability. It is therefore difficult, from the limited dataset, to unequivocally rule out any potential P_p influence on creep strain rates. However, if the results can be explained by sample variability then this implies that the rate at which reactive species can diffuse through the sample to crack tips is the limiting control on stress corrosion reactions, rather than the amount of reactive species present. However, it should also be noted that the chemistry of the pore fluid (initially, de-ionized distilled water) is likely to have changed during the 10 to 14 days that the experiments lasted; a potentially important issue highlighted by Ojala *et al*. [2003].

11.5 The influence of temperature on creep strain rates

Results from the constant strain rate experiments show that the short-term peak stress (σ_p) of all three sandstones (BHS, DDS, and COS) and EB is lower as temperature is increased from 20° to 75°C. The weakening is systematic and larger than any difference expected from sample variability. Previous studies, reviewed in Paterson and Wong [2005], have also consistently demonstrated systematic decreases in brittle rock strength with increasing temperature. The weakening observed in the experiments could be due either to a simple mechanical effect or to a thermally-enhanced chemo-mechanical mechanism such as stress corrosion. The most likely mechanical effect would be a thermally-induced change to the microstructure. However, as noted earlier, care was taken to run the experiments

at a maximum temperature of 75°C, a temperature too low to induce any thermal cracking in these materials [Glover *et al.*, 1995]. It can therefore be suggested that the weakening is due to an enhanced rate of thermally-activated stress corrosion cracking at the higher temperature. In principle, it should be possible to verify this suggestion by performing similar experiments at different strain rates. However, if the case of DDS is considered (where the strength reduction is approximately 9%), the data of Fig. 9.3 demonstrate that it would be necessary to perform experiments at strain rates either three orders of magnitude higher or three orders of magnitude lower to achieve the same level of weakening as that caused by the 55°C temperature difference. This would require constant strain rate experiments lasting either about 1.5 seconds or about 20 days, both of which are impractical. Instead, a stress-stepping creep experiment at an intermediate temperature of 45°C was performed; this is reported on these below. It must also be noted that the suggestion of the change in strain rate required to achieve the observed strength reduction is consistent with the observation of Paterson and Wong [2005], who noted that a 10^3-fold change in strain rate was required to induce an approximately 10% change in strength for a wide variety of rocks undergoing triaxial deformation (see also Chapter Two, Fig. 2.16).

As reported in Chapter Nine, a conventional creep experiment on DDS at 75°C and a constant differential stress of 129 MPa was also performed to confirm that it displays all three phases of creep (Fig. 9.2). In fact, all three measured proxies for crack damage (axial strain, porosity change and AE energy) display trimodal curves. Furthermore, the numerical value of each measure of damage at the onset of tertiary creep in our experiment at 75°C is essentially the same as those previously reported from conventional creep experiments on DDS performed at room temperature under the same Peff and differential stress [Chapter Eight, see also Baud and Meredith, 1997]. This provides further support to the suggestion of Baud and Meredith [1997] that a critical level of damage is required to trigger the onset of accelerating tertiary creep that eventually leads to failure. The creep strain rate during the

conventional experiment at 75°C (Fig. 9.2a) was 5.5 x 10^{-6} s^{-1}, and is also plotted as an open triangle on Fig. 9.3b. The data from this test is completely consistent with the data from the stress-stepping experiments at the same temperature, and provides further confirmation of the veracity of the latter methodology.

The results from the stress-stepping creep experiments on sandstone, illustrated in Fig. 9.3 and in the normalized plot of 11.10, show that the creep behaviour of the three sandstones is qualitatively similar. Under all conditions, small increases in differential stress result in large increases in creep strain rate; with a 10% increase in differential stress resulting in increases in strain rate ranging from a factor of about 10 for BHS and DDS at 20°C to a factor of about 300 for COS and BHS at 75°C. Again, for all three sandstones, even a modest increase in temperature from 20° to 75°C results in an increase in creep strain rate of several orders of magnitude for the same applied differential stress. However, the increase in creep strain rate is much more pronounced in DDS and BHS than in COS. These increases in creep strain rate are at least partially expected, since it is known from constant strain rate experiments at 10^{-5} s^{-1} that the peak stress decreases by 8 MPa, 13 MPa and 10 MPa for BHS, DDS and COS respectively, over the same temperature interval (Fig. 9.1). However, these decreases alone are not sufficient to explain the magnitudes of the changes seen in the data of Fig. 9.3, where the differences in differential stress for the two test temperatures at a strain rate of 10^{-5} s^{-1} are 15 MPa, 18 MPa and 17 MPa for BHS, DDS and COS respectively (as measured from the dashed lines extrapolated to a strain rate of 10^{-5} s^{-1} in Fig. 9.3). It can therefore be suggested that the larger changes occur because the rock samples are held at a continuously high level of differential stress throughout the creep experiments (thus enhancing stress-dependent stress corrosion), whereas this is not the case during the constant strain rate experiments. In the case of EB (Fig. 10.18), the significant increase in creep strain rate seen in DDS and BHS is not replicated; furthermore, the normalized plot of Fig.11.10 shows that the creep behaviour of

the EB is qualitatively different to that of the sandstones. Previous work in DT relaxation experiments on single cracks [Meredith and Atkinson, 1982; Meredith and Atkinson, 1983; Meredith and Atkinson, 1985] and triaxial creep experiments on granites [Kranz *et al.*, 1982] have highlighted that stress corrosion cracking is greatly increased at elevated temperatures (see Chapter Three, Fig. 3.20).

DT relaxation experiments have also shown that pure synthetic quartz is much more susceptible to an increase in temperature than in other compositionally more complex materials, including dolerite [see Fig. 11.11; Meredith and Atkinson, 1982;1983; and Atkinson, 1984 for a review]. Potentially explaining why larger changes in creep strain rate are observed in the sandstones compared with the basalt. In fact, the DT data plotted in Fig. 11.11 bears an astonishing resemblance to the trends seen between the basalt and the two high-porosity sandstones, DDS and BHS, in Fig. 11.10. This in spite of the fact that DT experiments measure the growth of a single tensile crack under essential zero confining pressure whilst brittle creep experiments measure the response of a population of cracks growing in compression that can coalesce and interact under a confining pressure.

Therefore, in the case of the sandstones, it might therefore be intuitive to assume that the higher the % quartz in the sample, the greater the impact on stress corrosion cracking caused by an increase in temperature. However, the data show that DDS (69% quartz) exhibits about the same increase in creep strain rate, under the same applied differential stress, with the increase in temperature as BHS (95% quartz); furthermore, COS (85% quartz) shows only a modest increase in creep strain rate compared to DDS (69% quartz). The significant difference in porosity between COS and the other two sandstones explain the difference in the observed behaviour. The effect of the increase in temperature in COS may not be substantial because either the volume of crack porosity is less and hence there are fewer reaction sites or the availability of active species is the limiting factor. However, it must be noted however that

Chapter Eight demonstrated that doubling the P_p from 20 MPa to 40 MPa (whilst maintaining a constant P_{eff} of 30 MPa), and therefore potentially doubling the availability of reactive species, did not influence the creep strain rate in DDS at 20°C.

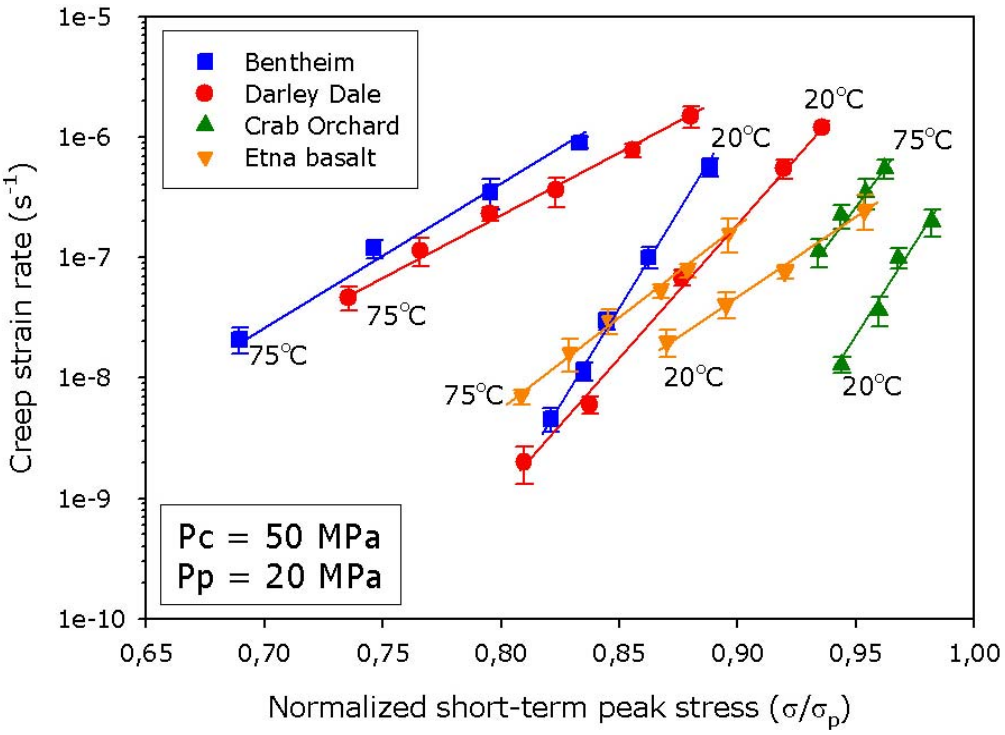

Figure 11.10. Creep strain rate data from stress-stepping creep experiments at elevated temperatures on DDS, BHS, COS and EB plotted on a log scale against normalized failure stress (normalized with respect to the short-term peak stress derived from conventional constant strain rate (1.0×10^{-5} s^{-1}) experiments). Experimental conditions are indicated on the figure. Error in the creep strain rate measurements are denoted by the error bars, error in the differential stress values are represented by the size of the datapoints. P_c – confining pressure; P_p – pore fluid pressure.

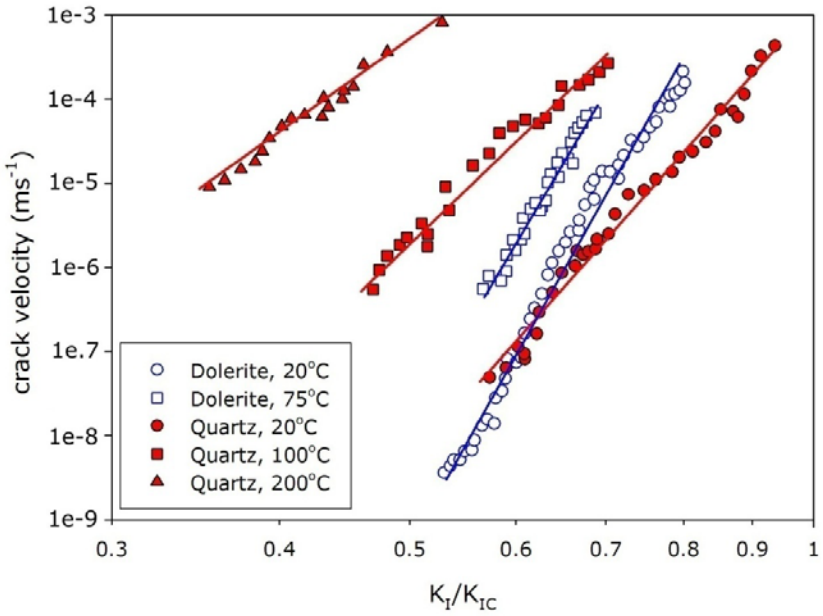

Figure 11.11. The influence of temperature on subcritical tensile crack growth in synthetic quartz (under a water vapour pressure of 300 Pa) [after Meredith and Atkinson, 1982] and dolerite [after Meredith and Atkinson, 1983]. Note the normalized stress intensity factor x-axis.

It can also be seen in the data of Figs. 9.3, 10.18 and 11.10 that increasing the temperature from 20° to 75°C results in decreases in the gradients (i.e. less stress-sensitive) of the strain rate-differential stress curves for all rocks. The decrease in gradient appears to be correlated with sample porosity; with the largest decrease seen for the highest porosity rock (BHS) and the smallest decrease seen for the lowest porosity rocks (COS and EB). At first sight this may appear counter-intuitive, since it is expected that stress corrosion to be enhanced at higher temperature. However, for example from Fig. 9.3b, at a differential stress of 125 MPa the creep strain rate in DDS is a factor of about 10^3 higher at 75°C than it is at 25°C. Thus, since the deformation rate is already so much higher at 75°C, the same incremental increase in differential stress has a proportionally smaller influence on the deformation rate. This was investigated further by performing an additional set of stress-stepping creep experiments on DDS at an intermediate temperature of 45°C. The full data set is presented in Fig. 11.12, which shows that not only

do the creep strain rates from the 45°C experiment plot between those for 20° and 75°C, but that the gradient of the strain rate-differential stress curve is also intermediate between the slopes for 20° and 75°C (see Table 11.3 and Fig. 11.13). Overall, these results suggest that the influence of the differential stress is greatest at the lower temperature where the deformation rate is also lower.

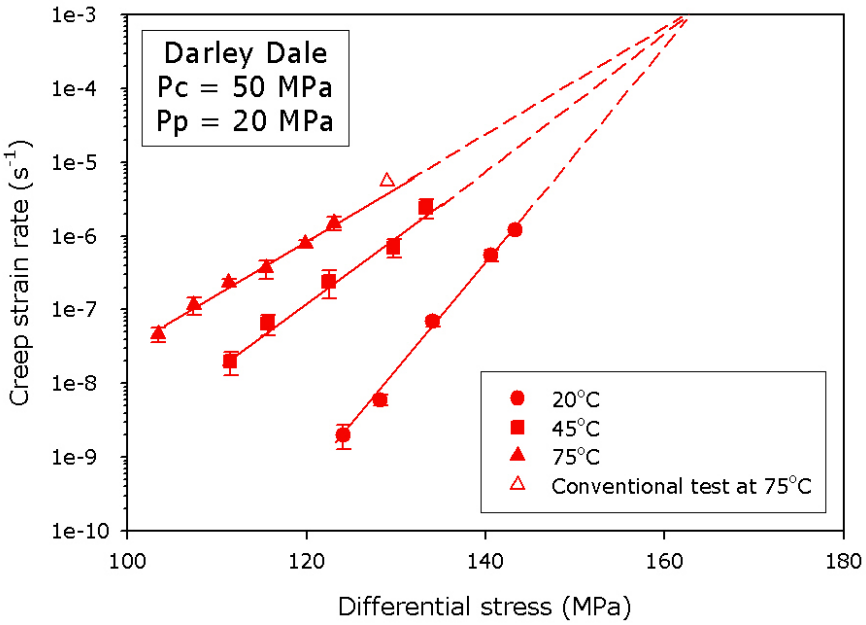

Figure 11.12. Extrapolation of creep strain rate data from stress-stepping creep experiments at temperatures of 20, 45 and 75°C on samples of DDS, plotted on a log scale against differential stress. Unfilled triangle in (b) represents the single conventional creep experiment on DDS (Chapter Nine, Fig. 9.2). Experimental conditions are indicated on the figure. Error in the creep strain rate measurements are denoted by the error bars, error in the differential stress values are represented by the size of the datapoints. P_c – confining pressure; P_p – pore fluid pressure. The position where the extrapolated lines meet is interpreted as the point where stress corrosion reactions cease to exert a significant influence on deformation rate.

As noted above, the observation that the strain rate-differential stress curves have different gradients at different temperatures suggests a difference dependence of stress corrosion driven deformation on differential stress at different temperatures. These lines have been extrapolated for the three curves of Fig. 11.12 to the point where they all meet (assuming in fact that the trend follows a power law). It can

be tentatively suggested that this may correspond to the point where the deformation is so rapid that time-dependent, chemo-mechanical processes such as stress corrosion cease to have adequate time to exert any significant influence on deformation rate. Similar observations have previously been reported for stress corrosion driven propagation of single cracks in double-torsion fracture mechanics experiments [Atkinson and Meredith, 1981; Meredith and Atkinson, 1982]. The curves meet at a differential stress of 162 MPa and a strain rate of 1 x 10^{-3} s^{-1}. This agrees with previous triaxial experiments that have shown the peak stress of rock to increase by approximately 10% for each 10^3 increase in strain rate [Brace and Martin, 1968; Masuda *et al.*, 1987; Masuda, 2001]. Experiments in this study have previously shown that the average σ_p determined at 1.0 x 10^{-5} s^{-1} is 152 MPa (see Chapter Eight, Fig. 8.6). The data of this study also suggest that stress corrosion will still exert some influence on deformation even at very fast deformation rates (i.e. below 8.0 x 10^{-3} s^{-1}).

Sample number	Confining pressure (MPa)	Pore fluid pressure (MPa)	Effective confining pressure (MPa)	Temperature (°C)	Power law gradient function (β)	Exponential gradient function (μ)	Power law R^2 value	Exponential R^2 value
DD-40-15Z	50	20	30	20	45.40	0.335	0.996	0.997
DD-40-54Z	50	20	30	45	24.71	0.200	0.986	0.986
DD-40-53Z	50	20	30	75	18.64	0.163	0.994	0.991

Table 11.3. Experimental conditions from the experiments on DDS at 20, 45 and 75°C and results of regression analysis of power law and exponential function fit to the data.

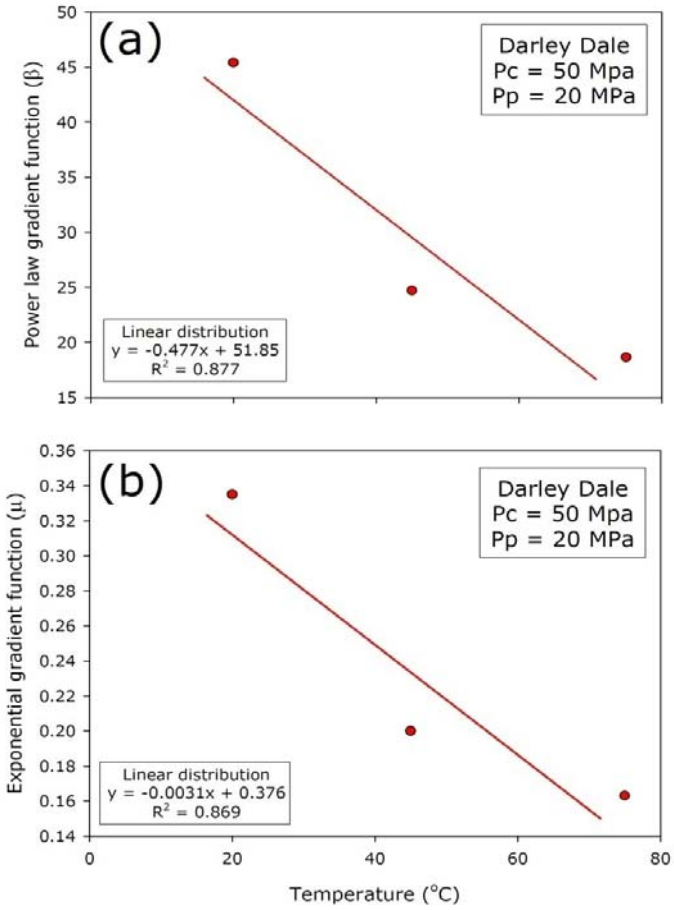

Figure 11.13. Graphs of the temperature dependence of the (a) power law gradient function, η and (b) the exponential gradient function, β (see also Table 11.2) in DDS using data derived from stress-stepping creep experiments. Experimental conditions are indicated on the figure. Pc – confining pressure; Pp – pore fluid pressure.

Interestingly, a similar trend has been observed in DT experiments on synthetic quartz at elevated temperatures (Fig. 11.14b) and using different corrosive fluids, namely water, 2N hydrochloric acid and 2N sodium hydroxide (Fig. 11.14a). Both Figs. 11.12 and 11.14 suggest that, for both compressive and tensile scenarios, there is a level of stress where the chemical influence on deformation (stress corrosion cracking) is zero. Deformation at this point must be controlled by mechanical processes, i.e. the cracks are growing faster than the reactive species can reach the crack tips. The curves from this point would not however continue on their projected paths. On the *K-v* diagram for instance (Fig. 11.14a), the

convergence of the curves is likely to define the position where the rate at which the active species can diffuse through to the crack tip becomes slower than the dissociative reaction rate. This results in a plateau in the crack velocity, since increasing the stress intensity further does not influence the diffusion of the active species to the crack tip, and signifies the start of region 2 [as defined by Freiman, 1984; see Chapter Three, Fig. 3.9]. This plateau has been experimentally observed in experiments at 200°C by Atkinson and Meredith [1982] (Fig. 11.14b). Since it is likely that the other *K*-*v* curves in Fig. 11.14b will plateau, perhaps even at the same crack velocity as the 200°C curve, a similar switch in behaviour could also be true for the bulk sample data collected under a confining pressure (Fig. 11.13) – the crack velocity at which the cracks are growing faster than the reactive species can reach the crack tips.

Pore chemistry is still a hugely important factor in the deformation of rocks in nature however. In nature, cracks will spend the vast majority of their time at the low velocity end of their *K*-*v* curve (Fig. 11.14) or at the low creep strain rate end of their strain rate-stress curve (Fig. 11.13), before they accelerate to failure. In fact, in long-term geological processes (involving low stress or slow strain rates) the fast crack velocity data make virtually no difference to predictions of time- and rate-dependent behaviour [Atkinson, 1980].

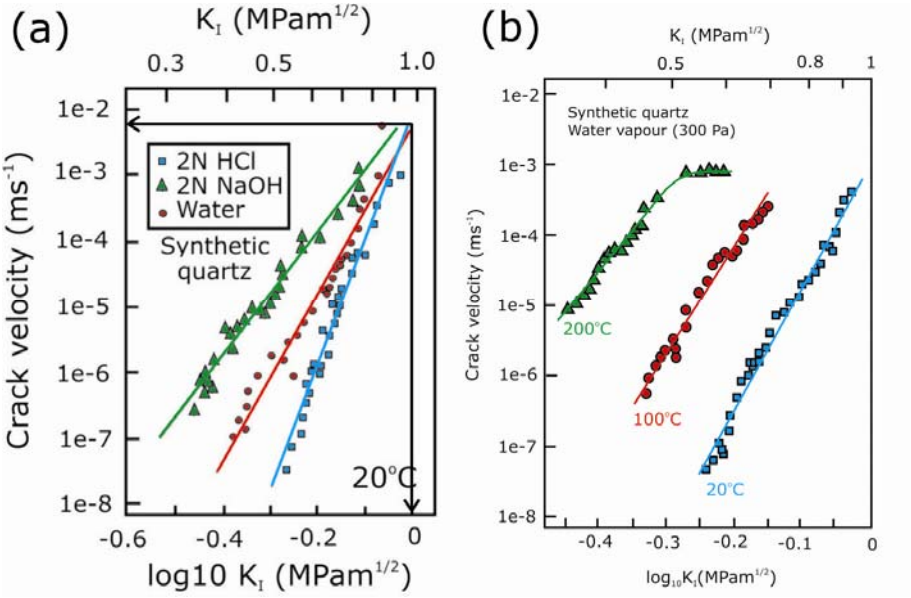

Figure 11.14. (a) The influence of pH of aqueous fluid environment on subcritical tensile crack growth in synthetic quartz at 20°C [redrawn from Atkinson and Meredith, 1981]. Arrows indicate the positions of where the chemical influence on deformation is effectively zero. (b) The influence of temperature on stress corrosion in synthetic quartz under a 300 Pa water vapour pressure [redrawn from Meredith and Atkinson, 1982].

11.6 Predicting rock failure under a constant stress

As discussed previously, the times-to-failure for DDS and EB at the same creep strain rate are markedly different (see Table 11.2). However, the proportion of time spent in each of the three creep phases is approximately the same regardless of creep strain rate, rock type or time-to-failure (Table 11.4 and Fig. 11.15). In general, both rock types spend 20% of their total creep duration in the primary creep phase, 60% in the secondary creep phase and the remaining 20% in the tertiary creep phase. This relationship is seen in all three proxies for damage. This is remarkably consistent, especially considering the significant differences between the two rock types (porous sandstone versus porphyritic alkali basalt) and the fact that it is observed over three orders of magnitude (see Fig. 11.15). If this observation holds true then the time-to-failure of a rock sample held under a high constant stress in the laboratory could be revealed

from the knowledge of the duration of a primary creep phase. It must be noted however that picking the end of the primary creep phase is difficult without the complete creep curve. Therefore, more rigorous method should be explored and employed. For example, the 2nd derivative of the creep curve could be plotted in real-time during experimentation (as in Chapter Three, Fig. 3.22c). When this curve trends towards zero it can be assumed that the primary creep phase has finished and the rock sample has undergone 20% of its total time-to-failure. Therefore, the time-to-failure can be easily approximated. Experimental trimodal creep curves for the high-temperature plastic creep of some metals have also demonstrated the same 20-60-20 proportions for the primary, secondary and tertiary creep phases [Poirier, 1985].

Sample	**Resultant creep strain rate (s^{-1})**	Time spend in primary creep phase		Proportion of time spend in secondary creep phase		Proportion of time spend in tertiary creep phase	
		(minutes)	(%)	(minutes)	(%)	(minutes)	(%)
DD-40-40Z	3.7×10^{-9}	1800	14	9000	69	2160	17
DD-40-22Z	1.3×10^{-8}	600	17	2400	67	600	17
DD-40-45Z	1.0×10^{-7}	30	19	90	56	40	25
DD-40-19Z	3.5×10^{-6}	2.5	25	6.5	65	1	10
EB-40-16Z	2.4×10^{-9}	1000	22	2700	60	800	18
EB-40-14Z	4.0×10^{-8}	60	17	165	61	45	17
EB-40-15Z	4.1×10^{-7}	5	20	15	60	5	20
EB-40-17Z	2.7×10^{-6}	0.9	20	2.8	62	0.8	18

Table 11.4. Summary of the time spent in each of the three creep curve phases for conventional creep experiments on DDS and EB. Experiments are shown in Figs. 7.8 and 9.7. Times are calculated by eye from the axial strain against time curves (creep curves). Percentages are rounded to the nearest percent.

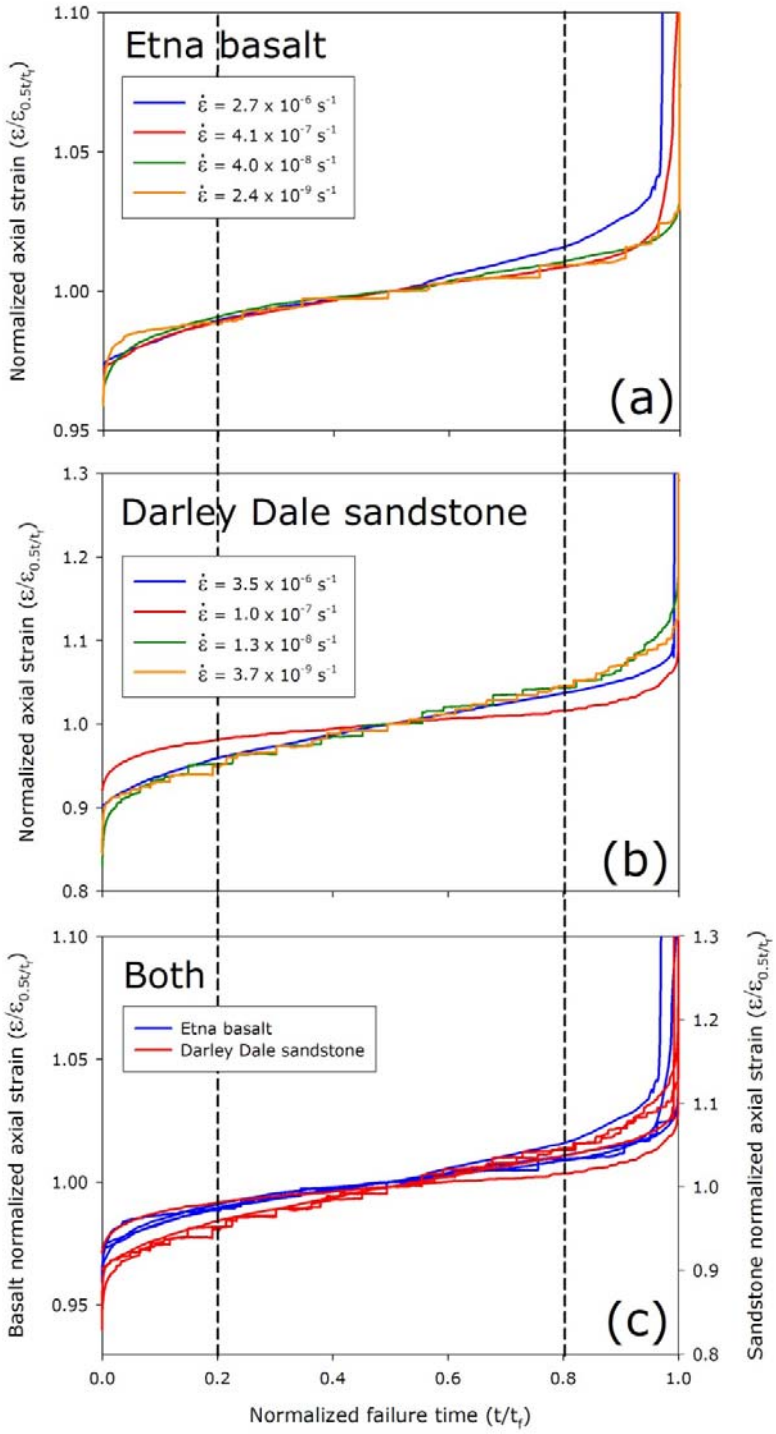

Figure 11.15. Normalized strain against normalized failure time for four conventional creep experiments on (a) EB and (b) DDS at different strain rates (indicated on the figures). (c) The two sets on data plotted on top of each other.

This method of rock failure prediction could also be applied to natural geophysical hazards, such as the failure of a rock mass or even volcanic eruption forecasting. The process of stress corrosion is the mechanism considered most likely to be responsible for the time-dependent precursory cracking, displacement and accelerating seismic activity that commonly precedes volcanic eruptions [Voight, 1988;1989; Kilburn and Voight, 1998; Vinciguerra, 1999; Vinciguerra, 2002; Kilburn, 2003] (see also section **11.8 Application of data in understanding large-scale geophysical problems**). The displacement and seismic activity curves seen in field data from active volcanoes that exhibit a part of the classic trimodal creep curve could in theory be used to predict volcanic eruption and flank collapse. More work would be required to fully investigate this concept.

Results have also shown that times-to-failure against applied differential stress adequately follow both a power law and exponential function fit for both DDS and EB, for the three orders of magnitude achievable in the laboratory (Chapter Eight, Fig. 8.18 and Chapter Ten, Fig. 10.13). Therefore, in nature, the knowledge of the stress field surrounding a rock mass that has been tested in the laboratory, e.g. the rock forming the edifice at Mt. Etna, could be translated into a time-to-failure, if such data can be extrapolated (Fig. 11.16). There are however many other external factors to include and the equations assume that the same trend is seen at strain rates lower than those achievable in the laboratory. However, when the lines are extrapolated to time-to-failure equals 1 min (the x-axis) the resultant differential stress is very similar to the σ_p derived from constant strain rate experiments (see Chapter Eight, Table 8.1 and Chapter Ten, Table 10.1).

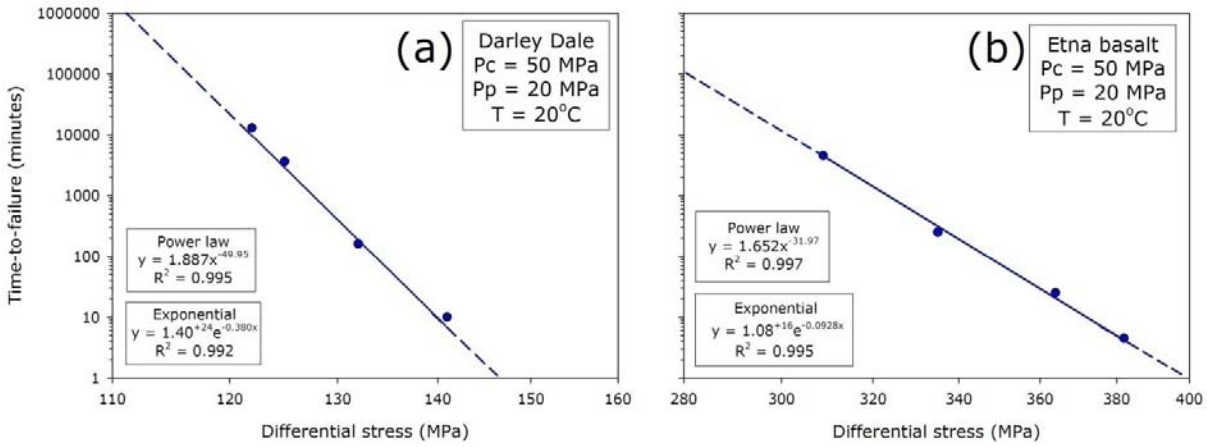

Figure 11.16. Time-to-failure data from multiple conventional brittle creep experiments on water-saturated (a) DDS and (b) EB plotted on a log scale against log applied differential stress. Experimental conditions are indicated on the figure. Power law and exponential function fits to the data are also shown on the figure. P_c – confining pressure; P_p – pore fluid pressure; T – sample temperature.

Studies on the compressive failure of ceramics (silicon carbide, silicon nitride and alumina) have demonstrated that the dependence of compressive strength (S^*_c) on strain rate (de/dt) follows a relationship of the form [Lankford, 1979; Lankford, 1981]:

$$S_c^* = \left(\frac{de}{dt}\right)^{\frac{1}{n'+1}} \qquad [11.1]$$

Where n' is an environment and material dependent constant for strain rates below 10^{-2} s^{-1}. Below such strain rates it was observed that the value for n' (Equation [11.1]) was very close to the value of n (the stress corrosion index). The failure of 'unflawed' ceramic specimens tested in bending has been shown to obey a tensile strength/strain rate relationship as in Equation [11.1], in which the observed equivalence between the exponent in the relationship and the stress corrosion index is accepted as proof that the strain rate dependence of tensile strength is based on thermally activated, tensile crack

growth [Evans, 1974]. It is postulated by Lankford [1981] that compressive failure described by Equation [11.1], with *n*' equal to *n* (within experimental error), supports the concept that the compressive strength in brittle rock is controlled by the growth of tensile, axial cracks. Further work on this concept could indeed be lucrative as it is possible to approximate the stress corrosion index (*n*) from triaxial brittle creep experiments where failure is compressive [Main and Meredith, 1991].

11.7 Macroscopic creep laws

In order to apply the concept of stress corrosion controlled, time-dependent cracking to large-scale geophysical problems, macroscopic creep models have been developed to describe this behavior, and are generally in one of two forms: (1) power law form (see Chapter Three, Eq. [3.6]) or (2) exponential form (see Chapter Three, Eq. [3.7])

The most widely-used and accepted theory of stress corrosion is Charles' power law [Charles, 1958] and has been used to describe virtually all experimentally determined data for geological materials [see Meredith and Atkinson, 1983; Atkinson, 1984; Swanson, 1984]. However, exponential forms, such as the Charles-Hillig-Wiederhorn theory [Charles and Hillig, 1962; Hillig and Charles, 1965; Wiederhorn and Bolz, 1970], have so far been shown to describe creep behaviour equally as well over the range of data achievable in the laboratory [see Costin, 1987; Lawn, 1993; Lockner, 1993; Ngwenya *et al.*, 2001]. More recently, mean-field theory of damage mechanics have been developed [Lockner, 1998; Main, 2000] that invokes a two stage process: (1) a phase of strain hardening involving distributed crack damage, and (2) a phase of strain softening involving crack interaction and coalescence. Phase (1) dominates in the early stage of deformation and phase (2) dominates in the later stage of deformation (see Chapter Three, Fig. 3.22).

Such models also therefore postulate a critical damage threshold where crack interaction leads to a rapid acceleration to failure on a localized fault plane. As the stress intensity at a crack tip is influenced by the length of the crack, given suitable conditions, the nonlinear relation between strain rate and stress given by stress corrosion theory means the rate at which a crack grows in time can accelerate even under a constant boundary stress. For a population of cracks growing in a rock sample held at constant stress, this process is embodied by accelerating strain rate and AE emission with time. In field data, where it is difficult to determine the absolute stress conditions, accelerating strain and seismic activity have been used to infer an underlying stress corrosion mechanism. The rate of deformation precursors to volcanic eruptions show both power law and exponential accelerations with time [Voight, 1988;1989], shown to be theoretically consistent with a stress corrosion process at constant boundary stresses [Main, 2000].

The mean field model for damage evolution developed by Main [2000] is based on laboratory observations of subcritical crack growth in a variety of composite materials, where the crack velocity V scales with the n'th power of the stress intensity factor $K \sim V^n$. In some single crystal experiments, a plateau of constant velocity is seen at intermediate K due to diffusion-limited crack growth, but this is neglected in the model at this stage. Depending on the loading configuration and a stress feedback exponent q, K scales with stress σ and crack length c according to $K \sim \sigma c^q$ [Costin, 1987]. For $nq<1$ these two equations predict decelerating crack growth (net negative feedback), and for $nq>1$ accelerating crack growth towards a singularity at the failure time (net positive feedback). Local negative feedback will lead to more distributed deformation in the form of a distributed array of microcracks, whereas positive feedback to localized deformation on a dominant macrocrack or fault [illustrated in Fig. 1 of Main *et al.*, 1993]. In the mean field theory (based on assuming similar behaviour for the mean crack

length <c>), no explicit account is taken for crack-crack interactions, except implicitly on their net effect on the feedback parameter *q*.

Assuming the degree of damage quantified by <*c*> is related to the strain, and a linear superposition of positive and negative feedback processes, the evolution of total strain, Ω with time is then described by Equation [3.9]. In the general case this amounts to 6 free parameters. However this is the minimum for a hybrid model, because both processes involve three parameters: amplitude (defining the stress axis scale), a time constant (defining the time axis scale) and a curvature term (here the power law exponent). When plotted on a graph Equation [3.9] predicts the spontaneous emergence of a long phase of steady-state creep at intermediate times between *T* and t_f i.e. there is no need to invoke a third process for such secondary creep. Equation [3.9] also predicts that the emergent 'steady-state' strain rate scales as a power law function of the creep stress [Main, 2000]. The AE hypocentre location plots in Fig. 11.3 confirm that distributed deformation dominates in the primary creep phase, whereas more localized deformation dominates in the tertiary creep phase. The mixed nature AE hypocentre locations in the steady-state phase validates the assumption in Main [2000] that secondary creep separate process, but an emergent phenomenon of primary and tertiary creep.

Here it is demonstrated that this mean-field damage mechanics power law model can closely reproduce the relation between strain and time observed in the conventional brittle creep experiments (Fig. 11.17) i.e. that it is not necessary to invoke a separate process for secondary creep. Due to complexities of inversion associated with the non-linearity in Equation [3.9] a simple trial-and-error fitting technique is used and in the first instance a co-dependence between the two amplitude terms is assumed. The model is able to produce the closest fit to the data for faster creep strain rates and during the accelerating tertiary creep phase. For the experiments on DDS at the slowest creep strain rates, the

model does not accurately reproduce the initial primary creep phase. The likely cause of this discrepancy is the fact that Equation [3.9] is based on mean-field damage mechanics that considers only the formation and interplay of cracks. At the lower stresses required to yield slow creep strain rates, processes such as pore space compaction could still be operative, explaining why the goodness of fit decreases with decreasing creep strain rate and why the model fits for tertiary creep despite the stain rate, since there will be only be the formation and coalescence of cracks at this point. This is reinforced by the fact that the model works almost seamlessly for EB, a rock that contains a large proportion of crack porosity. To incorporate the potential additional pore closure mechanism, the data from the experiments on DDS are re-fitted with Equation [3.9] but allowing Ω_I and Ω_{III} to vary independently (called modified Main [2000] power law). This is more consistent with the experimental data (Fig. 11.17) and suggests that the relative amplitudes of the primary and secondary components can differ significantly. The parameters used in the models are displayed in Table 11.5.

The parameters in Table 11.5 show that the amplitude of the decelerating process Ω_I is much smaller than that of the accelerating one Ω_{III}, by a few orders of magnitude, indicating that accelerating creep is the dominant process in terms of amplitude overall. Ω_{III} is relatively constant, whereas Ω_I decreases systematically as strain rate decreases, so that the relative importance of decelerating creep declines as the strain rate decreases. The failure time t_f increases systematically and non-linearly over several orders of magnitude with decreasing strain rate, but the transient time T for transient creep is more stable, decreasing by a factor of 4 or so only at the very slowest strain rates. This may be because different reactions can be activated at slower strain rates, or that different minerals have different relative effects at lower strain rates. The power law exponent m for transient creep is consistent (Table 11.5, with an exponent between 0.32 and 0.46 and 0.2 and 0.5 for DDS and EB respectively and no systematic change with strain rate. The power law exponent v for accelerating creep is much smaller

than *m*, indicating a much tighter curvature that can be seen on the normalized plots on Fig. 11.17. The exponent *v* ranges from 0.012 to 0.025 and 0.0032 to 0.01, with more rapid acceleration at high strain rates.

However, since the exponents *m* and *u* are related to the properties of the rock and that the P_{eff} and temperature remained constant during experimentation, it could be argued that such values should be identical between experiments on the same rock type. To test this, the data from three experiments on DDS were refitted to Equation [3.9] with the exponents *m* and *u* kept constant at 0.4 and 0.015 respectively (Fig. 11.18 and Table 11.5). These values were selected as they roughly represent the mean of the values first derived from the model fitting. Fig. 11.18 demonstrates that the model works well even when the exponents are fixed. Also included in Fig. 11.18 are the modified Main [2000] fits, where Ω_I and Ω_{III} can vary independently, for fixed values of *m* and *u*. In future work automated non-linear inversion procedures on all of the data sets should be used to ascertain if these small variations are significant, or whether a single solution for one or more of the optimal parameters can be found.

Equation [3.9] is only one example of a macroscopic creep law. Exponential or logarithmic macroscopic creep law models have also been shown to fit experimental data over the laboratory range of creep strain rates [e. g. Costin, 1987; Lawn, 1993]. However, previous studies have shown that, over the creep strain rates achievable in the laboratory, it is impossible to distinguish between the two models [Lockner, 1993; Ngwenya *et al.*, 2001; Armitrano and Helmstetter, 2006]. Further work, both experimental and statistical, is needed to rigorously distinguish between them, notably to achieve a much broader bandwidth of strain rate (see **10.4 Avenues for future research**).

Sample number	Creep strain rate (s^{-1})	Ω_I	Ω_{III}	τ_1	τ_3	m	u
DD-40-19Z	3.6×10^{-6}	0.0400	1.5587	0.2300	870.8	0.400	0.0120
DD-40-19Z Fixed	3.6×10^{-6}	0.0400	1.5587	0.2450	696.7	0.400	0.0150
DD-40-45Z	1.0×10^{-7}	0.0120	1.6275	0.2200	15975.3	0.350	0.0100
DD-40-45Z (mod)	1.0×10^{-7}	0.0120	1.6500	0.2200	11410.9	0.320	0.0140
DD-40-45Z Fixed	1.0×10^{-7}	0.0140	1.6255	0.6500	10650.2	0.400	0.0150
DD-40-45Z Fixed (mod)	1.0×10^{-7}	0.0100	1.6400	0.3500	10650.2	0.400	0.0150
DD-40-22Z	1.3×10^{-8}	0.0012	1.4679	0.0500	143669.3	0.480	0.0250
DD-40-22Z (mod)	1.3×10^{-8}	0.0011	1.5500	0.0500	143669.3	0.460	0.0250
DD-40-22Z Fixed	1.3×10^{-8}	0.0030	1.4661	0.0430	239448.8	0.400	0.0150
DD-40-22Z Fixed (mod)	1.3×10^{-8}	0.0024	1.5300	0.0480	239448.8	0.400	0.0150
DD-40-40Z	3.8×10^{-9}	0.0013	1.3875	0.0500	646465.6	0.410	0.0200
DD-40-40Z (mod)	3.8×10^{-9}	0.0008	1.4500	0.0500	430977.1	0.420	0.0300
EB-40-17Z	2.7×10^{-6}	0.0190	2.1090	0.2200	456.2	0.360	0.0100
EB-40-15Z	4.1×10^{-7}	0.0008	2.1267	0.0057	6275.9	0.500	0.0042
EB-40-14Z	4.0×10^{-8}	0.0021	2.1027	0.0240	88234.4	0.375	0.0032
EB-40-16Z	2.4×10^{-9}	0.0100	2.0878	0.1500	1125021.6	0.200	0.0040

Table 11.5. Parameters used in equation [10.3] for the Main [2000] and modified Main [2000] (see text for details) models to fit with the experimentally produced creep curves for both DDS and EB. The graphical representation of the macroscopic creep law fitting is shown in Fig. 11.17 (courtesy of A. Bell and I. Main).

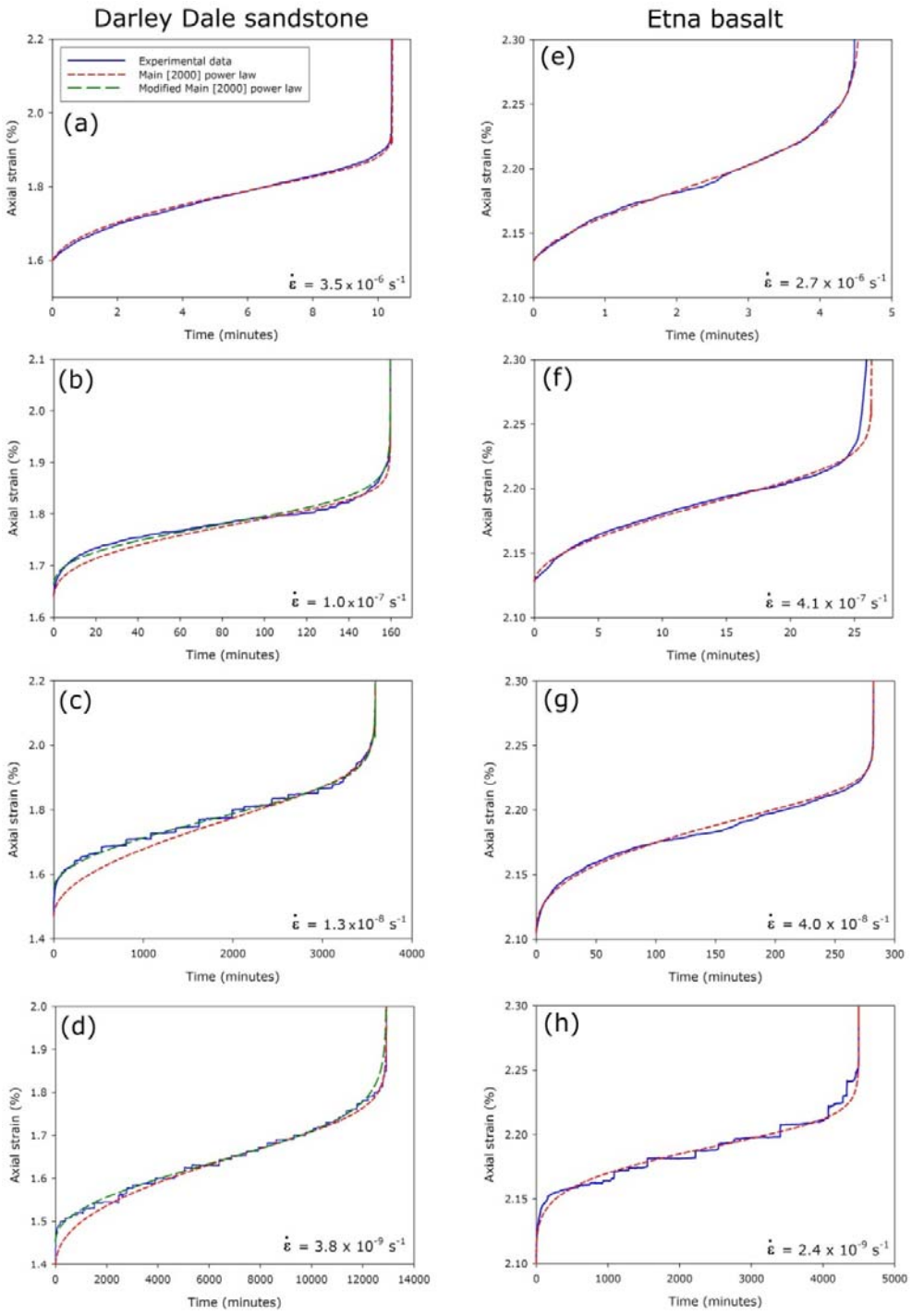

Figure 11.17. Axial strain against time for the four conventional brittle creep experiments on DDS shown in Chapter Eight, Figs. 8.11 and 8.14 and the four conventional brittle creep experiments on EB shown in Chapter Ten, Fig. 10.9 (solid blue lines) with the Main [2000] power law (Equation [3.9]) (short red dashed lines) and modified Main [2000] power law (long green dashed lines) (see text for details) fits superimposed (courtesy of A. Bell and I. Main).

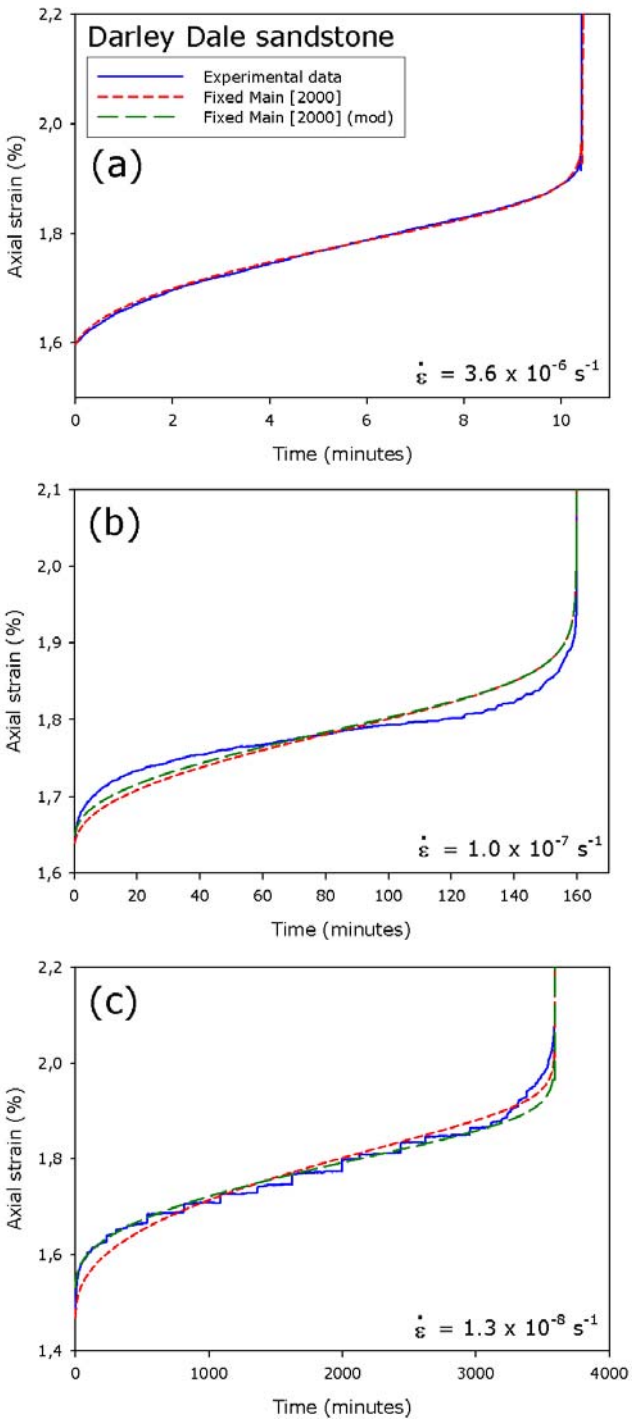

Figure 11.18. Axial strain against time for the three conventional brittle creep experiments on DDS shown in Chapter Eight, Fig. 8.11 (solid blue lines) with the Fixed Main [2000] power law (Equation [3.9]) (short red dashed lines) where both exponents *m* and *u* are kept constant and modified Fixed Main [2000] power law (long green dashed lines) (see text for details) fits superimposed (courtesy of A. Bell and I. Main).

11.8 Consideration of a creep flow law

For experimentalists, a flow law that defines 'steady-state flow' in rocks at a constant stress, effective confining pressure, pore fluid pressure, temperature, strain rate and microstructure is a useful goal. Therefore, data can be extrapolated to natural strain rates. Although most of the literature on the justification of this type of law is used to describe high temperature ductile deformation and plastic flow in metals and rocks [e.g. Walker *et al.*, 1990; Tullis *et al.*, 1991; Rutter, 1999], it will nevertheless be considered here for low temperature brittle creep. The form of the constitutive law for the flow of rocks will be of the form:

$$\dot{\varepsilon} = A\sigma_3^n P_p^m \sigma_1^p \exp\left(-\frac{H}{RT}\right) \qquad [11.2]$$

Where $\dot{\varepsilon}$ is the creep strain rate, A is a pre-exponential empirical constant, σ_3 is the effective confining pressure, P_p is the pore fluid pressure, σ_1 is the applied differential stress, T is the absolute temperature, R is the gas constant and H is the apparent activation enthalpy for flow. A flow law allows the relationship between creep strain rate and each of the independent variables to be investigated, whilst all the others remain constant. A single flow law for both DDS and EB will now be discussed in turn; however the explanation of how the flow law was computed will focus only on DDS as to avoid repetition. It must be noted that the pore pressure variable cannot be used in the case of EB as such experiments were never conducted.

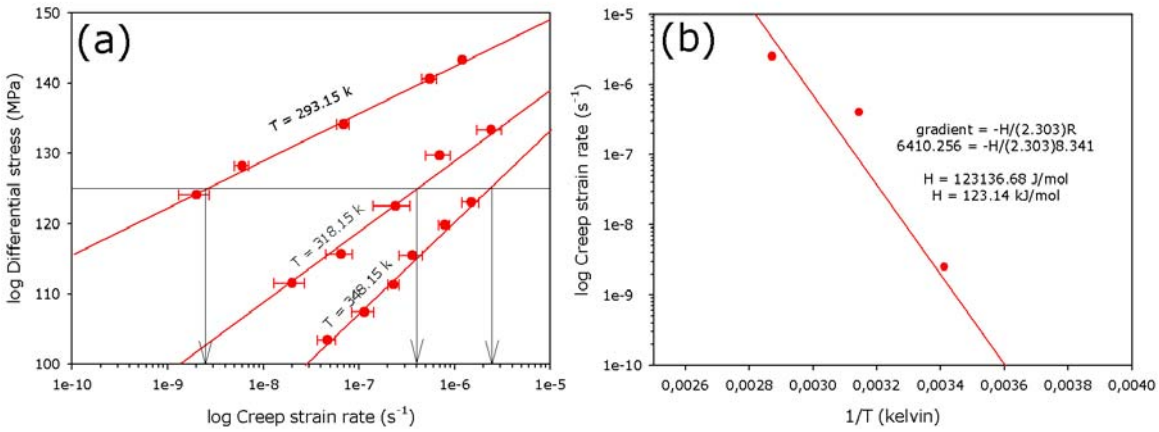

Fig. 11.19. (a) log stress against log strain rate plot showing data from three stress-stepping brittle creep experiments on DDS at three different temperatures (marked on each curve in Kelvin). The strain rates for the different curves at a constant stress of 125 MPa were determined from (a) and then plotted in (b) against 1/T. The gradient from (b) can be used to calculate the apparent activation enthalpy for flow. The same methodology was employed for EB.

Firstly, it is necessary to compute values for *H* and the pre-exponential term *A* for both rock types. *H* can be calculated from the gradient of the curve in a plot of creep strain rate at a constant stress for the different temperatures used in this study against 1/T (calculated as in Fig. 11.19). *H* was determined to be 123136.68 and 11642.014 J/mol for DDS and EB respectively. After *H* has been calculated, *A* can be determined by simply inserting the appropriate values into Eq. [11.2] for a value of creep strain rate and solving the equation to find *A*. However, the gradients of the creep strain rate-differential stress at different values for Peff are too steep to look at the influence of P_{eff} on creep strain rate under a constant applied differential stress. Therefore, despite the significant influence of P_{eff} on creep strain rate evident from these data (Chapter Eight, Fig. 8.23 and Chapter Ten, Fig. 10.16), this variable must be removed from Eq. [11.2]:

$$\dot{\varepsilon} = AP_p^m \sigma_1^p \exp\left(-\frac{H}{RT}\right) \qquad [11.3]$$

The exponents *m* and *p* in Eq. [11.3] were calculated by fitting a series of single linear regressions (power law) to the experimental data, whilst keeping all other variables constant (Fig. 11.20). Following this, *A* was calculated to be 3.90 x 10^{-80} and 1.93 x 10^{-84} for DDS and EB respectively. All of the calculated parameters used in the flow law of Eq. [11.3] are shown in Table 11.6. It must be noted that the flow law yields a dimensionless term, since *H* has the same dimensions as *RT* in the *exp(-H/RT)* term.

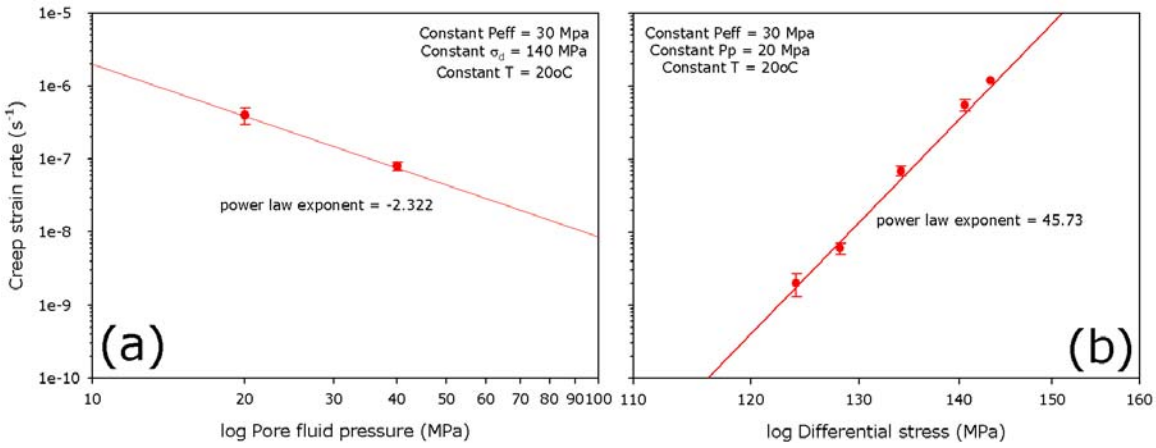

Figure 11.20. Data from stress-stepping brittle creep experiments on DDS showing (a) the influence of pore fluid pressure on creep strain rate, from which the exponent *m* in Eq. [11.3] was calculated and (b) the influence of differential stress on creep strain rate, from which the exponent *p* in Eq. [11.3] was calculated. All other variables were held constant. The same methodology was employed for EB.

Parameter	Darley Dale sandstone	Etna basalt
H (J/mol)	123136.68	11642.01
R (J/deg mol)	8.341	8.341
A	3.90 x 10^{-80}	1.93 x 10^{-84}
p	45.73	31.09
m	-2.322	N/A

Table 11.6. Calculated parameters for the brittle creep flow law to be used in Eq. [11.4]. Exponents are calculated from power law single linear regression fits (Fig. 11.20).

Now that all of the parameters have been determined, the goodness of fit of the flow law can be investigated using the parameters listed in Table 11.6. For simplicity of computation, logs of both sides were taken in Eq. [11.3]:

$$\log\dot{\varepsilon} = logA + plog\left(\sigma_1\right) + mlog\left(P_p\right) - \frac{H}{2.303\left(RT\right)} \qquad [11.4]$$

The results of the flow law fitting are shown in Fig. 11.21. For DDS (Fig. 11.21a), it can be seen that the fit for the 20°C is very good; however, as temperature is increased the fit of the flow law to the experimental data diminishes. The change in gradient in the experimental data curves suggest that *H* varies with stress or strain rate. Therefore, over the temperature range of the experiments, the relative contributions of the different rate controlling processes must be changing. This problem may be overcome by using a global nonlinear fitting method [Sotin and Poirier, 1984], and could be the focus of further investigation. This means that, on first inspection for these DDS data, a single flow law does not provide a good basis for extrapolation. However, for EB (Fig. 11.21b), there is a negligible change in the gradient in the experimental data curves. Therefore, the fit of the single flow law is very good and may provide basis for extrapolation. Using the flow law, the projected creep strain rate – differential stress curve for EB at 200°C has been plotted on Fig. 11.21b as a dashed line. It must be noted however that more experiments at higher temperature are now required to confirm this.

It must be noted however, even though it is postulated that it may not make an impact (see discussion in Chapter Eight), creep strain rates should be calculated at a position of constant permanent strain or microstructure. During these computations, this was not the case.

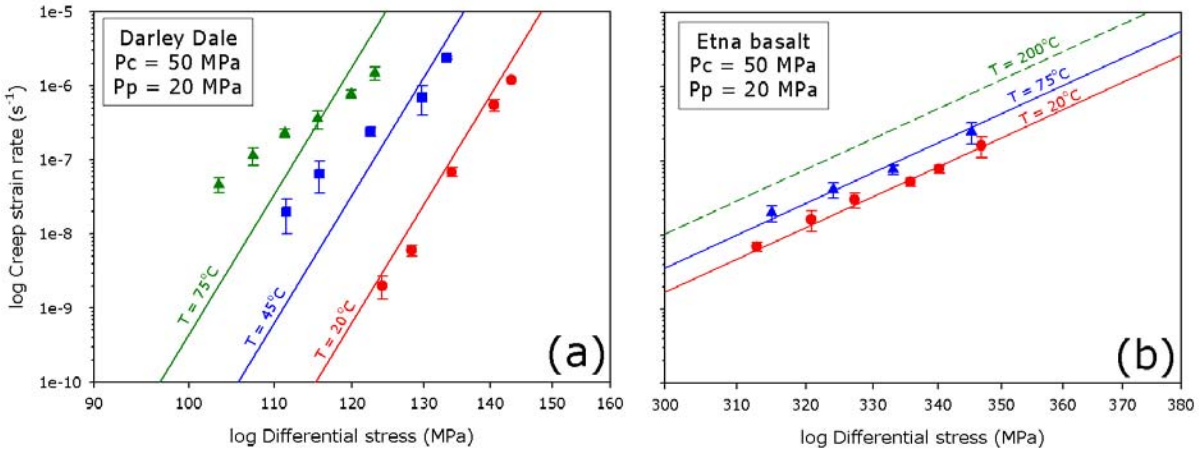

Figure 11.21. Plot of log creep strain rate against log differential stress showing experimental data from three stress-stepping brittle creep experiments on samples of DDS at temperatures of 20°, 45° and 75°C together with the predicted extrapolation lines from the creep flow law shown in Eq. [11.4].

11.9 Application of data in understanding large-scale geophysical problems

11.9.1 Volcanic Hazards

Subcritical crack growth, of which the most important mechanism in the upper 20 km of the Earth's crust is stress corrosion [see Atkinson, 1982], within the rock comprising a volcanic edifice is seen as a fundamental mechanism for the precursory activity seen prior to eruption within many active volcanoes. Numerous self-accelerating eruption precursory phenomena, such as ground deformation and seismic energy release, all simulate accelerating creep during the deformation of a volcanic edifice prior to eruption (Figs. 11.22 and 11.23).

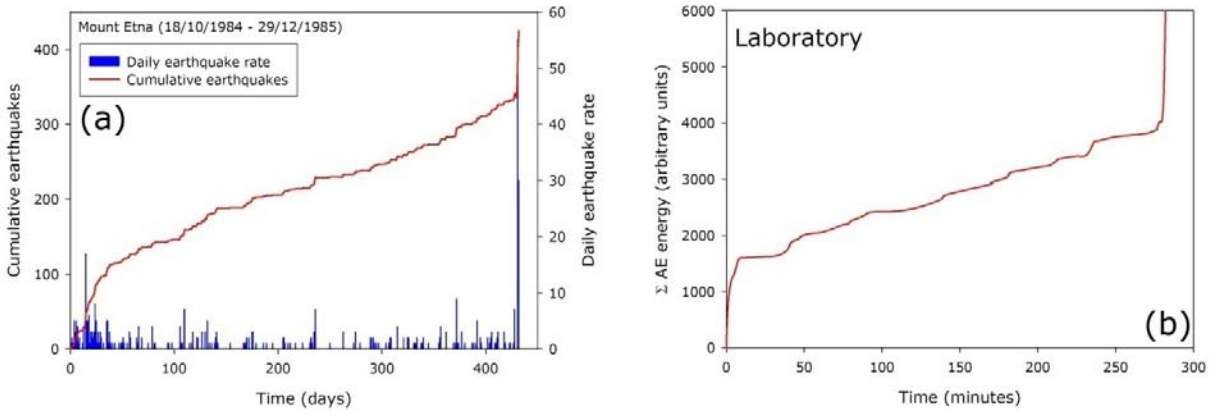

Figure 11.22. (a) Earthquake data from Mt. Etna between 18/10/1984 and 29/12/1985 (courtesy of A. Bell). (b) Recorded AE output during a conventional brittle creep experiment on EB under the conditions of a 30 MPa effective confining pressure (50 MPa confining pressure and a 20 MPa pore fluid pressure).

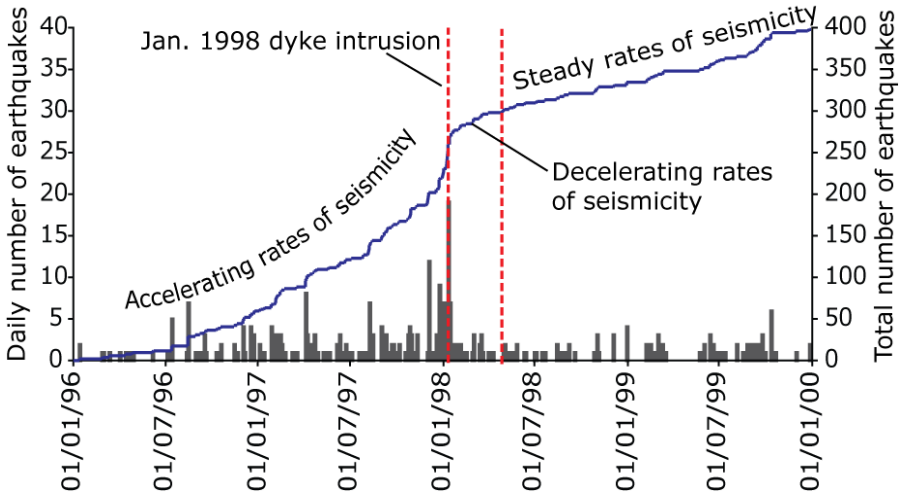

Figure 11.23. Earthquake data from Mt. Etna between 01/01/1996 and 01/01/2000 (courtesy of A. Bell).

The experimental evidence presented in Chapter Ten indicates that basalt is very likely to undergo brittle creep at conditions commonly found in a volcanic edifice. Specifically the pressures, temperatures and strain rates are, in theory, ideal for fast rates of stress corrosion. Stress corrosion will be facilitated by circulating geothermal or magmatic fluids above the magma chamber [Waza *et al.*, 1980; Michalske

and Freiman, 1982; Michalske and Bunker, 1987]. Such fluids have can an anomalously high pH [Brusca *et al.*, 2001] a factor that can accelerate the rate of stress corrosion cracking in rock with a lower solid phase pH bulk composition due to reaction rate kinetics [Atkinson and Meredith, 1981]. The elevated temperatures caused by the intrusion of magma at shallow depths and hot circulating fluids also accelerates the rate at which stress corrosion occurs [Atkinson, 1979; Kranz *et al.*, 1982; Meredith and Atkinson, 1982;1983;1985]. Furthermore, the rocks that comprise the edifice are also likely to contain a high degree of pre-existing crack damage due to cyclic mechanical stresses caused by pressurization and depressurization cycles (see Chapter Six) and thermal stresses [Vinciguerra *et al.*, 2005], providing ready fluid pathways and many likely nucleation sites to start and restart the process.

Basaltic volcanoes are known to deform extensively under loads caused by a combination of internal magmatic pressure, far-field or regional tectonics, and the gravitational instability of the edifice itself. At Mt Etna, for example, ground deformation and volcano-tectonic seismicity (an established proxy for brittle deformation) recorded over more than thirty years indicate the continuous accumulation of permanent strain at rates that vary through both time and space within the edifice [Patanè *et al.*, 2004; Patane *et al.*, 2004; Puglisi *et al.*, 2004]. Episodes of deformation can be observed that display characteristics consistent with phases of primary, 'steady-state' and tertiary creep (for examples see Figs. 11.22 and 11.23), exactly as seen in the laboratory on a much larger scale.

While the bulk patterns are similar for laboratory and field examples, confirming an underlying brittle creep mechanism (or any other specific mechanism) for observed volcanic deformation is challenging. Care is needed to ensure that signals are associated with rock volumes that experience loading conditions appropriate for brittle creep. There are no clear examples of what can realistically be interpreted as a whole classic creep curve in volcanic data. In most cases the spatial and temporal

evolution of stress is not well constrained (as it is in the laboratory), so it is difficult to determine when the observed deformation patterns are dominated by the time-dependent material response to a constant stress (creep) or a constant loading rate with time-varying stresses. The relationship between strain and acoustic emission properties in controlled laboratory tests of homogeneous samples is reasonably well understood, but its scaling to complex volcanoes in the natural world is poorly understood, although it is evidently highly non-linear.

The strong material, stress, temperature and pore-fluid spatial heterogeneity observed at volcanoes probably means that the time-dependent material response to a stress change (such as an increase in magma pressure) is much more complex than can currently be replicated in the laboratory. Volcanic deformation may be more likely to reflect the aggregate of deformation of many heterogeneous elements, all undergoing brittle creep, but with different material properties and subject to local stress conditions, temperatures and pore fluid conditions. Up-scaling of laboratory results to field-scale observations clearly remains a major challenge. The application of formal statistical techniques to strain and damage proxies may help to diagnose mechanistic similarities between laboratory and field studies, but this is yet to be proven. For example it could be expected from Figs. 11.22 and 11.23 that the bulk properties may be fitted to the same constitutive rules, but with different parameters at different scales in different parts of the volcanic system. Numerical modelling is needed to understand the role of edificial heterogeneity and differences in loading conditions in controlling the bulk deformation trends, given the local constitutive behaviour determined in the laboratory data presented here.

Kilburn and Voight [1998] demonstrated that, for the 1995 Soufriere Hills (Montserrat) eruption, a tenfold increase in seismicity immediately prior to eruption was consistent with a model of subcritical rock failure where the dominant mechanism is stress corrosion. Using seismic scaling exponents from

the September-October 1989 eruption at Mt. Etna, Italy, Vinciguerra [1999; 2002] found that the mechanism of stress corrosion could also be used to explain observations months before the onset of eruption. The seismic scaling exponents, derived from frequency-magnitude statistics, are consistent with both a mid (order of months) and short (days) term model of stress corrosion crack growth [see also Main and Meredith, 1991]. The model presented by Kilburn [2003] argues that the final stages of magma ascent are controlled by the coalescence of pre-existing cracks that are growing slowly by time-dependent stress corrosion cracking. Seismic patterns from Soufriere Hills and Pinatubo are consistent with this model and it is suggested that, for the aforementioned volcanoes, reliable forecasts of magmatic activity may eventually be feasible on the order of days before the eruption [Kilburn, 2003].

In all cases, stress corrosion is seen to act as a mechanism for the weakening of the rock comprising the edifice by promoting crack growth and coalesce that can open major pathways that serve as conduits for magma. It provides a plausible physical basis for the failure forecasting models to determine forecasts, and possibly predictions, for the onset of volcanic eruptions. Over longer time periods, repeated edifice fatigue may also determine eruption frequencies at volcanoes persistently charged with high-level magma, such as Etna or Stromboli [McGuire and Kilburn, 1997]. As McGuire and Kilburn [1997] note: 'further investigations of static fatigue at active volcanoes have considerable potential both for improving eruption forecasts, and for better understanding Earth's long-term rates of volcanic activity'. Despite this, there has been little experimental work designed to study the process of stress corrosion in basic rocks [see Atkinson and Meredith, 1987b for tabular review]. Waza *et al.* [1980] studied the rate of crack propagation and the stress intensity factor at a constant load in DT experiments on basalt and andesite. They found that crack velocities in their polycrystalline silicate rocks were greatly enhanced by water saturation and that stress corrosion should be considered as an important process in the deformation and fracture of silicate rock. Meredith and Atkinson [1983; 1985] also investigated stress

corrosion using DT experiments on Whin Sill dolerite, Ralston Intrusive and Black gabbro. They found that, compared to other crustal rocks, basic rocks have a high critical stress intensity factor. Therefore, more energy is required to propagate fast fractures in basic rocks than in more acidic crustal rocks. Swanson [1984] studied stress corrosion in basic rocks using a DT relaxation technique under room conditions to produce *K*-*v* diagrams; however, his method produced a considerable scatter in the resultant *K*-*v* curves. All of the data on subcritical crack growth or stress corrosion in basic rocks focus on the subcritical crack velocity in a single tensile crack using the DT method. This study is the first to provide rates of deformation and AE due to stress corrosion within a body of basic rock, where the microcracks can interact and coalesce under a confining pressure. The data from this study has shown that bulk samples of basic rock do creep in the brittle regime at the conditions commensurate with the depths of observed pre-eruptive seismicity.

In spite of this, many of the forecasting models that use seismic precursors to volcanic eruptions incorporate or imply the influence of the mechanism of stress corrosion. Voight's [1988; 1989] empirical method for forecasting eruptions, the Failure Forecasting Method (FFM) [see also Cornelius and Voight, 1995], uses the rate of seismicity or a similar self-accelerating process prior to eruption and is described by:

$$\ddot{\Omega} = A\dot{\Omega}^{\alpha} \qquad [11.5]$$

Where A and α are empirically derived constants and $\dot{\Omega}$ and $\ddot{\Omega}$ are the measured rate and acceleration of the deformation parameter (usually ground deformation or seismic energy release, both of which can be directly linked to strain release). Typically, α lies between 1 and 2.5, however process based models place it close to 2 [Cornelius and Scott, 1993; McGuire and Kilburn, 1997; Main, 1999; Kilburn, 2003].

Cornelius and Scott [1993] even related α to the exponent in Charles' law [Charles, 1958] for stress corrosion (Chapter Three, Equation [3.8]). Where α = 2, $\dot{\Omega}$ will increase hyperbolically with time. If it is assumed that an eruption will take place as rates approach infinity, then the failure time can be approximated by integrating Equation [11.5]. A failure time can be found by extending the inverse-rate trend to the time where $\dot{\Omega}^{-1}$ reaches zero. It has been previously noted that it may be difficult to obtain precise forecasts using the FFM due to the fact that the value of α is not known a priori [Cornelius and Voight, 1995]; however, laboratory AE data, such as those presented in this study, could be utilized to better constrain such forecasting models.

11.9.2 Earthquake rupture

Stress corrosion is also considered an important factor in time-dependent earthquake phenomena [Scholz, 1968a; Scholz, 1972; Rudnicki, 1980; Das and Scholz, 1981; Atkinson, 1982; Crampin *et al.*, 1984; Main and Meredith, 1991; Main *et al.*, 1992]. Scholz [1968a] suggested that the time sequence in earthquake aftershocks depends upon the time-dependent strength of the rock, identified by Scholz (1968a) as the result of static fatigue processes such as stress corrosion. Das and Scholz [1981] suggest that the observation that delayed multiple event occur and the aftershocks almost universally occur demonstrate that a time-dependent mechanism must be involved in the earthquake rupture mechanism. Furthermore, their model based on standard fracture mechanics assumes that the crack tip can extend sub-critically by stress corrosion. Crampin et al. [1984] suggested that subcritical crack growth produces dilatancy anisotropy throughout earthquake preparation zones and is a possible driving mechanism for earthquake precursors. Intermediate-term seismic quiescences of a magnitude similar to those observed before major earthquakes have been shown to be quantitatively consistent with a reduction in mean strain energy release for a fractal crack population [Main and Meredith, 1991].

Although any underlying mechanism could produce such a fractal array of fractures, the authors cite stress corrosion due to its importance in fracture within the Earth's brittle crust.

Earthquake zones are by their nature close to crustal plate boundaries where constant forcing caused by the motion of tectonic plates is likely to be driving deformation. However, this study has shown that time-dependent brittle deformation becomes more important as the applied differential stress increases; therefore, if plate loading is slow then it could be important prior to failure.

11.10 The importance of brittle creep with depth in the crust

This study has been demonstrated how creep deformation is influenced by increasing temperature, effective confining pressure and differential stress. We are therefore now in a position to estimate how the rate of deformation due to brittle creep may vary with depth in the shallow crust, based on the data for DDS. If an average geothermal gradient of 30°C/km, an average lithostatic pressure gradient of 25 MPa/km, and a hydrostatic pore pressure gradient of 10 MPa/km is assumed then the expected changes in creep strain rate over a depth interval of 2 km can be examined.

The corresponding increase in effective vertical stress is 30 MPa, and in both effective horizontal stresses is 10 MPa (assuming isotropy and a Poisson's ratio of 0.25). Therefore the increase in effective mean stress is 16.7 MPa, and in differential stress is 20 MPa. Using these figures together with the experimental data for DDS at an elevated temperature (Chapter Nine) and an elevated effective confining pressure (Chapter Eight), it can be estimated that the creep strain rate will (1) increase by about 2×10^3 due to the increase in temperature of 60°C, (2) increase by about 10^3 due to the increase in differential stress, and (3) decrease by about 3×10^3 due to the increase in effective mean stress.

The net result is an increase in creep strain rate of the order of 7 x 10^2. Even though this estimate is based on a number of gross approximations, it does suggest that there is an approximate balance between the increase in creep strain rate with depth due to the increasing differential stress and the decrease due to the increasing effective mean stress. Overall, this then suggests that it will be the increase in temperature with depth that dominates the rate of creep deformation in the Earth's shallow crust.

11.11 Avenues for future research

This avenues discussed here are by no means exhaustive and the above discussion has highlighted numerous areas of interest that could potentially be explored further. This section merely emphasizes the most pertinent routes of further study.

One of the biggest challenges for future work on brittle creep is to extend the bandwidth of creep strain rates towards those seen in nature (see Fig. 11.1). In the laboratory, creep strain rates down to about 10^{-9} s^{-1} can be achieved; however, in nature, strain rates are on the order of 10^{-12} to 10^{-15} s^{-1}. Equivalent relations can be derived for both exponential [Lockner, 1998] and power-law [Main, 2000] forms of the constitutive relation between stress intensity and crack velocity. A key point is that it is currently not possible to discriminate between these competing models due to the relatively narrow bandwidth of strain rate currently available from conventional laboratory experiments, as demonstrated in this study. From reaction rate theory it might be expected that the exponential form [Lockner, 1998] to dominate for relatively uniform materials such as single crystals, whereas from percolation theory we might expect an emergent power-law form [Main, 2000] for heterogeneous polycrystalline materials such as

rocks. However, they predict very different results when extrapolated from laboratory strain rates to tectonic strain rates (Fig. 11.24; see also Fig. 11.1).

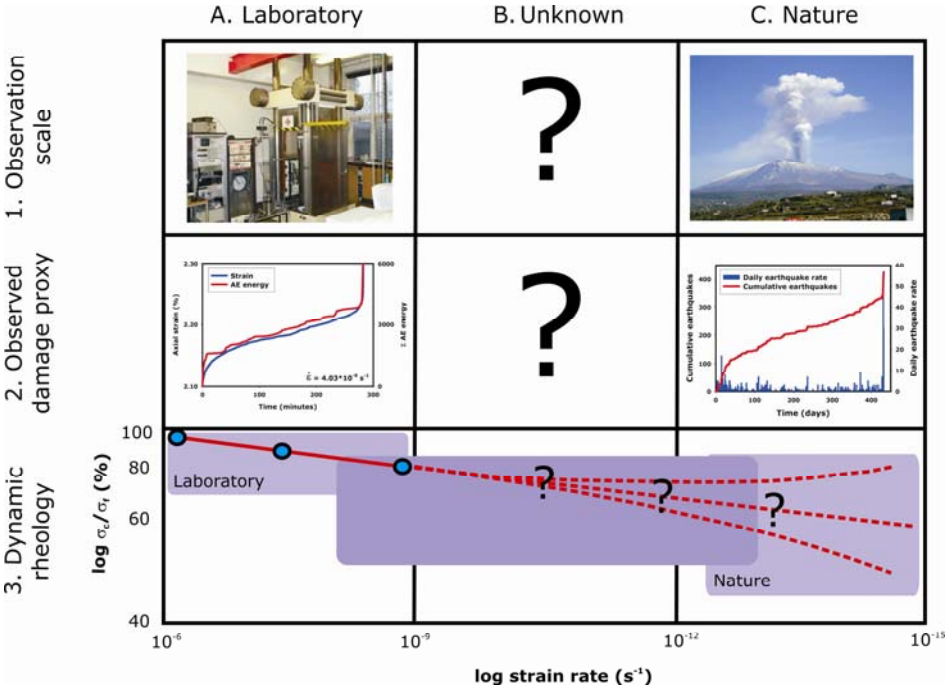

Figure 11.24. Scaling in space and time during brittle creep of Mt. Etna basalt, from the laboratory scale (taken from this study) to the field scale (from Mt. Etna volcano).

A novel way of tackling this problem has been proposed by the members of the Rock & Ice Physics Laboratory (RIPL), UCL. They have proposed that the creep strain rate gap can be bridged by performing brittle creep experiments in a 'deep-sea underwater observatory' were the deep-sea environment provides the stability to perform ultra-long (6 months to 2 years) brittle creep experiments. A pilot study has been successfully implemented [Meredith *et al.*, 2005a; Meredith *et al.*, 2005b] and demonstrates that the answer to this important question is achievable (Fig. 11.25).

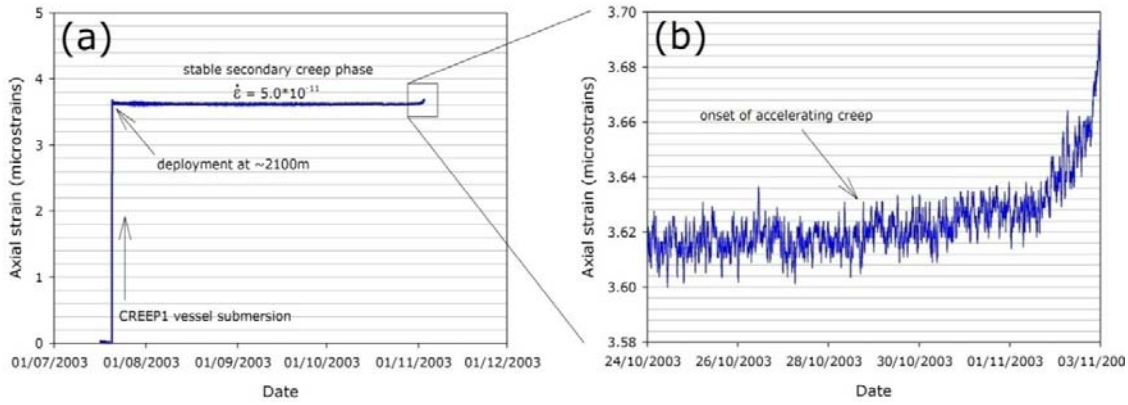

Figure 11.25. Strain against time data from the CREEP-1 project. The experiment was conducted over 110 days at 2100 m water by the Rock & Ice Physics Laboratory (RIPL) group at UCL.

A key related question then is; what is the minimum stress threshold (σ_{min}) for time-dependent crack growth to continue? Earlier experimental fracture mechanics studies of the growth of single tensile cracks at ambient pressure [Wilkins, 1980; Meredith and Atkinson, 1983; Swanson, 1984] showed that σ_{min} is less than 50% of σ_p. Theoretical calculations based on reaction rate theory [Atkinson, 1984] suggest that such cracking may occur down to stresses as low as 20% of σ_p, implying that time-dependent cracking will continue to be an important deformation mechanism over geological time and at typical tectonic strain rates. Therefore, further evaluation over a wider range of strain rates is essential, both to examine the generality of the laboratory observations across the temporal scales of interest, and to test competing hypotheses for time-dependent deformation at low strain rates, including those that explicitly include a finite threshold.

The mechanism of stress corrosion is a chemically-enhanced and thermally activated process. Hence, in order to quantify the process and discriminate between models, not only does the range of achievable strain rates require extending, but also to study systematically the influence of pore fluid chemistry. Studies of tensile crack growth in silicates have shown that the pH of pore fluids has a profound effect

on crack growth rates; with acid solutions suppressing crack growth and basic solutions enhancing crack growth [e.g. Atkinson and Meredith, 1981]. Since rock failure under compression proceeds by the growth and coalescence of primarily tensile microcracks, it can be hypothesized that pore fluid chemistry will also exert a crucial influence on brittle creep under triaxial compression.

Finally, in addition to considering the problem of scaling in time, size scaling between the laboratory sample scale and the crustal failure scale must also be considered. This can be achieved by applying the well-known frequency scaling relation of [Aki and Richards, 2002] to measured laboratory AE data. This has been successfully applied to up-scaling laboratory measurements of high-temperature fracture [Burlini *et al.*, 2007] and the long-period seismicity associated with rapid fluid flow in fractures [Benson *et al.*, 2008] over 5 orders of magnitude.

Chapter twelve

12. Conclusions

12.1 Introduction

This study has investigated the two end-members of deformation style, namely stress-cycling and constant stress deformation. Stress-cycling experiments have focused on measuring the evolution of static elastic moduli as crack damage is increased during cyclic loading. Such experiments look at the difference in elastic moduli development between wet and dry samples in both a porous sandstone and a thermally-cracked extrusive basalt. The data are interpreted in terms of microstructural observations and AE analysis. Constant stress (brittle creep) experiments have investigated time-dependent brittle deformation processes, of which the most important is the chemically-activated mechanism of stress corrosion, in a suite of sandstones and a thermally-cracked extrusive basalt. New methodology is presented that allows the influence of variables such as effective confining pressure (P_{eff}), pore fluid pressure (P_p) and temperature to be investigated more rigourously. The results are interpreted in terms of microstructural observations, acoustic emission (AE) hypocentre location analysis and fits to proposed macroscopic creep laws. This conclusion section is split into two parts: (1) conclusions of the work on stress-cycling and (2) conclusions of the work on time-dependent brittle deformation.

12.2 Results from stress-cycling experiments

1. *The evolution of elastic moduli with increasing crack damage*. The data demonstrate that cyclic stressing significantly affects the static elastic moduli in a number of different rock types. In all cases where the maximum stress was increased in successive cycles, the Young's modulus is seen to decrease and the Poisson's ratio to increase significantly. These changes are attributed to an increase in the level of crack damage with each increasing stress cycle. These observations are in agreement with those of Heap and Faulkner [2008].

2. *Analysis of AE output during stress-cycling*. AE output (micro-seismicity) re-commenced during any loading cycle at the same level of stress that it ceased during the unloading portion of the previous cycle. Where the stress in any loading cycle does not reach that at which AE ceased in the preceding cycle, then no further AE output is observed and the elastic moduli do not change. It is therefore concluded that no further crack damage is created during these cycles. This suggests that, in nature, only those stress episodes that are accompanied by volcano-seismicity will result in extra damage to the edifice and lead to changes in elastic moduli and seismic velocities. This suggestion is in agreement with the results of long-term seismological monitoring at Mt. Etna volcano [Lombardo and Cardaci, 1994; Bonaccorso *et al.*, 1996; Bonaccorso *et al.*, 2004].

3. *The influence of thermal cracking on the elastic moduli evolution of EB*. The slow thermal stressing of EB samples to 900°C does not result in any increase in crack damage or degradation of elastic moduli. These observations are entirely in agreement with the experimental observations of no changes in physical and transport properties of thermally stressed EB reported by Vinciguerra *et al.* [2005], and with the seismological data reported by Patanè *et al.* [2004].

12.3 Results from constant stress (brittle creep) experiments

1. *Creep strain rates and damage levels*. Conventional creep experiments have shown that applied differential stress exerts a crucial influence on both creep strain rate and time-to-failure. They have also demonstrated that a critical level of damage needs to be reached before the onset of accelerating tertiary creep. This is true for the two 'end-member' rock types of DDS and EB. This work represents the first experimental study on brittle creep in basalt and has proven that basalt does creep in the brittle regime. Detailed microstructural analysis on DDS has shown that crack densities at the onset of tertiary creep are relatively low (compared with that of a sample taken to failure); however, conditions are likely to represent a point that is well into the phase of dilatant cracking but that precedes crack coalescence and damage localization. A threefold increase in crack anisotropy is seen between the undeformed state and the onset of tertiary creep. This is strong evidence that the new damage induced during primary and secondary creep is dominated by the growth of axial cracks sub-parallel to the maximum principal stress. Furthermore, crack densities and anisotropy are similar for samples taken to this point under creep strain rates that differ by an order of magnitude, supporting the idea of a critical damage threshold. AE hypocentre location analysis suggests that AE behaviour during creep is (1) diffuse and distributed during primary creep, (2) distributed with some suggestion of localization or 'mixed mode' during secondary creep and (3) increasingly localized during tertiary creep. The suggestion that AE clustering might commence during the latter part of secondary creep appears to conflict with the idea of a critical damage threshold for the onset of tertiary creep and localization of deformation [e.g. Baud and Meredith, 1997]. However, this may merely highlight the difficulty of defining the onset of tertiary creep from an emergent strain-time curve.

2. *Influence of mineralogical composition and microstructure*. Stress-stepping creep experiments have shown that the brittle creep behaviour of the different rock types is remarkably similar. In each case, the creep strain rate has a crucial influence on the creep strain rate. Subtle differences do exist however. The sensitivity of creep strain rate to an increase applied differential stress is greater in the sandstones than basalt. This is interpreted in terms of the high crack velocity of quartz compared to other geological materials, as per previous DT experiments. The same interpretation holds for the three sandstones studied, the higher proportion of quartz the higher the 'creep sensitivity' to the applied differential stress. The proportion of the short-term peak stress (σ_p) at which a sample creeps at a given creep strain rate however is greater for the low porosity samples (EB and COS) than the high porosity samples (DDS and BHS).

3. *Influence of effective confining pressure and pore fluid pressure*. Stress-stepping creep experiments have shown that an increase in P_{eff} inhibits the process of stress corrosion in both DDS and EB. The most likely cause is a decrease in water mobility due to a reduction in crack aperture at higher P_{eff}. The opposite is true for a reduction in P_{eff}. However, a two-fold increase in P_p, whilst maintaining a constant P_{eff}, has no measurable effect on the rate of stress corrosion in DDS. Implying that the rate at which reactive species can diffuse through the sample to crack tips is the limiting control on stress corrosion reactions, rather than the amount of reactive species present.

4. *Influence of temperature*. The stress-stepping creep experiments presented in this study have demonstrated that an elevated temperature exerts an influence on the creep strain rate in all three sandstones (DDS, BHS and COS) and EB. The increase in creep strain rate for a given

applied differential stress is however much more substantial in the sandstones than basalt. Indeed, for a given applied differential stress, creep strain rate is some three orders of magnitude greater at 75°C than at 25°C for both DDS and BHS. This is interpreted in terms of the substantial increase in crack velocity for an increase in temperature in DT experiments on quartz. In contrast, similar experiments on dolerite (a useful analogue for basalt) only demonstrated a modest increase in response to an increase in temperature.

5. *Predicting rock failure under constant stress*. Conventional creep experiments on both DDS and EB have demonstrated that, despite the applied differential stress and the resultant creep strain rate and time-to-failure, the proportion of time spent in each creep phase is roughly the same. In general, samples spent 20, 60 and 20% of their total time-to-failure in the primary, secondary and tertiary creep phases respectively. It has been postulated, given that is very consistent between two 'end-member' rock types and over three orders of magnitude, that this observation could be used as a tool to predict rock failure.

6. *Macroscopic creep laws*. It is also shown that mean-field damage mechanics power law modelling can closely reproduce the relation between strain and time observed in conventional brittle creep experiments in both DDS and EB. It is therefore not necessary to invoke a separate process for secondary creep. However, at the slowest creep strain rates, the Main [2000] model does not accurately reproduce the initial primary creep phase in DDS. The likely cause of this discrepancy is the fact that it is based on mean-field damage mechanics that considers only the formation and interplay of cracks. During the primary creep phase, additional pore space compaction processes could be still be operative. This is corroborated by the fact that the model fits perfectly with experiments on EB, a rock composed almost entirely of microcracks. Allowing

the variables to act independently, creating a modified Main [2000] model, incorporates the potential additional mechanism and is more consistent with the experimental data for DDS during the primary creep phase.

7. *Consideration of a creep flow law*. For experimentalists, a flow law that defines 'steady-state flow' in rocks at a constant stress, effective confining pressure, pore fluid pressure, temperature, strain rate and microstructure is a useful goal. Therefore, data can be extrapolated to natural strain rates. For DDS, the flow law fit for the experimental data at 20°C is very good; however, as temperature is increased the fit of the flow law to the experimental data diminishes. This means that, on first inspection for these DDS data, a single flow law does not provide a good basis for extrapolation. However, for EB, there is a negligible change in the gradient in the experimental data curves. Therefore, the fit of the single flow law is very good and may provide basis for extrapolation. Using the flow law, the projected creep strain rate – differential stress curve for EB at 200°C has been determined.

8. *The importance of brittle creep with depth in the crust.* Using data from this study, it is now possible to estimate how the rate of deformation due to brittle creep may vary with depth in the shallow crust, for DDS. Initial calculations speculate that there will be a net increase in creep strain rate of the order of 7×10^2 for a depth increase of 2 km in the crust. Overall, this then suggests that it will be the increase in temperature with depth that dominates the rate of creep deformation in the Earth's shallow crust.

'But, how does it apply to volcano?'

References

Aki, K. and P. G. Richards (2002), Quantitative Seismology (Second Edition), University Science Books, California.

Allard, P., B. Behncke, S. D'Amico, M. Neri and S. Cambino (2006), Mount Etna 1993–2005: Anatomy of an evolving eruptive cycle, Earth Science Reviews, 78, 85-114.

Alm, O., L. Jaktlund and K. Shaoquan (1985), The influence of microcrack density on the elastic and fracture mechanical properties of Stripa granite, Phys. Earth Planet. Int., 40, 161-179.

Alparone, S., D. Andronico, S. Giammanco and L. Lodato (2004), A multidisciplinary approach to detect active pathways for magma migration and eruption at Mt. Etna (Sicily, Italy) before the 2001 and 2002–2003 eruptions, J. Geophys. Res., 136, 121-140.

Anderson, D. L., B. Minster and D. Cole (1974), The effect of orientated cracks on seismic velocities, J. Geophys. Res., 79, 4011-4015.

Anderson, O. L. and P. C. Grew (1977), Stress Corrosion Theory of Crack Propagation with Applications to Geophysics, Rev. Geophys., 15, 77-104.

Andrade, E. N. and R. F. Y. Randall (1949), The Rehbinder effect, Nature, 164, 1127.

Andrade, E. N. C. (1910), On the Viscous Flow in Metals, and Allied Phenomena, Proc. Royal Soc. Lon., 84, 1-12.

Andrade, E. N. C. (1914), The Flow in Metals under Large Constant Stresses, Proc. Royal Soc. Lon., 90, 329-342.

Andronico, D., S. Branca, S. Calvari, M. Burton, T. Caltabiano, R. A. Corsaro, P. Del Carlo, G. Garfi, L. Lodato, L. Miraglia, F. Mure, M. Neri, E. Pecora, M. Pompilio, G. Salerno and L. Spampanato (2004), A multi-disciplinary study of the 2002–03 Etna eruption: insights into a complex plumbing system, Bulletin of Volcanology, 67, 314-330.

Apuani, T., C. Corazzato, A. Cancelli and A. Tibaldi (2005), Physical and mechanical properties of rock masses at Stromboli: a dataset for volcano instability evaluation, Bull. Eng. Geol. Env., 64, 419-431.

Armitrano, D. and A. Helmstetter (2006), Brittle creep, damage, and time to failure in rocks, J. Geophys. Res., 111, doi: 10.1029/2005JB004252.

Atkinson, B. K. (1979), A fracture mechanics study of subcritical tensile cracking of quartz in wet environments, Pageoph, 117, 1011-1024.

Atkinson, B. K. (1979), A fracture mechanics study of subcritical tensile cracking of quartz in wet environments Pure Appl. Geophys, 117, 1011-1024.

Atkinson, B. K. (1980), Stress corrosion and the rate-dependent tensil failure of a fine-grained quartz rock, Tectonophysics, 65, 281-290.

Atkinson, B. K. (1982), Subcritical crack propagation in rock: theory, experimental results and applications, J. Struct. Geol., 4, 41-56.

Atkinson, B. K. (1984), Subcritical crack growth in geological materials, J. Geophys. Res., 89, 4077-4114.

Atkinson, B. K. (1987), Fracture Mechanics of Rock, Academic Press, London.

Atkinson, B. K. and P. G. Meredith (1981), Stress corrosion cracking of quartz: A note on the influence of chemical environment, Tectonophysics, 77(issue 1-2), 1-11.

Atkinson, B. K. and P. G. Meredith (1987), The theory of subcritical crack growth with applications to minerals and rocks, in Fracture Mechanics of Rock, edited by B. K. Atkinson, pp. 111-166, Academic Press, London.

Azzaro, R., M. S. Barbano, B. Antichi and R. Rigano (2000), Macroseismic catalogue of Mt. Etna earthquakes from 1832 to 1998, Acta. Vulcanol., 12 (1/2), 3-36.
Babcock, E. A. (1978), Measurements of subsurface fractures from dipmeter logs, Am. Assoc. Pet. Geo. Bull., 62, 1111-1126.
Baker, T. C. and F. W. Preston (1946), Wide range static strength testing apparatus for glass rods, J. Appl. Phys., 17, 162.
Balme, M. R., V. Rocchi, C. Jones, P. R. Sammonds, P. G. Meredith and S. Boon, A. (2004), Fracture toughness measurements on igneous rocks using a high-pressure, high-temperature rock fracture mechanics cell, J. Vol. Geotherm. Res., 132, 159-172.
Baud, P. and P. G. Meredith (1997), Damage accumulation during triaxial creep of Darley Dale sandstone from pore volumometry and acoustic emission, Int. J. Rock Mech. Min. Sci., 34:3-4, Paper No. 024.
Baud, P., V. Vajdova and T.-F. Wong (2006), Shear-enhanced compaction and strain localization: Inelastic deformation and constitutive modeling of four porous sandstones, J. Geophys. Res., 111, B12401, doi: 10.1029/2005JB004101.
Baud, P., W. Zhu and T.-F. Wong (2000), Failure mode and weakening effect of water on sandstone, J. Geophys. Res., 105, 16371-16389.
Behncke, B. and M. Neri (2003), Cycles and trends in the recent eruptive behaviour of Mount Etna (Italy), Canadian Journal of Earth Sciences, 40, 1405-1411.
Bell, J. S. (2003), Practical methods for estimating in situ stresses for borehole stability applications in sedimentary basins, J. Pet. Sci. Eng., 38, 111-119.
Bell, J. S. and D. I. Gough (1979), Northeast–southwest compressive stress in Alberta: evidence from oil wells, Earth Plan. Sci. Lett., 45, 475-482.
Benson, P. M., P. G. Meredith and E. S. Platzman (2003), Relating pore fabric geometry to acoustic and permeability anisotropy in Crab Orchard Sandstone: A laboratory study using magnetic ferrofluid, Geophys. Res. Lett., 30, No. 19, doi: 10.1029/2003GL017929.
Benson, P. M., P. G. Meredith, E. S. Platzman and R. E. White (2005), Pore fabric shape anisotropy in porous sandstones and its relation to elastic wave velocity and permeability anisotropy under hydrostatic pressure, Int. J. Rock Mech. Min. Sci., 42, 890-899.
Benson, P. M., A. Schubnel, S. Vinciguerra, C. Trovato, P. G. Meredith and R. P. Young (2006), Modeling the permeability evolution of microcracked rocks from elastic wave velocity inversion at elevated isostatic pressure, J. Geophys. Res., 111, B04202, doi: 10.1029/2005JB003710.
Benson, P. M., A. B. Thompson, P. G. Meredith, S. Vinciguerra and R. P. Young (2007), Imaging slow failure in triaxially deformed Etna basalt using 3D acoustic-emission location and X-ray computed tomography, Geophys. Res. Lett., 34, doi: 10.1029/2006GL028721.
Benson, P. M., S. Vinciguerra, P. G. Meredith and R. P. Young (2008), Laboratory simulation of volcano seismicity, Science, 322, 249-252.
Bernabé, Y. (1986), The Effective Pressure Law for Permeability in Chelmsford Granite and Barre Granite, Int. J. Rock Mech. Min. Sci. Geomech. Abstr., 23, No. 3, 267-275.
Bernabé, Y. and W. F. Brace (1990), Deformation and fracture of Berea sandstone, in The Brittle–Ductile Transition in Rocks, edited by A. G. Duba, W. B. Durham, J. Handin and H. F. Wang, pp. 91-101, American Geophysical Union Monograph 56,
Berryman, J. G. (1992), Effective Stress for Transport Properties of Inhomogeneous Porous Rock, J. Geophys. Res., 97, No. B12, 17409-17424.
Bieniawski, Z. T. (1967), Mechanism of brittle fracture or rock, Part II - Experimental studies, Int. J. Rock Mech. Min. Sci., 4, 407-423.
Birch, F. (1960), The velocity of compressional waves in rocks to 10 kilobars, 1, J. Geophys. Res., 65, 1083-1102.
Birch, F. (1961), The velocity of compressional waves in rocks to 10 kilobars, 2, J. Geophys. Res., 66, 2199-2224.

Boitnott, G. N. and C. H. Scholz (1990), Direct Measurement of the Effective Pressure Law: Deformation of Joints Subject to Pore and Confining Pressures, J. Geophys. Res., 95, No. B12, 19279-19298.
Bonaccorso, A. (2004), Mount Etna: Volcano Laboratory, edited by Bonaccorso, A., Calvari, S., Coltelli, M., Del Negro, C. and Falsaperla, S., American Geophysical Union Geophysical Monograph 143.
Bonaccorso, A., S. D'Amico, S. Mattia and D. Patane (2004), Intrusive mechanisms at Mt. Etna forerunning the July-August 2001 eruption from seismic and ground deformation data, Pure Appl. Geophys, 161, 1469-1487.
Bonaccorso, A. and P. M. Davis (1999), Models of ground deformation from vertical volcanic conduits with application to eruptions of Mount St. Helens and Mount Etna, J. Geophys. Res., 104, 10531-10542.
Bonaccorso, A., F. Ferrucci, D. Patane and L. Villari (1996), Fast deformation processes and eruptive activity at Mount Etna (Italy), J. Geophys. Res., 101, 17467-17480.
Brace, W. F. (1964), Brittle fracture of rocks, in State of stress in the Earth's crust, edited by W. R. Judd, pp. Elsevier, New York.
Brace, W. F. (1978), A Note on Permeability Changes in Geologic Material Due to Stress, Pure Appl. Geophys, 116, 627-633.
Brace, W. F. and R. J. Martin (1968), A test of the law of effective stress for crystalline rocks of low porosity Int. J. Rock Mech. Min. Sci. Geomech. Abstr., 5, 415-426.
Brace, W. F., B. W. Paulding and C. H. Scholz (1966), Dilatancy in the Fracture of Crystalline Rocks, J. Geophys. Res., 71, 3939-3953.
Branca, S., D. Carbone and F. Greco (2003), Intrusive mechanism of the 2002 NE-Rift eruption at Mt. Etna (Italy) inferred through continuous microgravity data and volcanological evidences, Geophys. Res. Lett., 30, 2077.
Brusca, L., A. Aiuppa, W. D. D'Alessandro, F. Parello, P. Allard and A. Michel (2001), Geochemical mapping of magmatic gas-water-rock interactions in the aquifer of Mount Etna volcano, J. Vol. Geotherm. Res., 108, 199-218.
Burlini, L., S. Vinciguerra, G. Di Toro, G. De Natale, P. G. Meredith and J.-P. Burg (2007), Seismicity preceding volcanic eruptions: new experimental insights, Geology, 35, 183-186.
Burton, M. R., M. Neri, D. Andronico, S. Branca, T. Caltabiano, S. Calvari, R. A. Corsaro, P. Del Carlo, G. Lanzafame, L. Lodato, L. Miraglia, G. Salerno and L. Spampinato (2005), Etna 2004–2005: An archetype for geodynamically-controlled effusive eruptions, 32, L09303, doi: 10.1029/2005GL022527.
Byerlee, J. (1967), Frictional Characteristics of Granite under High Confining Pressure, J. Geophys. Res., 72, 3639-3648.
Byerlee, J. (1978), Friction of rocks, Pageoph, 116, 615-626.
Carbone, D. and F. Greco (2007), Review of Microgravity Observations at Mt. Etna: A Powerful Tool to Monitor and Study Active Volcanoes, Pure Appl. Geophys, 164, 769-790.
Castellano, M., M. F. Bianco, S. Imposa, G. Milano, S. Menza and G. Vilardo (1997), Recent deep earthquake occurrencce at Mt. Etna (Sicily, Italy), Phys. Earth Planet. Int., 102, 227-289.
Cayol, V. and F. H. Cornet (1998), Effects of topography on the interpretation of the deformation field of prominent volcanoes - Application to Etna, Geophys. Res. Lett., 25, 1979-1982.
Chang, C. and B. Haimson (2000), True triaxial strength and deformability of the German Continental Deep Drilling Program (KTB) deep hole amphibolite, J. Geophys. Res., 105, 18999-19014.
Charles, R. J. (1958), Static fatigue of glass, J. Appl. Phys., 29, 1549-1560.
Chester, F. M. (1994), Effects of temperature on friction: constitutive equations and experiments with quartz gouge, J. Geophys. Res., 99, No. B4, 7247-7261.
Chester, F. M. and J. M. Logan (1986), Implications for Mechanical Properties of Brittle Faults from Observations of the Punchbowl Fault Zone, California, Pure Appl. Geophys, 124, 79-106.
Chmelík, F., P. Lukac, M. Janecek, F. Moll, B. L. Mordike, K.-U. Kainer and T. G. Langdon (2002), An evaluation of the creep characteristics of an AZ91 magnesium alloy composite using acoustic emission, Mat. Sci. Eng., A338, 1-7.

Chuang, T.-J. and E. R. Fuller (1992), Extended Charles–Hillig Theory for Stress Corrosion Cracking of Glass, J. Am. Ceram. Soc., 75, 540-545.
Cook, N. G. W. and K. Hodgson (1965), Some Detailed Stress-Strain Curves for Rock, J. Geophys. Res., 70, No. 12, 2883-2888.
Cornelius, R. R. and P. A. Scott (1993), A Materials Failure Relation of Accelerating Creep as Empirical Description of Damage Accumulation, Rock Mech. Rock Eng., 26 (3), 233-252.
Cornelius, R. R. and B. Voight (1995), Graphical and PC-software analysis of volcano eruption precursors according to the Materials Failure Forecast Method (FFM), J. Vol. Geotherm. Res., 64, 295-320.
Cornet, F. H. and B. Valette (1984), In Situ Stress Determination From Hydraulic Injection Test Data, J. Geophys. Res., 89, No. B13, 11,527-511,537.
Costin (1987), Time-dependent deformation and failure, in Fracture Mechanics of Rock, edited by B. K. Atkinson, pp. 167–216, Academic Press, London.
Cottrell, A. H. (1996), Andrade creep, Phil. Mag. Lett., 73, 35-37.
Cottrell, A. H. (1997), Logarithmic and Andrade creep, Phil. Mag. Lett., 75, 301-307.
Cox, S. J. D. and P. G. Meredith (1993), Microcrack formation and material softening in rock measured by monitoring acoustic emissions, Int. J. Rock Mech. Min. Sci. Geomech. Abstr., 30, 11-24.
Crampin, S., R. Evans and B. K. Atkinson (1984), Earthquake prediction: a new physical basis Geophys. J. Int., 76, 147-156.
Cruden, D. M. (1974), Static fatigue of brittle rock under uniaxial compression, Int. J. Rock Mech. Min. Sci., 11, 67-73.
Curran, J. H. and M. M. Carroll (1979), Shear Stress Enhancement of Void Compaction, J. Geophys. Res., 84, 1105-1112.
Dally, J. W. and W. F. Riley (1991), Experimental stress analysis, McGraw-Hill, New York.
Das, S. and C. H. Scholz (1981), Theory of Time-Dependent Rupture in the Earth, J. Geophys. Res., 86, 6039-6051.
Dennis, S. M. and B. K. Atkinson (1982), The influence of water on the stress supported by experimentally faulted Westerly granite, Geophys. J. Int., 71, 285-294.
Dewers, T. and A. Hajash (1995), Rate laws for water-assisted compaction and stress-induced water-rock interaction in sandstones, J. Geophys. Res., 100, 13093-13112.
Di Toro, G., D. L. Goldsby and T. E. Tullis (2004), Friction falls towards zero in quartz rock as slip velocity approaches seismic rates, Nature, 427, 436-439.
Diederichs, M. S. and P. K. Kaiser (1999), Tensile strength and abutment relaxation as failure control mechanisms in underground excavations, Int. J. Rock Mech. Min. Sci., 36, 69-96.
Dunning, J. D., B. Douglas, M. Miller and S. McDonald (1994), The Role of the Chemical Environment in Frictional Deformation: Stress Corrosion Cracking and Comminution, Pure Appl. Geophys, 143, 151-178.
Dunning, J. D., W. L. Lewis and D. E. Durr (1980), Chemomechanical weakening in the presence of surfactants, J. Geophys. Res., 85, 5344-5354.
Dutton, R. (1974), The propagation of cracks by diffusion, in Fracture Mechanics of Ceramics, Volume 2, edited by R. C. Bradt, D. P. H. Hasselman and F. F. Lange, pp. 649-657, Plenum Press, New York.
Eberhardt, E., D. Stead and B. Stimpson (1999), Quantifying progressive pre-peak brittle fracture damage in rock during uniaxial compression, Int. J. Rock Mech. Min. Sci., 36, 361-380.
Eccles, D. (2005), Laboratory Electrical Studies on the Thermo-Chemo-Mechanics of Faults and Fault Slip, PhD thesis, University College London.
Eccles, D., P. R. Sammonds and O. C. Clint (2005), Laboratory studies of electrical potential during rock failure Int. J. Rock Mech. Min. Sci., 42, 933-949.
Evans, A. G. (1972), A method for evaluating the time-dependent failure characteristics of brittle materials - and its application to polycrystalline alumina, J. Mat. Sci., 7, 1137-1146.

Evans, A. G. (1974), Slow crack growth in brittle materials under dynamic loading conditions, Int. J. Fracture, 10, 251-259.
Evans, A. G. and W. Blumenthal (1983), High temperature failure in ceramics in Fracture Mechanics of Ceramics, Volume 6, edited by R. C. Bradt, A. G. Evans, D. P. H. Hasselman and F. F. Lange, pp. Plenum Press, New York.
Evans, B., J. T. Frederich and T.-F. Wong (1990), The brittle-ductile transition in rocks: recent experimental and theoretical progress, in The brittle-ductile transition in rocks. The Heard volume, edited by A. G. Duba, W. B. Durham, J. Handin and H. F. Wang, pp. 1-20, American Geophysical Union, Geophys Monograph 56, Washington.
Fairhurst, C. (1965), Measurement of in-situ stresses with particular reference to hydraulic fracturing, Felsmech Ingenieurgeol II, 3-4, 129-147.
Fairhurst, C. (2003), Stress estimation in rock: a brief history and review, Int. J. Rock Mech. Min. Sci., 40, 957-973.
Faulkner, D. R., A. C. Lewis and E. H. Rutter (2003), On the internal structure and mechanics of large strike-slip fault zones: field observations of the Carboneras fault in southeastern Spain, Tectonophysics, 367, 235-251.
Faulkner, D. R., T. M. Mitchell, D. Healy and M. J. Heap (2006), Slip on 'weak' faults by the rotation of regional stress in the fracture damage zone, Nature, 444, 922-925.
Fortin, J., A. Schubnel and Y. Gueguen (2005), Elastic wave velocities and permeability evolution during compaction of Bleurswiller sandstone, Int. J. Rock Mech. Min. Sci., 42, 873-889.
Fortin, J., S. Stanchits, G. Dresen and Y. Gueguen (2006), Acoustic emission and velocities associated with the formation of compaction bands in sandstone, J. Geophys. Res., 111, doi: 10.1029/2005JB003854.
Fowler, C. M. R. (2005), The Solid Earth: An Introduction to Global Geophysics, Cambridge University Press, Cambridge.
Francois, D. and T. R. Wilshaw (1968), The Effect of Hydrostatic Pressure on the Cleavage Fracture of Polycrystalline Materials, J. Appl. Phys., 39, doi: 10.1063/1.1656943.
Freiman, S. W. (1974), Effect of Alcohols on Crack Propagation in Glass, J. Am. Ceram. Soc., 57, 350-353.
Freiman, S. W. (1984), Effects of the Chemical Environment on Slow Crack Growth in Glasses and Ceramics, J. Geophys. Res., 89, 4072-4077.
Fyfe, W. S., N. J. Price and A. B. Thompson (1978), Fluids in the Earth's crust, Elservier, Amsterdam.
Gangi, A. F. and R. L. Carlson (1995), An asperity-deformation model for effective pressure Tectonophysics, 256, 241-251.
Gehrke, E., C. Ullner and M. Hahnert (1991), Fatigue limit and crack arrest in alkalicontaining silicate glasses, J. Mat. Sci., 26, 5445-5455.
Gephart, J. W. and D. W. Forsyth (1984), An Improved Method for Determining the Regional Stress Tensor Using Earhtquake Focal Mechanism Data: Application to the San Fernando Earthquake Sequence, J. Geophys. Res., 89, 9305-9320.
Glover, P. W. J., P. Baud, M. Darot, P. G. Meredith, S. Boon, A., M. LeRevelec, S. Zoussi and T. Reuschle (1995), α/β phase transition in quartz monitored using acoustic emissions., Geophys. J. Int., 120, 775-782.
Glover, P. W. J., J. B. Gomez, P. G. Meredith, S. Boon, A., P. R. Sammonds and S. A. F. Murrell (1996), Modelling the stress-strain behaviour of saturated rocks undergoing triaxial deformation using complex electrical conductivity measurements Surveys in Geophysics, 17, 307-330.
Goldsby, D. L. and T. E. Tullis (2002), Low frictional strength of quartz rocks at subseismic slip rates, Geophys. Res. Lett., 29, doi: 10.1029/2002GL015240.
Grenet, L. (1899), Mechanical strength of glass, Bull. Soc. Enc. Industr. Nat. Paris (Ser. 5), 4, 838-848.
Griffith, A. A. (1920), The phenomenon of rupture and flow in solids, Royal Soc. Phil. Series A, 221, 163-198.

Griffith, A. A. (1924), The theory of rupture, in Proc Int Cong Appl Mech. Delft: Tech Boekhandel en Drukkerij J Walter Jr, edited by B. C. B. and B. J. M., pp. 54-63.
Griggs, D. (1939), Creep of Rocks, J. Geol., 47, 225-251.
Griggs, D. (1940), Experimental flow of rocks under conditions favoring recrystallization, Bull. Seis. Soc. Am., 51, 1001-1022.
Griggs, D. and J. Handin (1960), Rock Deformation, Geological Society of America Memoir 79.
Gueguen, Y. and A. Schubnel (2003), Elastic wave velocities and permeability of cracked rocks, Tectonophysics, 370, 163-176.
Guest, J. E. (1982), Styles of eruption and flow morphology on Mt. Etna, Mem. Soc. Geol. It., 23, 49-73.
Guin, J.-P. and S. M. Wiederhorn (2003), Crack growth threshold in soda lime silicate glass: role of hold-time, J. Non-Cryst. Solids, 316, 12-20.
Hadizadeh, J. and R. D. Law (1991), Water-weakening of Sandstone and Quartzite Deformed at Various Stress and Strain Rates, Int. J. Rock Mech. Min. Sci. Geomech. Abstr., 28, 431-439.
Haimson, B. (2006), True Triaxial Stresses and the Brittle Fracture of Rock, Pure Appl. Geophys, 163, 1101-1130.
Haimson, B. and C. Chang (2000), A new true triaxial cell for testing mechanical properties of rock, and its use to determine rock strength and deformability of Westerly granite Int. J. Rock Mech. Min. Sci., 37, 285-296.
Haimson, B. and C. Chang (2002), True triaxial strength of the KTB amphibolite under borehole wall conditions and its use to estimate the maximum horizontal in situ stress, J. Geophys. Res., 107, No. B10, doi: 10.1029/2001JB000647.
Handin, J., R. V. Hager, M. Friedman and J. N. Feather (1963), Experimental deformation of sedimentary rock under confining pressure: pore pressure effects, AAPG Bull., 47, 717-755.
Handin, J., H. C. Heard and J. N. Magouirk (1967), Effects of the Intermediate Principal Stress on the Failure of Limestone, Dolomite, and Glass at Different Temperatures and Strain Rates, J. Geophys. Res., 72, No. 2, 611-640.
Hawkes, I. and M. Mellor (1970), Uniaxial testing in rock mechanics laboratories, Eng. Geol., 4, 177-285.
Healy, D. (2008), Damage patterns, stress rotations and pore fluid pressures in strike-slip fault zones, J. Geophys. Res., 113, B12407, doi: 10.1029/2008JB005655.
Healy, D., R. R. Jones and R. E. Holdsworth (2006), Three-dimensional brittle shear fracturing by tensile crack interaction, Nature, 439, doi: 10.1038/nature04346.
Heap, M. J. and D. R. Faulkner (2008), Quantifying the evolution of static elastic properties as crystalline rock approaches failure, Int. J. Rock Mech. Min. Sci., 45, 564-573.
Heard, H. C. (1960), Transition from brittle fracture to ductile flow in Solenhofen limestone as a function of temperature, confining pressure, and interstitial fluid pressure, in Rock Deformation, edited by D. Griggs and J. Handin, pp. 193-226, (Geol. Soc. Am. Memoir 79).
Heggheim, T., M. V. Madland, R. Risnes and T. Austad (2005), A chemical induced enhanced weakening of chalk by seawater, J. Pet. Sci. Eng., 46, 171-184.
Heidbach, O., M. Tingay, A. Barth, J. Reinecker, D. Kurfess and B. Muller (2008), The release 2008 of the World Stress Map (available online at www.world-stress-map.org).
Hellmann, R., P. J. N. Renders, J.-P. Gratier and R. Guiguet (2002), Experimental pressure solution compaction of chalk in aqueous solutions Part 1. Deformation behavior and chemistry, in Water-rock interactions, ore deposits, and environmental geochemistry; a tribute to David A. Crerar, edited by R. Hellmann and S. A. Wood, pp. 129-152, The Geochemical Society, Special Publication No. 7, St. Louis, MO, USA.
Hénaux, S. and F. Creuzet (1997), Kinetic fracture of glass at the nanometer scale, J. Mat. Sci. Lett., 16, 1008-1011.
Hickman, S. H. and B. Evans (1987), Influence of geometry upon crack healing rate in calcite Phys. Chem. Earth (A), 15, 1432-2021.
Hillig, W. B. and R. J. Charles (1965), Surfaces, stress-dependent reactions, and strength, in High Strength Materials, edited by V. F. Zackay, pp. 682-705, John Wiley and Sons, New York.

Hirata, T., T. Satoh and K. Ito (1987), Fractal structure of spatial distribution of microfracturing in rock, Geophys. J. Int., 90, 369-374.
Hirth, G. and J. Tullis (1994), The brittle-plastic transition in experimentally deformed quartz aggregates, J. Geophys. Res., 99, No. B6, 11731-11747.
Holcomb, D. J. (1993), General theory of the Kaiser effect, Int. J. Rock Mech. Min. Sci., 30, 929-935.
Inglis, C. G. (1913), Stresses in a plastic due to presence of cracks and sharp corners, Trans. Inst. Naval Architects, 55, 219.
Irwin, G. R. (1958), Fracture, in Handbuch der Physik, edited by S. Flugge, pp. 551-591, Springer, Berlin.
Irwin, G. R. and R. de Wit (1983), A summary of fracture mechanics concepts, J. Test Eval., 11, 56-65.
Isacks, B., J. Oliver and L. R. Sykes (1968), Seismology and the New Global Tectonics, J. Geophys. Res., 73, 5855-5899.
Ito, S. and M. Tomozawa (1982), Crack Blunting of High-Silica Glass, J. Am. Ceram. Soc., 65, 368-371.
Jaeger, J., N. G. W. Cook and R. Zimmerman (2007), Fundamentals in Rock Mechanics (4th Edition), Blackwell Publishing, London.
Jaeger, J. C. (1969), Elasticity, fracture and flow, Chapman and Hall, London.
Kaiser, L. (1953), Erkenntnisse und Folgerungen aus der Messung von Geräuschen bei Zugbeanspruchung von metallischen Werkstoffen. Arch. für das Eisenhüttenwesen 24, pp. 43-45.
Karunaratne, B. S. B. and M. H. Lewis (1980), High-temperature fracture and diffusional deformation mechanisms in Si-AI-O-N ceramics, J. Mat. Sci., 15, 449-462.
Kato, N., K. Yamamoto, H. Yamamoto and T. Hirasawa (1993), A Stress-Corrosion Model for Strain-rate Dependence of the Frictional Strength of Rocks, Int. J. Rock Mech. Min. Sci. Geomech. Abstr., 30, 551-554.
Kehle, R. O. (1964), The Determination of Tectonic Stresses through Analysis of Hydraulic Well Fracturing, J. Geophys. Res., 69, 259-273.
Kilburn, C. R. J. (2003), Multiscale fracturing as a key to forecasting volcanic eruptions J. Vol. Geotherm. Res., 125, 271-289.
Kilburn, C. R. J. and B. Voight (1998), Slow rock fracture as eruption precursor at Soufriere Hills volcano, Montserrat Geophys. Res. Lett., 25, 3665–3668.
Klein, E., P. Baud, T. Reuschle and T.-F. Wong (2001), Mechanical Behaviour and Failure Mode of Bentheim Sandstone Under Triaxial Compression, Phys. Chem. Earth (A), 26, 21-25.
Kocer, C. and R. E. Collins (2001), Measurement of Very Slow Crack Growth in Glass, J. Am. Ceram. Soc., 84, 2585-2593.
Kranz, R. (1980), The Effect of Confining Pressure and Stress Difference on Static Fatigue of Granite, J. Geophys. Res., 85, 1854-1866.
Kranz, R., W. J. Harris and N. L. Carter (1982), Static fatigue of granite at 200^{o}C, Geophys. Res. Lett., 9, 1-4.
Kranz, R. and C. H. Scholz (1977), Critical dilatant volume of rocks at the onset of tertiary creep, J. Geophys. Res., 82, 4893-4898.
Kwon, O., A. K. Kronenberg, A. F. Gangi and B. Johnson (2001), Permeability of Wilcox shale and its effective pressure law, J. Geophys. Res., 106, No. B9, 19339-19353.
Lajtai, E. Z., R. H. Schmidtke and L. P. Bielus (1987), The Effect of Water on the Deformation and Fracture Time-dependent of a Granite, Int. J. Rock Mech. Min. Sci. Geomech. Abstr., 24, 247-255.
Lamb, T. W. and R. V. Whitman (1969), Soil Mechanics, John Wiley & Sons, New York.
Lankford, J. (1979), Uniaxial Compressive Damage in α-SiC at Low Homologous Temperatures, J. Am. Ceram. Soc., 62, 310-312.
Lankford, J. (1981), The Role of Tensile Microfracture in the Strain Rate Dependence of Compressive Strength of Fine-Grained Limestone Analogy with Strong Ceramics, Int. J. Rock Mech. Min. Sci. Geomech. Abstr., 18, 173-175.
Lau, J. S. O. and N. A. Chandler (2004), Innovative laboratory testing, Int. J. Rock Mech. Min. Sci., 41, 1427-1445.

Lavrov, A. (2003), The Kaiser effect in rocks: principals and stress estimation techniques, Int. J. Rock Mech. Min. Sci., 40, 151-171.
Lawn, B. (1993), Fracture of Brittle Solids, Cambridge University Press, Cambridge.
Leeman, E. R. (1964), The measurement of stress in rock; part I, the principles of rock stress measurements; part II, borehole rock stress measuring instruments, J. S. Afr. Inst. Min. Metall., 65, 45-114.
Lei, X., K. Kusunose, M. V. M. S. Rao, O. Nishizawa and T. Satoh (2000), Quasi-static fault growth and cracking in homogeneous brittle rock under triaxial compression using acoustic emission monitoring, J. Geophys. Res., 105, 6127-6139.
Lei, X., K. Masuda, O. Nishizawa, L. Jouniaux, L. Liu, W. Ma, T. Satoh and K. Kusunose (2004), Detailed analysis of acoustic emission activity during catastrophic fracture of faults in rock, J. Struct. Geol., 26, 247-258.
Li, C. and E. Nordlund (1993), Experimental Verification of the Kaiser Effect in Rocks, Rock Mech. Rock Eng., 26, 333-351.
Li, Y. and C. Xia (2000), Time-dependent tests on intact rocks in uniaxial compression Int. J. Rock Mech. Min. Sci., 37, 467-475.
Lockner, D. (1993), The Role of Acoustic Emission in the Study of Rock Fracture, Int. J. Rock Mech. Min. Sci. Geomech. Abstr., 30, 883-889.
Lockner, D. (1993), Room temperature creep in saturated granite, J. Geophys. Res., 98, 475-487.
Lockner, D. (1998), A generalized law for brittle deformation of Westerly granite, J. Geophys. Res., 103, 5107-5123.
Lockner, D. and J. Byerlee (1975), Acoustic emission and creep in rock at high confining pressure and differential stress Bull. Seis. Soc. Am., 67, 247-258.
Lockner, D. and J. Byerlee (1992), Fault growth and acoustic emissions in confined granite, Appl. Mech. Rev., 45, 165-173.
Lockner, D., J. Byerlee, V. Kuksenko, A. Ponomarev and A. Sidorin (1991), Quasi-static fault growth and shear fracture energy in granite, Nature, 350, 39-42.
Lockner, D., J. Byerlee, V. Kuksenko, A. Ponomarev and A. Sidorin (1992), Observations of Quasistatic Fault Growth from Acoustic Emissions, in Fault Mechanics and Transport Properties in Rock edited by J. R. Rice, B. Evans and T.-F. Wong, pp. 3-31, Academic Press, London.
Logan, J. M., C. A. Dengo, N. G. Higgs and Z. Z. Wang (1992), Fabrics of experimental fault zones: their development and relationship to mechanical behavior, in Fault Mechanics and Transport Properties of Rocks, edited by B. Evans and T.-F. Wong, pp. 33-69, Academic Press, New York.
Lombardo, G. and C. Cardaci (1994), The seismicity of the Etnean area and different features of observed seismic sequences, Acta. Vulcanol., 5, 155-163.
Louis, L., C. David and P. Robion (2003), Comparison of the anisotropic behaviour of undeformed sandstones under dry and saturated conditions Tectonophysics, 370, 193-212.
Lungarini, L., C. Troise, M. Meo and G. De Natale (2005), Finite element modelling of topographic effects on elastic ground deformation at Mt. Etna, J. Vol. Geotherm. Res., 144, 257-271.
Maes, C., A. Van Moffaert, H. Frederix and H. Strauven (1998), Criticality in creep experiments on cellular glass, Phys. Rev. B, 57, 4987-4990.
Main, I. G. (1999), Applicability of time-to-failure analysis to accelerated strain before earthquakes and volcanic eruptions, Geophys. J. Int., 139, F1-F6.
Main, I. G. (2000), A damage mechanics model for power-law creep and earthquake aftershock and foreshock sequences Geophys. J. Int., 142, 151-161.
Main, I. G. and P. G. Meredith (1991), Stress corrosion constitutive laws as a possible mechanism of intermediate-term and short-term seismic quiescence, Geophys. J. Int., 107, 363-372.
Main, I. G., P. G. Meredith and P. R. Sammonds (1992), Temporal variations in seismic event rate and b-values from stress corrosion constitutive laws, Tectonophysics, 211, 233-246.
Main, I. G., P. R. Sammonds and P. G. Meredith (1993), Application of a modified Griffith criterion to the evolution of fractal damage during compressional rock failure, Geophys. J. Int., 115, 367-380.

Manconi, A., T. R. Walter and F. Amelung (2007), Effects of mechanical layering on volcano deformation, Geophys. J. Int., 170, 952-958.
Maranini, E. and M. Brignoli (1999), Creep behaviour of a weak rock: experimental characterization, Int. J. Rock Mech. Min. Sci., 36, 127-138.
Martin, C. D. and N. A. Chandler (1994), The progressive fracture of Lac du Bonnet granite, Int. J. Rock Mech. Min. Sci., 31, 643-659.
Martin, R. J. (1972), Time-Dependent Crack Growth in Quartz and its Application to the Creep of Rocks, J. Geophys. Res., 77, No. 8, 1406-1419.
Martin, R. J. and W. B. Durham (1975), Mechanisms of Crack Growth in Quartz, J. Geophys. Res., 80, No. 35, 4837-4844.
Masuda, K. (2001), Effects of water on rock strength in a brittle regime, J. Struct. Geol., 23, 1653-1657.
Masuda, K., H. Mizutani and I. Yamada (1987), Experimental study of strain-rate dependence and pressure dependence of failure properties of granite, J. Phys. Earth, 35, 37-66.
Matsuki, K. and K. Takeuchi (1993), Three-dimensional in situ stress determination by anelastic strain recovery of a rock core Int. J. Rock Mech. Min. Sci. Geomech. Abstr., 30, 1019-1022.
McClintock, F. A. and G. R. Irwin (1965), Plasticity Aspects of Fracture Mechanics, Fracture Toughness Testing and Its Applications (ASTM, Philadelphia, 1965), pp. 84.
McClintock, F. A. and J. B. Walsh (1962), Friction on Griffith cracks under pressure, Proceeding of the 4th US National Congress on Applied Mechanics, 1015-1021.
McGuire, W. J. and C. R. J. Kilburn (1997), Forecasting volcanic events: some contemporary issues, Geol. Rundsch., 86, 439-445.
McTigue, D. F. and P. Segall (1988), Displacements and Tilts from Dip-Slip Faults and Magma Chambers Beneath Irregular Surface Topography, Geophys. Res. Lett., 15, No. 6, 601-604.
Menéndez, B., W. Zhu and T.-F. Wong (1996), Micromechanics of brittle faulting and cataclastic flow in Berea sandstone, J. Struct. Geol., 18, 1-16.
Meredith, P. G. and B. K. Atkinson (1982), High-temperature tensile crack propagation in quartz: Experimental results and application to time-dependent earthquake rupture, Earthquake Predict. Res., 1, 377-391.
Meredith, P. G. and B. K. Atkinson (1983), Stress corrosion and acoustic emission during tensile crack propagation in Whin Sill dolerite and other basic rocks, Geophys. J. Int., 75, 1-21.
Meredith, P. G. and B. K. Atkinson (1985), Fracture toughness and subcritical crack growth during high-temperature tensile deformation of Westerly granite and Black gabbro, Phys. Earth Planet. Int., 39, 33-51.
Meredith, P. G., S. Boon, A., S. Vinciguerra and N. Group (2005), CREEP: Long-term time-dependent rock deformation in a deep-sea laboratory in the Ionian sea: a pilot study, Geophysical Research Abstracts, 7, 06491.
Meredith, P. G., S. Boon, A., S. Vinciguerra, C. R. J. Kilburn and N. Group (2005), Long-term time-dependent rock deformation at constant stress: a mechanism for accelerated deformation preceding volcanic eruptions., Geophysical Research Abstracts, 7, 07793.
Michael, A. J. (1987), Use of focal mechanisms to determine stress: A control study, J. Geophys. Res., 92, 357-369.
Michalske, T. A. (1983), The stress corrosion limit: its measurement and implications, in Fracture Mechanics of Ceramics, Vol. 5, Surface Flaws, Statistics, and Microcracking, edited by R. C. Bradt, A. G. Evans, D. P. H. Hasselman and F. F. Lange, pp. 277-289, Plenum Press, New York.
Michalske, T. A. and B. Bunker, C. (1987), Steric Effects in Stress Corrosion Fracture of Glass, J. Am. Ceram. Soc., doi: 10.1111/j.1151-2916.1987.tb04879.x.
Michalske, T. A. and S. W. Freiman (1982), A molecular interpretation of stress corrosion in silica, Nature, 295, 511-512.
Michalske, T. A. and S. W. Freiman (1983), A Molecular Mechanism for Stress Corrosion in Vitreous Silica, J. Am. Ceram. Soc., 66, 284-288.

Michalske, T. A., W. L. Smith and B. Bunker, C. (1991), Fatigue Mechanisms in High-Strength Silica-Glass Fibers, J. Am. Ceram. Soc., 74, 1993-1996.
Mitchell, T. M. and D. R. Faulkner (2008), Experimental measurements of permeability evolution during triaxial compression of initially intact crystalline rocks and implications for fluid flow in fault zones, J. Geophys. Res., 113, B11412, doi: 10.1029/2008JB005588.
Mogi, K. (1958), Relations between the eruptions of various volcanoes and the deformations of the ground surfaces around them, Bull. Earthq. Res. Inst., Univ. Tokyo, 36, 99-134.
Mogi, K. (1967), Effect of the Intermediate Principal Stress on Rock Failure, J. Geophys. Res., 72, No. 20, 5117-5131.
Mogi, K. (1971), Effect of the triaxial stress system on the failure of dolomite and limestone, Tectonophysics, 11, 111-127.
Mogi, K. (1972), Effect of the triaxial stress system on fracture and flow of rocks, Phys. Earth Planet. Int., 5, 318-324.
Murrell, S. A. F. (1963), A criterion for brittle fracture of rocks and concrete under triaxial stress and the effect of pore pressure on the criterion, in Proc. 5th Rock Mechanics Symp., edited by C. Fairhurst, pp. 563-577, Pergamon, Oxford.
Murrell, S. A. F. (1964), The theory of the propagation of elliptical Grifith cracks under various conditions of plane strain or plane stress: Part I, Brit. J. Appl. Phys., 15, 1195-1210.
Murrell, S. A. F. (1965), The Effect of Triaxial Stress Systems on the Strength of Rocks at Atmospheric Temperatures, Geophys. J. Int., 10, 231-281.
Murrell, S. A. F. and P. J. Digby (1970), The Theory of Brittle Fracture Initiation under Triaxial Stress Conditions, Geophys. J. Int., 19, 309-334.
Nara, Y. and K. Kaneko (2006), Sub-critical crack growth in anisotropic rock, Int. J. Rock Mech. Min. Sci., 43, 437-453.
Ngwenya, B. T., I. G. Main, S. C. Elphick, B. R. Crawford and B. G. D. Smart (2001), A constitutive law for low-temperature creep of water-saturated sandstones, J. Geophys. Res., 106, 21811-21826.
Nishizawa, O. and H. Noro (1990), Self-exciting process of acoustic emission occurrence in steady creep of granite under uniaxial stress, Geophys. Res. Lett., 17, 1521-1524.
Nishizawa, O., K. Onai and K. Kusunose (1984), Hypocenter distribution and focal mechanism of AE events during two stress stage creep in Yugawara andesite, Pure Appl. Geophys, 122, 36-52.
O'Connell, R. J. and B. Budiansky (1974), Seismic velocities in dry and saturated cracked solids, J. Geophys. Res., 79, 5412-5426.
Obreimoff, J. W. (1930), The Splitting Strength of Mica, Proc. Royal Soc. Lon., 127, 290-297.
Obrizzo, F., F. Pingue, C. Troise and G. De Natale (1994), Bayesian inversion of 1994–1998 vertical displacements at Mt Etna: evidence for magma intrusion, Geophys. J. Int., 157, 935-946.
Oda, M., T. Takemura and T. Aoki (2002), Damage growth and permeability change in triaxial compression tests of Inada granite, Mech. Mat., 34,
Ohnaka, M. (1973), The quantitative effect of hydrostatic confining pressure on the compressive strength of crystalline rocks, J. Phys. Earth, 21, 125-140.
Ohnaka, M. (1975), Frictional characteristics of typical rocks, J. Phys. Earth, 23, 87-112.
Ohnaka, M. (1983), Acoustic emission during creep of brittle rock, Int. J. Rock Mech. Min. Sci. Geomech. Abstr., 20, 121-134.
Ohno, N., N. Okamoto, T. Miyake, S. Nishide and S. Masaki Jr (1994), Acoustic emission and fiber damage in creep of unidirectional SCS-6/Ti-15-3 metal matrix composite at 450°C, Scripta Metallurgica et Materialia, 31, 1549-1554.
Ojala, I. O., B. T. Ngwenya, I. G. Main and S. C. Elphick (2003), Correlation of microseismic and chemical properties of brittle deformation in Locharbriggs sandstone, J. Geophys. Res., 108(B5), doi: 10.1029/2002JB002277.
Olson, J. E. (1993), Joint Pattern Development: Effects of Subcritical Crack Growth and Mechanical Crack Interaction, J. Geophys. Res., 98, 12251-12265.

Olsson, W. A. (1991), The Compressive Strength of Tuff as a Function of Strain Rate from 10-6 to 10-3/sec, Int. J. Rock Mech. Min. Sci. Geomech. Abstr., 28, 115-118.
Orowan, E. (1944), The Fatigue of Glass Under Stress, Nature, 154, 341-343.
Orowan, E. (1949), Fracture and strength of solids, Rep. Prog. Phys., 12, 185-232.
Patanè, D., G. Barberi, O. Cocina, P. De Gori and C. Chiarabba (2006), Time-Resolved Seismic Tomography Detects Magma Intrusions at Mount Etna, Science, 313, 821-823.
Patanè, D., O. Cocina, S. Falsaperla, E. Privitera and S. Spampanato (2004), Mt. Etna Volcano: A Seismological Framework, in Mt. Etna: Volcano Laboratory, edited by A. Bonaccorso, S. Calvari, M. Coltelli and S. Falsaperla, pp. 147-166, American Geophysical Union Geophysical Monograph 143.
Patane, D., O. Cocina, S. Falsaperla, E. Privitera, S. Spampinato, A. Bonaccorso, S. Calvari, M. Coltelli, C. Del Negro and S. Falsaperla (2004), Mt. Etna volcano: A seismological framework, in Mt. Etna: Volcano laboratory, edited by pp. 147,
Patanè, D., P. De Gori, C. Chiarabba and A. Bonaccorso (2003), Magma ascent and the pressurization of Mount Etna's volcanic system, Science, 299, 2061-2063.
Patanè, D., A. Montalto, S. Vinciguerra and J. C. Tanguy (1996), A model of the 1991 - 1993 eruption onset of Etna (Italy), Phys. Earth Planet. Int., 97, 231-245.
Paterson, M. S. (1958), Experimental deformation and faulting in Wombeyan marble Bull. Seis. Soc. Am., 69, 465-475.
Paterson, M. S. and T.-F. Wong (2005), Experimental Rock Deformation - The Brittle Field, Springer, New York.
Paul, B. (1968), Macroscopic criteria for plastic flow and brittle fracture, in Fracture. An Advanced Treatise, edited by H. Liebowitz, pp. 313-496,
Poirier, J.-P. (1985), Creep of Crystals: High-Temperature Deformation Processes in Metals, Ceramics and Minerals, Cambridge University Press, Cambridge.
Price, N. J. (1966), Fault and Joint Development in Brittle and Semi-brittle Rock, Pergamon Press, New York.
Puglisi, G., P. Briole, A. Bonforte, A. Bonaccorso, S. Calvari, M. Coltelli, C. Del Negro and S. Falsaperla (2004), Twelve years of ground deformation studies on Mt. Etna volcano based on GPS surveys, in Mt. Etna: Volcano laboratory, edited by pp. 321,
Read, M. D., M. R. Ayling, P. G. Meredith and S. A. F. Murrell (1995), Microcracking during triaxial deformation of porous rocks monitored by changes in rock physical properties, II. Pore volumometry and acoustic emission measurements on water-saturated rocks Tectonophysics, 245, 223-235.
Reches, Z. and D. Lockner (1994), Nucleation and growth of faults in brittle rocks, J. Geophys. Res., 99, No. B9, 18159-18173.
Rehbinder, P. A. (1948), Hardness reducers in drilling (translated from Russian), CSIR, Melbourne.
Renshaw, C. E. and D. D. Pollard (1994), Numerical simulation of fracture set formation: A fracture mechanics model consistent with experimental observations, J. Geophys. Res., 99, 9359-9372.
Reuschle, T., S. Gbaguidi Haore and M. Darot (2003), Microstructural control on the elastic properties of thermally cracked granite, Tectonophysics, 370, 95-104.
Rice, J. R. (1968), Mathematical analysis in the mechanics of fracture, in Fracture, edited by H. Liebowitz, pp. 191-311, Academic Press, New York.
Rice, J. R. (1968), A path independent integral and the approximate analysis of strain concentration by notches and cracks, J. Appl. Mech., 34, 379-386.
Roa, M. V. M. S. and Y. V. Ramana (1992), A Study of Progressive Failure of Rock Under Cyclic Loading by Ultrasonic and AE Monitoring Techniques, Rock Mech. Rock Eng., 25, 237-251.
Robin, P. Y. F. (1973), Note on effective pressure, J. Geophys. Res., 78, 2434-2437.
Rocchi, V. (2002), Fracture of Basalts under Simulated Volcanic Conditions, PhD thesis, University College London.

Rocchi, V., P. R. Sammonds and C. R. J. Kilburn (2004), Fracturing of Etnean and Vesuvian rocks at high temperatures and low pressures, J. Vol. Geotherm. Res., 132, 137-157.
Rudnicki, J. W. (1980), Fracture mechanics applied to the Earth's crust, Ann. Rev. Earth. Planet Sci., 8, 489-525.
Rummel, F. and C. Fairhurst (1970), Determination of the post-failure behavior of brittle rock using a servo-controlled testing machine Rock Mech. Rock Eng., 2, 189-204.
Rutter, E. H. (1972), The Effects of Strain-Rate Changes on the Strength and Ductility of Solenhofen Limestone at Low Temperatures and Confining Pressures, Int. J. Rock Mech. Min. Sci. Geomech. Abstr., 1972, 183-189.
Rutter, E. H. (1995), Experimentals tudyo f the influenceo f stress,t emperature,a nd strain on the dynamic recrystallization of Carrara marble, J. Geophys. Res., 100, No. B12, 24651-24663.
Rutter, E. H. (1999), On the relationship between the formation of shear zones and the form of the flow law for rocks undergoing dynamic recrystallization, Tectonophysics, 303, 147-158.
Rutter, E. H. and D. H. Mainprice (1978), The Effect of Water on Stress Relaxation of Faulted and Unfaulted Sandstone, Pageoph, 116, 634-654.
Sammonds, P. R., P. G. Meredith and I. G. Main (1992), Role of pore fluids in the generation of seismic precursors to shear fracture, Nature, 359, 228-230.
Sano, O., I. Ito and M. Terada (1981), Influence of Strain Rate on Dilatancy and Strength of Oshima Granite Under Uniaxial Compression, J. Geophys. Res., 86, No. B10, 9299-9311.
Savalli, L. and T. Engelder (2005), Mechanisms controlling rupture shape during subcritical growth of joints in layered rocks, GSA Bulletin, 117, 436-449.
Sayers, C. M. and M. Kachanov (1995), Microcrack induced elastic wave anisotropy in brittle rocks, J. Geophys. Res., 100, 4149-4156.
Scholz, C. H. (1968), The frequency-magnitude relation of microfracturing in rock and its relation to earthquakes, Bull. Seis. Soc. Am., 58, 399-415.
Scholz, C. H. (1968), Microfractures, aftershocks, and seismicity, Bull. Seis. Soc. Am., 58, 1117-1130.
Scholz, C. H. (1972), Static fatigue of quartz, J. Geophys. Res., 77, 2104-2114.
Scholz, C. H. (2002), The mechanics of earthquakes and faulting, Cambridge Press, Cambridge.
Shimamoto, T. and A. Tsutsumi (1994), A new rotary-shear high-speed frictional testing machine: its basic design and scope of research (in Japanese with English abstract), J. Tectonic. Res. Group of Japan, 39, 65-78.
Sigurdsson, H. and S. R. J. Sparks (1978), Lateral magma flow within rifted Icelandic crust, Nature, 274, 126-130.
Simmons, C. J. and S. W. Freiman (1981), Effect of Corrosion Processes on Subcritical Crack Growth in Glass, J. Am. Ceram. Soc., 64, 683-686.
Skempton, A. W. (1961), Effective stress in soils, concrete and rock, In Proceedings of the Butterworth conference on pore pressure and suction in soils, London.
Soga, N., H. Mizutani, H. Spetzlet and R. J. I. Martin (1978), The effect of dilatancy on velocity anisotropy in Westerly granite, J. Geophys. Res., 83, 4451-4458.
Sotin, C. and J.-P. Poirier (1984), Analysis of high-temperature creep experiments by generalized nonlinear inversion, Mech. Mat., 3, No. 4, 311-317.
Stanchits, S., S. Vinciguerra and G. Dresen (2006), Ultrasonic Velocities, Acoustic Emission Characteristics and Crack Damage of Basalt and Granite, Pure Appl. Geophys, 163, 975-994.
Swain, M. V., J. S. Williams, B. Lawn and J. J. H. Beek (1973), A comparative study of the fracture of various silica modifications using teh Hertzian test, J. Mat. Sci., 8, 1153-1164.
Swanson, P. L. (1984), Subcritical Crack Growth and Other Time- and Environment-Dependent Behavior in Crustal Rocks, J. Geophys. Res., 89, 4137-4152.
Takemura, T. and M. Oda (2005), Changes in crack density and wave velocity in association with crack growth in triaxial tests of Inada granite, J. Geophys. Res., 110, B05401, doi: 10.1029/2004JB003395.

Tanguy, J. C., M. Condomines and G. Kieffer (1997), Evolution of the Mount Etna magma: Constraints on the present feeding system and eruptive mechanism, J. Vol. Geotherm. Res., 75, 221-250.
Terzaghi, K. (1943), Theoretical Soil Mechanics, John Wiley and Sons, New York.
Thompson, B. D., R. P. Young and D. Lockner (2006), Fracture in Westerly Granite under AE Feedback and Constant Strain Rate Loading: Nucleation, Quasi-static Propagation, and the Transition to Unstable Fracture Propagation, Pure Appl. Geophys, 163, 995-1019.
Townend, E., B. D. Thompson, P. M. Benson, P. G. Meredith, P. Baud and R. P. Young (2008), Imaging compaction band propagation in Diemelstadt sandstone using acoustic emission locations, 35, doi: 10.1029/2008GL034723.
Trasatti, E., C. Giunchi and N. P. Agostinetti (2008), Numerical inversion of deformation caused by pressure sources: application to Mount Etna (Italy), Geophys. J. Int., 172, 873-884.
Tsutsumi, A. and T. Shimamoto (1997), High-velocitfyr ictionapl ropertieosf gabbro, Geophys. Res. Lett., 24, No. 6, 699-702.
Tullis, J. and R. A. Yund (1992), The brittle-ductile transition in feldspar aggregates: An experimental study, in Fault Mechanics and Transport Properties of Rocks, edited by B. Evans and T.-F. Wong, pp. 89-117, Academic Press, New York.
Tullis, T. E., F. G. Horowitz and J. Tullis (1991), Flow Laws of Polyphase Aggregates from End-Member Flow Laws, J. Geophys. Res., 96, No. B5, 8081-8096.
Twiss, R. J. and E. M. Moores (1992), Structural Geology, WH Freeman, New York.
Underwood, E. E. (1970), Quantitative stereology, Addison Wesley, Reading.
Vinciguerra, S. (1999), Seismic scaling exponents as a tool in detecting stress corrosion crack growth leading to the September-October 1989 flank eruption at Mt. Etna volcano, Geophys. Res. Lett., 26, 3685-3688.
Vinciguerra, S. (2002), Damage mechanics preceding the September-October 1989 flank eruption at Mount Etna volcano inferred by seismic scaling exponents, J. Vol. Geotherm. Res., 113, 391-397.
Vinciguerra, S., V. Latora, S. Bocciato and R. T. Kamimura (2001), Identifying and discriminating seismic patterns leading flank eruptions at Mt. Etna Volcano during 1981-1996, J. Vol. Geotherm. Res., 106, 211-228.
Vinciguerra, S., C. Trovato, P. G. Meredith and P. M. Benson (2005), Relating seismic velocities, thermal cracking and permeability in Mt. Etna and Iceland basalts, Int. J. Rock Mech. Min. Sci., 42, 900-910.
Vinciguerra, S., C. Trovato, P. G. Meredith, P. M. Benson, C. Troise and G. De Natale (2006), Understanding the seismic velocity structure of Campi Flegrei caldera (Italy): from the laboratory to the field scale, Pure Appl. Geophys, 163, 2205-2221.
Voight, B. (1988), A method for prediction of volcanic eruptions, Nature, 332, 125-130.
Voight, B. (1989), A Relation to Describe Rate-Dependent Material Failure, Science, 243, 200-203.
Vutukuri, V. S., R. D. Lama and S. S. Saluja (1974), Handbook on mechanical properties of rocks: testing techniques and results, Trans Technical Publications, Ohio.
Walker, A. N., E. H. Rutter and B. K. H. (1990), Experimental study of grain-size sensitive flow of synthetic, hotpressed calcite rocks, in Deformation Mechanisms, Rheology and Tectonics, edited by R. J. Knipe and E. H. Rutter, pp. 259-284, Geological Society Special Publication.
Walsh, J. B. (1965), The effect of cracks on the compressibility of rock, J. Geophys. Res., 70, 381-389.
Wawersik, W. R. and W. F. Brace (1971), Post-failure behavior of a granite and diabase Rock Mech. Rock Eng., 3, 61-85.
Wawersik, W. R. and W. S. Brown (1973), Creep fracture in rock, Utah University Salt Lake City Department of Mechanical Enginnering, Final report. 28 Dec 71-28 Jul 73.
Wawersik, W. R. and C. Fairhurst (1970), A study of brittle rock fracture in laboratory compression experiments, Int. J. Rock Mech. Min. Sci., 7, 561-575.
Waza, T., K. Kurita and H. Mizutani (1980), The effect of water on the subcritical crack growth in silicate rocks, Tectonophysics, 67, 25-34.

Whitten, C. A. (1956), Crustal movements in California and Nevada, Transactions of the American Geophysical Union, 37, 393-398.
Wiederhorn, S. M. (1967), Influence of Water Vapor on Crack Propagation in Soda-Lime Glass, J. Am. Ceram. Soc., 50, 407-414.
Wiederhorn, S. M. (1968), Moisture assisted crack growth in ceramics, Int. J. Fract. Mech., 4, 171-177.
Wiederhorn, S. M. (1978), Mechanisms of subcritical crack growth in glass, in Fracture Mechanics of Ceramics, Volume 4, edited by R. C. Bradt, D. P. H. Hasselman and F. F. Lange, pp. 549-580, Plenum Press, New York.
Wiederhorn, S. M. and L. H. Bolz (1970), Stress Corrosion and Static Fatigue of Glass, J. Am. Ceram. Soc., 53, 543-548.
Wiederhorn, S. M., A. Dretzke and J. Rodel (2002), Crack Growth in Soda–Lime–Silicate Glass near the Static Fatigue Limit, J. Am. Ceram. Soc., 85, 2287-2292.
Wiederhorn, S. M., A. Dretzke and J. Rodel (2003), Near the static fatigue limit in glass, Int. J. Fract. Mech., 121, 1-7.
Wiederhorn, S. M., S. W. Freiman, E. R. Fuller and C. J. Simmons (1982), Effects of water and other dielectrics on crack growth, J. Mat. Sci., 17, 3460-3478.
Wiederhorn, S. M. and H. Johnson (1972), Effect of Electrolyte pH on Crack Propagation in Glass, J. Am. Ceram. Soc., 56, 192-197.
Wiederhorn, S. M. and H. Johnson (1973), Influence of Sodium-Hydrogen Ion Exchange on Crack Propagation in Soda-Lime Silicate Glass, J. Am. Ceram. Soc., 56, No. 2, 108-109.
Wilkins, B. J. S. (1980), Slow Crack Growth and Delayed Failure of Granite, Int. J. Rock Mech. Min. Sci. Geomech. Abstr., 17, 365-369.
Wilkins, B. J. S. and R. Dutton (1976), Static Fatigue Limit with Particular Reference to Glass, J. Am. Ceram. Soc., 59, 108-112.
Winkler, K. W. and W. F. Murphy III (1995), Acoustic velocity and attenuation in porous rocks, in Rock Physics and Phase Relations, edited by T. J. Ahrens, pp. 20-34, AGU reference shelf.
Wong, T.-F. (1982), Effects of temperature and pressure on failure and post-failure behaviour of Westerly granite, Mech. Mat., 1, 3-17.
Wong, T.-F., C. David and W. Zhu (1997), The transition from brittle faulting to cataclastic flow in porous sandstones: Mechanical deformation, J. Geophys. Res., 102, 3009-3025.
Wood, D. S. (1973), Patterns and magnitudes of natural strain in rocks, Phil. Trans. R. Soc. Lond., 274, 373-382.
Wu, F. J. and L. Thomsen (1975), Microfracturing and deformation of Westerly granite under creep condition, Int. J. Rock Mech. Min. Sci. Geomech. Abstr., Abst. 12, 167-173.
Wu, X. Y., P. Baud and T.-F. Wong (2000), Micromechanics of compressive failure and spatial evolution of anisotropic damage in Darley Dale sandstone, Int. J. Rock Mech. Min. Sci., 37, 143-160.
Yanagidani, T., S. Ehara, O. Nishizawa, K. Kusunose and M. Terada (1985), Localization of dilatancy in Ohshima granite under constant uniaxial stress, J. Geophys. Res., 94, 6840-6858.
Yoshida, S., O. C. Clint and P. R. Sammonds (1998), Electric potential changes prior to shear fracture in dry and saturated rocks, Geophys. Res. Lett., 25, No. 10, 1577-1580.
Zang, A., F. C. Wagner and G. Dresen (1996), Acoustic emission, microstructure, and damage model of dry and wet sandstone stressed to failure, J. Geophys. Res., 101, 17507-17521.
Zhang, J., T.-F. Wong and D. M. Davis (1990), Micromechanics of Pressure-Induced Grain Crushing in Porous Rocks, J. Geophys. Res., 95, No. B1, 341-352.
Zhu, W. and T.-F. Wong (1997), The transition from brittle faulting to cataclastic flow: Permeability evolution, J. Geophys. Res., 102, No. B2, 3027-3041.
Zoback, M. D. and J. D. Byerlee (1975), The Effect of Microcrack Dilatancy on the Permeability of Westerly Granite J. Geophys. Res., 80, No. 5, 752-755.
Zoback, M. L. and M. Magee (1991), Stress magnitudes in the crust: constraints from stress orientation and relative magnitude data, Phil. Trans. R. Soc.: Phys. Eng. Sci., 337, 181-194.

Zoback, M. L., M. D. Zoback, J. Adams, M. Assumpcao, S. Bell, E. A. Bergman, B. P., N. R. Brereton, D. Denham, J. Ding, K. Fuchs, N. Gay, S. Gregersen, H. K. Gupta, A. Gvishiani, K. Jacob, R. Klein, P. Knoll, M. Magee, J. L. Mercier, B. C. Muller, C. Paquin, K. Rajendran, O. Stephansson, G. Suarez, M. Suter, A. Udias, Z. H. Xu and M. Zhizhin (1989), Global patterns of tectonic stress, Nature, 341, 291-298.